Department of Physics, Imperial College London

A thesis submitted in partial fulfilment of the requirements for the degree of Doctor of Philosophy

---

Novel materials and device architectures for high-efficiency solar cells

---

Phoebe May Pearce

Supervisors

Dr. N. J. Ekins-Daukes

Prof. J. Nelson

Dr. A. D. Johnson

Imperial College London

January 25, 2021

Abstract

High-efficiency solar photovoltaic cells require suitable high-quality semiconductor materials and careful optical design. This thesis offers a comprehensive overview of the spectroscopic characterization of a novel alloy for use in multi-junction solar cells, silicon-germanium-tin (SiGeSn), and of simulation and theoretical methods suitable for designing efficient solar cells and modelling realistic devices.

The SiGeSn material study uses spectroscopic ellipsometry, temperature and power-dependent photoluminescence, photoreflectance, and reflection and transmission measurements to investigate the band structure of Ge-rich SiGeSn alloys with up to 10% Si and 3% Sn. These epitaxially-grown alloys are shown to be lattice-matched to Ge and GaAs substrates through X-ray diffraction (XRD) measurements, allowing them to be incorporated into commonly-used multi-junction solar cell architectures. A 1 eV direct transition, useful for two, three or four-junction solar cells, is observed for SiGeSn compositions around 8% Si and 2% Sn, although the alloy retains a fundamentally indirect bandgap at these compositions. A novel technique for analyzing photoreflectance data, incorporating both interference effects and critical point features in a self-consistent way, was also developed to fit the SiGeSn photoreflectance data.

Optical modelling of solar cell structures is essential for efficient device design, to maximize absorption in the photovoltaic layers, and for understanding the behaviour of real devices. This thesis demonstrates the use of multiple modelling techniques, including rigorous coupled-wave analysis (RCWA), used to design and model diffraction grating structures for ultra-thin (< 100 nm) GaAs cells, and the transfer matrix method (TMM), used to model multi-junction cells containing SiGeSn and spectrum-splitting multi-junction devices targeting efficiencies over 40%. An integrated modelling method based on angular redistribution matrices calculated through a combination of ray-tracing and the transfer matrix method was used to investigate the infra-red emissivity of silicon heterojunction cells and a perovskite/Si tandem cell. In each case, much original work was done on the code base for these methods, including contributions to open-source solar cell modelling codes.

Statement of Originality

I declare that the contents of this thesis are my own work. The results of previous work by others, including figures and data, are credited through citation in the text. Contributions by others to this work, such as measurements used in the analysis, are acknowledged where relevant. No part of the results or materials presented in this thesis have previously been submitted for any other academic degrees or qualifications.

Copyright Declaration

The copyright of this thesis rests with the author. Unless otherwise indicated, its contents are licensed under a Creative Commons Attribution-Non Commercial 4.0 International Licence (CC BY-NC). Under this licence, you may copy and redistribute the material in any medium or format, under the conditions that you credit the author and do not use it, or any derivative works, for a commercial purpose. You may also create and distribute modified versions of the work. When reusing or sharing this work, ensure you make the licence terms clear to others by naming the licence and linking to the licence text. Where a work has been adapted, you should indicate that the work has been changed and describe those changes. Please seek permission from the copyright holder for uses of this work that are not included in this licence or permitted under UK Copyright Law.

Acknowledgements

First of all, I would like to thank Ned for proposing the project that ultimately became this thesis (and proofreading it twice!), and guiding me along the way, even after moving to a different continent. Although there are certainly downsides to having a supervisor who lives on the other side of the world, being able to visit Sydney for work also has its perks, like being able to escape British winters! Having the freedom to work on topics I was interested in with someone supporting me along the way and always encouraging me to visit conferences and collaborators has made my PhD a great experience and I really feel like I have learned a lot in the past four years. Although it has now sadly come to an end at Imperial, it was a privilege to work in the Quantum Photovoltaics group and I would like to thank all the group members who helped me along the way, gave advice, and made group dinners at Belgo such a fun experience. I would also like to thank Jenny Nelson for stepping in as my Imperial supervisor when necessary, being available to talk through my work, and letting me join her research group (and Jenny, I am sorry for all the additional admin being my supervisor caused for you!). A big part of this thesis would not have been possible without the financial and scientific support of IQE, and especially my industrial supervisor Andrew Johnson – it was great to feel that my input was always taken seriously and made a real difference to the work at IQE, and getting that kind of real-time feedback is something a lot of scientists don't get to experience!

The work in this thesis would not have happened, or would certainly be much worse, without the help of a large number of people at Imperial and collaborating institutions. In particular I'd like to thank Tom Wilson and Diego Alonso Álvarez for their guidance in the labs at Imperial (and with Python!), Louise Hirst, Larkin Sayre and Eduardo Camarillo Abad at the University of Cambridge, Michael Nielsen and Jessica Yajie Jiang at UNSW, Chris Broderick at the Tyndall National Institute, Aled Morgan at IQE, and Eng Soon Tok and Ong Sheau Wei at the National University of Singapore. Louise Hirst deserves a special mention for making so much effort to get me access to labs and resources at Cambridge as the Quantum Photovoltaics group at Imperial came to an end, and I am looking forward to continuing to work with her as a postdoc in the coming months.

I'd like to thank Tom, Daan and Elysia for sharing both the highs and lows of post-graduate life with me and being willing to sacrifice their own productivity for countless coffee breaks in the Level 5 common room and overly long lunches (with the rest of the regular EXSS lunch crew) in the Level 8 common room. Many thanks to Ellen, Charlotte, Sam, John, Harry, Shenyue, Eddy and Eva, and everyone else who helped me maintain some work-life balance and allowed me to periodically bore you with my laments about academic life.

I would probably not have ended up doing a PhD if it weren't for the encouragement

and support of my parents and my sister when I was at school and university, although this encouragement does mean I have spent most of the last ten years away from home. Chris, Hermien, Sarah: I promise I will try to get a job in the Netherlands in the not-too-distant future!

Finally, I would like to thank Luis for encouraging me to learn R, but more importantly for remaining positive and helping me find perspective when I was struggling by having a much stronger belief in my abilities than I do.

Contents

List of Figures **10**

List of Tables **15**

List of Publications **17**

List of Abbreviations **19**

1 Introduction & background **21**
1.1 Solar spectrum . . . 21
1.2 Photovoltaic technologies . . . 22
1.3 High-efficiency photovoltaics . . . 24
1.3.1 Multi-junction photovoltaics . . . 24
1.4 SiGeSn in multi-junction solar cells . . . 29
1.4.1 Growth of SiGeSn . . . 30
1.4.2 Band structure of Si, Ge and Sn and SiGeSn . . . 31
1.4.3 Optical and structural measurements of SiGeSn . . . 34
1.5 Advanced light management strategies . . . 36
1.5.1 Light trapping design and modelling . . . 37
1.5.2 Ultra-thin GaAs cells . . . 39
1.5.3 Emissivity of solar cells . . . 41
1.6 Structure of the thesis . . . 42

2 Theory **44**
2.1 Direct and indirect semiconductors . . . 44
2.2 Optical constant models . . . 47
2.2.1 Critical point parabolic band models . . . 47
2.2.2 Critical point analysis . . . 50
2.3 Light-trapping . . . 54

2.3.1 Transfer matrix model . . . 54
2.3.2 Fabry-Perot and guided mode analysis . . . 57
2.3.3 Rigorous coupled-wave analysis . . . 59
2.4 Solar cell operation . . . 62

3 Experimental and computational methods 67
3.1 SiGeSn sample growth . . . 67
3.1.1 Composition and structural measurements . . . 68
3.2 Spectroscopic ellipsometry . . . 68
3.2.1 Measurement . . . 68
3.2.2 Optical constant fits . . . 70
3.2.3 Critical point fits . . . 72
3.3 Photoreflectance . . . 72
3.3.1 Measurement . . . 74
3.3.2 Fitting . . . 74
3.4 Photoluminescence measurements . . . 77
3.4.1 Measurement of the laser spot size . . . 78
3.4.2 Spectral corrections . . . 80
3.5 FTIR reflection and transmission measurements . . . 81
3.6 Electrical measurements . . . 81
3.7 Differential evolution . . . 81

4 Development of optical modelling tools 84
4.1 Solcore . . . 85
4.1.1 Transfer-matrix method . . . 85
4.1.2 Rigorous coupled-wave analysis . . . 86
4.1.3 Comparison of optical models . . . 87
4.1.4 Use of custom materials . . . 88
4.2 Integrating coherent and incoherent models: RayFlare . . . 90
4.2.1 Ray-tracing . . . 91
4.2.2 Ray-tracing with integrated TMM . . . 98
4.2.3 Matrix framework for multi-scale optical calculations . . . 99
4.2.4 Absorption in individual layers . . . 105
4.2.5 Absorbing incidence media . . . 107
4.2.6 Ideal cases . . . 108
4.2.7 Storing information . . . 109
4.2.8 Matrix method validation . . . 109
4.2.9 Application of integrated optical modelling . . . 114

4.2.10 Planned further work . . . 116
4.3 The effect of optical constants on modelling results . . . 120
4.3.1 Optical constant sources . . . 122
4.3.2 Simulated structures . . . 123
4.3.3 Simulation method . . . 123
4.3.4 Optimization . . . 124
4.3.5 Results . . . 126
4.3.6 Case study of impact on solar-cell modelling . . . 129
4.3.7 Origin of divergence . . . 129
4.3.8 Defining the Spectral Absorption Enhancement Factor of metals . . . 131

5 Characterization of silicon-germanium-tin alloys 133
5.1 Structural measurements . . . 133
5.2 Investigation of the direct transitions . . . 137
5.2.1 Spectroscopic ellipsometry results . . . 137
5.2.2 Photoreflectance . . . 141
5.2.3 Reflection and transmission measurements . . . 141
5.2.4 Comparison of ellipsometry and photoreflectance results . . . 144
5.3 Photoluminescence . . . 145
5.3.1 Room-temperature power-dependence . . . 147
5.3.2 Peak fits . . . 150
5.3.3 Temperature-dependence . . . 152
5.3.4 Assignment of PL peaks . . . 155
5.4 Summary of critical points and theory comparison . . . 157
5.5 Device modelling . . . 158

6 Light management in advanced cell designs 163
6.1 Ultra-thin GaAs solar cells . . . 163
6.1.1 Device growth and measurement . . . 164
6.1.2 RCWA simulations . . . 167
6.1.3 Optical constants . . . 167
6.1.4 Structure optimization . . . 168
6.1.5 Guided mode analysis . . . 169
6.1.6 Device measurements . . . 171
6.1.7 Predicted efficiencies . . . 174
6.1.8 Conclusions . . . 174
6.2 Emissivity of heterojunction devices in the infrared . . . 176
6.2.1 Methods & structures . . . 176

6.2.2 Results . . . 178
6.2.3 Designing low-emissivity cells . . . 180
6.3 Application of Solcore to spectrum-splitting multi-junction cell design . . 183
6.3.1 Cell designs . . . 183
6.3.2 Results . . . 185

7 Conclusions **191**
7.1 Development of optical modelling tools . . . 191
7.2 Application of SiGeSn to multi-junction cells . . . 192
7.3 Optical design of advanced devices . . . 193

Bibliography **195**

Appendices **208**

A Proof of Adachi dielectric function representation **210**

B Wavevectors and power flow in absorbing media **213**

C Solcore code listings **217**

D Convergence of ray-tracing calculations **220**

E Ellipsometry of ultra-thin GaAs cell structures **223**

F Critical point fitting **225**
F.1 Details of photoreflectance equation . . . 225
F.2 Photoreflectance model fitting details . . . 226
F.3 Second-derivative critical point fits . . . 227

G SiGeSn structural measurements & photoluminescence **230**
G.1 Structural measurements . . . 230
G.2 Room-temperature photoluminescence of SiGeSn . . . 234
G.3 Temperature-dependent PL . . . 237
G.4 Multi-junction device simulation . . . 238

H Copyright permissions **244**

List of Figures

1.1 Standard solar spectra. . . . 22
1.2 Best research cell efficiency, grouped by cell technology. This plot is courtesy of the National Renewable Energy Laboratory, Golden, CO. . . . 23
1.3 Fundamental losses in solar cells. . . . 24
1.4 The AM1.5G solar spectrum [15] in terms of photon flux, and where different parts of the spectrum would be absorbed in a 4J device made of materials with 'perfect' bandgaps. . . . 25
1.5 Energy gap versus lattice parameter of group III-V and IV materials and their alloys. . . . 26
1.6 Variation of 4J cell efficiency depending on the bandgaps of the middle cells. . . . 27
1.7 Illustration of how sub-cells in a multi-junction cell are connected by a tunnel junction. . . . 27
1.8 External quantum efficiency and light I-V curve of a typical InGaP/InGaAs/Ge triple-junction solar cell. . . . 28
1.9 Electronic band structures of a) Si, b) Ge and c) α-Sn, calculated through a non-local pseudopotential method. From [49]. . . . 31
1.10 Calculated lattice constant and transition energies for SiGeSn alloys. . . . 33
1.11 Band alignment for SiGeSn grown on Ge with different barrier layers. . . . 35
1.12 Optical sheets with a) planar surface and b) a randomizing surface texture with acceptance angle θ. . . . 36

2.1 Electronic band structure of Ge and GaAs. . . . 45
2.2 Phonon dispersion for Ge. From [49]. . . . 46
2.3 Emission and absorption in direct and indirect semiconductors. . . . 46
2.4 Absorption coefficients of undoped Si [129], Ge [130] and GaAs [131]. . . . 47
2.5 Functional form of the contribution to the imaginary part of the dielectric constant from different types of critical points in the band structure, in two and three dimensions. From [87]. 49
2.6 Critical Point Parabolic Band (CPPB) model fit to optical constant data for Ge. . . . 51
2.7 The relationship between derivatives of the dielectric function and photomodulation spectroscopy in Ge. . . . 52
2.8 Resonant Fabry-Perot (thin-film) and guided modes in an ultra-thin solar cell. . . . 57
2.9 Convergence of RCWA algorithm S^4 for structure containing metal/dielectric interfaces. . . . 61
2.10 Schematic of a p-n junction solar cell. . . . 64
2.11 Example of IV and EQE measurements. . . . 65

3.1 Schematic of the layer structure of the epitaxial SiGeSn samples. . . . 67
3.2 Schematic of ellipsometry measurement. . . . 69

3.3 Illustration of fitting to the second derivative of the dielectric function. 73
3.4 Diagram of the photoreflectance measurement setup. 74
3.5 Schematic of the photoluminescence setup. 78
3.6 Measurement of the laser spot size. 79
3.7 Normalized detector response for the Hamamatsu G7754-01 extended InGaAs detector (based on data supplied by Hamamatsu). 80

4.1 Overall structure and workflow of Solcore. From [161]. 84
4.2 Coherent and incoherent optical calculations using the TMM in Solcore. 86
4.3 Polarization-dependent optical calculations using the TMM in Solcore. 86
4.4 Comparison of the Beer-Lambert law, TMM, and RCWA optical solvers in Solcore applied to a GaAs cell with scattering nanoparticles. 87
4.5 The optical constants of one of the SiGeSn samples, as measured through spectroscopic ellipsometry (see Section 5.2). 89
4.6 Comparing the optical constants of silver from different sources using Solcore. 89
4.7 Schematic of the angular matrix framework. 91
4.8 a) Intersection of a line with a finite, triangular plane. b) Reflection and transmission of a ray through an interface (in this case, from low to high refractive index). 93
4.9 Schematic of 3D pyramid ray-tracing. 95
4.10 Comparison of the performance of RayFlare's ray-tracer and PVLighthouse. 96
4.11 Path length enhancement in an Si substrate with regular and random pyramid texturing. . . 97
4.12 Comparison of the bulk absorption and front surface reflection R_0 for different structures with increasingly Lambertian behaviour. 99
4.13 Schematic showing the labelling conventions used in RayFlare. 100
4.14 Schematic of the angle conventions used in RayFlare, and how they are transformed for incoming and outgoing light paths. 102
4.15 Schematic of a) the layout of the redistribution matrices for each surface and the angular vector $\vec{v}$ and b) the corresponding processes at the interface. 104
4.16 Four-junction solar cell structure used for validation of the RayFlare angular matrix method. 109
4.17 Validation of the different RayFlare optical methods for a planar multi-layer structure. 110
4.18 Validation of the different RayFlare optical methods for a planar multi-layer structure with angle and polarization variation. 111
4.19 Comparison of the results generated by RayFlare and OPTOS. 112
4.20 Examples of the angular redistribution matrices generated by RayFlare. 113
4.21 Structure of a perovskite/Si tandem cell structure. 114
4.22 Optical response (reflection and absorption per layer) of the perovskite/Si tandem cell modelled using RayFlare. 115
4.23 Redistribution matrices for the perovskite/Si tandem cell. 115
4.24 Example of the reflection, transmission, and absorption probability lookup-tables produced using TMM in RayFlare. 117
4.25 Escape reflection and absorption in the Si per pass for the perovskite/Si structure. 118
4.26 Wavelength-dependent absorption profiles in the perovskite-Si tandem cell, and the effect of modifications to the structure. 118
4.27 Optical constants for metals. 121

4.28 LSPQ values for metals. . . . 121
4.29 Schematic of the model solar cell structure for investigation into optical constant discrepancies for metals. . . . 123
4.30 Convergence of the GD-calc RCWA simulations, and optimal grating thickness for the model solar cell. . . . 125
4.31 Predicted photogenerated current J_{ph} as a function of array period and metal coverage using various Ag optical constant data sets. . . . 125
4.32 Optimum configuration of nanodisks for each optical constant source. . . . 126
4.33 Current variation with metal coverage for all simulations. . . . 127
4.34 Absorptivity in an optimized solar cell structure for several Au optical constant data sets. . . . 127
4.35 Absorption and photogenerated current in a thin GaAs cell as reported in Massiot et al. (2014) when different optical constant sources for Ag are used. . . . 130
4.36 Demonstration of the predictive value of the Spectral Absorption Enhancement Factor. . . . 131

5.1 Composition of the SiGeSn samples and critical thickness estimates for epitaxial SiGeSn. . . . 134
5.2 XRD reciprocal space maps and optical microscopy of SiGeSn samples. . . . 136
5.3 Ellipsometric angles Ψ and Δ for the different SiGeSn sample sets. . . . 137
5.4 Pseudo-dielectric functions for the different SiGeSn sample sets. . . . 138
5.5 Dielectric function of the SiGeSn samples obtained through ellipsometry data fitting. . . . 138
5.6 Simplified band structure of SiGeSn showing key transition energies. . . . 139
5.7 Critical point fitting for the second derivative of the dielectric constant around E_0. . . . 139
5.8 Photoreflectance measurements of Ge and SiGeSn samples around the E_0 energy. . . . 140
5.9 Critical point fits to PR data. . . . 141
5.10 Combined critical point and interference model fit to PR data of SiGeSn samples. . . . 142
5.11 Reflection, transmission, and calculated absorption in SiGeSn samples. . . . 143
5.12 Summary of centre energies for the different direct transitions extracted from SE and PR data. 145
5.13 Power-dependent room-temperature PL of a piece of Ge substrate measured with incident laser intensity between 1.05 and 10.5 kW/cm^2. . . . 147
5.14 Power-dependent room-temperature PL of SiGeSn samples. . . . 148
5.15 Integrated room-temperature PL intensity variation with laser power. . . . 148
5.16 Low-temperature power-dependent PL of Ge. . . . 150
5.17 Gaussian and Lorentzian fitting to Ge and SiGeSn PL data. . . . 151
5.18 Power dependence of individual peaks in the room-temperature Ge PL spectra. . . . 152
5.19 Temperature-dependent PL, on a logarithmic scale, of Ge measured at a laser intensity of 2.04 kW/cm^2. . . . 153
5.20 Low-temperature PL spectra of Ge and SiGeSn. . . . 154
5.21 Centre energies for the highest-energy room-temperature PL peak for each sample 155
5.22 Indirect bandgaps estimated from photoluminescence data of the SiGeSn samples. . . . 156
5.23 Device architectures for MJ solar cells with a SiGeSn sub-cell. . . . 159
5.24 Simulated EQE and J-V curves under illumination for monolithic device architectures containing SiGeSn. . . . 161

6.1 Ultra-thin GaAs device and grating structure. . . . 165

6.2 Direction of travel for several diffraction orders from a hexagonal grating at different grating periods. . . . 166
6.3 Refractive indices of the materials used in the ultra-thin GaAs cells. . . . 167
6.4 Absorption and reflection for optimized structures at different grating periods. . . . 168
6.5 Results of the differential evolution optimization of the ultra-thin GaAs cells. . . . 169
6.6 Comparison of RCWA results and guided mode analysis in the ultra-thin cells, depending on grating period and wavelength. . . . 170
6.7 Light IV and EQE measurements of on-substrate devices. . . . 172
6.8 EQE measurement and models of devices with metal gratings. . . . 173
6.9 Structure of a silicon heterojunction solar cell. . . . 177
6.10 The layers used to calculate R, A and T probabilities using TMM for a) the front surface and b) the rear surface . . . 177
6.12 Calculated emissivity for the heterojunction cell, with and without ITO on the front surface. 179
6.13 Calculated emissivity for the heterojunction cell with different ITO layer thicknesses. . . . 181
6.14 Schematic of a spectrum-splitting setup design with a selectively reflecting dielectric filter in front of the 3J cell. . . . 184
6.15 Schematic of the lattice-matched 3J cell structure. From [204]. . . . 184
6.16 Modelled EQE and light IV of a standard 3J lattice-matched (LM) cell. . . . 186
6.17 Modelled EQE and light IV of a 3J LM cell with integrated DBR. . . . 187
6.18 Modelled EQE and light IV of a standard 3J metamorphic (MM) cell. . . . 189
6.19 Modelled EQE and light IV of a MM cell with integrated DBR. . . . 190

A.1 The function $y = \frac{\gamma}{x^2+\gamma^2}$ evaluated at different values of γ. . . . 211

B.1 Variation of the real and imaginary part of the complex wavevector angle $\tilde{\theta}$ for a Poynting vector travelling at a certain incidence angle. . . . 215
B.2 R and T for unpolarized light incident from air on a medium with $n = 2$ and varying κ. . . . 216
B.3 R for light incident from a medium with $n = 4$ on a medium with $n = 2$ at incidence angles θ between 0 and 90 degrees. . . . 216

D.1 Variation of the RMS error depending on the number of rays traced at each wavelength and surface points scanned. . . . 221
D.2 Convergence of the absorption vs. wavelength calculation for a 200 µm Si wafer with inverted, regular pyramids on the front surface and a planar rear surface . . . 222

E.1 Spectroscopic ellipsometry data and multi-layer model fit at three different incidence angles for an epitaxial ultra-thin GaAs sample. . . . 224

F.1 Fits (lines) to the E_1 and $E_1 + \Delta_1$ critical point for Ge and Set A and Set B SiGeSn samples. The arrows indicate the critical point centre energies fitted. . . . 227
F.2 Fits (lines) to the E_0' critical point for Ge and Set A and Set B SiGeSn samples. The arrows indicate the critical point centre energies fitted. . . . 228
F.3 Fits (lines) to the E_2 critical point for Ge and Set A and Set B SiGeSn samples. The arrows indicate the critical point centre energies fitted. . . . 228

G.1 XRD reciprocal space maps (RSM) for Set A SiGeSn samples. 231
G.2 Optical microscopy using a polarizer and Nomarski prism of Set A SiGeSn samples 232
G.3 Optical microscopy using a polarizer and Nomarski prism of Set B SiGeSn samples 233
G.4 Low-energy power-dependent PL at room temperature of the four SiGeSn samples with weaker PL intensities. 234
G.5 Dependence of fitted peak centre energy and peak strength on laser intensity for the individual peaks fitted to Set A SiGeSn PL data. 235
G.6 Dependence of fitted peak centre energy and peak strength on laser intensity for the individual peaks fitted to Set B SiGeSn PL data. 236
G.7 Temperature-dependent PL of SiGeSn, showing the raw data and smoothed lines. 237

List of Tables

1.1 Literature values for transition energies in Si, Ge and α-Sn at room temperature, and their lattice constants. . . . 34

2.1 The functional forms as given by the Adachi model for the lowest-energy transitions contributing to the dielectric function of Ge. . . . 50

4.1 Layer structure of a perovskite/Si tandem cell. . . . 113
4.2 Sources used for metallic optical constant data. . . . 122
4.3 Detailed simulation results showing the J_{ph} without nanoparticles and the optimal arrangement in terms of period and metal coverage leading to maximum photogenerated current. . . . 128
4.4 Best and worst outcomes, and the mean, using the nanodisk arrangements highlighted in Table 4.3. . . . 128

5.1 Sample structures, thickness (from SE fitting) d_{SiGeSn}, and composition of the SiGeSn samples. 135
5.2 Summary of centre energies fitted to model dielectric constants from SE, and to PR data, of SiGeSn and Ge samples. . . . 146
5.3 Key parameters fitted to the photoreflectance and ellipsometry data. . . . 146
5.4 Power law exponents fitted to the peak and integrated intensity of PL data for Ge and SiGeSn samples. . . . 149
5.5 Summary of some parameters from this and previous work on Ge photoluminescence. . . . 149
5.6 Summary of the peaks observed in the room-temperature PL spectra of Ge and the SiGeSn samples, and the bandgap obtained from the data. . . . 152
5.7 Summary of low-temperature PL peak locations and shift relative to Ge for the SiGeSn samples. 156
5.8 Efficiencies, open-circuit voltages (V_{OC}) and short-circuit currents (J_{SC}) for different cell designs incorporating SiGeSn sub-cells. . . . 160
5.9 Comparison of the simulated SiGeSn devices under 1 Sun and 400 Sun concentration. . . . 162

6.1 Calculated photogenerated current J_{ph} for several ultra-thin GaAs cell structures, as well as predicted efficiencies η under an AM0 spectrum. . . . 173
6.2 Layer thicknesses in the SHJ structure shown in Fig. 6.9, and the optical constant sources for each layer. . . . 178
6.3 The sub-cell short-circuit currents and efficiencies of the different 3J cell designs, and the Si cell and total efficiencies for the spectrum-splitting designs. . . . 185

E.1 Structure of the six ultra-thin GaAs epitaxy samples with different layers removed through chemical etching, and the layer thicknesses fitted to these structures. 223

F.1 All parameters used in fitting the photoreflectance data to a model incorporating both the critical point feature and the effects of thin-film interference. 226
F.2 Parameters fitted to the second derivative (multiplied by E^2) of the real and imaginary parts of the dielectric function of Ge and SiGeSn samples. 229
F.3 Full results of fits to the photoreflectance data using the combined thin-film interference and critical point model. 229

List of Publications

Journal Publications

1. **Pearce, P.**, Mellor, A. and Ekins-Daukes, N. (2019). *The importance of accurate determination of optical constants for the design of nanometallic light-trapping structures*, Solar Energy Materials and Solar Cells, 191, pp. 133–140. doi: 10.1016/j.solmat.2018.11.008.

2. Alonso-Álvarez, D., Wilson, T., **Pearce, P.**, Führer, M., Farrell, D., Ekins-Daukes, N. (2018). *Solcore: a multi-scale, Python-based library for modelling solar cells and semiconductor materials*, Journal of Computational Electronics, 17(3), pp. 1099–1123. doi: 10.1007/s10825-018-1171-3

3. Wilson, T., Hylton, N. P., Harada, Y., **Pearce, P.**, Alonso-Álvarez, D., Mellor, A., Richards, R. D., David, J. P. R. and Ekins-Daukes, N. J. (2018). *Assessing the Nature of the Distribution of Localised States in Bulk GaAsBi*, Scientific Reports, 8(1), p. 6457. doi: 10.1038/s41598-018-24696-2.

4. Alonso-Álvarez, D., Augusto, A., **Pearce, P.**, Llin, L. F., Mellor, A., Bowden, S., Paul, D. J. and Ekins-Daukes, N. (2019). *Thermal emissivity of silicon heterojunction solar cells*, Solar Energy Materials and Solar Cells, 201, p. 110051. doi: 10.1016/j.solmat.2019.110051.

5. Jiang, Y., Keevers, M. J., **Pearce, P.**, Ekins-Daukes, N. and Green, M. A. (2019). *Design of an intermediate Bragg reflector within triple-junction solar cells for spectrum splitting applications*, Solar Energy Materials and Solar Cells, 193, pp. 259–269. doi: 10.1016/j.solmat.2019.01.011.

6. Pusch, A., **Pearce, P.** and Ekins-Daukes, N. J. (2019). *Analytical Expressions for the Efficiency Limits of Radiatively Coupled Tandem Solar Cells*, IEEE Journal of Photovoltaics, 9(3), pp. 679–687. doi: 10.1109/JPHOTOV.2019.2903180.

Conference Proceedings

1. **Pearce, P.**, Wilson, T., Johnson, A., Roucka, R., Clark, A., Thomas, T., Führer, M., Ekins-Daukes, N., Hoffman Jr, R., Begarney, D. (2017). *SiGeSn as a 1.0 eV component sub-cell in III-V multi-junction solar cells*, in 13th Photovoltaic Science, Applications and Technology Conference (PVSAT-13), Bangor, Wales.

2. **Pearce, P.**, Wilson, T., Johnson, A. and Ekins-Daukes, N. (2017). *III-V Multi-Junction Solar Cells Utilising Group IV SiGeSn Alloys as a 1.0 eV Component Sub-Cell*, in 33rd European Photovoltaic Solar Energy Conference and Exhibition, Amsterdam. pp. 1248–1252. doi: 10.4229/EUPVSEC20172017-4CV.4.5.

3. **Pearce, P.**, Wilson, T., Johnson, A. and Ekins-Daukes, N. (2018). *Characterization of SiGeSn for Use as a 1 eV Sub-Cell in Multi-Junction Solar Cells*, in IEEE 7th World Conference on Photovoltaic Energy Conversion (WCPEC) (A Joint Conference of 45th IEEE PVSC, 28th PVSEC 34th EU PVSEC), Waikoloa, Hawaii. pp. 0943–0948. doi: 0.1109/PVSC.2018.8547764.

4. **Pearce, P.**, Mellor, A. and Ekins-Daukes, N. (2018). *Quantifying Parasitic Losses From Metal Scattering Structures in Solar Cells: How Uncertainty in Optical Constants Affects Simulation Results*, in IEEE 7th World Conference on Photovoltaic Energy Conversion (WCPEC) (A Joint Conference of 45th IEEE PVSC, 28th PVSEC 34th EU PVSEC), Waikoloa, Hawaii. pp. 2918–2923. doi: 10.1109/PVSC.2018.8548090.

5. **Pearce, P.** and Ekins-Daukes, N. (2019). *Open-source integrated optical modelling with RayFlare*, in IEEE 46th Photovoltaic Specialists Conference (PVSC), Chicago, Illinois. pp. 2627–2633. doi: 10.1109/PVSC40753.2019.8980868.

6. **Pearce, P.**, Sayre, L., Johnson, A., Hirst, L., Ekins-Daukes, N. J. (2020). *Design of photonic light-trapping structures for ultra-thin solar cells*, in Physics, Simulation, and Photonic Engineering of Photovoltaic Devices IX, SPIE Photonics West 2020, San Francisco, California. doi: 10.1117/12.2550136

List of Abbreviations

AFM	Atomic force microscopy
AM	Air Mass
AM	Air Mass
ARC	Anti-reflection coating
BL	Beer-Lambert(absorption law)
CB	Conduction band
CPPB	Critical point parabolic band
CPV	Concentrator photovoltaics
CVD	Chemical vapour deposition
CW	Continuous wave
DBR	Distributed Bragg Reflector
DE	Differential evolution
DLARC	Double-layer anti-reflection coating
DTL	Displacement Talbot Lithography
EDX	Energy-dispersive X-Ray spectroscopy
EQE	External quantum efficiency
F-P	Fabry-Perot
FGR	Fermi's Golden Rule
FTIR	Fourier-transform infrared spectroscopy
IMM	Inverted metamorphic
IQE	Internal quantum efficiency
IR	Infrared
ITO	Indium tin oxide
IV	Current-voltage (measurement)
$\mathbf{J_{SC}}$	Short-circuit current density
LM	Lattice-matched
LSP	Localized surface plasmon
LSPQ	Localised surface plasmon quality factor
MBE	Molecular beam epitaxy
MIR	Mid-infrared
MJ	Multi-junction
MJSC	Multi-junction solar cell
MM	Metamorphic

MOVPE	Metal-organic vapour-phase epitaxy
NIR	Near-infrared
PL	Photoluminescence
PR	Photoreflectance
PSEMI	Parametrized semiconductor oscillator model
PV	Photovoltaic
RCWA	Rigorous coupled-wave analysis
RSM	Reciprocal space map (XRD)
SHJ	Silicon heterojunction solar cell
S-Q	Shockley-Queisser (limit)
SAEF	Spectral Absorption Enhancement Factor
SE	Spectroscopic ellipsometry
SEM	Scanning electron microscopy
TE	Transverse electric (*s*-polarized)
TEM	Transmission electron microscopy
TM	Transverse magnetic (*p*-polarized)
TMM	Transfer-matrix method
UHV	Ultra-high vacuum
UMM	Upright metamorphic
VASE	Variable-angle spectroscopic ellipsometry
VB	Valence band
$\mathbf{V_{OC}}$	Open-circuit voltage
XRD	X-ray diffraction

Chapter 1

Introduction & background

The world's total primary energy consumption in 2017 was 9,700,000 ktoe (kilotonne of oil equivalent), or 113,000 TWh, having more than doubled since the 1970s [1]. Around 20% of this energy is in the form of electricity, with the majority of energy consumed in the form of chemical fuels for heating and transport. As the mitigation of climate change becomes increasingly urgent, renewable energy technologies play a key role in reducing carbon dioxide and other greenhouse gas emissions, especially when combined with increased electrification of heating and transport. Currently, over 2500 GW of generation capacity from renewable energy sources (hydropower, wind energy, marine energy, solar energy, bioenergy, geothermal energy) is installed worldwide, accounting for 25% of electricity production, with the largest contributing energy source being hydropower [2]. Solar photovoltaic power generation accounts for 600 GW of the installed capacity, and is the fastest-growing renewable generation technology, with around 100 GW, or 20% of total globally-installed solar capacity, coming online in 2019. Solar energy is an incredibly abundant natural resource; assuming a reasonable average daytime solar irradiation inside the Earth's atmosphere of 1000 W/m^2, an amount of energy equal to that consumed annually (of all types) falls on the Earth in around an hour. Of course, the technological challenge is harnessing the Sun's energy efficiently. This chapter will introduce the solar spectrum as a resource, and provide an overview of current state-of-the-art photovoltaic technologies and how these relate to the current work. The final section outlines the structure of the rest of the thesis.

1.1 Solar spectrum

Radiation from the Sun closely approximates that of a black body at 5800K, the approximate temperatures of the Sun's surface, as shown in Fig. 1.1. The solar spectrum covers a wavelength range from the ultraviolet ($\approx$ 250 nm) to the mid-infrared ($\approx$ 3 µm). As shown in Fig. 1.1, sunlight above the atmosphere (AM0) has different properties to sunlight at the Earth's surface; the terrestrial spectrum shows significant gaps due to absorption of mainly infrared light by molecules in the atmosphere (most of the loss is due to water vapour, H_2O, O_2 (oxygen), O_3 (ozone) and CO_2 (carbon dioxide) also cause absorption). The 'AM' in the names of these spectra refers to the Air Mass, calculated as AM = $1/\cos(\beta)$, where β is the zenith angle of the Sun (for sunlight coming from directly overhead, the zenith angle is 0° and the Air Mass is 1); the larger the Air Mass, the longer the path of the light through the Earth's atmosphere. The AM1.5G spectrum gives typical global irradiance, including diffuse sunlight due to e.g. scattering by the atmosphere. The solar spectrum at the Earth's surface depends on location, cloud cover, time of day and other factors, which

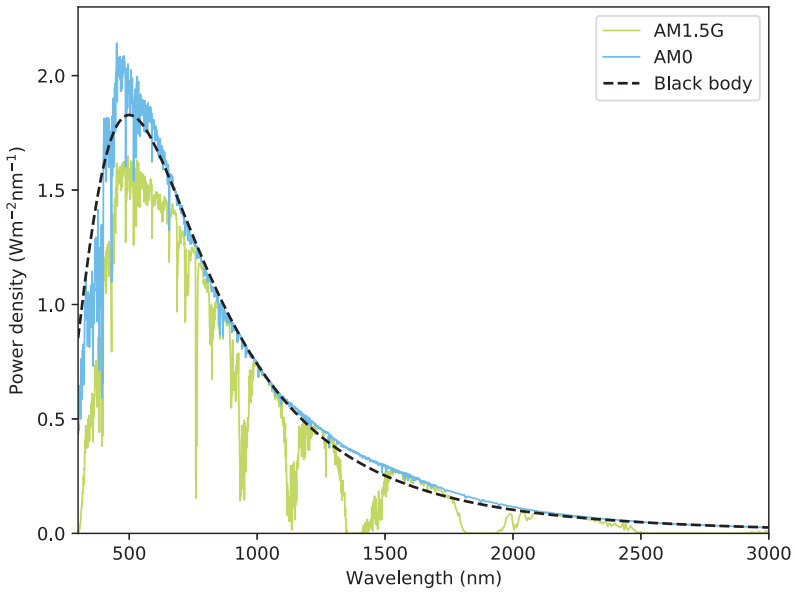


Figure 1.1: Three commonly-used standard spectra: the terrestrial AM1.5G (global irradiance) spectrum, the AM0 spectrum for space applications, and a black body at 5800 K (the temperature of the surface of the Sun).

may significantly affect the performance of a solar cell [3]. For benchmarking of solar cell technologies, solar simulators which can closely simulate reference spectra are used; these are generally AM1.5G for terrestrial, flat-plate photovoltaic (PV) applications and AM0 for space applications. The AM1.5G spectrum has a total power density of 1000 W/m^2, also called '1 Sun' of intensity, while the AM0 spectrum has a power density of 1366 W/m^2.

1.2 Photovoltaic technologies

Photovoltaic cells convert photons (light), usually from the Sun, into electricity. Silicon-based solar cells, both mono- and multi-crystalline silicon, currently make up over 90% of the market, with the remaining share divided between thin-film technologies, mostly copper indium gallium sulfide (CIGS) and cadmium telluride (CdTe). Mono- and multi-Si, CdTe, and CIGS solar cells are commercially mass-produced and available from multiple manufacturers. Many other PV technologies have been developed but have not been scaled up and commercialized to the same extent. Perovskite solar cells, containing both organic and inorganic materials, have made remarkable efficiency gains in only just over a decade of active research, but continue to suffer from stability issues. GaAs solar cells are a mature technology and have reached record efficiencies for single-junction solar cells, but are not mass-produced on the scale of other thin-film technologies or Si. Closely related to GaAs cells, and generally made using similar production methods, group III-V semiconductor based multi-junction cells are used primarily for space (e.g. satellite) applications and concentrator photovoltaics (CPV), and are available from various manufacturers but at extremely high cost compared to mass-produced technologies. The US National Renewable Energy Laboratory (NREL) tracks research cells with the highest certified efficiency of each type, as shown in Fig. 1.2. The efficiency of a solar cell is the percentage of energy in the solar spectrum converted into electrical energy. The highest efficiencies

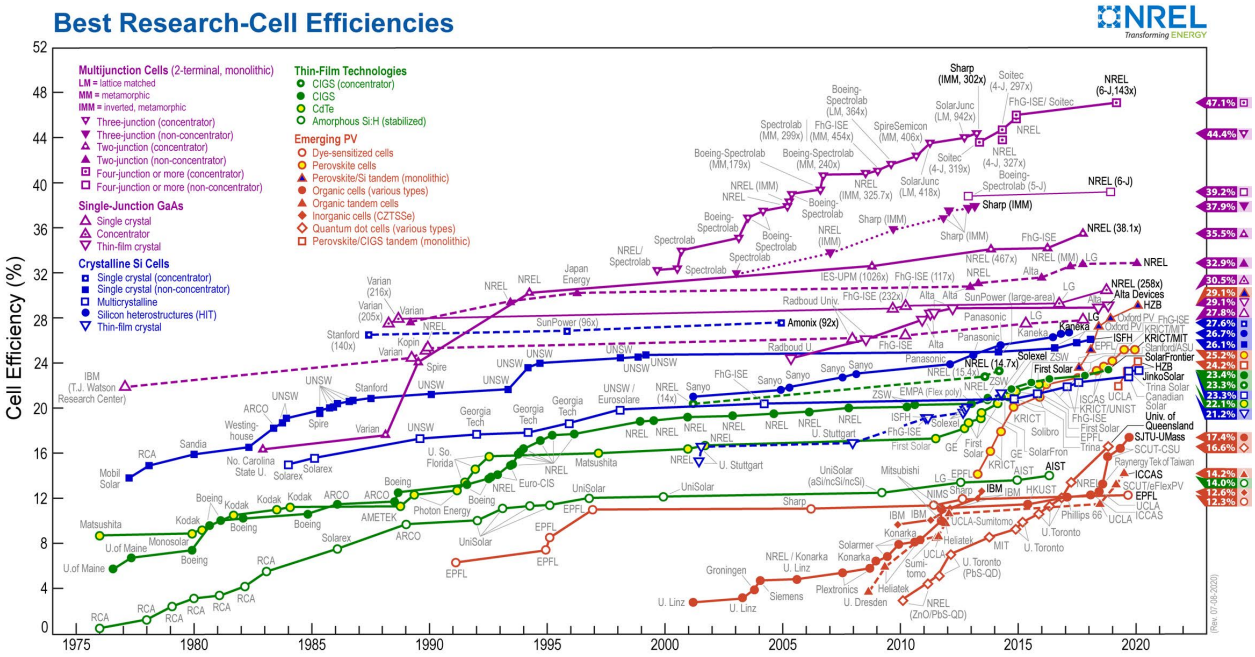


Figure 1.2: Best research cell efficiency, grouped by cell technology. This plot is courtesy of the National Renewable Energy Laboratory, Golden, CO.

are reached by multi-junction cells and single-junction GaAs cells (purple symbols), both with and without concentration of sunlight. The rapid increase in efficiency of perovskite solar cells since the mid-2010 is also clearly visible; perovskite solar cells are now reaching efficiencies similar to crystalline silicon cells, and perovskite-silicon tandem cells have recently been able to exceed the efficiency of crystalline silicon alone (the concept of 'tandem' or 'multi-junction' solar cells is discussed further in the next section).

Prices for solar cells are generally given in terms of US$/Wp ("watt-peak"), or kWp ("kilowatt-peak"), meaning the price per unit of installed PV which produces 1 W (or 1 kW) of power when illuminated at standard 1-Sun conditions. Si solar cells have seen dramatic cost reductions since 2010, with average module prices falling from around $2/Wp by about a factor of 5 to current prices, with current wholesale prices for typical Si cells (multi- and mono-Si) and modules around $0.30/Wp [4]. Multi-Si cells are somewhat cheaper than mono-Si cells, reflecting their generally slightly lower efficiencies. The low price of Si cells makes it difficult for other technologies, lacking the large cost reductions seen in Si driven by extensive R&D and economies of scale, to compete for standard large-area, flat-plate applications such as solar farms and rooftop PV, but other technologies are still promising in filling more niche applications where high efficiencies or high power density per unit volume/mass are important. Record efficiency Si cells have reached 26% efficiency without concentration of sunlight, approaching their fundamental physical limit of 31%, meaning that cell and module efficiencies of c-Si cells of this type will not undergo drastic efficiency improvements, although continued steady improvement in high-quality commercial products is likely. Silicon solar cells are also thicker and thus heavier than other PV technologies due to the intrinsic material properties of silicon (see Section 2.1). This means that for high-efficiency applications, for instance for use on satellites where space is very limited, and for applications where high power per unit area and/or unit mass are critical, other PV technologies remain of interest.

GaAs is ideally suited as a material for PV due to its fundamental properties, including a direct bandgap

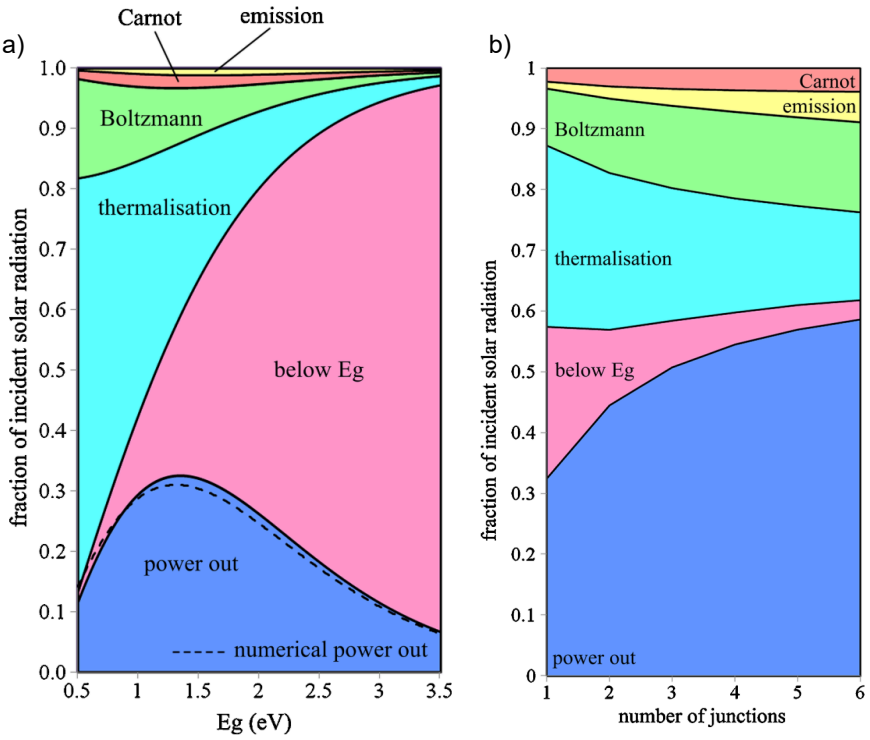


Figure 1.3: a) Fundamental losses in a single-junction solar cell as a function of bandgap energy. b) Fundamental losses in solar cells as a function of the number of junctions, assuming ideal bandgap combinations. From [6].

(as discussed in Section 2.1) at 1.42 eV, which is close to the optimum for a single-junction solar cell absorbing sunlight (see Fig. 1.3a), high electron mobilities, and high radiation tolerance. The record highest-efficiency thin-film cells made of a single junction (like the Si, CIGS and CdTe cells discussed above) are currently held by a GaAs cell at 29.1% [5]. However, the epitaxy-based production methods required to achieve high-quality GaAs (and related GaAs-based multi-junction cells), where atomic layers are deposited one at a time, lead to extremely high costs. GaAs-based cells are mostly used for space applications (e.g. satellites) and for use in concentrator photovoltaics (CPV); these are highly specialized applications, and thus these cells are not currently widely commercially available.

1.3 High-efficiency photovoltaics

1.3.1 Multi-junction photovoltaics

While single-junction solar cells have reached efficiencies of 29% (achieved by a thin-film crystal GaAs device [7, 5]), they are fundamentally limited by the Shockley-Queisser (S-Q) limit [8]. This assumes a solar cell consisting of a single material with an abrupt bandgap which absorbs all photons with energy above the bandgap, and none below, and has radiative recombination of electrons and holes as its only loss mechanism. Such loss due to radiative recombination is unavoidable; if photons can be absorbed and converted into energetic electrons in the conduction band, the reverse process must also be possible through the principle of detailed balance. Assuming a realistic solar spectrum (AM1.5G), the Shockley-Queisser limiting efficiency

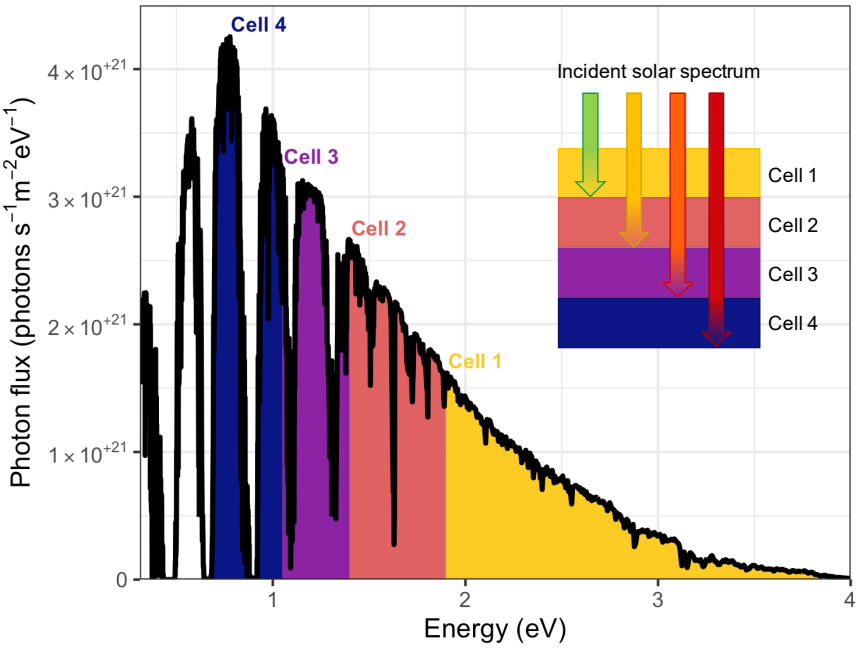


Figure 1.4: The AM1.5G solar spectrum [15] in terms of photon flux, and where different parts of the spectrum would be absorbed in a 4J device made of materials with perfect, abrupt bandgaps of 1.9 eV, 1.4 eV, 1.05 eV, and 0.66 eV (no absorption below the bandgap, 100% absorption above the bandgap), as shown in the inset.

is 33% for a semiconductor with an ideal bandgap. Although five contributing factors to intrinsic losses can be identified [6], the two dominant loss mechanisms are non-absorption of below-bandgap photons and thermalisation to the band edge[1], as shown in Fig. 1.3a. To mitigate one or both of these losses, alternatives to a single-bandgap p-n junction photovoltaic device must be used: possibilities for exceeding the S-Q limit include intermediate band solar cells [9], photon ratchet structures [10], up- or down-conversion [11], hot carrier capture [12, 13], multiple exciton generation [14] and multi-junction (MJ) cells.

Of the possible mechanisms for overcoming the S-Q limit, the only method which has exceeded this limit in practice are MJ cells. In MJ cells, junctions made of materials with different bandgaps are stacked so that each junction absorbs a part of the solar spectrum. An example of the absorption per cell for a four-junction (4J) device is shown in Fig. 1.4. Absorbing across multiple bandgaps, with light hitting the highest-gap material first (see the inset in Fig. 1.4), can reduce both non-absorption and thermalisation losses if a favourable combination of bandgaps is chosen, as shown in Fig. 1.3b. In the ideal case, sub-cells will transmit all photons which are too low in energy to be absorbed across their bandgap, allowing these photons to reach the lower sub-cells in the structure. While the different material layers must be optically connected, the sub-cells do not necessarily have to be electrically connected in series; some or all of the cells can have their own set of electrical contacts (a mechanically stacked cell) [16]. However, the need for multiple pairs of contacts introduces additional material requirements and manufacturing complexity, leading to higher costs and increasing the mass and footprint of the cell. A MJ cell with the sub-cells grown connected in series electrically, with one set of contacts, is called a monolithic two-terminal cell. Although

[1]Real solar cells also suffer further losses due to e.g. resistance, non-radiative recombination and contact shadowing; these losses, however, are theoretically avoidable ('extrinsic'), and thus not included in calculations of theoretical limiting efficiency [6].

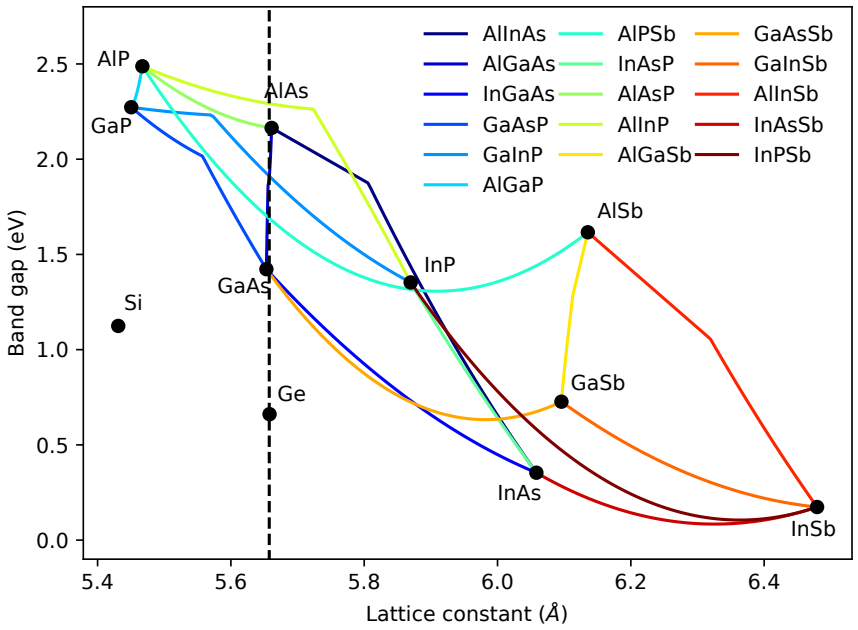


Figure 1.5: Energy gap versus lattice parameter of group III-V and IV materials and their alloys. The black dashed line shows the lattice constant of Ge.

the monolithic approach requires less material for contacting and reduces bulk, other issues arise: since the sub-cells are connected in series, their voltages will add, but the overall current which can flow through the device will be limited by the lowest sub-cell current. Thus, in constructing a monolithic MJ device, careful attention must be paid to the balance of photons absorbed in each layer in order to current-match the sub-cells. Monolithic devices also pose challenges on the material growth side; growing materials with very different lattice constants in a single stack is challenging and likely to introduce defects. Growing connected layers of different materials requires either matching of the lattice constant ('lattice-matching') between each different layer or the use of other strategies such as wafer-bonding or grading layers to gradually change the lattice constant, since lattice-matched materials with the desired bandgap may not be available (Fig. 1.5).

Most multi-junction cells, especially those for commercial applications, use a two-terminal architecture. The individual sub-cells are connected electrically in series by way of tunnel junctions, generally a high-bandgap (compared to the adjacent sub-cells), highly-doped semiconductor (see Section 2.1) which ideally has low electrical resistance and low optical loss at wavelengths relevant for the subsequent cells in the stack. This is illustrated for an $In_{0.5}Ga_{0.5}P/GaAs$ two-junction cell connected by an $Al_{0.8}Ga_{0.2}As$ tunnel junction in Fig. 1.7. The tunnel junction is essentially a thin diode which allows electrons to tunnel through it. Since each sub-cell is a p-n junction (see Section 2.4), connecting the cells directly without the use of a tunnel junction would result in an oppositely-directed p-n junction being formed, with the p-doped region of one sub-cell in contact with the n-doped region of another sub-cell; this reduces the overall voltage. Because current flow is limited to that of the sub-cell with the lowest photogenerated current, care must be taken to design a structure with a combination of material bandgaps, layer thicknesses, and light-trapping strategies such that the currents in the sub-cells are as closely matched as possible. One key focus of research into developing new architectures for MJ cells is the growth and characterization of new materials. This work will focus on materials and device architectures for two-terminal applications.

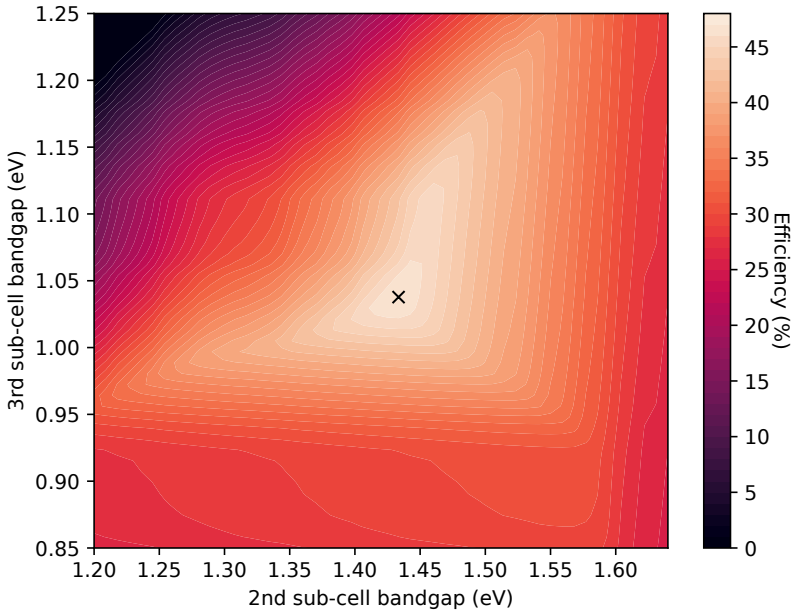


Figure 1.6: Variation of cell efficiency for a 4J cell with a top cell bandgap of 1.9 eV ($In_{0.5}Ga_{0.5}P$) and a bottom cell bandgap of 0.67 eV (Ge), as the bandgaps of the middle two cells are varied. The detailed-balance limit with perfect absorption above the bandgap is assumed.

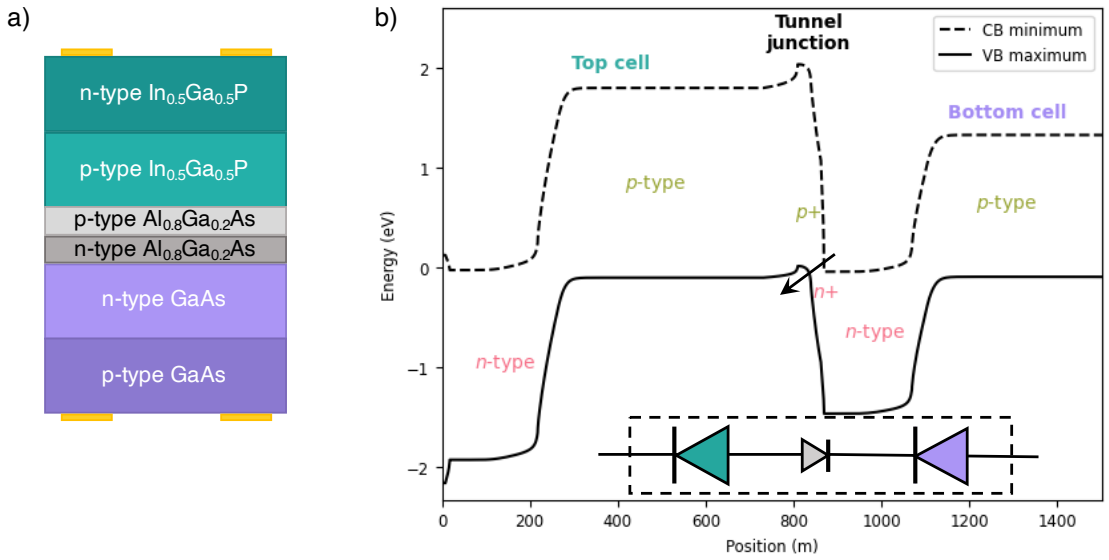


Figure 1.7: Illustration of how sub-cells in a multi-junction cell are connected by a tunnel junction; a) shows the layers of a two-junction InGaP/GaAs solar cell, connected by an AlGaAs tunnel junction. The conduction band minimum and valence band maximum are shown in b), along with an equivalent circuit for the sub-cells and tunnel junction.

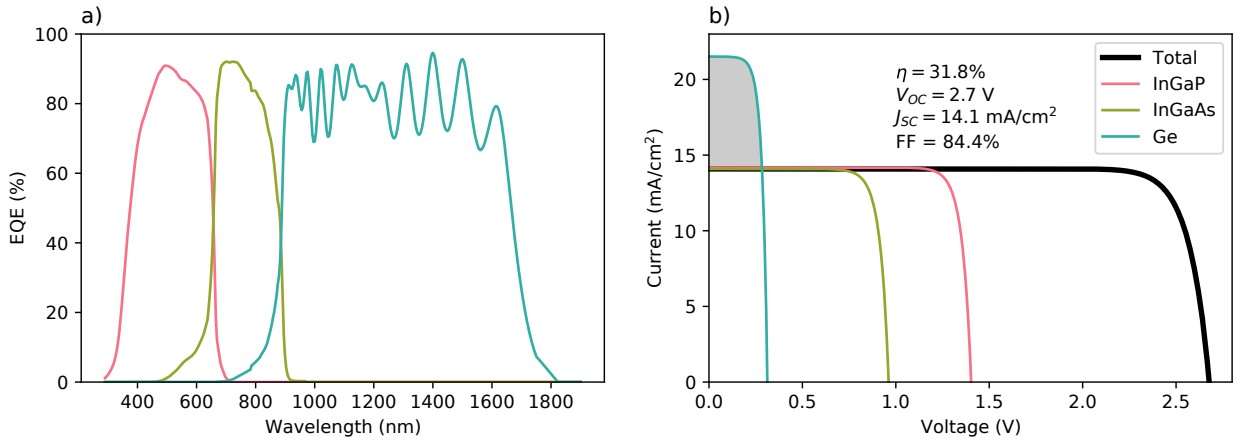


Figure 1.8: a) External quantum efficiency and b) light I-V curve of a typical InGaP/InGaAs/Ge triple-junction solar cell, also showing key device performance metrics. These values are calculated through Solcore simulations (see Section 4.1) using a realistic cell architecture and material parameters. The overproduction of current in the bottom Ge sub-cell relative to the two other sub-cells is clearly visible in b), with the shaded area showing the current lost.

Increasing the number of junctions in a solar cell increases the potential voltage which can be achieved, but reduces the current in each sub-cell. Theoretically, increasing the number of junctions in a cell increases the achievable efficiency [17, 6] – however, in practice, the engineering challenges associated with adding additional junctions mean it is difficult to produce a very efficient cell with a large number of junctions, due to resistive losses, optical losses due to non-ideal refractive index combinations, and non-radiative losses at interfaces and due to material quality (e.g. defects and dislocations). The current overall efficiency record for a solar cell, both under concentration and under 1-Sun, is held by a six-junction inverted metamorphic (IMM) device [18]; however, prior to this device (demonstrated in 2019), the overall efficiency record had been held by 3 or 4-junctions devices for twenty years (see Fig. 1.2).

A commonly-used architecture for high-efficiency multi-junction cells is the GaInP/(In)GaAs/Ge triple-junction cell, with bandgaps of 1.9/1.44/0.67 eV [19]. As shown in Fig. 1.5, these materials can be grown at the same lattice constant, with alloy compositions for the III-V materials around $Ga_{0.5}In_{0.5}P$ and $In_{0.01}Ga_{0.99}As$[2] (the addition of a very small atomic fraction of InAs to GaAs is to improve the lattice match between Ge and (In)GaAs, but has a minimal effect on the bandgap). While this architecture has previously set record efficiencies, it has the disadvantage that the Ge significantly overproduces current compared to the other two sub-cells, as shown in Fig. 1.8. As discussed above, in a two-terminal device architecture the current is limited by the lowest sub-cell current, so the additional current is wasted and cannot be used to draw power from the device. This suggests two possible improvements:

1. Inserting an additional sub-cell (with a bandgap lower than that of GaAs and higher than that of Ge) between the Ge and GaAs junctions, to utilize the current which would otherwise be wasted in the Ge cell. If current-matching can be achieved, this will increase the V_{OC} of the cell without reducing the J_{SC}.

2. Replacing the Ge sub-cell with a higher-bandgap material; this will reduce the current generated in

[2]Notation such as $Ga_{0.5}In_{0.5}P$ and $In_{0.01}Ga_{0.99}As$ denotes alloying between two III-V compounds (GaP and InP in the first case, and InAs and GaAs in the second.)

the bottom sub-cell, which will not degrade cell performance unless the bottom cell becomes current-limiting, and increase the voltage and thus the efficiency of the device.

Both of these improvements require a sub-cell with a bandgap between that of the bottom cell (0.67 eV for Ge) and the middle cell (1.44 eV for GaAs), and simulations indicate that the optimum bandgap in each case is around 1–1.1 eV (see Fig. 1.6) [19, 20]. This poses a challenge; as can be seen in Fig. 1.5, there is a lack of available III-V alloys with a suitable bandgap with the same lattice parameter as Ge/(In)GaAs/InGaP, and thus novel materials are required, or the condition for lattice-matching must be relaxed.

There are multiple ways to deal with lattice mismatch to include materials with different lattice constants in one device (e.g. $In_{0.3}Ga_{0.7}As$ with a 1 eV bandgap). This can be done in a so-called metamorphic structure [21], with grading layers separating sections with different lattice parameters to prevent the formation of defects inside the sub-cells; such structures can be grown upright (upright metamorphic, UMM) or inverted (inverted metamorphic, IMM) depending on the materials used. However, the necessary inclusion of grading layers to avoid threading dislocations in epitaxial layers which are not lattice-matched to the substrate results in thicker (and thus heavier) cells, and higher material costs. Lattice mismatch can also be dealt with through wafer-bonding; the current efficiency record for a four-junction (4J) cell is held by a wafer-bonded device, with InGaP (1.88 eV) / GaAs (1.42 eV) grown on a GaAs substrate and InGaAs (0.74 eV) / GaInPAs (1.09 eV) grown on an InP substrate, with the GaAs and GaInPAs subsequently bonded together and the GaAs substrate removed from the top of the resulting structure [22]. Such a wafer-bonding process requires multiple substrates for production of a single device, and introduces additional manufacturing steps, and thus costs, for the wafer-bonding and substrate removal.

Thus, a fully lattice-matched 4J device which can be grown monolithically remains a desirable solution from a device fabrication and processing cost point of view, especially in order to eventually manufacture more cost-competitive cells. Novel materials to provide the 1 eV bandgap have therefore been a topic of considerable research interest. These materials include dilute nitrides and bismides such as GaInNAsSb [23] and GaAsBi(N) [24, 25], with the former having been used in a previously world-record holding cell with an efficiency of 43.5% at 500 Suns (a solar spectrum at 500× concentration) [23]. However, the incorporation of N poses growth challenges [23] and can introduce defect states, including mid-bandgap defect states [26] which will significantly degrade the solar cell performance. An alternative candidate material for 1 eV sub-cells is silicon-germanium-tin (SiGeSn), a ternary group IV alloy. By adding relatively small amounts of Si and α-Sn to Ge, a material with a direct transition around 1 eV can be produced, although the material remains an indirect semiconductor with a fundamental bandgap around 0.8 eV, which will limit the voltage of the SiGeSn sub-cell. However, absorption across the direct gap will dominate the absorption coefficient of the material, due to absorption across an indirect gap being relatively much weaker as it requires phonon interactions (Section 2.1). The next section will discuss the expected behaviour of SiGeSn at different compositions, and previously-reported measurements of its optoelectronic properties.

1.4 SiGeSn in multi-junction solar cells

This section will outline the growth, band structure, and measurements of silicon-germanium-tin alloys, focusing on those with relatively high Ge fractions as these are most relevant for the photovoltaic applications discussed above. However, the previous literature discussed here spans a wide range of proposed or implemented applications for SiGeSn, including use in group IV lasers (e.g. with GeSn [27, 28]), photovoltaics [29, 30, 31], photodiodes [32] and light-emitting diodes (LEDs) [31, 33].

1.4.1 Growth of SiGeSn

High-quality SiGeSn alloys have been grown mainly, and most successfully, through chemical vapour deposition (CVD) and molecular beam epitaxy (MBE) [34]. Ultra-high vacuum CVD (UHV-CVD) growth of SiGeSn was pioneered by the group of Kouvetakis and Menéndez at Arizona State University, who produced the first SiGeSn epitaxial layers on an Si(100) substrate with a GeSn buffer layer [35], and were also the first group to report photoluminescence signal from SiGeSn [36]. The samples grown by ASU make use of deuterated tin (SnD_4); this precursor was also used in the fabrication of the most successful (published) demonstration of a multi-junction cell with a SiGeSn sub-cell [37]. Despite producing precursor material stacks for 4J devices [29] of the type discussed in this work (InGaP/InGaAs/SiGeSn/Ge) and 1 eV-bandgap photodiodes [32, 31], only prototype photovoltaic devices with very low voltage (0.14 V) and fill factor have thus far been published by the ASU group [31]. SiGeSn samples have also been grown successfully through both reduced-pressure CVD, using the commercially available precursor $SnCl_4$ [38, 39, 40] and MBE [41, 42] at the Forschungszentrum Jülich. SiGeSn grown through MBE has also been produced at Stanford University [43]. This development of SiGeSn epitaxy has happened in conjunction with the epitaxy of direct-bandgap GeSn alloys for laser applications, mostly in heterostructures containing (Si)GeSn. For research applications, custom-built epitaxy reactors or highly-customized commercial reactors are often used, in combination with different precursors for Si and Ge depending on the composition being grown [44]. In addition to SnD_4, silicon and germanium hydrides (Ge_nH_{2n+2} and Si_nH_{2n+2}) with $n > 1$ are commonly used, which are more expensive than the common commercial precursors silane and germane (GeH_4 and SiH_4).

The solid solubility of α-Sn in both Ge and Si (and the binary SiGe system) is low: $< 1.1\%$ in pure Ge and $< 0.1\%$ in pure Si [45] (the SiGe alloy, conversely, is completely miscible). Sn also has a low melting point, around 500K, and thus above this temperature it will not be incorporated in significant amounts into the epitaxial material [46], and a low free surface energy which increases the risk of surface segregation. For technologically relevant applications, much higher concentrations than the solid solubility limit must be reached, and thus non-equilibrium growth is required. The key difficulty is to avoid the phase separation of Sn through either bulk precipitation or surface segregation [46, 34]. Atomic-scale studies through atom probe tomography also indicate a repulsion between Si and Sn atoms in SiGeSn alloys, shown by a deviation away from a perfectly random distribution of Si atoms with respect to Sn atoms; however, this deviation is not observed for samples with $< 4\%$ Sn [47], the region being targeted for photovoltaic applications (see below). Segregation increases with increased temperature [46], which (in addition to the low melting point of Sn) mean relatively low growth temperatures are typically used ($< 400°C$). The similar challenges in overcoming the difficulties of incorporating Sn into SiGe and into Ge explain why much of the research effort in developing SiGeSn for optoelectronic applications has been pioneered by groups, such as the ASU and Jülich groups, with extensive experience in GeSn epitaxy. The advantage of SiGeSn over binary GeSn alloys is the additional flexibility in engineering the direct and indirect bandgaps and lattice constant (see Fig. 1.10); in addition, density functional calculations and comparison of the growth of GeSn and SiGeSn alloys with similar Sn content indicate that the ternary alloy has a lower Gibbs free energy than the binary alloy with the same atomic percentage of Sn, meaning an increased mixing entropy and a more stable material [48]. For photovoltaic applications at the Ge/GaAs lattice-constant, while the desired optical properties could be achieved with binary SiGe alloys, the addition of Sn is needed to maintain a close lattice-match.

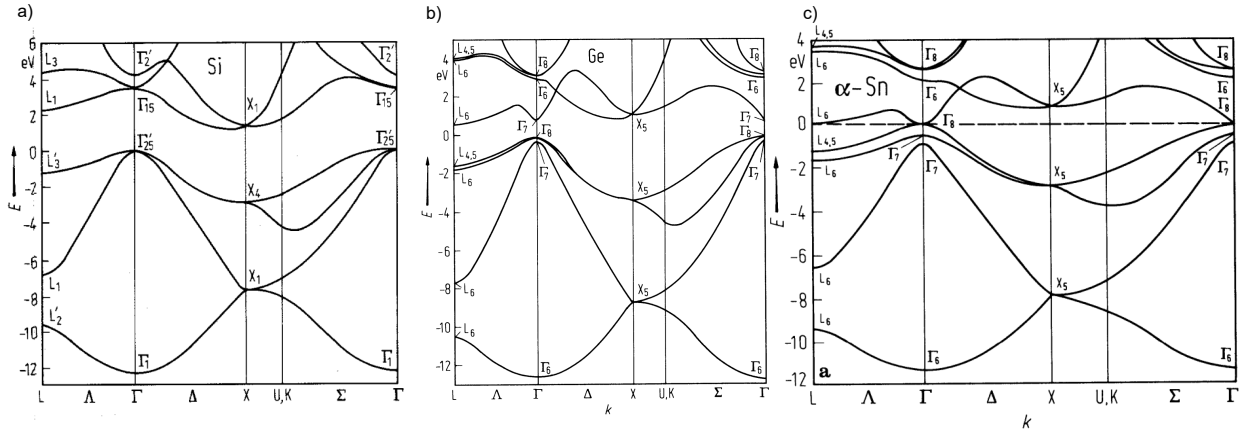


Figure 1.9: Electronic band structures of a) Si, b) Ge and c) α-Sn, calculated through a non-local pseudopotential method. From [49].

1.4.2 Band structure of Si, Ge and Sn and SiGeSn

While the very different physical and thus optoelectronic properties of SiGeSn lead to challenges with material growth, they also provide for a very interesting and flexible design space. Si, Ge and α-Sn are all group IV elements with a diamond-cubic structure. Si and Ge are semiconductors, while α-Sn is a semi-metal; its valence and conduction bands overlap slightly at their extrema, thus resulting in a zero (or negative) bandgap. Tin has a second allotrope, metallic β-Sn, with the transition occurring at 13.2 °C; this phase has a body-centered tetragonal structure. The electronic band structures (explained further in Section 2.1) along the $\Gamma \rightarrow L$ and $\Gamma \rightarrow X$ symmetry directions for the three elements are shown in Fig. 1.9. Table 1.1 lists their indirect gap and several direct transition energies (where known), as well as lattice constants, and the points in the band structures these transition energies correspond to. The key to producing SiGeSn close to the lattice constants of Ge and GaAs, with a 1 eV direct gap, is that adding Si to Ge pushes up the E_0 transition energy significantly, since the E_0 energies of Ge and Si are 0.8 and 4.1 eV respectively. However, this also takes the resulting material away from the Ge lattice constant, since Si has a smaller lattice parameter than Ge. In order to maintain the lattice match, a small amount of Sn, which has a larger lattice constant than Ge, can be added. The addition of Sn will also reduce the E_0 energy, since Sn has a negative value of E_0. Thus, the ratio of Si:Sn must be balanced to obtain both lattice-matching and the desired E_0.

The predicted direct and indirect bandgap of SiGeSn at various compositions, and its utility for optoelectronic applications, have been of interest since at least 1991 [50]. These early, simple theory results indicated that depending on the composition a direct or indirect bandgap at a range of lattice constants can be achieved, which has been shown to be the case over subsequent years in both theoretical and experimental work. Since SiGeSn is a true ternary alloy (unlike e.g. InGaAs or other III-V compound alloys), the design space is extremely large, with the alloy compositions most commonly investigated experimentally, including in this work, generally being Ge-rich and growing out of research into the related binary alloy GeSn [34], which as discussed above poses many of the same growth challenges. Theoretical calculations using density functional theory [51], the self-consistency pseudo-potential plane-wave method [52], and tight-binding/virtual crystal approximation [30] all indicate that over the full range of compositions for SiGeSn, the alloy may show a "Sn-like" (direct bandgap at the Γ point), a "Ge-like" (indirect bandgap $\Gamma \rightarrow L$) or a "Si-like" (indirect

bandgap $\Gamma \rightarrow X$) fundamental bandgap. Some energy transitions will be very close in energy at certain compositions, and thus it may be hard to distinguish a single point as the direct-to-indirect crossover. A set of compositions of special interest, especially for photovoltaics, are those alloys which are lattice-matched to Ge or GaAs (which have very similar room-temperature lattice constants), which enable strain-free epitaxial growth on Ge and GaAs substrates (or virtual substrates/buffer layers on e.g. Si). Using Vegard's law [53] to calculate the lattice constant of the alloys, such lattice-matched alloys should have a Si:Sn ratio around 3.7:1 to have the same lattice constant as Ge (see below). These lattice-matched alloys are predicted to have a fundamental indirect bandgap between ≈ 0.8 and 1.4 eV, with the fundamental bandgap being a 'Ge-like' indirect $\Gamma \rightarrow L$ transition at high Ge compositions, and an 'Si-like' indirect $\Gamma \rightarrow X$ transition at high Si compositions ($\gtrapprox 40\%$), keeping the Si:Sn ratio around 4:1. At this lattice constant, the unstrained alloy is expected to be fundamentally indirect over the whole range, as at least one of the indirect transitions always lies lower in energy than the minimum-energy direct transition at the Γ point (E_0), as can be seen in the theoretical results summarized in Fig. 1.10 [52], meaning that the ≈ 1 eV E_0 transition will not be the fundamental bandgap. This means that for photovoltaic applications, the absorption in a SiGeSn sub-cell will be dominated by the lowest direct transition energy, due to the relatively much weaker absorption across the indirect gap (see Section 2.1), but the voltage will be affected by the ability of photogenerated carriers to thermalize to a lower conduction band edge at the X or L point.

For useful application in lattice-matched solar cell architectures, the lattice parameter of the SiGeSn alloys considered should be equal to, or close to, $d_{Ge} = 5.6575$ Å. To achieve a 1 eV direct transition, only relatively low ($< 10\%$) Si and Sn concentrations are necessary, as discussed below. Assuming that at these concentrations, Vegard's law [53] (a simple linear interpolation between the lattice constants of the constituent materials according to atomic composition) is valid, the lattice constant is given by:

$$d_{SiGeSn}(x, y) = (1 - x - y)d_{Ge} + xd_{Si} + yd_{Sn} \tag{1.1}$$

where x is the atomic Si fraction of the alloy and y the atomic Sn fraction. More complex expressions for the lattice constants involving bowing parameters have been proposed [54], but measurements indicate a closer match to Vegard's law [41]. Solving the Vegard's law equation so that $d_{SiGeSn} = d_{Ge}$ gives $\frac{x}{y} = \frac{d_{Ge} - d_{Sn}}{d_{Si} - d_{Ge}} = 3.67$, i.e. the ratio Si:Sn necessary for an exact lattice-match is around 3.7:1. Some of the samples in this work were grown on GaAs substrates; for GaAs substrates, the ratio required for lattice-matching is 5.35:1. Fig. 1.10 shows predicted lattice constants, indirect bandgaps, and E_0 values for the full range of SiGeSn compositions [52]. The compositions of interest lie at relatively low Si ($\approx 10\%$) and Sn ($\approx 3\%$) fractions; this has also been demonstrated experimentally [44]. At these compositions, the alloy remains fundamentally indirect with an expected Ge-like bandgap around 0.75-0.8 eV (Fig. 1.10b) and an Si-like bandgap around 0.95 eV (Fig. 1.10c). Due to the adverse effect of a lower-lying indirect transition on the voltage, a fundamentally direct bandgap at 1 eV would be preferable, but while SiGeSn can achieve a direct fundamental bandgap, this will be at a much lower energy than is useful for the application targeted here. Direct SiGeSn with a high Sn fraction is predicted to have bandgaps between 0.2 and 0.6 eV [52], in addition to a range of "slightly indirect" alloys where the direct gap lies around 0.8 eV (identical to Ge) and the indirect gap lies within ≈ 0.1 eV below the direct gap. Such slightly indirect alloys have been demonstrated experimentally [55, 56]. Strain engineering can be used to lower the direct bandgap relative to the indirect bandgap in Ge [57] to produce a direct material, but a similar effect in SiGeSn would also produce a bandgap which is too low for a circa-1 eV sub-cell application.

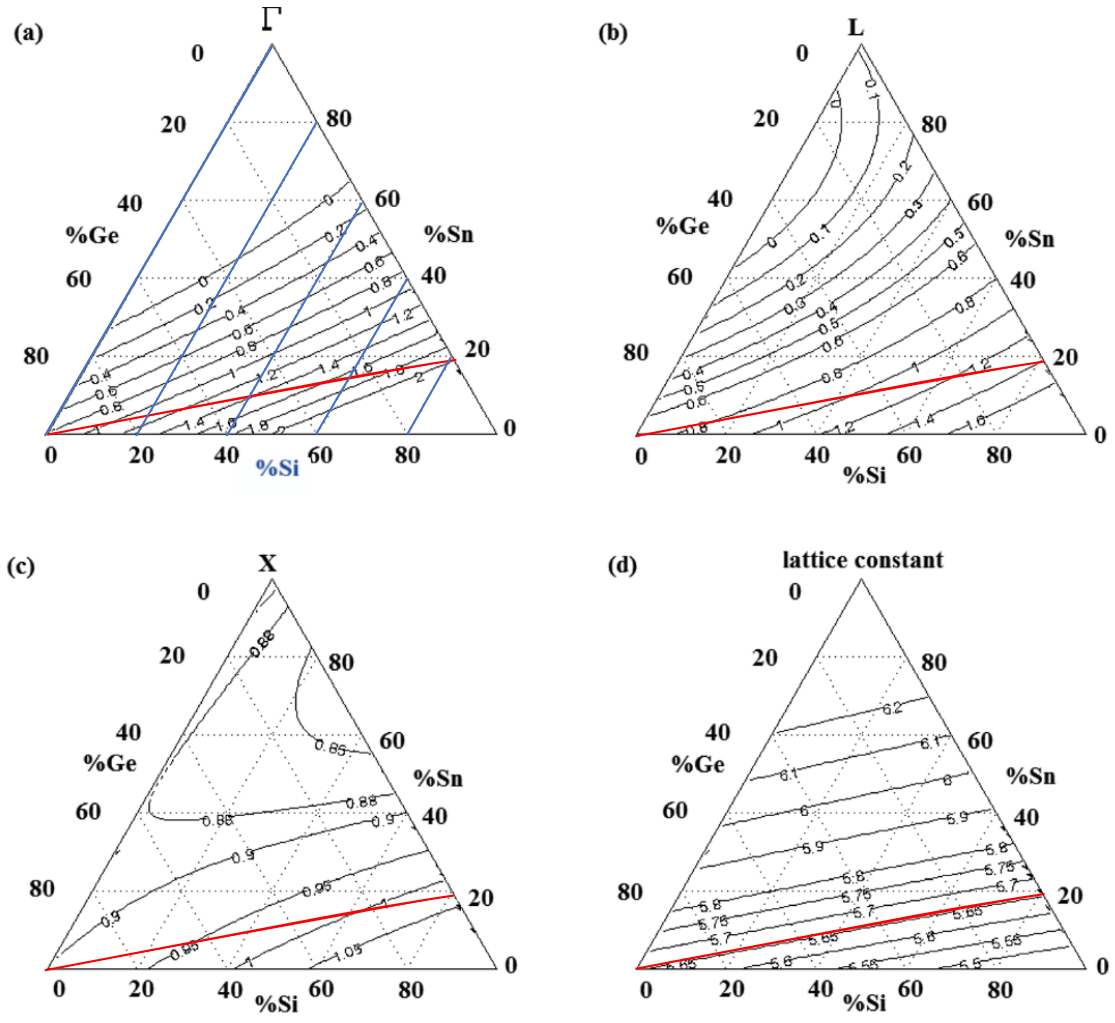


Figure 1.10: Ternary plots showing theoretical predictions of the transition energies for (a) the direct $\Gamma_{VB} \rightarrow \Gamma_{CB}$ transition (E_0), b) the indirect $\Gamma_{VB} \rightarrow L_{CB}$ ($E_{g,Ge}$) gap, c) the indirect $\Gamma_{VB} \rightarrow X_{CB}$ ($E_{g,Si}$) gap and d) the lattice constant (in Å) of SiGeSn alloys over the full possible range of compositions. The lattice constant was calculated using Vegard's law with bowing parameters, while the bandgap is calculated from empirical pseudopotential theory. The red line in each plots shows where $d_{SiGeSn} = d_{Ge}$. Adapted from [52].

Table 1.1: Literature values for transition energies in Si, Ge and α-Sn at room temperature, and their lattice constants, and the band structure transitions these energies correspond to. The labelling is consistent with Fig. 1.9b, the band structure of Ge; the superscript v and c labels refer to the valence and conduction band, respectively.

Label	***Transition***	***Energy (eV)***		
		Ge [58, 59]	**Si** [58, 59]	α**-Sn** [59]
E_g^{ID}	$\Gamma_8^v \rightarrow L_6^c$	0.67	1.11	
E_0	$\Gamma_8^v \rightarrow \Gamma_7^c$	0.79	4.06	-0.41 [52]
$E_0 + \Delta_0$	$\Gamma_7^v \rightarrow \Gamma_7^c$	1.09	4.13	
E_1	$L_{4,5}^v \rightarrow L_6^c$	2.12	3.38	1.36
$E_1 + \Delta_1$	$L_6^v \rightarrow L_6^c$	2.34		1.84
E_0'	$\Gamma_8^v \rightarrow \Gamma_6^c$	3.13	3.32	2.28
$E_0' + \Delta_0'$	$\Gamma_8^v \rightarrow \Gamma_8^c$			2.63
E_2	$X_5^v \rightarrow X_5^c$	4.35	4.31	3.72
Lattice constant (Å)				
d		5.658	5.431	6.489

1.4.3 Optical and structural measurements of SiGeSn

Determining all relevant transition energies in SiGeSn around the compositions of interest for photovoltaics is experimentally challenging; due to the weak contribution of indirect transitions to the dielectric function and absorption, these can generally not be observed in ellipsometry, (photo)reflectance, or electroreflectance measurements, which are well-suited to investigate the direct transitions (as in e.g. [44, 43, 42]). Conversely, the lowest direct gap E_0, and any higher-energy transitions, are generally not visible in photoluminescence measurements for alloy compositions which remain fundamentally indirect, unless the direct and indirect gaps are close in energy ($\Delta E < 0.1$ eV) since carriers generally thermalize to the lowest-energy conduction and valence band states before recombining and emitting a photon. Thus, a combination of multiple experimental techniques is usually necessary to get a full picture of the critical points in the alloy band structure.

There has been interest in SiGeSn for photovoltaics and other electronic applications for at least three decades [34, 50]; in that time, there have been a large number of papers focusing on theoretical band structure calculations [51, 50, 30]. Of the papers focusing on material growth, many report XRD [43, 37, 60, 61, 62] or ellipsometry [37, 62, 63, 54, 29, 42, 64, 65] results. The lowest direct gap has also been measured through photoreflectance [43], external quantum efficiency measurements of photodiodes [32, 61] and photoluminescence [66, 56]. The measurement of the direct gap through photoluminescence was demonstrated for alloys with a high Sn fraction (at. % Sn > at. % Si), making the alloy either fundamentally direct with a lower value of E_0 than Ge [66], or almost direct with only a small energy difference between E_g and E_0 ($\lessapprox$ 60 meV) [56, 55]. Much of the previous work focused on Ge-rich SiGeSn has considered only the higher-energy direct transitions, likely due to the fact that these transitions are much more visible in reflectance-based measurements such as spectroscopic ellipsometry and photo/electro-reflectance, the lack of good-quality PL measurements from epitaxial SiGeSn samples, and the need for specialized infrared detectors to make measurements. Reports of PL from SiGeSn are relatively scarce, with no known previous reports of photoluminescence from SiGeSn grown directly on a Ge or GaAs substrate, although there have been several reports of photoluminescence from SiGeSn epitaxial layers [67, 61, 55, 41, 64, 33, 56] or quantum-well structures containing GeSn and SiGeSn [68, 33, 69, 28] grown on Si substrates with a Ge buffer, often called a Ge virtual substrate (Ge-VS). The lack of PL data for SiGeSn grown directly on Ge substrates, rather than Ge-buffered Si, is likely because Ge has a lower fundamental bandgap than an SiGeSn alloy

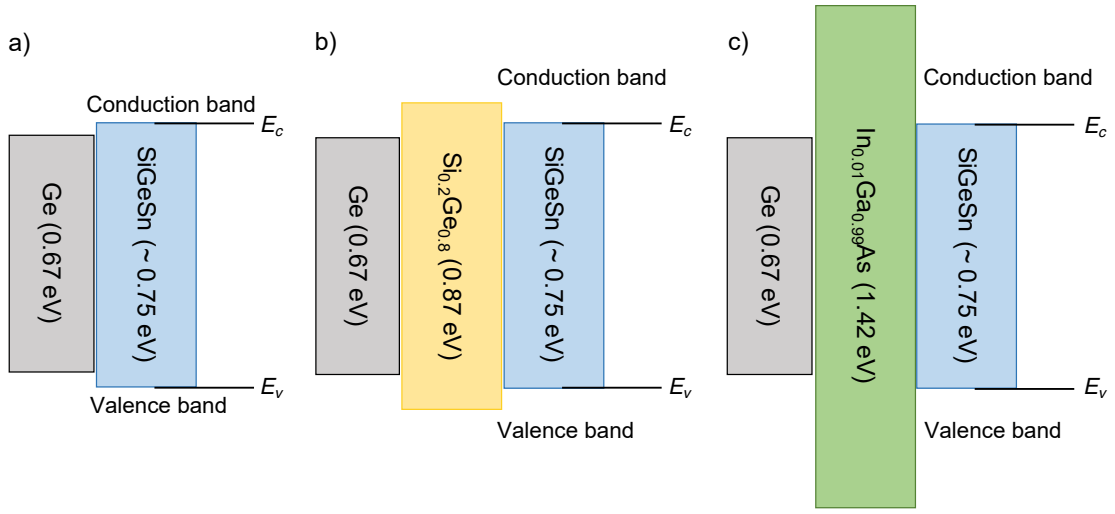


Figure 1.11: Illustration of the energetic barrier (or lack thereof) for electrons and holes for a) SiGeSn grown directly on Ge, b) SiGeSn grown on a $Si_{0.2}Ge_{0.8}$ layer on Ge and c) SiGeSn grown on an $In_{0.01}Ga_{0.99}As$ layer on Ge.

lattice-matched to it; this means that any carriers generated in the epitaxial SiGeSn layer can diffuse to the Ge substrate without any energetic barrier. Our initial PL measurements of SiGeSn found that only Ge-like PL could be observed from SiGeSn grown directly on Ge, despite evidence of a high-quality SiGeSn layer from ellipsometry measurements [70], and this issue has also been reported by the ASU group [55]. For SiGeSn compositions targeting a higher bandgap than Ge, it is necessary to include a higher-bandgap layer between the SiGeSn and Ge, or grow directly onto a higher-bandgap substrate such as GaAs, as illustrated in Fig. 1.11. No previous reports of PL measured from samples grown on GaAs substrates (such as the Set A samples in this work, see Section 3.1) or on Ge substrates with a higher-bandgap barrier (such as the Set B samples in this work) to prevent carrier diffusion were found.

Predicting the indirect bandgap E_g and the lowest-energy direct transition E_0, which are of particular interest for photovoltaic applications, over the full composition range is difficult, and the bowing parameters reported vary significantly across the literature. Often, bowing parameters are obtained by extrapolating data over a wide composition range (for example in [43]) even though only a small region of the alloy compositions is explored. Fischer et al. [42] compare their experimentally observed transition energies to the bowing parameter expressions from [63] and find that there is neither quantitative nor qualitative agreement, indicating that there is little predictive value in extrapolating bowing parameters for the full compositional range for samples which cover only a small experimental range. The bowing parameter b_{SiSn} in particular appears to be composition-dependent [71, 41], and SiSn is also by far the least-studied of the three related binary alloys GeSn, SiGe and SiSn, leading to a lack of data on e.g. bowing parameters which may be transferable to the ternary alloy.

Previous reports of PL from SiGeSn show issues with low intensity and unexpected temperature-dependent behaviour, including a reduction of integrated and peak PL intensity at low temperatures in some samples (the opposite of the behaviour observed in most semiconductors, including Ge [72]), PL from defects [64, 33], and a large variation in signal intensity between samples measured under similar conditions. PL appears to be especially difficult to observe in samples with a relatively large separation between the direct and indirect gaps [55]. Photoluminescence from GeSn is generally easier to measure due to the increased 'directness' of

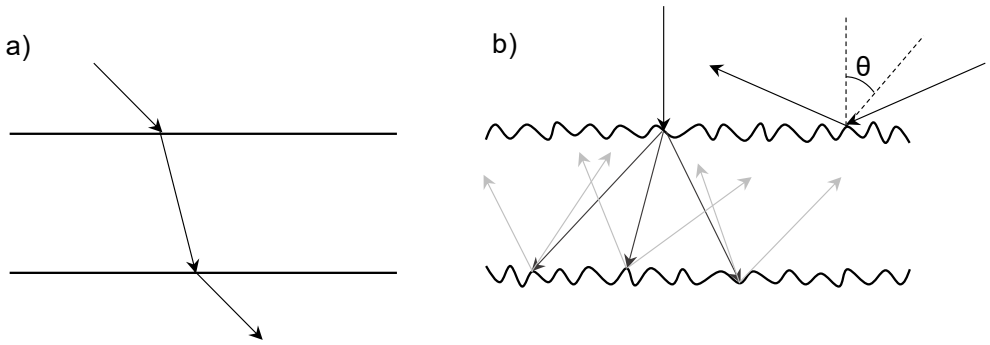


Figure 1.12: Optical sheets with a) planar surface and b) a randomizing surface texture with acceptance angle θ.

the alloy as the Sn fraction increases, especially close to the direct-indirect crossover which happens at relatively low Sn fractions ($\approx 7\%$ [73]), as is expected due to the increased radiative efficiency of direct materials compared to indirect materials. Most of the literature reports of PL from SiGeSn are from materials with a higher atomic composition of Sn than Si, which behave in a more 'direct' way. Where photoluminescence from the indirect gap is clearly observed, it has not previously been analyzed in detail in terms of different phonon transitions; either only a single peak could be observed due to a lack of resolution/noise [67], or a constant peak offset from the indirect gap was assumed [73].

The lowest-energy direct transition, E_0, is often characterized using spectroscopic ellipsometry. The theory and fitting of SE data is discussed in further detail in Section 2.2.2. By computing the second derivative of the dielectric function, the energies of critical points in the band structure can be clearly observed and used to extract centre energies for these transitions. This technique was used by Vina et al. [74] in 1984 to investigate the dielectric function of Ge, and more recently by D'Costa et al [65, 75] in 2006 to investigate SiGeSn and related binary alloys, and has become a widely-used method for studying the direct transitions of SiGeSn.

1.5 Advanced light management strategies

In order to produce electricity, a solar cell must first absorb photons, and thus maximizing how much sunlight is absorbed by a solar cell is unsurprisingly an important research area for improving solar cell efficiency. Light-trapping strategies range from relatively simple, for example the use of reflective materials such as metals at the rear surface of a cell, to highly-engineered nanophotonic structures to maximize broadband absorption of sunlight in very thin layers. Strategies to maximize absorption fall broadly into two categories: minimizing front-surface reflection, and making sure light which is able to enter the cell remains trapped until it is absorbed in the photovoltaic layers (some structures, such a pyramids on an Si cell, may perform both of these functions). Modelling the effectiveness of different light-management structures to aid device design and predict performance is also a rich area of research in photovoltaics and optics, and this thesis will discuss modelling-based strategies for maximizing the efficiency of ultra-thin GaAs cells, silicon cells for hybrid thermal-photovoltaic applications, and spectrum-splitting multi-junction cells, discussed in Chapter 6. Extensive work to build new software for optical simulations, improve existing code, and address common issues which arise in optical modelling of solar cells was also undertaken as discussed in Chapter 4.

1.5.1 Light trapping design and modelling

The optical design of solar cells is extremely important for all types of device, whether they are III-V-based, (multi)-crystalline or amorphous Si, thin-film devices, organic materials or otherwise. There are many strategies for increasing the path length inside the cell to increase absorption, e.g. causing light to travel at a more oblique angle and/or have multiple passes due to internal reflection. Assuming light enters perpendicularly to the cell interface with no front surface reflection and makes a single pass through the cell, and is not reflected at the back surface, the total absorption in the layer will be given simply by the Beer-Lambert law:

$$A_{BL} = 1 - e^{-\alpha d} \tag{1.2}$$

A theoretically simple enhancement which significantly boosts absorption in a cell is to assume perfect rear reflection, so that the light makes a double pass through the cell (again, assuming normal incidence):

$$A_{DP} = 1 - e^{-2\alpha d} \tag{1.3}$$

However, absorption can be improved further by scattering the light into more oblique angles inside the cell, increasing the path length. A theoretical upper limit to absorption enhancement can be derived using a thermodynamic approach; according to Minano [76], in this limit the average path length of rays entering into a cell is given by:

$$\bar{l}_{th} \leq \frac{4n^2}{\sin^2(\theta)} \tag{1.4}$$

With the upper limit occurring when all ray paths in the cell are illuminated at maximum brightness [77]. The angle θ is the "angular acceptance" of the cell: only incident light within a cone of θ from the surface normal can enter the cell (see Fig. 1.12). In general, for a planar surface being illuminated isotropically, light may enter from any θ between 0 and 90°, and the expression for the limit reduces to:

$$\bar{l}_{Lam} = 4n^2 \tag{1.5}$$

Yablonovitch and Cody [78] showed that the mean path length for ideal Lambertian scattering is identical to equation 1.5; a Lambertian scatterer is an ideal diffuse reflector, having the same radiance (radiant flux per unit projected unit solid angle) regardless of the viewing angle. This increase in path length leads to an absorption given by:

$$A_{\mathrm{YC}} = \frac{4n^2\alpha d}{1 + 4n^2\alpha d} \tag{1.6}$$

In fact, although this value can be computed at any wavelength with corresponding values of n and α, it is only physically meaningful in the limit of low absorption ($\alpha \to 0$). Green [79] generalized the Lambertian limit over all wavelengths, giving:

$$A_{\mathrm{Green}} = \frac{1 - e^{-4\alpha d}}{1 - \left[1 - \frac{1}{n^2}\right] e^{-4\alpha d}} \tag{1.7}$$

As expected, A_{Green} reduces to A_{YC} in the limit $\alpha d \ll 1$, so that $e^{-4\alpha d} \approx 1 - 4\alpha d$.

Practically, increased path lengths inside cells can be achieved in various ways, including through diffrac-

tion gratings [77, 80], random or periodic scattering structures [81], reflectors [78], and plasmonic structures involving metals [82, 83]. Such structures can be placed on the front and/or rear of the cell, or even between junctions of a multi-junction cell [80] depending on the device design. Highly efficient Si cells generally have random or regular pyramidal textures to reduce front-surface reflectivity, and increase path length inside the cell by redirecting light into more oblique angles and increasing internal reflection [84, 85, 86]. The Green/Lambertian limit applies to the maximum possible amount of broadband path enhancement without wavelength restriction. However, in a solar cell, we generally only require light-trapping over a limited wavelength range, generally at energies just above the bandgap where absorption is weakest, and thus it is possible to exceed the Green limit over a limited wavelength range [87, 77, 88, 89, 90] by using periodic scattering structures.

Optical simulations are key in developing, analysing and optimizing novel concepts for light-trapping architectures. A number of different optical modelling methods appropriate for different types of structures are discussed in Chapter 4. Depending on the device structure and light-trapping strategies used, very different modelling methods may be appropriate. The methods used in this work are:

1. The Beer-Lambert law (eq. 1.2), describing absorption in a bulk material without scattering or additional front surface or interface reflections; it is often used in conjunction with other methods or to provide initial estimates of the absorption.

2. Ray-tracing. A geometrical optics method in which light is treated as a collection of rays which can reflect or refract at material interfaces. These methods are appropriate when describing the interaction of light with material layers and features with characteristic sizes much larger than the wavelength, a regime in which wave-optical effects such as diffraction and interference can be neglected. The concepts, mathematics and computational implementation of ray-tracing are discussed in Section 4.2.1.

3. Transfer-matrix method (TMM) [91]. A wave-optical method which deals correctly with the reflection of light at multiple interfaces, and resulting interference. This method can only describe planar layers; any structure such as a grating or nanoparticles can only be described using an effective medium approximation (EMA) which treats the structure as a one-dimensional layer with an effective refractive index. The theory behind this method is discussed in Section 2.3.1 and its implementation for various applications is discussed further in Chapter 4.

4. Rigorous coupled-wave analysis [92, 93]. A wave-optical Maxwell solver also referred to as the Fourier modal method (FMM). RCWA is a method for solving Maxwell's equations in layer stacks which may contain structures such as gratings. The theory behind this method is discussed in Section 2.3.3.

5. Guided mode analysis [94, 95]. By treating the solar cell as a waveguide, in which certain guided modes can be excited through diffraction by a periodic structure (depending on the geometry and period of the grating). However, the effectiveness of diffraction into each possible mode will depend on the precise specifications of the grating, and thus this method can only predict where resonant features may occur; thus it can be used to inform the development of structures alongside e.g. RCWA. The theory behind this method is discussed in Section 2.3.2.

Separate implementations for each of these methods exist, but for certain light-trapping architectures which combine optical features over multiple length scales, it may not be physically appropriate or computationally efficient to use a single method for the full structure. For example, for a silicon cell with a

thickness on the order of 100 µm with a rear-side grating with a period of 1 µm [96] it is possible to use a Maxwell solver such as RCWA, or alternative Finite Element (FEM) or Finite Difference Time Domain (FDTD) methods, to describe the behaviour of the full structure, but this will be extremely inefficient computationally due to the very large difference in feature sizes between the bulk thickness and the grating. Another technologically relevant example is the implementation of perovskite on Si tandem cells; the thin perovskite layers will need to be treated with e.g. TMM, while the silicon cell will generally be more suited to geometric optics (ray-tracing) methods if it has a pyramidal texture [97]. These problems have led several groups to independently develop matrix methods which can combine different optical methods across interfaces; implementations include GenPro4, developed by Santbergen et al. at TU Delft [98], the OPTOS formalism developed by Tucher, Eisenlohr et al. at Fraunhofer ISE [86, 99] and by Li et al. at UNSW Sydney [100]. For e.g. thin-film on Si tandem cells, methods combining ray-tracing for the pyramidal textures with reflection, transmission and absorption probabilities calculated through TMM have also been developed both in conjunction with general matrix methods, as for GenPro4 [98] or separately, including the CROWM simulator by Lipovšek et al. B [101] (University of Ljubljana). The research undertaken for this thesis combined several optical simulation methods to establish a new Python package, RayFlare [102]; the coupled optical model approach and its implementation in RayFlare is described in Section 4.2.

1.5.2 Ultra-thin GaAs cells

Ultra-thin III-V devices are currently being developed for a variety of applications due to their lower mass per unit area and thus higher specific power per unit mass compared to 'standard' cells (assuming good efficiencies can be maintained). There is no universally accepted thickness which qualifies a solar cell as ultra-thin, and the reasonable range of thicknesses will also vary significantly with the technology and semiconductor material being considered; a GaAs cell 3 µm thick is certainly not 'ultra-thin', while a crystalline Si cell with the same thickness could be considered as such. Here, we will use this label to refer to GaAs cells with an active layer thickness of around 200 nm or less.

The lower mass and higher specific power of ultra-thin cells can be of use in e.g. portable power generation applications and for use on unmanned aerial vehicles (UAVs) intended to fly for long periods without landing while generating power from solar cells during sunlight hours, which is stored in batteries for night-time power. Another already well-established industry where low mass is highly desirable is for space applications; there is a cost incentive to reducing the mass of e.g. a satellite to be launched into orbit as much as possible, giving an advantage to direct semiconductor materials such as GaAs over indirect silicon. While for most terrestrial applications the main constraint on PV installation is cost, which makes silicon extremely competitive, GaAs has an advantage for space applications where the available area and allowed mass are extremely limited, since much thicker and thus heavier layers of silicon are required to reach similar efficiencies.

Efficient, thin GaAs cells using epitaxial lift-off were pioneered by researchers at Radboud University (Nijmegen, the Netherlands) [103], using their novel weight-induced epitaxial lift-off procedure [104]. These solar cells were grown through metal-organic vapour-phase epitaxy (MOVPE) on GaAs substrates, and show that a thin-film cell can outperform a similarly-fabricated on-substrate device with the same active layer thickness due to increased reflection at the rear interface, showing optimal performance around a total cell thickness of 1.7 µm. The same group demonstrated a 26.1% efficient (under a 1–Sun AM1.5G spectrum) thin-film GaAs cell in 2009 [105] with a V_{OC} of 1.05 V, a J_{SC} of 29.5 mA/cm^2 and a FF of 84.6%, a world record at the time [106]. The current world-record for a single-junction cell has been held by Alta Devices

since 2011 [7], with several consecutive cell improvements breaking their own record, up to an efficiency of 29.1% in 2018 [5], with a V_{OC} of 1.13 V, a J_{SC} of 29.8 mA/cm^2 and a FF of 86.7%, demonstrating small increases in J_{SC} and the FF relative to the Radboud lifted-off cell but a significant 8% increase in the V_{OC}. This is attributed by Kayes et al. (Alta Devices) [7] to efficient photon recycling in the cell, meaning that photons which are radiatively emitted by the GaAs are re-absorbed by the cell itself, increasing the carrier density in the cell. This increases the quasi-Fermi level splitting (see Section 2.4), increasing the V_{OC}. This is equivalent to considering photon recycling similar to an increase in light concentration which reduces the Boltzmann loss [6]; photon recycling leads to an increase in the external luminescent efficiency of the cell, meaning a larger fraction of the internally radiated photons are able to escape out of the front surface of the cell. Perhaps counter-intuitively, a high luminescence efficiency corresponds to a high V_{OC} [107] by reducing the mismatch between absorption and emission angles [6]. In the ideal case, all the absorbed photons either generate carriers or are radiatively emitted (radiative emission is unavoidable due to the principle of detailed balance), in which case they may be re-absorbed to generate carriers or be emitted again, etc. While the exact thickness of the Alta Devices is proprietary and not reported in the literature, the cells are fabricated using epitaxial lift-off with a metal back structure [7] giving high rear reflectivity.

GaAs cells with a thickness around 100 nm or less have a further advantage for space applications beyond those inherent to direct semiconductors as described above; they are much more radiation-tolerant than standard GaAs devices with a typical GaAs thickness of several microns [108]. PV arrays on spacecraft are bombarded with highly energetic protons and electrons originating from solar particle events (SPEs) and the Van Allen radiation belts. These particles can displace atoms from the crystal lattice of the solar cell absorber material and thus degrade the material quality by introducing defects states, which in terms of energy may be located in the otherwise energetically forbidden region between the valence and conduction bands of the material (see Section 2.1). Such mid-bandgap defect states provide alternative recombination pathways and lead to a reduction in the voltage and the carrier diffusion length, the latter leading in turn to reduced photocurrent [108]. The reduction in photocurrent can be minimized by using an ultra-thin absorber layer; if the total thickness of the active photovoltaic layer is similar to or less than the diffusion length after the material has degraded, most carriers will still be collected even after the defect states are introduced. However, ultra-thin GaAs cells need extremely effective anti-reflection and light-trapping strategies to counteract high transmission losses, especially at longer wavelengths ($\approx 500-930$ nm for GaAs).

A large amount of research in the past 15 years has been focused on the application of plasmonics to light management in thin solar cells [82, 83]. Plasmons are a collective oscillation of free electrons in a conductor, which can be treated as a quasi-particle; if a plasmon resonance due to a metallic nanoparticle can be coupled to a waveguide mode in the absorbing semiconductor, this can increase the absorption. For the design of plasmonic structures containing metallic conductors in photovoltaics, both localized surface plasmons (LSPs) excited in individual nanoparticles and surface plasmon polaritons (SPPs) propagating at the metal/semiconductor or metal/dielectric interface are of interest [109]. Arrays of metal nanoparticles [110], other diffracting structures using metal grids [111] or perforated films [112], and randomly arranged scattering nanoparticles [113, 114] have all been investigated as methods for improving absorption in solar cells using plasmonic and diffraction effects [109, 83, 82]. In such structures, absorption in metal layers is generally parasitic (excluding e.g. hot carrier effects) as it does not contribute to the J_{SC}, and thus in order to accurately predict solar cell performance (e.g. quantum efficiency and short-circuit current) it is critical to accurately quantify absorption in the target layer and in any parasitically absorbing layers.

Although the application of plasmonic light-trapping structures to solar cells has been a topic of active

research for over a decade, demonstrations of clear enhancement from these structures compared to similar cell designs without plasmonic structures are quite rare. For instance, significant current enhancement compared to a planar cell can be achieved using silver nanoparticles at the rear of a microcrystalline Si solar cell [115]; however, such cells have not exceeded the performance of cells fabricated on textured substrates not designed for plasmonic effects [116]. Although the plasmonic effects can enhance absorption, they also necessarily introduce parasitic absorption [115, 83, 117] due to the presence of metal in close proximity to the active absorber layer, and may affect the effectiveness of a rear structure as a reflector [118]. In addition, the absorption enhancement induced in the semiconductor by plasmons often occurs close to the high-recombination semiconductor-metal interface [83]; thus, even if the theoretically photogenerated current in the cell is high, this current may not be effectively collected. In addition, the additional processing required increases the device complexity and can also reduce the electrical performance by degrading the fill factor [115]. Historically, simulations have often overestimated the potential short-circuit current, especially for structures involving silver, by using optical constant data set giving high reflectivity and low parasitic absorption [119, 117]; this issue is discussed further in Section 4.3. As a result of high parasitic absorption in structures with front side metallic structures [111], recent development of ultra-thin GaAs cells has focused on the use of rear-side structures: Chen et al. [95] recently reported a 19.9% efficiency GaAs cell with a 205 nm GaAs p-n junction and a total III-V layer thickness (including the window layer and back surface field) of 330 nm. The J_{SC} enhancement was almost 100% relative to an on-substrate device with the same structure, and 21% relative to a structure with a planar back mirror without periodic structure, demonstrating the capability of these textures to outperform simpler light-trapping features for thin GaAs cells.

1.5.3 Emissivity of solar cells

The thermal emissivity of solar cells plays an important part in controlling the operating temperature of a device, especially those without active cooling mechanisms, such as the majority of commercial c-Si modules currently in operation. The performance of solar cells generally degrades at increasing temperature; for Si cells, the output power of most cells decreases linearly with increasing temperature, falling around 0.45% per 1° C temperature increase [120]; thus, a modest operating temperature increase of 10 °C leads to a 4.5% drop in the output power which for a reasonably efficient crystalline Si cell is around 1 percentage point efficiency decrease. In general, to maintain a low operating temperature which improves device performance, it is desirable to maximise emissivity in the infrared. Thus, past work in this area has focused primarily on ways to reduce cell temperature through engineering either passive [121, 122] or active [123, 93] cooling mechanisms in order to maintain high operating efficiency. Through Kirchhoff's law of thermal radiation, emissivity is equal to absorptivity; this is also true for scattering surfaces such as those with nanostructures, although in this case the emissivity and absorptivity become dependent on the direction. In general, for an object with a well-defined, uniform temperature T [124]:

$$\varepsilon(\lambda, \theta, \phi, T) = A(\lambda, \theta, \phi, T) \tag{1.8}$$

Although for PV systems high emissivity in the infrared is often desirable, for certain applications, low emissivity is useful. For instance, in a hybrid solar PV/thermal system [125], the aim is to capture and use as much of the heat generated as possible, and prevent it from being radiatively emitted; thus, rather than encouraging infrared emission by engineering high emissivity in the infrared, the aim is to minimize the infrared emissivity/absorptivity while maintaining the absorption at short wavelengths relevant

for photovoltaic performance as close to unity as possible. This in effect resembles an active cooling system where the heat extracted is captured in order to e.g. provide residential heating or hot water.

Previous work at Imperial College focused on determining the magnitude of the emissivity of aluminium back surface field (Al-BSF) c-Si solar cells and its origins [126]. This work used the two-dimensional OPTOS matrix formalism [99] to couple optical models for the front and back surface, using a 2D integrated TMM/ray-tracer formalism to calculate the matrix entries. This work showed that the absorptivity/emissivity of these Al-BSF cells was high ($> 80\%$) over the wavelength range 1-20 µm due to the highly-doped emitter and back-surface field layers and the aluminium rear contact. The naive expectation is that the silicon heterojunction (SHJ) cells studied in this work (Section 6.2) will have a much lower emissivity due to the lack of highly-doped layers of any significant thickness, and the use of indium tin oxide (ITO), which performs well as a low-emissivity coating [127], on the front surface.

1.6 Structure of the thesis

The next chapter of this thesis will outline key theory on semiconductor physics, optical constant models and their relationship to experimentally-measured quantities. It provides some mathematical detail for the optical modelling tools which were used for the work presented. Finally, a basic overview of solar cell operation and relevant figures of merit for quantifying cell performance are given.

In Chapter 3, the experimental and computational methods used in this work are detailed. The sample growth of the SiGeSn structures, and the structural measurements used to measure the composition, lattice constant, and other structural features of the SiGeSn alloys are explained. Sections 3.2 through 3.5 detail the spectroscopic measurements used to study SiGeSn: spectroscopic ellipsometry, photoreflectance, photoluminescence measurements, and Fourier-transform infrared reflection and transmission measurements. Electrical measurements (external quantum efficiency and current-voltage characteristics) of solar cells are discussed. The final section explains differential evolution, a black-box optimization method used for multiple applications throughout this thesis.

In Chapter 4, the extensive work undertaken in further developing the optical modelling capabilities of the Quantum Photovoltaics Group's open-source Python package Solcore [128] is discussed, in addition to the development of a novel Python package, RayFlare [102], a matrix framework for multi-scale optical calculations, which aims to provide a flexible and powerful way of combining optical models across layer stacks and length scales. The effect of using optical constants reported in different sources for the same material is explored, showing that seemingly small variations in measured or modelled optical constants can drastically effect the design of light-trapping structures for solar cells, and their predicted efficiency. It was found that this effect can be quantified, at least in the case of a thin GaAs cell, without computationally-intensive simulations in terms of a newly-proposed Spectral Absorption Enhancement Factor (SAEF).

Chapter 5 presents the results of extensive characterization studies of SiGeSn alloys. The transition energies of direct and indirect critical points in the band structure, obtained through the spectroscopic measurements as described in Chapter 3, are discussed. As expected, the lowest direct and indirect transition energies of the SiGeSn alloys show a blueshift with respect to Ge, and a number of the samples are shown through multiple measurements to have the targeted direct transition around 1 eV. Informed by these measurements, the final part of this chapter presents device modelling of two, three and four-junction devices incorporating SiGeSn along III-V materials commonly used in PV. These results show that the potential efficiency of the 3J and 4J devices is over 35% under 1–Sun illumination with a terrestrial solar spectrum

(AM1.5G), and over 45% under 400–Sun concentrated sunlight.

Finally, Chapter 6 presents the results of several different investigations into device designs with advanced light-management needs: an ultra-thin GaAs solar cell targeted for space applications, which uses a metal/dielectric grating to trap light; a silicon hetero-junction cell with textured pyramidal surfaces with the aim of having low infrared emissivity; and a spectrum-splitting multi-junction cell design, which reflects part of the infrared solar spectrum onto a silicon cell to increase the overall efficiency.

Chapter 2

Theory

2.1 Direct and indirect semiconductors

Fundamentally, the formation of allowed bands of energy for electrons in a crystalline solid arises from the Pauli Exclusion Principle (since electrons are fermions), which causes the energies of allowed states to split compared to the energy levels in a single atom. When a very large number of atoms (on the order of 10^{23} for a macroscopic solid) are brought together and allowed to interact, a large number of simplifications must be made to obtain usable solutions to the Schrödinger equations describing the motion of each electron and atomic nucleus. The derivation of the Hamiltonian for a crystal is covered in detail in many textbooks, e.g [87]. The key to the mathematical treatment of the behaviour of electrons in a crystal is the Bloch wavefunction, which takes into account the periodicity of the lattice of almost immobile nuclei and thus the equivalence of the potential experienced by an electron when it is subjected to certain translations:

$$\Phi(\mathbf{k}, \mathbf{r}) = e^{(\mathrm{i}\mathbf{k}\cdot\mathbf{r})} u_{\mathbf{k}}(\mathbf{r}) \tag{2.1}$$

where $\mathbf{r}$ is the real space location in the crystal and $u_{\mathbf{k}}$ is a function with the same periodicity as the potential $V(\mathbf{r})$ due to the atomic nuclei, with translational period $\mathbf{R}$ such that $V(\mathbf{r}) = V(\mathbf{r} + \mathbf{R})$. The wave vectors $\mathbf{k}$ describe the crystal in reciprocal space. Simplifying to one spatial dimension, both k and $k + (2n\pi/R)$ where n is any integer will satisfy eq. 2.1, leading to different bands of solutions corresponding to different values of n. Each band will form a continuous set of solutions along k. The energy corresponding to this solution is the eigenvalue for that solution of the Schrödinger equation (methods for the solution of the Schrödinger equation are discussed in more detail in [87]). The eigenfunctions of the electronic part of the Hamiltonian must be expressed as some linear superposition of Bloch functions in order to have the correct translational symmetry. Generalizing to three spatial dimensions, band structures are generally complicated and are usually shown in terms of specific high-symmetry points inside a single Brillouin zone (the primitive cell of the crystal in reciprocal space). The calculated electronic band structures of two semiconductors important for this work, GaAs and Ge, are shown in Fig. 2.1.

The electrons in a solid will fill these allowed energy bands; without thermal excitation, the lowest-lying bands in terms of energy will be filled first. Bands which are completely filled with electrons at absolute zero are referred to as valence bands, while bands which are empty are conduction bands. For the optoelectronic properties discussed in this work, the important bands are the highest-energy valence bands and the lowest-energy conduction bands. The classification of a material as an insulator, semiconductor or

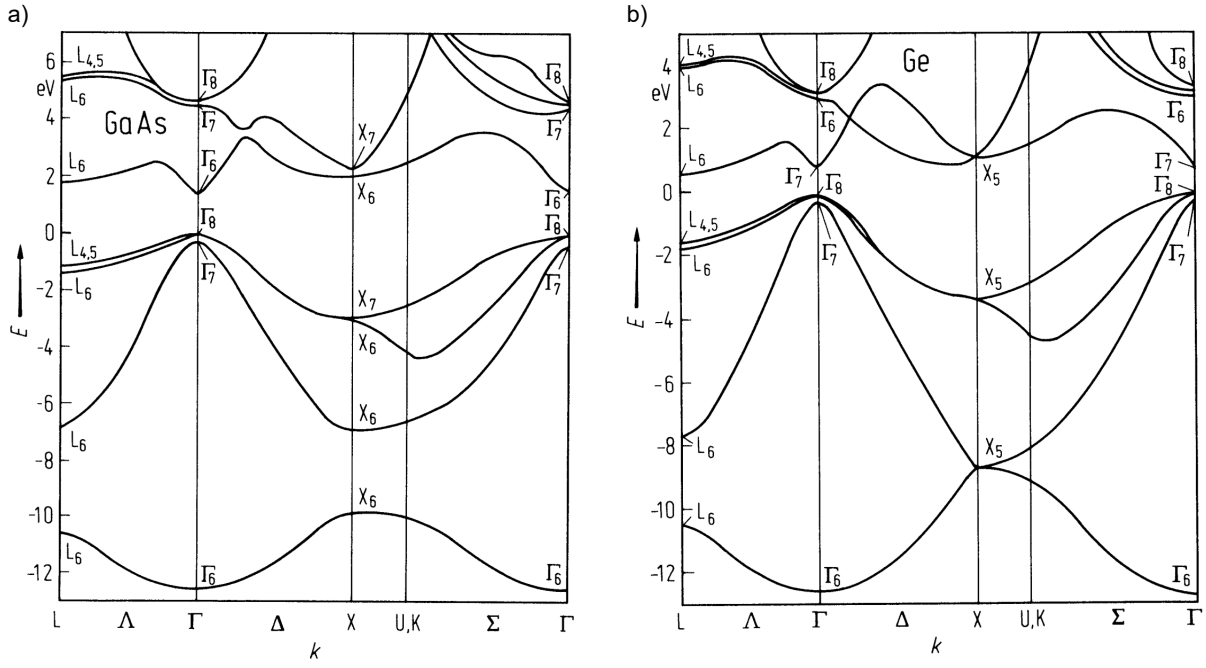


Figure 2.1: Electronic band structure calculated through non-local pseudopotential theory of a) direct semiconductor GaAs (the transition corresponding to the fundamental bandgap occurs at $\Gamma_8 \rightarrow \Gamma_6$) and b) indirect semiconductor Ge (the transition corresponding to the fundamental bandgap occurs at $\Gamma_8 \rightarrow L_6$). From [49].

metal depends on the relative position of the maximum valence band energy and the minimum conduction band energy. If the lowest-energy conduction band and highest-energy valence band overlap (zero bandgap), the material is a metal or semi-metal. Materials with an energy gap up to 3–4 eV [87] are usually designated as semiconductors, while larger gap materials are insulators.

If the conduction band (CB) minimum and valence band (VB) maximum of a material occur at the same value of the electron wavevector $\mathbf{k}$, with an energy gap in the range discussed above, this is described as a direct-bandgap semiconductor, while a difference in the $\mathbf{k}$ values gives an indirect semiconductor; Fig. 2.1 shows the band structures for a direct semiconductor (GaAs) and an indirect semiconductor (Ge). The label of 'direct' or 'indirect' refers to the VB $\rightarrow$ CB transition with the lowest possible energy, called the fundamental bandgap; in general, many direct and indirect transitions are possible in semiconductors of both types. In a direct semiconductor, the energy of an incident photon can be used to directly excite an electron from the valence band maximum to the conduction band minimum, while in an indirect semiconductor an additional process is necessary for photon absorption at the bandgap energy to overcome the difference in the crystal momentum $\mathbf{k}$. The absorption and emission of photons across indirect bandgaps is mediated by phonons, which are the quanta of lattice vibrations in the quantum-mechanical description of the lattice dynamics of a solid in terms of independent normal modes. As in the case of electron dispersion, band structures can be calculated for phonons in different materials; quantum mechanically, phonons are bosons (an infinite number can occupy the same quantum state), and the splitting of the dispersion relation into different bands arises from the normal modes of lattice vibration in the periodic structure. Fig. 2.2 shows the phonon dispersion for Ge. Through emission or absorption of a suitable phonon, the necessary change in

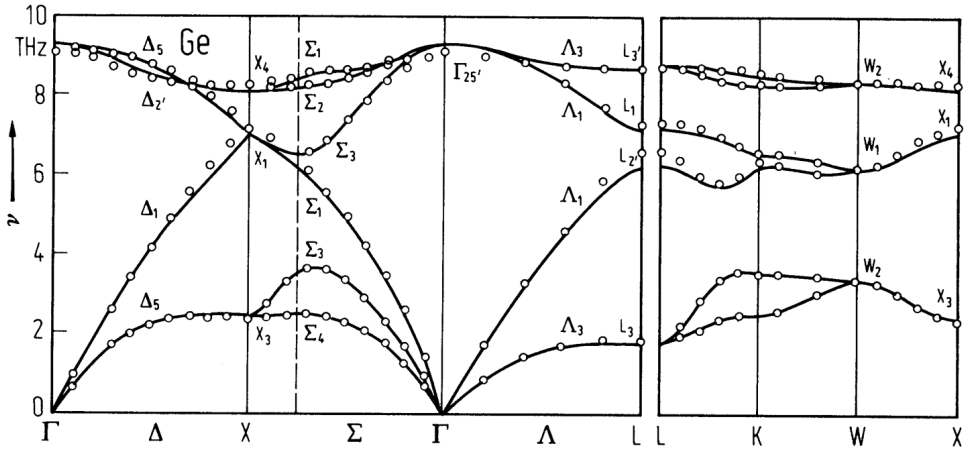


Figure 2.2: Phonon dispersion for Ge. From [49].

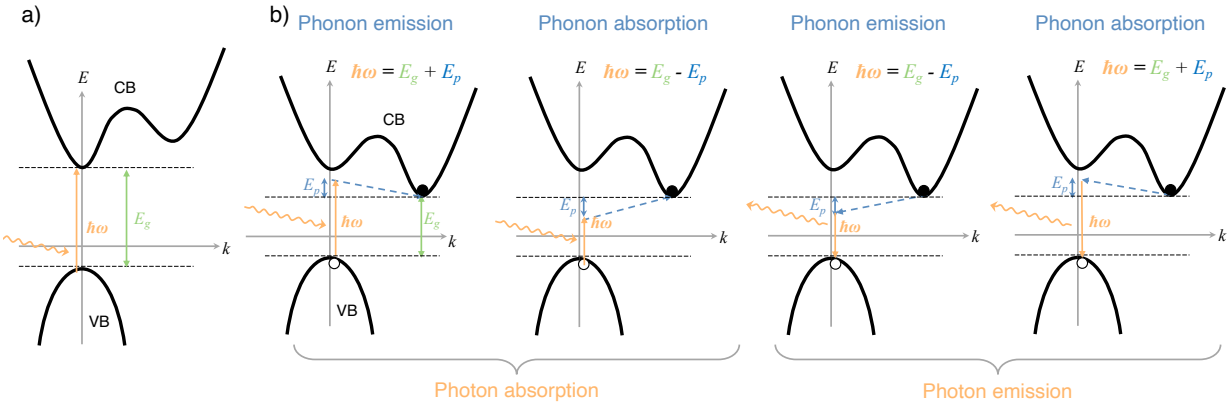


Figure 2.3: Schematic representation of a) photon absorption in a direct semiconductor and b) photon absorption and emission in an indirect semiconductor, assisted by either phonon emission or phonon absorption.

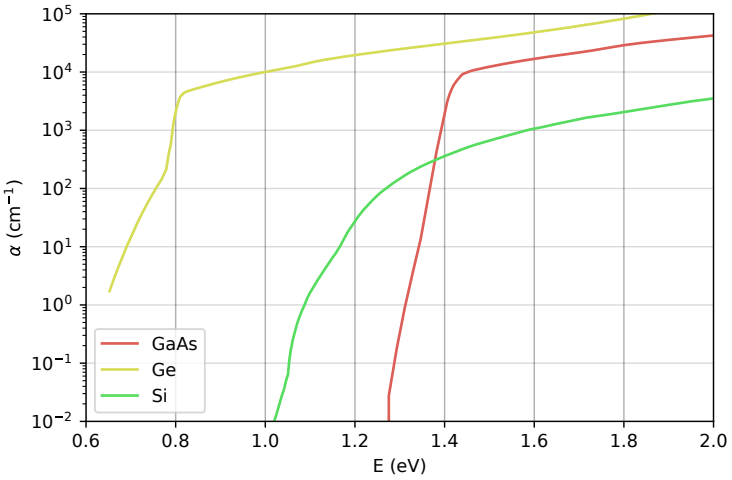


Figure 2.4: Absorption coefficients of undoped Si [129], Ge [130] and GaAs [131].

k to allow photon absorption or emission can take place. The process of absorption and emission of photons in direct and indirect semiconductors is shown schematically in Fig. 2.3, showing how the energy of the photon which is absorbed or emitted is affected by the involvement of a phonon. Absorption and emission across indirect bandgaps occurs at a much lower rate than absorption and emission across direct bandgaps, due to the additional need for a phonon; this is why a semiconductor such as Si is a much weaker absorber per unit length than e.g GaAs. The lowest direct energy transition in Si occurs at > 3 eV (see Table 1.1), and thus the majority of light in the solar spectrum can only be absorbed across an indirect transition. This means that much thicker layers of Si (generally hundreds of microns) are needed to obtain near-unity absorption of incident sunlight, compared to < 10 µm for a typical GaAs cell. The absorption coefficients of Si, Ge and GaAs are shown for comparison in Fig. 2.4; this clearly shows that the absorption onset for GaAs is much sharper than that of Si, and absorption coefficients just above the bandgap are 1-2 orders of magnitude higher. Ge is a fundamentally indirect semiconductor with a room-temperature bandgap of 0.67 eV, but the lowest direct transition is relatively close in energy at 0.8 eV, and thus Ge shows sharper, more GaAs-like absorption around 0.8 eV.

2.2 Optical constant models

The formation of bands of allowed energies in solids as discussed in the previous section clearly has implications for the optical behaviour of these materials, dictating how photons of different energies will be involved in interband (CB to VB and vice versa) transitions. This section will outline the contribution of critical points (stationary points in the band structure) to the dielectric function of materials, and how the dielectric function can be modelled for real materials.

2.2.1 Critical point parabolic band models

To obtain contributions to the dielectric function $\tilde{\varepsilon}$ due to interband transitions, we can use Fermi's Golden Rule (FGR) for transitions between quantum eigenstates (derivations for the concepts in this section are based on [132] and [133, Chapter 2]). For FGR to be a valid approximation, we must assume that the Hamiltonian

H' for the electromagnetic interaction is a weak perturbation. Applying FGR to find the probability per unit time of a photon of energy $\hbar\omega$ being absorbed and causing a (direct) valence to conduction band transition gives:

$$W_{\mathbf{k}} = \frac{2\pi}{\hbar}|\langle v|H'|c\rangle|^2\delta(E_c(\mathbf{k}) - E_v(\mathbf{k}) - \hbar\omega)$$

Where $\mathbf{k}$ is the wavevector at the point in the band structure where the transition takes place (assumed here to be constant) and $\langle v|H'|c\rangle$ is the matrix element for the electromagnetic perturbation taken between the valence and conduction band Bloch states. The Dirac delta function expresses the conservation of energy for photon absorption and the resulting transfer of an electron from the valence to the conduction band. To obtain the total probability per unit time at any point in the band structure, we must integrate over $\mathbf{k}$:

$$W = \frac{2\pi}{\hbar}\int |\langle v|H'|c\rangle|^2\delta(E_c(\mathbf{k}) - E_v(\mathbf{k}) - \hbar\omega)\frac{2}{8\pi^3}d^3k$$

Assuming that $|\langle v|H'|c\rangle|^2$ is independent of $\mathbf{k}$, this term becomes a constant of proportionality and the remaining integral is the so-called density of states, ρ_{cv}:

$$\rho_{cv}(\hbar\omega) = \frac{2}{8\pi^3}\int \delta(E_c(\mathbf{k}) - E_v(\mathbf{k}) - \hbar\omega)d^3k$$

By transforming this expression to an integral over a surface of constant energy, and integrating once, this can be rewritten as:

$$\rho_{cv}(\hbar\omega) = \frac{2}{8\pi^3}\int\int \frac{dS}{|\nabla_k(E_c - E_v)|_{E_c-E_v=\hbar\omega}} \tag{2.2}$$

Clearly, the largest contribution to the integral is made when the denominator becomes very small, i.e. when $E_c - E_v$ is stationary so that its gradient vanishes. This happens around critical points in the band structure, for instance where a minimum in the conduction band and a maximum in the valence band coincide at the same $\mathbf{k}$. However, the result of integrating equation 2.2 depends on the nature of the critical points. These critical points are called van Hove singularities, and can be categorized according to the type of critical point occurring in $(E_c - E_v)$. The types of critical points possible depend on the dimensionality of the system; in 1D, only minima and maxima are possible, while in 2D and 3D saddle points are possible (one and two different types, respectively). One assumption which simplifies the expressions for $(E_c - E_v)$ is the parabolic band approximation, which assumes that in the vicinity of critical points in the band structure, the curvature of the band can be described as having a quadratic dependence on the components k_i of the three-dimensional $\mathbf{k}$ vector (i.e. only the first term in the Taylor expansion of $(E_c - E_v)$ is used):

$$E_c(\mathbf{k}) - E_v(\mathbf{k}) = E_g(\mathbf{k_0}) + \sum_{i=1}^{3} a_i\left(k_i - k_{0i}\right)^2 \tag{2.3}$$

where the sum runs over the three spatial directions, $\mathbf{k_0}$ is the wavevector at the critical point, and the a_i coefficients are the second derivative of the energy difference for each component of $\mathbf{k}$, $a_i = \frac{\partial^2}{\partial k_i^2}\left[E_c(\mathbf{k}) - E_v(\mathbf{k})\right]$. The type of critical point (labelled as M_0, M_1 etc.) depends on how many of the coefficients a_i are negative. The curvature of the bands is often described in terms of the effective mass m^* of the charge carriers (electrons in the CB and holes in the VB), treating the energy dispersion of the particle in the band structure analogous to a free particle with some mass:

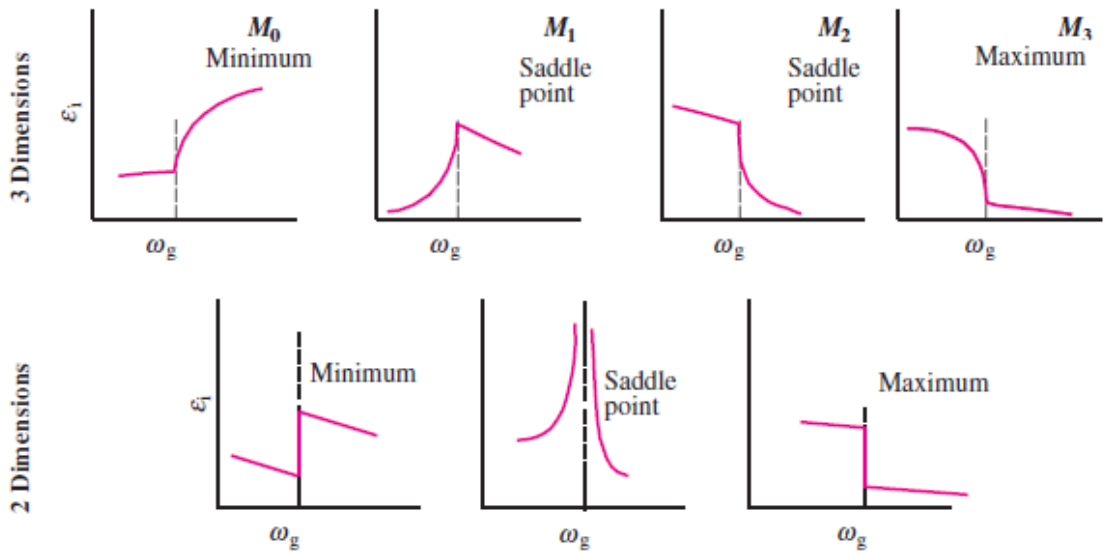


Figure 2.5: Functional form of the contribution to the imaginary part of the dielectric constant from different types of critical points in the band structure, in two and three dimensions. From [87].

$$E_c(\mathbf{k}) = \frac{E_g}{2} + \frac{\hbar^2|\mathbf{k}|^2}{2m^*} \tag{2.4}$$

The probability per unit time of a photon being absorbed, as given by the expression for W above, is clearly related to the absorption coefficient and thus the imaginary part of the dielectric function ($\varepsilon_2 \propto W$); it is given in [134] as:

$$\varepsilon_2(\omega) = \frac{4\hbar^2 e^2}{\pi\mu_0\omega^2}|\langle v|p|c\rangle|^2\rho_{cv}(\omega) \tag{2.5}$$

In fact, a factor of $f(E_v) - f(E_c)$, where f is the Fermi distribution (see Section 2.4), has been neglected here. This describes the occupancy of the states from and to which the transition happens; if we assume the conduction band is mostly empty ($f(E_c) \approx 0$) while the valence band is mostly full ($f(E_v) \approx 1$), this factor is ≈ 1. The functional forms of the contribution to ε_2 arising from different types of critical points in two and three dimensions are shown in Fig. 2.5.

Adachi [58, 135, 134] used a critical point parabolic band (CPPB) model to calculate the functional form of contributions to ε_2. A (proportional) expression for ε_2 can thus be obtained by determining the dimensionality and type of critical point, and finding the corresponding functional form for ρ_{cv}. The full dielectric function $\tilde{\varepsilon} = \varepsilon_1 + i\varepsilon_2$ can be found by applying a Kramers-Kronig transformation[1] to ε_2 to find ε_1 [135]. Adachi's description of his model (e.g. [58, 135, 134]) relies on the following identity:

$$\lim_{\nu\to 0} \varepsilon_1(\omega + i\nu) = \varepsilon_1(\omega) + i\varepsilon_2(\omega) \tag{2.6}$$

However, no proof of this statement, or reference to one, is provided; therefore, a novel (as far as I am aware) proof is provided in Appendix A. This also elucidates how the ν parameter relates to broadening of the

[1]The Kramers-Kronig relations are used to find the real part of a physical response function from the analytic form of the imaginary part, or vice versa. They can be derived from the causality required of a response function such as the dielectric function (the system cannot react to an external change before that change is applied).

Table 2.1: The functional forms as given by the Adachi model [135, 134] for the lowest-energy transitions contributing to the dielectric function of Ge. These give the real and imaginary parts of the dielectric function through eq. 2.6. The E_0' triplet refers to three transitions at the Γ point: E_0', $E_0' + \Delta_0'$ and $E_0 + \Delta_0' + \Delta_0$ (see Fig. 1.9); the E_0' triplet and E_2 transitions are modelled by Adachi as damped harmonic oscillators (DHOs) as they are attributed to a mixture of several types of critical point [58].

Energy transition	**Type**	**Functional form**
E_{gap}	Indirect	$\varepsilon(\omega) = \frac{2D}{\pi}\Big\{ -\frac{E_{gap}^2}{(\hbar\omega+i\Gamma)^2}\ln\left(\frac{E_c}{E_{gap}}\right) + \frac{1}{2}\left(1+\frac{E_{gap}}{\hbar\omega+i\Gamma}\right)^2\ln\left(\frac{\hbar\omega+i\Gamma+E_c}{\hbar\omega+i\Gamma+E_{gap}}\right)$ $+\frac{1}{2}\left(1-\frac{E_{gap}}{\hbar\omega+i\Gamma}\right)^2\ln\left(\frac{\hbar\omega+i\Gamma-E_c}{\hbar\omega+i\Gamma-E_{gap}}\right)\Big\}$
$E_0/E_0+\Delta_0$	3D M_0	$\varepsilon(\omega) = A\frac{E_0^{-1.5}}{(\hbar\omega+i\Gamma)^2}\Big\{E_0^2[2-(1+\frac{\hbar\omega+i\Gamma}{E_0})^{0.5}-(1-\frac{\hbar\omega+i\Gamma}{E_0})^{0.5}]$ $+\frac{1}{2}\left(\frac{E_0}{E_0+\Delta+0}\right)^{1.5}(E_0+\Delta_0)^2[2-(1+\frac{\hbar\omega+i\Gamma}{E_0+\Delta_0})^{0.5}-(1-\frac{\hbar\omega+i\Gamma}{E_0+\Delta_0})^{0.5}]\Big\}$
$E_1/E_1+\Delta_1$	3D M_1	$\varepsilon(\omega) = -B_1\frac{E_1^2}{(\hbar\omega+i\Gamma)^2}\ln\left(1-(\frac{\hbar\omega+i\Gamma}{E_1})^2\right) - B_2\frac{(E_1+\Delta_1)^2}{(\hbar\omega+i\Gamma)^2}\ln\left(1-(\frac{\hbar\omega+i\Gamma}{E_1+\Delta_1})^2\right)$
E_2	DHO	$\varepsilon(\omega) = C\frac{1}{\left(1-(\frac{\hbar\omega}{E_2})\right)^2 - i\frac{\Gamma}{E_2}}$
E_0' triplet	DHOs	$\varepsilon(\omega) = \sum_i C_i\frac{1}{\left(1-(\frac{\hbar\omega}{E_i'})\right)^2 - i\frac{\Gamma_i}{E_i'}}$

ε peaks as discussed in [134]. An expression for the contribution of indirect transitions, relevant here because SiGeSn is an indirect-bandgap semiconductor, can also be derived similarly by considering conservation of energy of the electron and photon and the density of states [132, 134]. The resulting functional forms in the Adachi model of the most important direct and indirect transitions for the materials in this work are given in Table 2.1.

Fig. 2.6 shows the fit reported by Adachi to the model described in [135]. Clearly, while this can be used to illustrate the usefulness of a rigorous physical model in representing real optical behaviour with reasonable accuracy, it is difficult to use it to predict parameters such as transition energies and strengths for a material with unknown optical properties (such as SiGeSn), since a close fit to the data cannot be achieved. While fitting a physical model to the ellipsometric data provides the most information regarding critical points in the band structure, several complicating factors may prevent a good fit from being obtained using an Adachi-type model; real materials may exhibit non-uniform peak broadening [136], and the behaviour in an alloy such as SiGeSn may deviate even further from the ideal behaviour. This means that in practice, more flexible parametric models are often used to fit measurements of the dielectric constants through e.g. ellipsometry.

A model type which has been previously used to fit the optical constants of novel materials is the Psemi (Parametric Semiconductor) oscillator model [137], which allows various peak types to be defined, with a large amount of freedom in determining the peak shape while maintaining Kramers-Kronig consistency. A Psemi model fitted to experimental Ge data is included in the Woollam WVASE software which is used to measure and analyse ellipsometric data, and this was used as a starting point for fitting the SiGeSn data. The fitting procedure used for the SiGeSn samples is further explained in Section 3.2.

2.2.2 Critical point analysis

A common technique for identifying direct transition energies is the use of third-derivative modulation spectroscopy such as photoreflectance [138], as discussed in Section 3.3, or explicit computation of the second

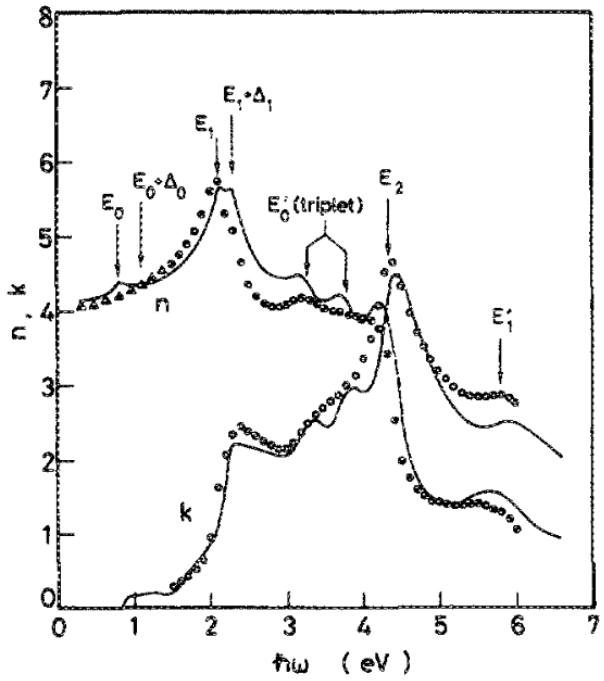


Figure 2.6: The fit given by Adachi of his CPPB-type model to experimental Ge dielectric function data using the critical point types in Table 2.1. No contribution due to the indirect bandgap was included. From [135].

or third derivative of the dielectric function (Section 3.2.3). Such data is commonly fitted with expressions of the form:

$$S = Ce^{i\theta}(E - E_0 + i\Gamma)^{-n} \tag{2.7}$$

where S is either the photoreflectance signal, $\Delta R/R$, or the second or third derivative of the dielectric function. C is the strength of the transition, θ is a phase factor, E_0 is the transition energy and Γ describes the peak broadening. The value of the exponent n depends on the dimensionality and critical point type of the van Hove singularity, as discussed above.

However, an examination of the expected forms of ε_1 and ε_2 (the real and imaginary parts of the dielectric function, respectively) shows that this form is somewhat inconsistent with the parabolic band approximation both in the case of fitting photoreflectance data and for fitting the second derivative of the dielectric function explicitly. Photoreflectance is a contactless modulation spectroscopy technique useful for investigating the energies of interband transitions through modulation of the internal electric field. Carriers are photogenerated with a laser pump beam, modulating the internal electric field of the sample, and the reflectivity of the sample is measured with a probe beam with and without the effect of the pump beam, allowing the change in reflectivity (ΔR) due to the pump beam to be measured. Referring to the original work by Aspnes [138], in the low-field limit the reflectance difference spectrum is given by:

$$\frac{\Delta R}{R} = \mathrm{Re}\left\{\left[C_\mathrm{s} C_\mathrm{ex} C_\mathrm{in} e^i e^j \Delta\varepsilon^{ij}\right]\right\} \tag{2.8}$$

The full form and meaning of the prefactors C_s, C_{ex}, C_{in}, e^i and e^j is given in Appendix F.1. The key

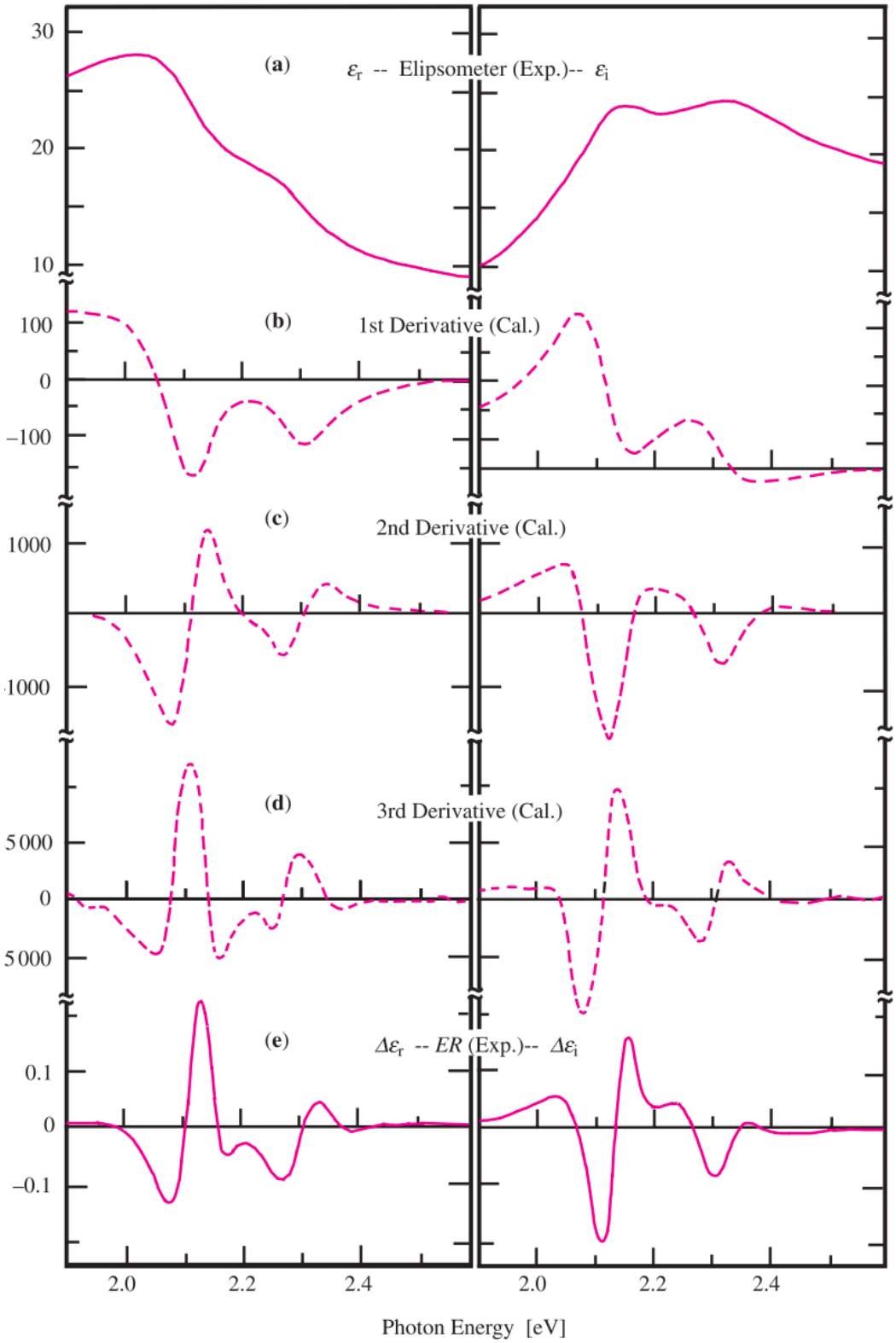


Figure 2.7: The relationship between derivatives of the dielectric function and photomodulation spectroscopy for Ge, showing a) the real and imaginary parts of ε, b) its first derivative $E^{-2}(d(E^2\varepsilon))/dE$, c) its second derivative $E^{-2}(d^2(E^2\varepsilon))/dE^2$, and d) its third derivative $E^{-2}(d^3(E^2\varepsilon))/dE^3$. e) $\Delta\varepsilon$ as obtained through electroreflectance measurement. From [87].

non-constant factor in eq. 2.8 is $\Delta\varepsilon^{ij}$, which is given by:

$$\Delta\varepsilon^{ij} = \frac{e^2\hbar^2\mathcal{E}^k\mathcal{E}^l}{24E^2}\left(\mu^{-1}\right)^{kl}\frac{\partial^3}{\partial E^3}\left(E^2\varepsilon^{ij}(\Gamma, E)\right) \tag{2.9}$$

where $\mathcal{E}$ is the electric field strength, μ is the effective mass tensor, and the indices k and l denote summation. The index notation in $\Delta\varepsilon^{ij}$ is used because in the most general case, the dielectric behaviour of a material is described by a tensor (the dispersion may be spatially anisotropic). There is one clearly dispersive term, the factor of E^{-2}. A heuristic derivation of the same quantity in [87, Chapter 6] similarly gives:

$$\Delta\varepsilon = \frac{1}{6E^2}\frac{e^2\mathcal{E}^2\hbar^2}{2\mu}\frac{\partial^3(E^2\varepsilon)}{\partial E^3} \tag{2.10}$$

also giving the quadratic dependence on the electric field strength $\mathcal{E}$ and the E^{-2} dependence. This shows that:

$$\frac{\Delta R}{R} \propto \frac{1}{E^2}\frac{\partial^3 E^2\varepsilon}{\partial E^3} \tag{2.11}$$

where constants which are expected to be weakly dispersive have been neglected. This form of the reflection difference is further illustrated by the experimental data for Ge shown in Fig. 2.7, which shows the dielectric function of Ge and its explicitly computed derivatives, compared to electroreflectance data. The quantity $E^{-2}(\partial^3 E^2\varepsilon)/(\partial E^3)$ shows a remarkable similarity to the electroreflectance measurement.

The factor of E^2, clearly apparent in eq. 2.11, is generally neglected in critical point fits, even in the original work by Aspnes, where he gives the form in eq. 2.7 as suitable for fitting data and notes that "C and θ are amplitude and phase factors that vary slowly with E", implying the E^2 factor is subsumed into C. However, there appears to be no reason, with the use of modern fitting algorithms, not to explicitly include the E^2 factor in order to remove an obvious part of the energy-dependence of the constants and obtain a (slightly) more accurate fit. Since the fits are generally carried out over a relatively small energy range, the factor of E^2 will not dramatically affect the E_0 or Γ values fitted. For fitting explicit derivatives of the dielectric constants, the functional form of the $\frac{\partial^2 E^2\varepsilon}{\partial E^2}$ factor is expected to be equal to eq. 2.7, as discussed below.

Considering the appropriate expressions to fit the explicit second or third derivative of dielectric functions, it is reasonable to start with expressions for ε derived from the parabolic band approximation, as discussed in Section 2.2. From [87, Chapter 6]:

$$\varepsilon_2(\omega) = \begin{cases} AE^{-2}\left(E - E_g\right)^{1/2} & \text{for } E > E_g \\ 0 & \text{for } E < E_g \end{cases} \tag{2.12}$$

for a 3D M_0-type critical point, such as the E_0 transition in Ge or GaAs. This can be obtained from eq. 2.5. Applying a K-K transformation to this equation gives:

$$\varepsilon_1(\omega) = \begin{cases} C + AE^{-2}\left[2E_g^{1/2} - \left(E_g + E\right)^{1/2}\right] & \text{for } E > E_g \\ C + AE^{-2}\left[2E_g^{1/2} - \left(E_g + E\right)^{1/2} - \left(E_g - E\right)^{1/2}\right] & \text{for } E < E_g \end{cases} \tag{2.13}$$

where C is a constant[2]. Lifetime broadening in real materials can be taken into account by substituting $E \to E + i\Gamma$ [134]. Examining these equations, it is clear that computing $\partial^2\varepsilon_1/\partial E^2$ and $\partial^2\varepsilon_2/\partial E^2$ directly can never give an equation of the form in eq. 2.7, which is assumed in e.g. [74, 75]; due to the E^{-2} pre-factor, multiple terms are generated when differentiating the expression due to the product rule, leading to a very complicated expression for $\partial^2\varepsilon_2/\partial E^2$. However, if ε_2 is first multiplied by E^2, differentiating eq. 2.12 will give an expression of the form $(E - E_g)^{-n}$. The work on SiGe by Vina et al. [74], cited by both [75] and [42], fits similar expressions to the E_1 and $E_1 + \Delta_1$ critical points, and states explicity that:

$$\varepsilon \sim C - \ln(E - \omega - i\Gamma)e^{i\phi} \tag{2.14}$$

where it appears the E^{-2} factor in ε which arises due to eq. 2.5 has been explicitly neglected.

Summarizing, this means that photoreflectance data in this work has been fitted with expressions of the form:

$$\frac{\Delta R}{R} = \mathrm{Re}\left\{CE^{-2}e^{i\theta}(E - E_0 + i\Gamma)^{-n}\right\} \tag{2.15}$$

where $n = 3$ for 2D CPs, $n = 5/2$ for 3D CPs, and $n = 2$ for exciton features (the fitting method is discussed further in Section 3.3). Critical point analysis using the dielectric functions obtained through ellipsometry is done by computing $\frac{\partial^2(E^2\varepsilon)}{\partial E^2}$ as described in Section 3.2.3 and fitting equations of the form:

$$\frac{\partial^2(E^2\varepsilon)}{\partial E^2} = Ae^{i\theta}(E - E_0 + i\Gamma)^{-m} \tag{2.16}$$

where $m = 2$ for 2D CPs, $m = 3/2$ for 3D CPs, and $n = 1$ for exciton features (one lower than the exponents for the PR fits, since these are second rather than third derivatives of $E^2\varepsilon$).

2.3 Light-trapping

2.3.1 Transfer matrix model

The transfer matrix model is a wave-optical model which describes the reflection, transmission, refraction and absorption of light in structures with one or more material layers, taking into account wave interference due to reflection at different interfaces. This behaviour can be derived fully from the Fresnel equations. Light incident on and travelling inside the structure is assumed to be a plane wave with a forward and backward-travelling component, and reflection and transmission at each interface are described by a matrix which describes the complex reflection and transmission amplitudes. The change of phase of the wave as it travels through a material (including absorption) can similarly be represented by a matrix.

The Fresnel equations, and thus these matrices, will depend on both the wavelength (for a dispersive material) and the incidence angle and polarization of the light [91]:

$$\begin{array}{ll} r_s = \frac{n_1\cos\theta_1 - n_2\cos\theta_2}{n_1\cos\theta_1 + n_2\cos\theta_2} & r_p = \frac{n_2\cos\theta_1 - n_1\cos\theta_2}{n_2\cos\theta_1 + n_1\cos\theta_2} \\ t_s = \frac{2n_1\cos\theta_1}{n_1\cos\theta_1 + n_2\cos\theta_2} & t_p = \frac{2n_1\cos\theta_1}{n_2\cos\theta_1 + n_1\cos\theta_2} \end{array} \tag{2.17}$$

For an electromagnetic plane wave interacting with a layered structure, the electric field can be written as the sum of forward ($\mathbf{E}_f$) and backward-travelling ($\mathbf{E}_b$) amplitudes:

[2]Note that the form of ε_1 is very similar to that given in Table 2.1; these forms differ slightly because Adachi constrains the strength parameters A of the E_0 and $E_0 + \Delta_0$ transitions in relation to one another, as they both occur along the same symmetry point.

$$\mathbf{E}(\mathbf{r}) = \mathbf{E}_f^0 e^{i(\mathbf{k}_f \cdot \mathbf{r} - \omega t)} + \mathbf{E}_b^0 e^{i(\mathbf{k}_b \cdot \mathbf{r} - \omega t)} \tag{2.18}$$

Here, $\mathbf{k}_f$ and $\mathbf{k}_b$ are the wavevectors for the forward and backward-travelling components of the wave, respectively. The wavevectors describe the direction in which the wavefronts of the plane wave are travelling; in addition, the z-component may describe absorption in a material with $\kappa > 0$. $\mathbf{r}$ is a position within the medium (with $z = 0$ being the front surface). $\mathbf{E}_f^0$ and $\mathbf{E}_b^0$ are the vector amplitudes of the forward and backward-travelling plane wave components, respectively. Their form depends on whether the incident light is s-polarized (also frequently described as TE or transverse electric polarization) or p-polarized (TM or transverse magnetic). For a plane wave, the H field can be found directly from the E field through $\mathbf{H} = \frac{1}{\mu_0 \omega}\mathbf{k} \times \mathbf{E}$ [139]; thus, we will only discuss the E field, as it contains all the information about the plane wave. Assuming, without loss of generality, that the incident waves are in the x-z plane, s polarization has $\mathbf{E}_f^0 = E_f \hat{\mathbf{j}}$, giving $\mathbf{H}_f \propto nE_f(-\cos\theta \hat{\mathbf{i}} + \sin\theta \hat{\mathbf{k}})$, while for p polarization $\mathbf{H}_f^0$ lies in the $\hat{j}$ direction so that $\mathbf{E}_f = E_f(+\cos\theta \hat{\mathbf{i}} - \sin\theta \hat{\mathbf{k}})$, where E_f is a scalar amplitude. $\mathbf{k}_f$ and $\mathbf{k}_b$, the forward and backward-travelling parts of the wavevector, can be written explicitly as:

$$\mathbf{k}_f = \frac{2\pi\tilde{n}}{\lambda}(\hat{\mathbf{k}}\cos\theta + \hat{\mathbf{i}}\sin\theta) \quad , \quad \mathbf{k}_b = \frac{2\pi\tilde{n}}{\lambda}(-\hat{\mathbf{k}}\cos\theta + \hat{\mathbf{i}}\sin\theta) \tag{2.19}$$

Where $\tilde{n}$ is the complex refractive index of the medium ($\tilde{n} = n + i\kappa$), λ is the vacuum wavelength, and θ is the angle the wavevector makes relative to the surface normal. At this point, it can be noted that if $\kappa > 0$, as for any absorbing material, the components of the $\mathbf{k}$ vectors may become complex. Only the z-component of the wavevector for a plane wave may be complex while the x-component must remain real; an imaginary x-component would describe power dissipation in the directions parallel to the interfaces, which would mean the light is not a plane wave. This indicates that $\sin\theta$ and $\cos\theta$ must be complex and thus θ is complex. The meaning and treatment of the complex angle of the wavevector in absorbing materials is discussed further in Appendix B. For now, it can be noted that if the z-component of the k vector has a positive imaginary part ($\kappa > 0$), the result in eq. 2.18 is a decaying amplitude as the electric field propagates through the layer, corresponding to absorption in the layer.

Considering a multi-layer stack with reflection and transmission at all interfaces, we can construct an equation for the electric field amplitudes travelling forwards and backwards near the interfaces, e.g. $E_{b1} = E_{f1}r_{12} + E_{b2}t_{21}$; the backward-travelling amplitude of the E-field in material 1 at the interface with material 2 is the reflected amplitude of the forward-travelling amplitude in material 1 and the amplitude of the backward-travelling component transmitted from medium 2 into medium 1. Similarly $E_{f2} = E_{f1}t_{12} + E_{b2}r_{21}$. These intuitive expressions can be validated by deriving them from the plane-wave definitions using the electromagnetic boundary conditions (the tangential component of the electric field $\mathbf{E}$ and the normal component of the magnetic flux density $\mathbf{B}$ are continuous across an interface), as is done in e.g. Born and Wolf [139, Chapter 1].

Now, general equations which relate the forward and backward-travelling amplitudes in adjacent layers at their interface can be constructed. For example, the amplitude travelling forwards at the start of layer 3 and the amplitude travelling backwards at the start of layer 2 can be related to the amplitudes in adjacent layers as:

$$\begin{aligned} f_3 &= f_2 e^{i\delta_2} t_{2/3} + b_3 r_{3/2} \\ b_2 &= f_2 e^{i\delta_2} r_{2/3} e^{i\delta_2} + b_3 t_{3/2} e^{i\delta_2} \end{aligned} \tag{2.20}$$

The δ_2 factor accounts for the phase change of the amplitude across the layer, and is equal to $k_z d$ where d is the layer thickness and k_z is the z-component of the $\mathbf{k}$ vector ($= \frac{2\pi n \cos\theta}{\lambda_{vac}}$). The values r and t are amplitude reflection and transmission probabilities, where $r_{2/3}$ denotes the probability of light travelling from medium 2 into medium 3 being reflected back into medium 2 at the interface. Similarly, $t_{2/3}$ denotes light which is transmitted from medium 2 to medium 3 at the same interface. These expressions can be generalized to any layer in the structure:

$$\begin{aligned} f_{n+1} &= f_n e^{i\delta_n} t_{n/n+1} + b_{n+1} r_{n+1/n} \\ b_n &= f_n e^{2i\delta_n} r_{n/n+1} + b_{n+1} t_{n+1/n} \end{aligned} \tag{2.21}$$

Rearranging these equations and substituting the first equation into the second, b_n and f_n can be expressed in terms of b_{n+1} and f_{n+1}:

$$\begin{aligned} f_n &= \frac{e^{-i\delta_n}}{t_{n/n+1}}(f_{n+1} - b_{n+1} r_{n+1/n}) \\ b_n &= f_n r_{n/n+1} e^{2i\delta_n} + b_{n+1} t_{n+1/n} e^{i\delta_n} \\ &= \left(f_{n+1} - b_{n+1} r_{n+1/n}\right) \frac{e^{i\delta n}}{t_{n/n+1}} r_{n/n+1} + b_{n+1} t_{n+1/n} e^{i\delta_n} \\ &= e^{i\delta_n}\left[f_{n+1}\left(\frac{r_{n/n+1}}{t_{n/n+1}}\right) + b_{n+1}\left(\frac{-r_{n+1/n} r_{n/n+1} + t_{n+1/n} t_{n/n+1}}{t_{n/n+1}}\right)\right] \\ &= \frac{e^{i\delta_n}}{t_{n/n+1}}\left(f_{n+1}\left(r_{n/n+1}\right) + b_{n+1}\right) \end{aligned} \tag{2.22}$$

In the final simplifying step for the b_n expression, the identity $t_{a/b} t_{b/a} - r_{a/b} r_{b/a} = 1$, which can be derived from the Fresnel equations, was used. Taking the expression for f_n and the final expression for b_n, these equations can be written in matrix form as:

$$\begin{aligned} \begin{pmatrix} f_n \\ b_n \end{pmatrix} &= \frac{1}{t_{n/n+1}} \begin{pmatrix} e^{-i\delta_n} & -e^{-i\delta_n} r_{n+1/n} \\ e^{i\delta_n} r_{n/n+1} & e^{i\delta_n} \end{pmatrix} \begin{pmatrix} f_{n+1} \\ b_{n+1} \end{pmatrix} \\ \begin{pmatrix} f_n \\ b_n \end{pmatrix} &= \frac{1}{t_{n/n+1}} \begin{pmatrix} e^{-i\delta_n} & 0 \\ 0 & e^{i\delta_n} \end{pmatrix} \begin{pmatrix} 1 & r_{n/n+1} \\ r_{n/n+1} & 1 \end{pmatrix} \begin{pmatrix} f_{n+1} \\ b_{n+1} \end{pmatrix} \\ \begin{pmatrix} f_n \\ b_n \end{pmatrix} &= M_n \begin{pmatrix} f_{n+1} \\ b_{n+1} \end{pmatrix} \end{aligned} \tag{2.23}$$

where in the first step, the identity $r_{a/b} = -r_{b/a}$ was used, which can be seen from the Fresnel equations. This matrix equation relates the amplitudes in one layer to the amplitudes of the layer below. Generalizing for the full stack, given that $f_1 = 1$, $b_1 = r$, $f_N = \mathrm{t}$ and $b_N = 0$ (the Nth layer is the semi-infinite transmission medium), we can write:

$$\begin{aligned} \begin{pmatrix} 1 \\ r \end{pmatrix} &= M_1 M_2 \cdots M_N \begin{pmatrix} t \\ 0 \end{pmatrix} \\ \begin{pmatrix} 1 \\ r \end{pmatrix} &= \begin{pmatrix} \tilde{M}_{11} & \tilde{M}_{12} \\ \tilde{M}_{21} & \tilde{M}_{22} \end{pmatrix} \begin{pmatrix} t \\ 0 \end{pmatrix} \end{aligned} \tag{2.24}$$

The matrix elements of $\tilde{M}$ can be calculated with knowledge of the optical constants, layer thicknesses,

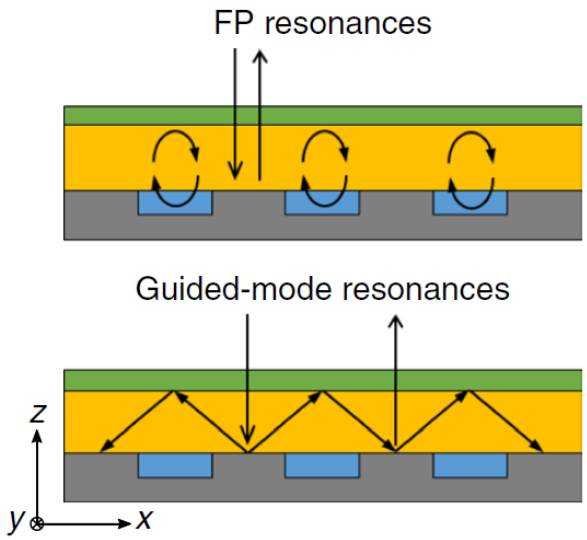


Figure 2.8: Two types of resonant mode in an ultra-thin solar cell: Fabry-Perot (thin-film) and guided modes due to diffraction. From [95].

and incidence angle for all layers. Inspecting eq. 2.24, it is possible to calculate r and t as:

$$\begin{aligned} t =& \frac{1}{\tilde{M}_{11}} \\ r =& \tilde{M}_{21} t = \frac{\tilde{M}_{21}}{\tilde{M}_{11}} \end{aligned} \tag{2.25}$$

Once the values of r and t are known, it is then possible to work out the amplitudes at the start of every layer, and thus calculate quantities such as absorption per layer and overall reflection and transmission. Calculation of power flow and depth-dependent absorption profiles using the TMM is discussed in Section 4.2.4.

2.3.2 Fabry-Perot and guided mode analysis

For the ultra-thin cells with metal/dielectric gratings considered in Section 6.1, the peaks in the absorption or quantum efficiency spectrum can generally be attributed to either Fabry-Perot (thin-film) interference, or resonant guided modes due to diffraction from the grating; both of these effects are illustrated in Fig. 2.8. To analytically investigate the origin of resonance lines in the absorption spectrum due to different diffracted orders, a solar cell can be considered as a waveguide, using a model for an asymmetric waveguide (this method of analysis was applied to the high-efficiency ultra-thin GaAs cell with a metallic grating in [95]). The allowed diffracted directions in which light can travel after interacting with the grating depend on the optical constants (and thus also the wavelength) of the material in which the light is travelling and the reciprocal lattice vectors (determined by the period and symmetry) of the grating. The allowed diffraction directions can be calculated analytically from the Fraunhofer equation [77]:

$$\begin{aligned} \mathbf{k}_{\parallel(m_1,m_2)} &= m_1\mathbf{b_1} + m_2\mathbf{b_2} + \mathbf{k}_{\parallel\mathbf{0}} \\ n\mathbf{u}_{\parallel(m_1,m_2)} &= \frac{m_1\mathbf{b_1}\lambda_0}{2\pi} + \frac{m_2\mathbf{b_2}\lambda_0}{2\pi} + \mathbf{u}_{\parallel 0} \end{aligned} \tag{2.26}$$

with the first expression in terms of the wavevectors $\mathbf{k}$ and the second in terms of the real space unit direction vectors. λ_0 is the wavelength in vacuum, $\mathbf{b_1}$ and $\mathbf{b_2}$ are the reciprocal lattice vectors of the grating, and n is the refractive index in the layer in which the diffracted order is travelling. $\mathbf{u}_\parallel = u_x\mathbf{e}_x + u_y\mathbf{e}_y$ is the unit vector which describes the in-plane direction of the plane wave, and $\mathbf{k}_\parallel$ is the in-plane wavevector. $\mathbf{u}_{\parallel 0}$ is the in-plane unit direction, and $\mathbf{k}_{\parallel,\mathbf{0}}$ the in-plane wavevector, of the incident light (both are equal to (0, 0) for normal incidence). m_1 and m_2 are the integer diffraction order indices along the reciprocal lattice vectors $\mathbf{b_1}$ and $\mathbf{b_2}$ respectively. The relationship between the real space lattice vectors $\mathbf{d_1}$ and $\mathbf{d_2}$ and the reciprocal lattice vectors for a grating with hexagonal symmetry, such as those used for the ultra-thin cells discussed in Section 6.1, as well as the in-plane propagation directions for orders up to $-2 \leqslant m_{1,2} \leqslant 2$ are illustrated in Fig. 6.2.

To calculate the allowed guided modes, a model of an asymmetrical waveguide made of three layers is used as described in [94, Chapter 11.2]. This simplifies the solar cell structure, which generally has more than three layers (while it is possible to treat the layer stack in full using a more complex TMM-based model, this was not done here). To give a guided mode, a specific diffraction angle must be trapped inside the guiding layers (e.g. the GaAs in an ultra-thin GaAs cell) and give rise to constructively interfering waves in the "waveguide"; for each grating period, this will only be true at specific wavelengths, which can be solved for semi-analytically. This method of analysis gives the wavelengths at which guided modes can exist, but does not calculate how well light will be diffracted into any particular order; to calculate this, a Maxwell solver such as RCWA (discussed in the next section) is required.

In addition to guided modes which can occur due to diffraction from the grating, thin-film interference due to specular reflection at the interfaces within the solar cell also occurs. The origin of peaks in the absorption spectrum due to such Fabry-Perot (F-P) interference can be analysed by considering the phase change in every layer of the structure, in addition to that due to reflection at the front and rear surfaces, and finding wavelengths at which the phase change is a multiple of 2π for constructive interference [95]:

$$2\sum_i k_{z,i} d_i + \varphi = 2\pi m \tag{2.27}$$

where m is any integer, $k_{z,i} = 2\pi n_i/\lambda$ is the z-component of the wavevector (for normal incidence) in layer i with refractive index n_i, d_i is the thickness of layer i and φ is the additional phase change due to reflection at the front and back surface, which can be worked out from the Fresnel equations:

$$\begin{aligned} \varphi &= \varphi_{\text{front}} + \varphi_{\text{back}} \\ &= \angle\, r_{\text{front}} + \angle\, r_{\text{back}} \end{aligned} \tag{2.28}$$

where r_{front} and r_{back} are the Fresnel reflection coefficients (eq. 2.17), evaluated with the appropriate complex refractive indices n_1 and n_2; for r_{front}, n_1 describes the incidence medium and n_2 describes the first layer of the stack, and for r_{back} the n_1 value is for the final layer in the stack and n_2 describes the substrate (assuming the F-P mode occurs inside the full stack). The symbol $\angle$ denotes the phase of the complex number.[3]

Defining the cavity in which the Fabry-Perot oscillation happens can be somewhat arbitrary; reflection generally takes place at every interface, as discussed in Section 2.3.1. In a solar cell, many of the layers may

[3]For normally incident light, evaluating r_s and r_p give the same answer to within a factor of -1, or $e^{\pm i\pi}$, meaning the contribution to φ will differ by $\pm\pi$ depending on whether r_s or r_p is evaluated. However, when the contributions for front and back are added up, these factors will cancel out, so the same result for the phase difference is reached as long as the equation for either r_s or r_p is used for both contributions.

have a similar refractive index, leading to low reflection at the interfaces, and there may only be one or two possible cavities. Generally, comparison with e.g. TMM calculations is necessary to identify which layers are involved in a specific thin-film feature. In simulations of structures containing a grating, Fabry-Perot modes will be distinct from guided modes when a large number of grating periods and geometries are simulated, as their location will not be dependent on the grating features (Fig. 6.6 is an illustration of this).

2.3.3 Rigorous coupled-wave analysis

Rigorous coupled-wave analysis (RCWA), also called the Fourier modal method (FMM) is a semi-analytical method for solving Maxwell's equations, originally developed by Gaylord and Moharam [140]. RCWA is a suitable method for calculating scattering effects due to periodic structures. This is done by defining a structure which is periodic in two linearly independent lateral directions, parallel to the layer interfaces. The electromagnetic field and permittivity at a particular height perpendicular to the lateral directions can then be represented in terms of Fourier series, and differential equations following from Maxwell's equations can be developed to solve for the field's Fourier coefficients as it propagates through the structure [92]. There are multiple implementations of RCWA available, using different programming languages; GD-Calc (Grating Diffraction Calculator) [92], a proprietary MATLAB-based simulation tool, and S^4 [141], an open-source C-based program with a Python interface, were used in this work.

Defining a coordinate system with $\hat{e_2}$ and $\hat{e_3}$ as the grating-tangential coordinate vectors and $\hat{e_1}$ as the grating-perpendicular direction, we can write the E-field of an incident (i) electromagnetic plane wave as:

$$\vec{E}_i(\vec{x}) = \vec{A}_i e^{i\vec{k_i}\cdot\vec{x}}$$

Where the wave vector $\mathbf{k}$ can be written as:

$$\mathbf{k}_i = k_{i,1}\hat{e_1} + k_{i,2}\hat{e_2} + k_{i,3}\hat{e_3}$$

The reflected (r) and transmitted (t) fields will consist of a superposition of different diffraction orders m_1 and m_2 (in two dimensions):

$$\vec{E}_{r/t}(\vec{x}) = \sum_{m_1,m_2=0}^{\infty} \vec{A}_{r/t}(m_1, m_2) e^{i\mathbf{k}_{r/t}(m_1,m_2)\cdot\vec{x}}$$

Where $\vec{A}_{r/t}(m_1, m_2)$ is the diffraction efficiency into the reflected and transmitted order (m_1, m_2), as discussed in the previous section. Any grating g considered using RCWA must be periodic, so two linearly independent vectors $\vec{d_1^g}$ and $\vec{d_2^g}$ can be defined under which the grating permittivity is translationally invariant. Thus, if the incident field is translated by e.g. $\vec{d_1^g}$, this should have no effect on the reflected or transmitted field other than a translation by the same amount (analogous to the discussion of Bloch functions in Section 2.1):

$$\vec{E}(\vec{x} + \vec{d_1^g}) = \vec{E}(\vec{x}) e^{i\vec{k_i}\cdot\vec{d_1^g}} \tag{2.29}$$

The total field is the incident + reflected fields for the space above the grating and the transmitted field for the space below the grating. The translational invariance vectors do not depend on $\hat{e_1}$, and so only the grating-tangential component of $\vec{k_i}$ is important in equation 2.29:

$$\vec{E}(\vec{x}+\vec{d_1^g}) = \vec{E}(\vec{x})e^{i\vec{k_{ip}}\cdot\vec{d_1^g}} \tag{2.30}$$

where the p in $\vec{k_{ip}}$ indicates the grating-parallel component.

Dividing both sides of this equation by $e^{i\vec{k_{ip}}(\vec{x}+\vec{d_1^g})}$ gives:

$$\frac{\vec{E}(\vec{x}+\vec{d_1^g})}{e^{i\vec{k_{ip}}(\vec{x}+\vec{d_1^g})}} = \frac{\vec{E}(\vec{x})}{e^{i\vec{k_{ip}}\cdot\vec{x}}} = f(\vec{x}) = f(\vec{x}+\vec{d_1^g}) \tag{2.31}$$

i.e. a function periodic with $\vec{d_1^g}$. Clearly, a similar expression can be derived for periodicity in $\vec{d_2^g}$. This means we can write the function $f(\vec{x})$ as a two-dimensional Fourier series:

$$f(\vec{x}) = \sum_{m_1,m_2} \vec{A}(m_1,m_2)(x_1)e^{i(m_1\vec{k_1^g}+m_2\vec{k_2^g})\cdot\vec{x}}$$

Multiplying by $e^{i\vec{k_{ip}}}$ to get $\vec{E}(\vec{x})$:

$$\vec{E}(\vec{x}) = \sum_{m_1,m_2} \vec{A}(m_1,m_2)(x_1)e^{i(m_1\vec{k_1^g}+m_2\vec{k_2^g}+\vec{k_{ip}})\cdot\vec{x}} \tag{2.32}$$

In general, for the exact expression of the E and H fields, the sums over m_1 and m_2 run from $-\infty$ to $+\infty$, but for computational purposes only a finite number of orders can be retained.[4]

A similar expression to equation 2.32 can be derived for the H-field. Having established the functional form of the electric and magnetic fields, these forms can be inserted into Maxwell's equations to determine a set of differential equations for the Fourier coefficients. In order for these equations to be solved, only a finite number of Fourier orders can be retained; keeping a larger number of orders increases accuracy but decreases computation speed (as shown in Fig. 2.9f, the computation time scales with the cube of the number of Fourier orders). Although the plane wave approach introduced here is only valid in a region of space which is homogeneous in the $\hat{e_1}$ direction, with a periodic structure in the $\hat{e_2}$ and $\hat{e_3}$ directions, the effect of a multi-layered grating can be modelled by dividing it into infinitesimal layers and calculating a "scattering matrix" for each layer, which describes how an electromagnetic field is affected by it. A version of the derivation above and the construction of the differential equations and scattering matrices is given in [142].

Knowledge of the electric and magnetic field amplitudes in each diffraction order at different depths in the structures allows the absorbed and transmitted power to be calculated using the Poynting vector $\mathbf{S} = \mathbf{E}\times\mathbf{H}^*$. Specifically, calculating the z-component $\mathbf{S}\cdot\mathbf{z}$ at different heights in the structure allows changes in power flow across layers of interest to be calculated, and the amount of power in different diffracted modes can also be calculated.

It is well-documented that the inclusion of some materials, especially metals, can lead to instabilities in RCWA simulations. This can lead to slow convergence of the calculations and unphysical oscillations at material boundaries, leading to inaccurate near-field results [143]. When metals are used in simulations with dielectrics or semiconductors, as is often the case in simulations of solar cell structures, the dielectric contrast at interfaces is very large at certain wavelengths where the real part of the dielectric function ε is negative in the metal (generally, this occurs at the optical and infrared frequencies relevant for solar cell operation). Such discontinuities in the dielectric function at interfaces leads to slow convergence of the

[4]The most obvious truncation is to keep orders which satisfy $|m_1| = |m_2| \leq m_{max}$ where m_{max} is a positive integer, but other truncation rules (e.g. $|m_1| + |m_2| \leq m_{max}$) can also be used.

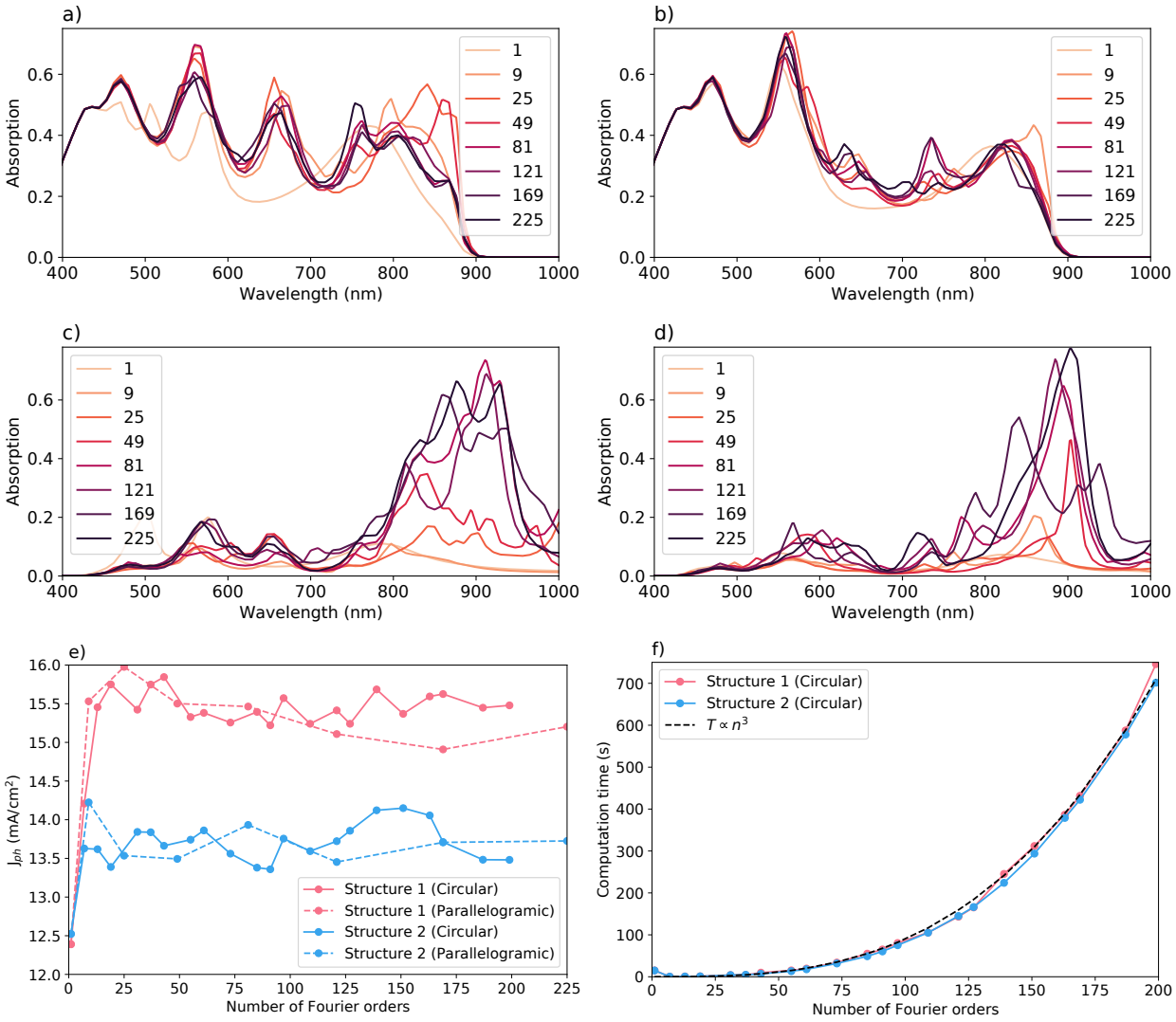


Figure 2.9: Convergence of S^4 for two structures containing metal. Structure 1 and Structure 2 are as defined in the main text. a) The absorption in the GaAs layer of Structure 1 with different number of Fourier orders, as given in the legend. b) The absorption in the GaAs layer in Structure 2. c) The absorption in the grating (Ag/SiN) layer of Structure 1. d) The absorption in the grating layer of Structure 2. e) The calculated photogenerated current for both structures using different number of Fourier orders for circular and parallelogramic choice of basis vectors – a) to d) show the results with the parallelogramic basis vector choice. f) The computation time, which scales as N^3 where N is the number of Fourier orders retained.

Fourier series representation [141], and some structures suffer from instability in the calculated near-field results even with a large number of Fourier orders due to the Gibbs phenomenon. When a Fourier series is used to represent a piecewise function with a discontinuity, this representation has oscillations near the discontinuity. The height of the overshoot caused by these oscillations cannot be reduced by increasing the number of Fourier orders, but is an inherent feature of the representation of jump discontinuities through Fourier series. These oscillations near the interfaces cause a phenomenon called 'ringing' in the real-space reconstruction, introducing additional interfaces where the dielectric function crosses zero which do not exist in reality [141]. Various improvements to RCWA formulations have been suggested and implemented to alleviate these issues, such as Lanczos smoothing [144] or a modified representation of the electric field to reduce the ringing issues proposed by Weismann et al. [143].

As discussed above, two different RCWA implementations were used over the course of the PhD: the MATLAB-based proprietary code GD-Calc was used for the investigation of the effect of inconsistently reported metallic optical constants presented in Section 4.3. This implementation of RCWA seems to be relatively stable even when metallic structures are included, and shows good convergence (Fig. 4.30a). S^4 was used for all other RCWA results presented, and shows more instability when metals are used; the effect of this instability is shown in Fig. 2.9 for two different structures of the type also considered in Section 6.1. Structure 1 has a silver/silicon nitride (SiN) rear grating with a hexagonal arrangements of discs with a period of 600 nm and a disk diameter of 300 nm. Structure 2 has a similar grating with a period of 500 nm and a disk diameter of 160 nm. Both structures have a thin (86 nm) GaAs solar cell (further details of the layers in this structure are given in Section 6.1). Figures 2.9a-d show the calculated absorption vs. wavelength in the GaAs layer (leading to photocurrent in the solar cell) and in the grating itself, for different numbers of retained Fourier orders. Fig. 2.9e shows the resulting photogenerated current from absorption in the GaAs depending on the number of Fourier orders used. There is initial rapid convergence of the photogenerated current J_{ph}, but the result then oscillates around some mean value for both Structure 1 and Structure 2 due to the instabilities discussed previously. Structure 1 consistently performs better than Structure 2 in terms of photogenerated current, and it was found that although the exact location and strength of the diffraction peaks in the absorption spectrum oscillate depending on the number of Fourier orders and lattice truncation method used [141], the trends for optimal designs in terms of grating thickness, disk radius etc. were very consistent for different numbers of Fourier orders. The RCWA simulations are primarily used to compare different grating and device structures to find optimal designs and are thus a suitable method, despite the convergence issues due to the Gibbs phenomenon.

2.4 Solar cell operation

As this work is mostly concerned with the development of novel materials for solar cells and cell architectures to improve light management, as opposed to the specifics of device fabrication and electrical performance, the physics of p-n junctions and solar cell devices will not be covered in great detail. However, a basic overview is included here to clarify commonly used terms and metrics for solar cell performance [145].

The semiconductors discussed in Sections 2.1 and 2.2 were assumed to be so-called intrinsic semiconductors: perfect crystals with no impurities. At absolute zero, all valence band states in the semiconductor are filled, and all conduction band states are empty, and the Fermi level (the energy level with a 50% probability o being occupied at thermal equilibrium) lies mid-gap. At finite temperatures, some electrons will gain enough kinetic energy to be promoted to the conduction band, above the Fermi level. For a semiconductor

in thermal equilibrium at temperature T, the probability that an energy level at energy E in the conduction band is occupied is given by the Fermi-Dirac distribution:

$$f_0(E, E_f, T) = \frac{1}{e^{(E-E_F)/k_BT} + 1} \approx e^{(E_f - E)/k_BT} \tag{2.33}$$

where k_B is the Boltzmann constant. In the second step, the Boltzmann approximation is made: if $E - E_f \gg k_BT$ (i.e. the energy difference between the conduction band and the Fermi level is much greater than the thermal energy), as is the case generally for solar cells under normal operating circumstances, the exponential term in the denominator dominates, and the Fermi-Dirac distribution simplifies to a Boltzmann distribution. It follows that the probability that there *is not* an electron at an energy E is $1 - f_0 \approx e^{(E-E_f)/k_BT}$ (in the Boltzmann approximation). Such a missing electron in the valence band is called a hole.

Solar cells are typically made up of layers of doped semiconductors, possibly in combination with intrinsic regions. The process of doping involves the purposeful introduction of impurity atoms during material growth to change the electronic nature of the resulting material. For n-type (negative) doping, impurity atoms are introduced which introduce free electrons. For instance, a Group IV semiconductor such as Ge or Si could be doped with a Group V element such as phosphorus, referred to as a donor atom. Phosphorus has one additional valence electron which is not needed for bonding when it replaces a silicon or germanium atom in the lattice. These additional electrons must go in the conduction band at zero temperature (since all the states in the valence band are already occupied), and thus the Fermi level must now lie between the mid-gap point and the conduction band (raised relative to the intrinsic semiconductor). Conversely, for a p-doped material, impurities with one fewer valence electron are introduced, for example Group III element boron in a group IV intrinsic semiconductor. Such an impurity is an acceptor atom; it needs one more electron for bonding than it can contribute, and thus will remove an electron from the valence band, or equivalently, add a hole to the valence band. This means there are missing electrons in the valence band in a p-doped semiconductor at 0 K, and the Fermi level is thus lowered compared to the intrinsic case.

Fig. 2.10 illustrates a typical p-n junction, where p and n-doped regions are brought into contact, at equilibrium. The top diagram shows the doping profile of the p-type and n-type layers, which have widths x_p and x_n respectively. The lower part of the diagram shows the band profiles. In the p-type semiconductor, there are extra holes in the valence band (VB) and the Fermi level lies closer to the VB, while in the n-type region the Fermi level lies closer to the conduction band (CB) due to additional electrons in the CB. In equilibrium, the overall Fermi level in the junction must be constant since charge carriers can redistribute themselves in the material (while the nuclei of the doping atoms remain fixed in place), which leads to band bending. In general, the behaviour of such a junction can be described by solving the semiconductor transport equations and Poisson's equation simultaneously; however, this is a complicated problem which is generally solved numerically (e.g. using Solcore [128]). To understand the operation of a solar cell, some assumptions can be made, including the so-called depletion approximation: the junction region will be completely depleted of both electrons and holes, as excess holes in the p-type region allow the excess electrons in the n-type region to recombine, and is called the depletion or space charge region (in Fig. 2.10 it occupies the width between $-w_p$ and w_n). An electric field across the junction is formed by the presence of (immobile) impurity nuclei: there are more protons on the n-type side. Thus the electric field points from the n-type to the p-type region (or equivalently, the n-type side is at a higher potential).

When a photovoltaic cell is exposed to light at or above the bandgap energy, interband (CB to VB) absorption may occur, where an electron from the valence band gains enough energy from the photon to reach the conduction band, leaving a hole in the valence band. Exposure to light means the cell is no longer

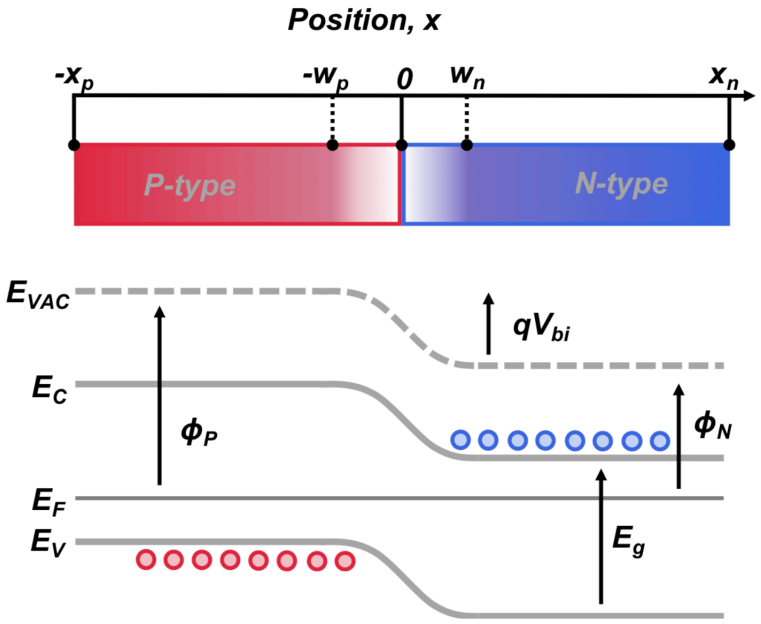


Figure 2.10: Schematic of the depth profile of doping and the corresponding valence and conduction band offsets for a p-n junction solar cell. From [146].

at equilibrium. Generally, carrier relaxation to the band edge within the valence or conduction band is several orders of magnitude faster than carrier relaxation between the bands, and it can be assumed that the electrons in the VB and the holes in the CB each achieve a state of quasi-thermal equilibrium, each following their own Fermi-Dirac distribution relative to a so-called quasi Fermi level.

The movement of carriers through the p and n-doped materials happens through two mechanisms: diffusion of carriers, driven by a gradient in electron and hole populations, and carrier drift, due to the electric field at the p-n junction. With reference to Fig. 2.10, the built-in electric field of the junction causes electrons to move to the right, into the n-type region, and holes to move to the left, into the p-type region, often referred to as minority carriers being driven across the barrier (electrons are driven out of the p-type region, where they are the minority carrier, into the n-type region, and vice versa). At zero external bias, this generates a photocurrent J_{SC} of electrons flowing to the n-type contact. When a forward bias is applied to a p-n junction (without illumination), electrons are injected into the n-type side and removed from the p-type side (or equivalently, holes are injected into the p-type side). The electron and hole quasi Fermi levels split and since the applied voltage opposes the built-in voltage, the potential barrier is reduced (the bands flatten), and there will be a net current of electrons from the n-type side to the p-type side. This current will be voltage dependent and is called the dark current, $J_{dark}(V)$; it flows in the opposite direction to the current which results from carrier drift across the junction (the photocurrent is a reverse bias current), as illustrated in Fig. 2.11a. For a photovoltaic cell in operation, exposed to both optical and electrical bias, the current is given by:

$$J(V) = J_{SC} - J_{dark}(V) \tag{2.34}$$

The efficiency of a solar cell, η, is defined as the useful electrical power which can be extracted from the cell as a fraction of the total solar power incident on the cell area, when the cell is operated at the voltage

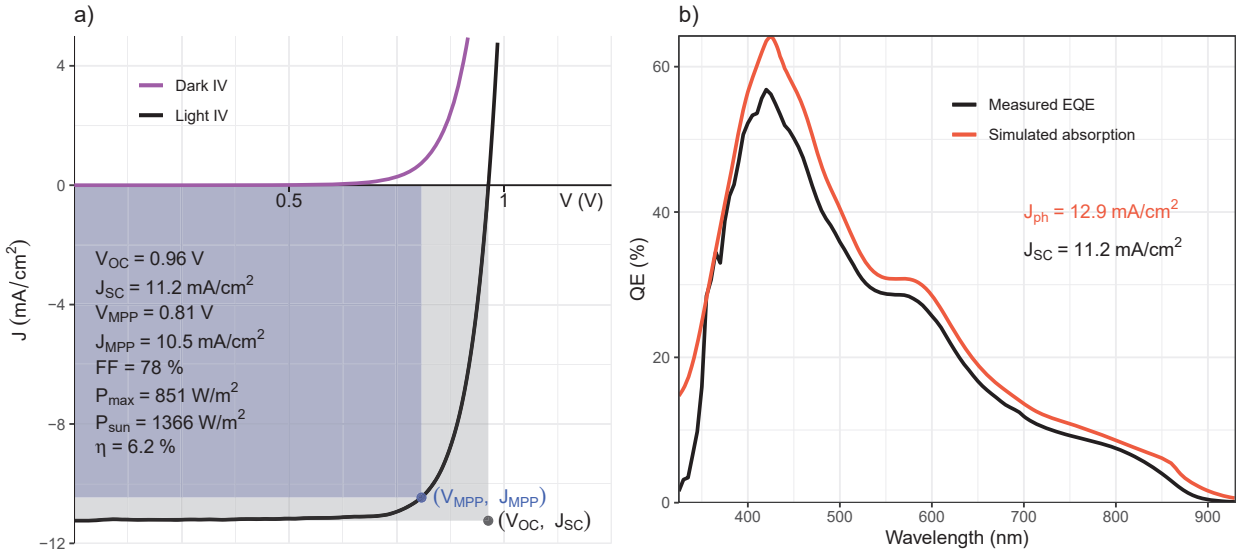


Figure 2.11: a) J-V (current density-voltage) relationship of a thin GaAs cell under illumination and in the dark, showing key points and values for solar cell performance. b) A comparison between measured EQE and calculated total absorption in the thin GaAs cell.

where it produces maximum power ($P = IV$). Expressed in terms of power density (power per unit area):

$$\eta = \frac{P_{\text{cell}}}{P_{\text{Sun}}} = \frac{J_{\text{MPP}} V_{\text{MPP}}}{P_{\text{Sun}}} = \frac{J_{\text{SC}} V_{\text{OC}} FF}{P_{\text{Sun}}} \tag{2.35}$$

where P_{Sun} is the incident power density (intensity) of sunlight. J_{MPP} and V_{MPP} are the current density (current per unit area) and voltage at the maximum power point, respectively. The efficiency is often expressed in terms of the open-circuit voltage V_{OC} and short-circuit current J_{SC} instead, related to the values at the maximum power point by the fill factor FF:

$$FF = \frac{J_{\text{MPP}} V_{\text{MPP}}}{J_{\text{SC}} V_{\text{OC}}} \tag{2.36}$$

An example of these quantities for a J-V curve for a real cell under illumination is shown in Fig. 2.11a.

In an idealized model of a solar cell, all above-bandgap photons are absorbed and generate carriers, and the number of carriers which can be extracted is limited only by the necessity of some carriers to recombine across the bandgap and be re-radiated (the principle of detailed balance) [8]. However, in a real material 100% absorption above the bandgap can never be achieved; some light will be reflected at the front surface, and the absorption edge is not infinitely sharp (see Fig. 2.4). The external quantum efficiency (EQE) of a cell is defined as the number of charge carriers which can be collected from the cell divided by the number of incident photons. The internal quantum efficiency is the number of collected charge carriers divided by the number of photons which are absorbed by the cell. This means that the EQE takes into account both optical losses due to non-unity absorption and incomplete charge collection, while the IQE measures how efficiently photogenerated carriers are collected. The EQE measured at zero voltage and integrated over the solar spectrum gives the short-circuit current:

$$J_{SC} = q \int_0^\infty \Phi(\lambda) \text{EQE}(\lambda) d\lambda \tag{2.37}$$

where $\Phi(\lambda)$ is the photon flux of the relevant solar spectrum (e.g. AM1.5G for terrestrial applications, or AM0 for space applications). In purely optical simulations, a useful figure of merit is the photogenerated current J_{ph}:

$$J_{ph} = q \int_0^\infty \Phi(\lambda) A_{\text{active}}(\lambda) d\lambda \tag{2.38}$$

where A_{active} is the fraction of incident light absorbed in the photovoltaically active layers (e.g. the p-n junction). In practice, the integration runs over wavelengths above 250 nm, as there are very few photons below this wavelength in the solar spectrum, up to λ_g, i.e. the bandgap wavelength of the semiconductor above which no photons will be absorbed (in practice, the numerical integration will be run over slightly longer wavelengths to account for any sub-bandgap absorption due to e.g. excitonic effects). The J_{ph} reflects the short-circuit current which would be achieved with 100% internal quantum efficiency, rather than an actual short-circuit current which can be achieved in a real device. Fig. 2.11b shows the measured EQE and simulated absorption in the GaAs for an ultra-thin GaAs device (see Section 6.1).

Chapter 3

Experimental and computational methods

3.1 SiGeSn sample growth

SiGeSn samples were grown through low-pressure CVD (chemical vapour deposition) by IQE plc. using an ASM Epsilon 2000 CVD epitaxy reactor, with germane (GeH_4), disilane (Si_2H_6) and tin chloride ($SnCl_4$) precursors with H_2 as the carrier gas. Two sets of samples across the composition range are considered here: one set grown on GaAs substrates with a thin (≈ 60 nm) Ge seed layer (Set A), and one set grown on Ge substrates which were overgrown with approximately 500 nm of lattice-matched $In_{0.012}Ga_{0.988}As$ grown through MOVPE (Set B). The layer structure of the samples is shown in Fig. 3.1. Samples were grown at different compositions, all aiming for an approximately 4:1 ratio of Si:Sn to achieve the same lattice constant as Ge (Section 1.4.2).

Both sets of samples include three different compositions of SiGeSn, with the aim of keeping the Si:Sn ratio constant in order to maintain lattice-matching to Ge while varying the optical and electronic properties of the samples. In addition to the three different compositions, samples in Set B were also grown with two different SiGeSn thicknesses. The resulting sample structures, compositions and layer thicknesses are summarized in Table 5.1.

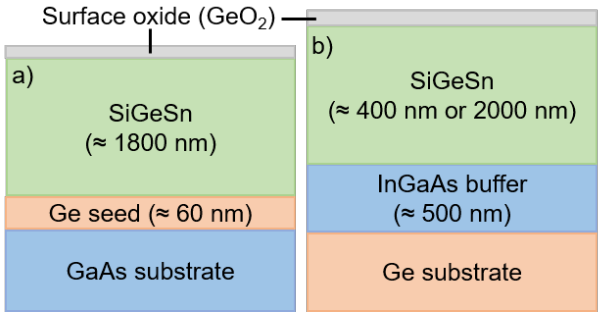


Figure 3.1: Schematic of the layer structure of the epitaxial SiGeSn samples. Note that the surface oxide layers are shown as they are included in the spectroscopic ellipsometry fits, but are not part of the epitaxial layer stack (these layers form spontaneously as the samples are exposed to air).

3.1.1 Composition and structural measurements

Optical microscope images of the SiGeSn samples were obtained using an Olympus BX51 Microscope equipped with a polarizer and Nomarski prism and taken at 10×, 20×, 50× and 100× magnification. Further surface scans were performed using a JEOL scanning electron microscope (SEM) JSM6700F equipped with backscattered electron mode and an Oxford instruments X-Max 150mm^2 silicon drift detector for energy dispersive X-ray (EDX) measurements, used to determine the sample composition. The sample composition was measured at 10 points on the surface of each sample (averages and standard deviations are reported in Table 5.1); measurements of the same samples during different measurement sessions showed these results to be repeatable.

The samples were investigated for their crystalline quality and lattice constant using a Malvern-Panalytical Empyrean X-ray diffractometer, used to measure both rocking curves and reciprocal space maps (RSMs) around the symmetrical (004) and asymmetrical (224) reflections.

These imaging and structural measurements were carried out by collaborators at the National University of Singapore, primarily by Dr. Sheau Wei Ong working in Prof. Eng Soon Tok's research group.

3.2 Spectroscopic ellipsometry

3.2.1 Measurement

Spectroscopic ellipsometry (SE) measurements were performed using a J. A. Woollam Co. VASE ellipsometer with a spectral range of incident light of 250-1700 nm. The V-VASE ellipsometer is a variable-angle, rotating analyzer spectroscopic ellipsometer; the basic configuration is a light source (passed through a monochromator to provide only a narrow band of wavelengths), which passes through a polarizer which linearly polarizes the incident beam. As shown in Fig. 3.2, this beam is incident on the sample at the chosen angle of incidence, and the reflected signal, which will be elliptically polarized, is passed through a continuously rotating analyzer before entering the detector ("analyzer" is used to refer to a polarizer placed just before the detector in order to pick out the desired polarization state). Lock-in techniques, using a chopped beam and synchronous detection techniques, are used to minimize the effect of ambient light. The measured quantity in SE measurements is ρ, the ratio of the complex Fresnel reflection coefficients $\tilde{R}_p$ and $\tilde{R}_s$ for p and s-polarized incident light, respectively:

$$\rho = \frac{\tilde{R}_p}{\tilde{R}_s} = \tan(\psi)e^{i\Delta} \tag{3.1}$$

ρ is expressed through the ellipsometric angles ψ and Δ, with $\tan(\psi)$ being the magnitude and Δ the phase of the complex number.

The measured SE signal will be the result of light reflected from the front surface of the sample interacting with any light which is reflected internally at any intermediate layer interfaces or the back surface, as discussed in the explanation of the transfer matrix model (Section 2.3.1). The electromagnetic waves reflecting from different surfaces will interfere, giving the overall SE signal, which is very sensitive to the front surface reflection and the layer structure of the sample. If a bulk sample (a thick sample without any overlayers such as a surface oxide) is being measured, the dielectric function can be calculated directly from ρ:

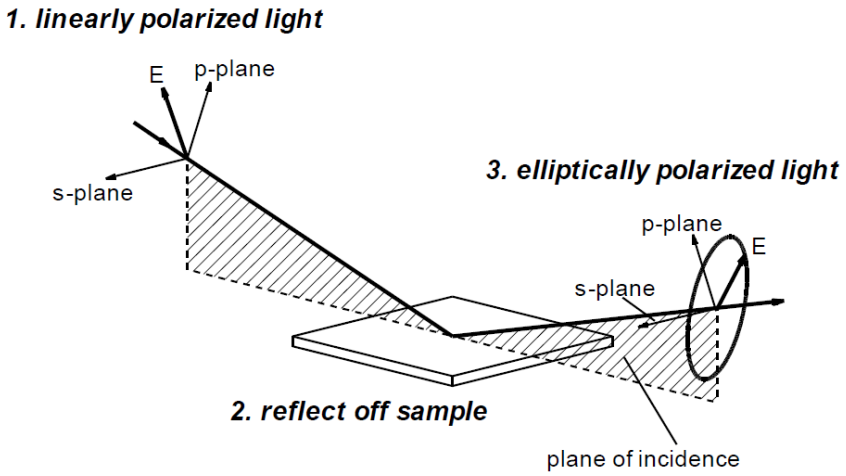


Figure 3.2: Diagram of ellipsometry measurement, also showing the meaning of s and p-polarization. From [147].

$$\langle\tilde{\varepsilon}\rangle = \langle\varepsilon_1\rangle - i\langle\varepsilon_2\rangle = \sin^2\phi\left[1 + \tan^2\phi\left(\frac{1-\rho}{1+\rho}\right)^2\right] \tag{3.2}$$

where ϕ is the incidence angle of the light [147]. When applied to a multi-layer structure, this equation gives the so-called pseudo-dielectric constant, as it ignores layers in the structure and calculates the dielectric constants directly from ρ assuming the sample is a bulk structure. Since the ellipsometry measurement is most sensitive to the top layers of a structure, calculating the pseudo-dielectric constant can often give a useful indication of the dielectric function behaviour (e.g. redshifting or blueshifting relative to some reference material), but it will not give accurate values for the dielectric constants of any individual layer (see Fig. 5.4 for an example of the pseudo-dielectric constants of SiGeSn).

All samples were measured at incidence angles of 75°, 77° and 79° from the normal. These angles are chosen because the most sensitive measurements of the complex reflectance ratio ρ are obtained around the pseudo-Brewster angle of the sample, where R_p reaches a minimum [148, 147]. The pseudo-Brewster angle is given by $\widetilde{\theta_B} = \arctan\frac{n_1}{n_0}$ [147]; taking $n_0 = 1$ for air, $\widetilde{\theta_B}$ is 77° for Ge at 500 nm. The samples measured are not pure Ge, and $\widetilde{\theta_B}$ depends on wavelength since n_1 is dispersive; thus the samples are measured at three incident angles around the initial estimate of pseudo-Brewster angle. In addition to obtaining accurate data around the pseudo-Brewster angle, measuring at several incidence angles and calculating the pseudo-dielectric constants also provides a simple way of checking for non-ideal behaviour such as depolarization of the measured signal. The pseudo-dielectric constants calculated from data taken at different angles should be the same; if this is not the case, it indicates other behaviours (such as depolarization or scattering from the sample surface due to e.g. surface defects) are affecting the measurement. Depolarization occurs when a thick (compared to the wavelength of the incident light) sample becomes transparent, causing light to travel through the sample and reflect at the back side. This light can then travel back through the sample and be collected with the light reflected at or close to the sample surface, but due to having travelled (in the case of the SiGeSn samples discussed here) hundreds of microns as opposed to (at most) hundreds of nanometres for light reflecting from the front of the sample or at intermediate interfaces, this light will no longer be fully coherent with the rest of the signal due to the finite coherence length of the incident light. This causes the measured signal to become depolarized, affecting the value of ρ that is measured. For instance, this occurs

in germanium at energies lower than its lowest direct bandgap (0.8 eV); as absorption across the indirect gap is weak, light is able to travel through the sample without being absorbed.

3.2.2 Optical constant fits

Unless a bulk sample is being measured, extracting the optical constants of individual layers from measured SE data requires constructing a model which takes into account the layer structure of the sample, since reflection and transmission at layer interfaces and absorption within layers will all affect the value of ρ measured; this is evident in the pseudo-dielectric constants shown in Fig. 5.4 which show clear Fabry-Perot fringes. If the layer structure and all the optical constants (ε_1 and ε_2, or n and κ) of the materials are known, it is generally straightforward to fit the layer thicknesses, at least for a small number of layers, and assuming light at some of the measurement wavelengths is able to reach all the layers. If the optical constants of one or more of the layers are not known, as is the case for the SiGeSn samples studied here, it is possible to fit the optical constants for the layer of interest in various ways. Three possible approaches to fitting ellipsometric data are to fit the data point by point (at each angle and wavelength), to fit a physical model such as the Adachi model, or to fit a more flexible parametric model. In the first case, the number of fit parameters is twice the number of wavelengths at which ρ is measured, since ε_1 and ε_2 (or equivalently, n and κ) can be chosen freely for each point. This makes it difficult to ascertain that a unique fit has been found, Kramers-Kronig consistency between ε_1 and ε_2 is not enforced, and there can be strong, discontinuous fluctuations in the ε_1 and ε_2 values fitted as each point is fitted independently; therefore, the values fitted are not necessarily physically meaningful, especially if a good starting point for the layer thicknesses is not chosen. A physical model such as the Adachi model, discussed in Section 2.2, has far fewer parameters (three for each critical point in the band structure: the strength of the transition, the centre energy, and the damping, or four if the damping is allowed to vary with energy [136]), and enforces Kramers-Kronig consistency, but is quite inflexible and generally difficult to fit to real data (see Fig. 2.6), even for well-known materials. In the case of the SiGeSn data, it was found that no good fits to the data could be obtained with an Adachi-type model. A more flexible parametric model, such as the Herzinger-Johs Parametrized Semiconductor Oscillator ("Psemi") model [137], has the advantages of reducing the number of fitting parameters compared to point-by-point fitting and enforcing Kramers-Kronig consistency [147, 137], while increasing the flexibility of the peak shapes compared to a more physically-constrained critical point model. This model, and efficient fitting algorithms, are implemented in the Woollam WVASE software used to measure and fit the SE data. Thus, a Psemi model was used to fit the SiGeSn optical constants, taking as a starting point the parametric model for Ge built into the WVASE software used to fit the data. The drawback of such a parametric model is that the fitting parameters drawn from it are not necessarily physically meaningful; e.g. the centre energy of a peak does not necessarily correspond directly to a specific transition energy in the material's band structure.

Layer thicknesses and optical constants of the SiGeSn layer in each sample were extracted from the SE data by fitting a model based on the layer structures shown in Fig. 3.1 for the different sample types, which includes the Ge or GaAs substrate, the InGaAs layer (in the case of the Set B samples), the SiGeSn layer and a GeO_2 surface layer [149]. The inclusion of a thin surface layer is necessary to achieve a good fit to the data, including for a reference measurement of a Ge substrate; GeO_2 was used since the samples are mostly Ge, so it was assumed the surface oxide is mostly Ge-based. For a Ge substrate sample, the GeO_2 thickness fitted was 5 nm, while for the SiGeSn samples it was between 1 and 2 nm for all samples; this difference may be due to the difference in age between the samples, as the oxide on Ge is known to increase in thickness over time, or because the formation of the oxide differs depending on the sample composition and deposition

method. A similar method to the fitting procedure for the SiGeSn optical constants outlined in [75] was used. The starting point for the layer thicknesses were the nominal thicknesses targeted during MOVPE growth. To initially fit the thicknesses, the SiGeSn layer was assumed to be pure Ge; since we are considering Ge-heavy ($> 80\%$) samples of SiGeSn, using the well-known optical constants of Ge initially gives a very good starting point for the fit of the layer thicknesses. For the Set B samples, the GaAs thickness was also allowed to vary at this stage; in each case the deviation from the nominal thickness of 500 nm was ≤ 10 nm. The starting point for the Psemi model fits for SiGeSn was the built-in model for Ge [147]. Since the model allows for very flexible peak shapes, each feature is described by seven variable parameters which control the peak strength, location and broadening, with further parameters controlling the shape and asymmetry of the peak. Only the peak strength (A), centre energy (E_0) and broadening (B) were fitted, with the other parameters kept fixed at the Ge values. This was to avoid unreasonable peak shapes, including discontinuities in the dielectric function, especially in the low-energy region where thin-film interference and noise due to signal depolarization affects the SE measurements. It was found very good fits to the data could be achieved without varying the other peak shape parameters. The parameters for the SiGeSn optical constants were fitted starting at high energies, initially fitting only the centre energies of the peak followed by allowing the peak strength and broadening to vary. The layer thickness of the SiGeSn is allowed to continue to vary while the optical constants are fitted. The data measured at all the incidence angles (75, 77 and 79°) are fitted simultaneously. The optical constants for the other layers (GaAs, Ge, InGaAs and GeO_2) came from the WVASE software database, except for those of GeO_2 which were defined as a Sellmeier model using data from [149].

After the layer thicknesses have been determined exactly as described above, a point-by-point fit where ϵ_1 and ϵ_2 are fitted separately at each measurement wavelength is also performed, keeping the layer thicknesses fixed. The two fitting methods agree very well for energies above ≈ 1 eV (depending on the SiGeSn composition). Below these energies (i.e. below the lowest direct transition in the SiGeSn, where SiGeSn is only very weakly absorbing) the presence of thin-film interference fringes in the data significantly affect the point-by-point fit. Thus, for the subsequent analysis of ellipsometric data, the point-by-point fits were used for energies > 1.5 eV to fit E_1, $E_1 + \Delta_1$, E_0' and E_2 while the Psemi fit was used for lower energies to fit E_0. For the samples from Set B, the optical constants of the SiGeSn layer were obtained using the data for thicker samples at each composition, and checked by fitting the SE data of the thinner sample at that composition by allowing only the layer thicknesses, and not the optical constants of the SiGeSn, to vary. This gave a good fit to the data in each case, indicating that the composition is constant across the two sample thicknesses.

The fundamental indirect gap, at 0.67 eV for Ge at room temperature and blueshifted to 0.7-0.8 eV for the SiGeSn samples (as determined by photoluminescence measurements), is not included in the Psemi model. Even considering the expected blueshift in this bandgap relative to Ge for the SiGeSn samples, this transition occurs very close to or beyond the longest wavelength which can be measured using the V-VASE ellipsometer. In addition, because indirect transitions contribute much more weakly to the optical constants than direct transitions (as discussed in Section 2.1), and the layer of SiGeSn is relatively thin (2 µm at most), even additional measurements with an IR-VASE ellipsometer capable of longer wavelength measurements did not clearly show the indirect gap. The validity of omitting the indirect gap in the ellipsometric model is confirmed by absorption measurements (Section 3.5), which show a clear absorption edge around 1 eV due to the lowest-energy direct transition, but no clear absorption edge due to the lower-lying indirect bandgap (see Section 5.2.3).

3.2.3 Critical point fits

Although the Psemi model will fit centre energies for the different peaks, these are not necessarily physically meaningful, and so in order to obtain the energy of the critical points, a method similar to [44] was used to fit the second derivative of the real and imaginary part of the dielectric function multiplied by E^2 (as explained in Section 2.2.2). This second derivative was obtained using a Savitzky-Golay filter in order to preserve lineshape but remove very short-range oscillations (i.e. noise) between measurement points. Here, a polynomial of order 3 with a filter window length of 31 points (with data in steps of 0.0025 eV) was used to describe the data, chosen to reduce noise but preserve lineshape. The filter coefficients for $E^2\varepsilon_1$ and $E^2\varepsilon_2$ were then differentiated twice to obtain the numerical second derivative of the dielectric function multiplied by E^2. Low-energy data around the E_0 and $E_0 + \Delta_0$ critical point was fitted to the results of the derivatives of the parametric model fit, while the higher-energy transitions used the point-by-point fit, as discussed above.

The second derivative is fitted to expressions of the form:

$$\frac{\partial^2(E^2\varepsilon)}{\partial E^2} = \frac{A_i e^{i\Phi_i}}{(E - E_i + i\Gamma_i)^2} \tag{3.3}$$

$$\frac{\partial^2(E^2\varepsilon)}{\partial E^2} = \frac{A_i e^{i\Phi_i}}{(E - E_i + i\Gamma_i)^{3/2}} \tag{3.4}$$

where for each transition A_i, Φ_i, E_i and Γ_i are the amplitude, phase angle, centre energy and broadening, respectively. Equation 3.3 is used to fit 2D critical points (E_1, $E_1 + \Delta_1$, E_0' and E_2) and equation 3.4 is used to fit 3D critical points (E_0 and $E_0 + \Delta_0$) [58, 150]. Although Adachi attributes the E_1 and $E_1 + \Delta_1$ features to a 3D M1-type CP (see Table 2.1), this feature has been treated as a 2D CP by others [74, 65] and it was found that using the expression for a 2D CP resulted in better fits. What is treated here as a single E_0' feature here is likely made up of contributions from E_0', $E_0' + \Delta_0'$ and $E_0' + \Delta_0' + \Delta_0$, but these are not clearly resolved and are thus fitted as a single peak[1]. Computationally, the equations 3.3 and 3.4 are separated into real and imaginary parts, which are fitted to the $\frac{\partial^2(E^2\varepsilon_1)}{\partial E^2}$ and $\frac{\partial^2(E^2\varepsilon_2)}{\partial E^2}$ data respectively. The overall fit is optimized simultaneously for the real and imaginary parts using a Levenberg-Marquardt non-linear least-squares algorithm [151]. All the parameters are fitted, with the constraint that the phase angles Φ_i are the same for the pair $E_1/E_1 + \Delta_1$, as these correspond to the same type of critical point. An example of a fit to all the critical points visible for sample B3 is shown in Fig. 3.3. The phase of $E_0/E_0 + \Delta_0$ would be similarly constrained, but the $E_0 + \Delta_0$ was not fitted to the derivatives of the dielectric function as its contribution is extremely weak.

3.3 Photoreflectance

Photoreflectance is a contactless modulation spectroscopy technique which allows the measurement of transition energies of interband transitions in semiconductors through modulation of the internal electric field as carriers are photogenerated with a laser pump beam, modulating the internal electric field of the sample. The reflectivity is measured with a probe beam with and without the effect of the pump beam, allowing the change in reflectivity (ΔR) due to the pump beam to be measured.

[1] $E_0' + \Delta_0$ is not included because it is dipole forbidden [58].

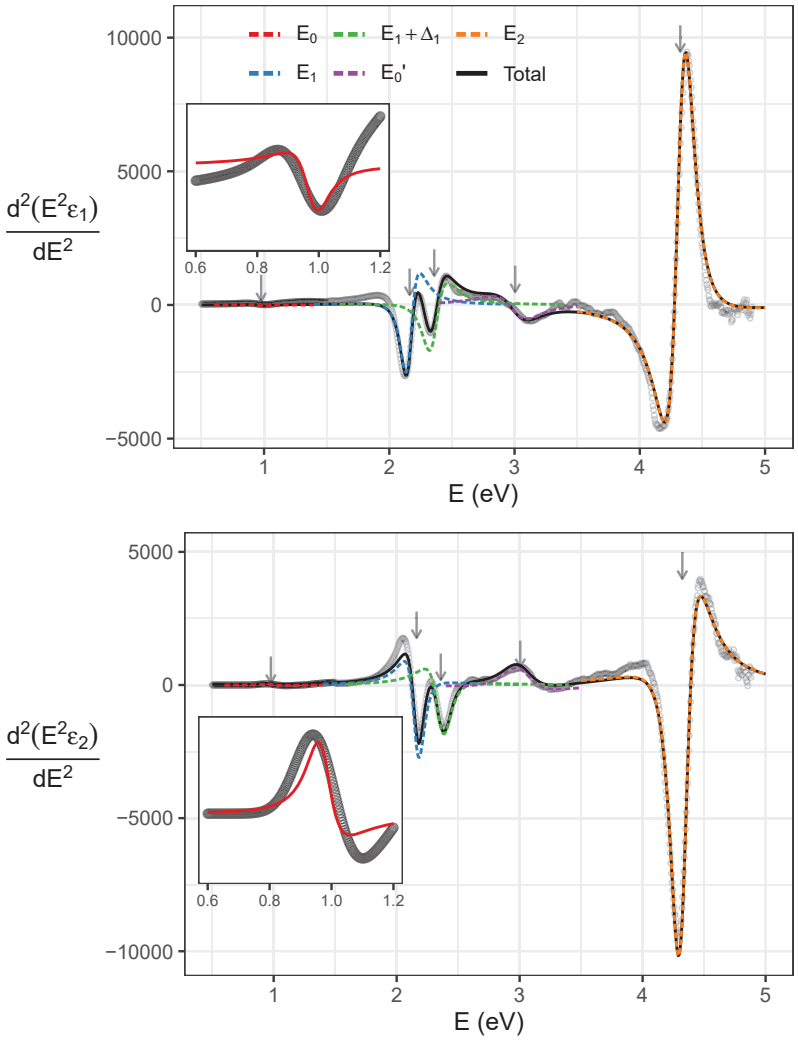


Figure 3.3: Example of a fit to the second derivative of the real and imaginary parts of the dielectric function (open circles); dashed coloured lines show the contributions of the individual critical points, with the black line showing their sum. The arrows indicate the fitted centre energy of each critical point. Data below 1.5 eV was obtained by differentiating the parametric form of the dielectric function fit, while data above 1.5 eV was from the point by point fit. The inset shows the fit to the E_0 critical point in more detail.

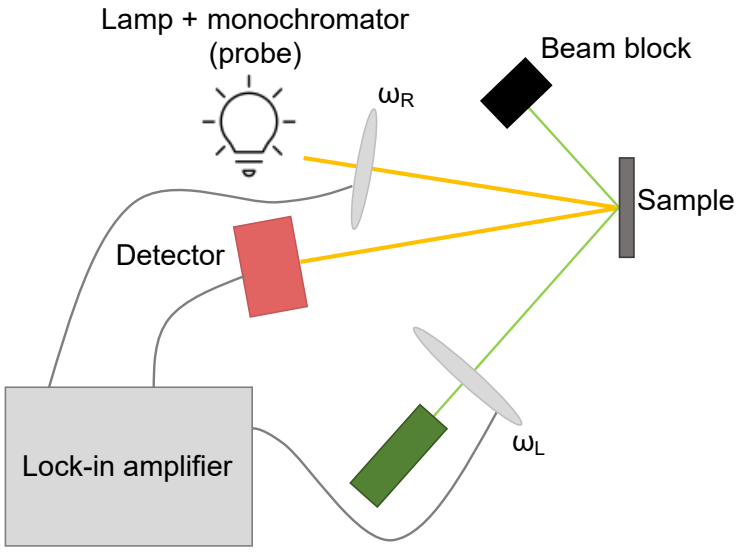


Figure 3.4: Schematic of the setup used for photoreflectance measurements. The probe beam is chopped at a frequency of ω_R and the laser pump beam is chopped at a frequency of ω_L.

3.3.1 Measurement

The measurement setup is shown schematically in Fig. 3.4. The pump beam used is a GEM 532 nm continuous-wave laser incident at an angle of $\approx 5°$ with a power density of 164 W/cm^2. The probe beam is generated via a Bentham IL1 100 W halogen lamp coupled to a Bentham TMC300 monochromator. The spectral range here is limited by the laser wavelength (532 nm) at the low wavelength end, since there will be very significant noise around the laser wavelength, and the detector response at the high end (1700 nm). The probe beam is focused on the sample at an angle of 45° and the reflected beam measured with a Thorlabs DET10N2 biased InGaAs detector with a detection range of 500–1700 nm.

In order to remove the effect of photoluminescence from the photoreflectance measurements, both the probe and pump beams are chopped at different frequencies (as shown in Fig. 3.4) in a double demodulation method [152]. As such the ΔR signal is measured at the sum frequency of the probe and pump beams, while the R signal was directly measured at the probe chopping frequency. Photoluminescence, occurring at the pump chopping frequency, can thus be eliminated from the desired $\Delta R/R$ result, and the necessary signals, ΔR and R, can be measured simultaneously during a single measurement using a single detector and extracted via lock-in detection with a Zurich Instruments HF2 lock-in amplifier. Signal gain was accomplished with a Zurich Instruments HF2TA current amplifier.

3.3.2 Fitting

The photoreflectance signal due to critical points in the energy range of interest for the E_0 and $E_0 + \Delta_0$ transitions is fitted to expressions of the form:

$$\frac{\Delta R}{R} = \mathrm{Re}\left[\frac{A_0 e^{i\Phi_0}}{(E - E_0 + i\Gamma_0)^{5/2}} + \frac{A_{ex} e^{i\Phi_{ex}}}{(E - E_{ex} + i\Gamma_{ex})^2} + \frac{A_{\Delta_0} e^{i\Phi_{\Delta_0}}}{(E - E_{\Delta_0} + i\Gamma_{\Delta_0})^{5/2}}\right] \tag{3.5}$$

where $E_{\Delta_0} = E_0 + \Delta_0$. Because we are treating photoreflectance as a third-derivative modulation spectroscopy technique, similar to electroreflectance [138], the first and third terms in this expression have

the functional form of the derivative with respect to E (assuming all constants are absorbed into A_i) of eq. 3.4, which was fitted to the second derivative of the dielectric function explicitly. The second term represents the excitonic contribution to the optical behaviour around the E_0 critical point. The PR data for Ge (Fig. 5.8) shows a symmetrical peak shape, with three sharp extrema. It is not possible to achieve this peak shape by fitting only a single critical point feature at the E_0 feature, hence the inclusion of the exciton.[2]

The PR data for the SiGeSn samples with a layer thickness around 2 µm showed multiple oscillation fringes around, and below, the expected E_0 energy (Fig. 5.8), while the data for the thinner Set B samples shows more clearly defined E_0 and $E_0 + \Delta_0$ features which blueshifts with increasing Si/Sn composition. Although fringes due to Franz-Keldysh oscillations (FKOs) can occur in photoreflectance measurements [153], these occur at energies above the critical point, and the oscillations observed here are below the E_0 energies expected from theory and observed in the analysis of the SE data. Comparing the data for the thicker and thinner Set B samples shows that the oscillations here are mainly visible at energies below and close to the critical point feature. The width of the fringes corresponds exactly to the width expected due to thin-film oscillations for light incident at 45° (the probe beam's angle of incidence). The samples were thus fitted with a novel combined critical point and interference fringe model described below, with the exception of the Ge reference sample, which was fitted with equation 3.5 directly.

Combined interference/critical point model

Previous work investigating the appearance of interference fringes in PR data matching the sample thickness [154, 155, 156] have attributed the fringes to either modulation of the refractive index of doped materials [154, 155] or temperature changes in the sample [156]. This model assumes the fringes are due to the former, and expands on the existing models by self-consistently calculating the modulated optical constants and reflectivity to give the total photoreflectance signal.

Assuming the anomalous features observed in the PR of the SiGeSn samples are interference fringes due to reflection at the (In)GaAs interface, the period of oscillations of the fringes is determined by the SiGeSn layer thickness, while the envelope shape of the oscillations depends on the modulation of the refractive index by the pump beam. While Kallergi [155] and Huang [154] attribute the interference to modulation of the refractive index of doped GaAs substrates, rather than modulation of the refractive index of the epi-layer, this explanation is unlikely for the SiGeSn samples as the thickness of the samples ($\approx 1.8-2$ µm) means that very little (<1%) of the high energy photons from the pump beam (532 nm laser) incident on the sample are able to reach the GaAs substrate (Set A) or InGaAs buffer layer (Set B). However, the model presented in [155] and [154] can be adapted relatively simply to assume modulation of the epilayer refractive index rather than the substrate.

The photoreflectance signal $\Delta R/R$ is the relative change in the reflectivity with and without the pump beam, so $\Delta R/R = (R' - R)/R$ where R' is the modulated reflectivity and R is the unmodulated reflectivity. For instance, for Set A, considering the three layers in the epitaxial structure (SiGeSn, Ge seed layer, and GaAs substrate), the reflectivity is a function of the relevant thicknesses and refractive indices: the unmodulated reflectivity $R(E, n_{SiGeSn}, n_{Ge}, n_{(In)GaAs}, d_{SiGeSn}, d_{Ge})$ and the modulated reflectivity $R'(E, n_{SiGeSn} + \delta n_{SiGeSn}, n_{Ge} + \delta n_{Ge}, n_{GaAs} + \delta n_{GaAs}, d_{SiGeSn}, d_{Ge})$ where the n are the complex

[2]Note that excitonic contributions were not included in fitting the second derivative of the dielectric function derived from fits to SE data. Below energies of 1.5 eV, where the point-by-point fit to the SE data was too noisy, the parametric form of the resulting dielectric constant fits was used. Due to how this model is constructed, by including one critical point for E_0 and one for $E_0 + \Delta_0$, the E_0 transition is represented only by a single 3D critical point, and thus it should not be possible to observe any excitonic contribution in the parametric dielectric function.

refractive indices. Assuming the refractive indices of the Ge and GaAs are not significantly affected since very little pump light is able to reach these layers, the functional dependence of the modulated reflectivity simplifies to $R'(E, n_{SiGeSn} + \delta n_{SiGeSn}, n_{Ge}, n_{GaAs}, d_{SiGeSn}, d_{Ge})$. Because of the presence of the Ge seed layer, the multi-layer reflectivity model is more complex than in [155] and [154], and rather than constructing an analytical expression for the multi-layer interference, Solcore's TMM optical model [128] was used to calculate the theoretical $(R' - R)/R$ due to modulation of the dielectric function of the SiGeSn. The change in the refractive index was expressed as in [155]:

$$\delta n_{SiGeSn} \propto (n_{SiGeSn}^2 - 1)\frac{\Delta R_e}{R_e} \tag{3.6}$$

where $\Delta R_e/R_e$ is expressed as an exponential function of energy $Ae^{-\gamma E}$. The SiGeSn thickness, A, γ and an arbitrary phase factor ϕ were fitted to the data (d_{Ge} was kept fixed at 60 nm). The inclusion of a phase factor as a fitting parameter is justified because during the experiment, the phase is fixed arbitrarily, and may differ between measurements.

Optical constants for the different SiGeSn compositions were obtained from ellipsometry, and these can be used in this model for n_{SiGeSn}. However, this raises an issue, since the location of the critical points which occur in the PR data is what leads to certain values of n and κ; using externally imposed values of n and κ, the interference fringes due to optical constant modulation are fitted, but the PR signal arising from the critical point itself is not. However, it is possible to instead fit the interference fringes and signal from the critical point simultaneously by expressing the optical constants in terms of an analytical model such as the Adachi model and fitting the optical constant modulation using the optical constants, and the photoreflectance signal to the third derivative of the optical constants.

This model, which fits the full photoreflectance signal, has a large number of parameters to account for the layer thicknesses, peak strength and broadening, phase factors, and degree of optical constant modulation. The differential evolution optimization technique discussed in Section 3.7 was used to fit the model to the data for all nine SiGeSn samples. Since the model has a large number of parameters, the differential evolution was run multiple times for each sample to identify whether multiple model fits gave equally good results. The fits with the lowest root mean square error (RMSE) are shown in Fig. 5.10. Further details of the model implementation and each parameter fitted, and how the expected photoreflectance signal is computed from these parameters, is given in Appendix F.2. A list of all parameters fitted and the bounds imposed is given in Table F.3.

As the Set B samples were grown after the Set A samples, when the effect of interference of the PR signal had been identified, two versions of each composition were grown; ≈ 2 µm samples, similar to the Set A samples, and thinner ≈ 400 nm SiGeSn layers were grown as part of Set B. The expectation was that for the thinner samples, the interference fringes would be significantly wider, and the photoreflectance signal arising from the critical points would be more easily identifiable; this can be seen clearly in the data in Fig. 5.10g-j. The two different thicknesses of Set B samples were fitted independently, but the values for E_0 and Δ_0 are in good agreement for each composition, validating the model presented here for simultaneous fitting of the critical points and interference fringes.

3.4 Photoluminescence measurements

The photoluminescence setup used is shown schematically in Fig. 3.5. Although a number of lasers are available in this setup, which is designed to make the interchange of different laser sources and detectors straightforward, all the measurements discussed in this work were measured using excitation from a continuous-wave Spectra-Physics Millennia V Nd:YVO_4 laser with a wavelength of 532 nm (2.33 eV) and incident power between 100 mW and 4 W. This is a diode-pumped laser, where high output power from laser diodes is used to pump the Nd:YVO_4 lasing medium, which emits primarily at 1064 nm. This light is converted to 532 nm light through second harmonic generation in a nonlinear crystal. The Millennia V laser was used for measurements of PL from SiGeSn due to its high output power densities, required to observe PL from indirect materials, some with additional material quality issues which reduce photoluminescence efficiency, and due to its relatively high incident energy. The high photon energy means that most of the incident photons are absorbed within a few hundred nanometres of the sample surface, which ensures carriers are excited in the epitaxial layer rather than the substrate (Ge or GaAs). Assuming that the absorption in the epitaxial SiGeSn layers considered here is germanium-like at high incident photon energies of 2.33 eV, $>$ 99% of the incident laser power will be absorbed in the first 500 nm of material.

The laser light was optically chopped at a frequency around 200 Hz before being focused on the sample. The laser power can be set directly between 0.2 W and 5 W on the Millennia V laser, and a flip-in calibrated Si photodiode is used as a power meter to verify the power used. The laser power incident on the sample can be controlled further using a removable filter wheel with varying optical density. Initial PL measurements of some of the SiGeSn samples showed effects from residual laser light at 1064 nm. To prevent this, a Thorlabs TF1 IR blocking filter was placed in the beam path after the adjustable filter wheel; this has around 95% transmission at 532 nm, but blocks any light at wavelengths above 650 nm with an optical density of $>$ 6. Laser light reflected from the sample or otherwise scattered (e.g. from the cryostat windows) is stopped close to the sample using a beam blocker for safety reasons and to prevent stray laser light from affecting the measured signal. The photoluminescence generated by the sample is collected using a collimating lens. A 780 nm long-pass coloured glass filter is placed just after the collimating lens to block any stray laser light from entering the monochromator. An additional lens focuses the collected PL onto the entrance slit of the monochromator, a 0.5 m Princeton Acton SP2500i spectrometer. This is a Czerny-Turner monochromator; since the light is focused on the entrance slit, it disperses inside the monochromator, where it is directed onto an aspheric mirror which collimates the light. The light is directed onto a diffraction grating mounted on a rotating turret and the diffracted light directed to a second aspheric mirror which directs the now diffracted light, in a narrow wavelength band, towards the exit slit. The monochromator has two gratings: 600 grooves/mm and 300 grooves/mm, both blazed at 1 µm. For the results in Chapter 5, the 300 grooves/mm grating was used due to higher diffraction efficiency around the wavelengths of interest ($\approx$ 1100-2100 nm).

The diffracted light at the exit slit is detected by a Hamamatsu G7754-01 extended InGaAs detector, cooled with liquid nitrogen. For the measurements in Chapter 5, the monochromator was scanned across a wavelength range of 1000 to 2100 nm (not all samples were measured across the full wavelength range at each power and temperature, depending on where PL signal was detected). The PL signal is processed using standard phase sensitive detection techniques using a Stanford SR830 lock-in amplifier and recorded using custom-written Python software [157]. This same software also controls the monochromator, lock-in amplifier (allowing the integration time per wavelength point and the waiting time between points to be set), and the temperature controller for the cryostat. The samples are mounted to a copper disc using a small amount of vacuum grease and attached to the cold finger of the cryostat. Room-temperature measurements

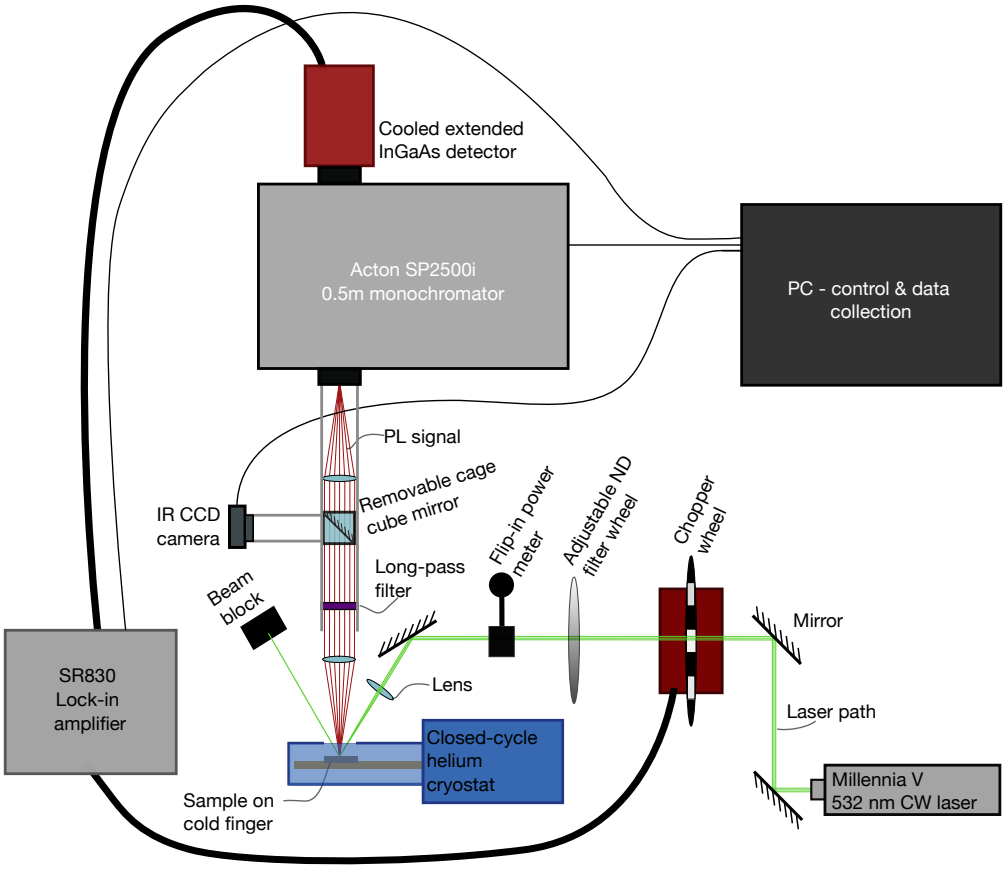


Figure 3.5: Schematic of the photoluminescence setup.

are done without the cryostat shielding to maximize the PL intensity collected. For low-temperature and temperature-dependent measurements, the temperature of the closed-cycle helium cryostat is controlled using an Oxford Instruments programmable temperature controller (also accessible via the same software which performs the PL measurements), which can achieve stable temperatures between 30K up to room temperature. The sample can also be imaged using a removable cage mirror using the same optical path as the collected PL signal (see Fig. 3.5); a Thorlabs DCC1545M IR charge-coupled device (CCD) camera is used for imaging, allowing alignment of the laser spot on the sample.

3.4.1 Measurement of the laser spot size

The laser spot size was measured using the Thorlabs CCD camera also used for sample alignment positioned in the same location where the cryostat sample stage is during measurement. Using low laser power, and additional neutral density filters in the beam path to further reduce the intensity incident on the camera ensuring the centre of the laser spot does not saturate the camera, an image of the laser spot is captured (Fig. 3.6a). In order to extract the laser spot size, the intensity of the pixels is transformed into a matrix, and then renormalized to span the intensity range 0 to 1 (Fig. 3.6b). The laser spot radius was determined as the radius from the centre of the laser spot at which the intensity falls to $1/e^2$ (the intensity at the maximum is 1 after the renormalization). In order to determine this, the centre of the laser spot was taken to be the pixel with maximum intensity; the data was then binned by radial distance from this point

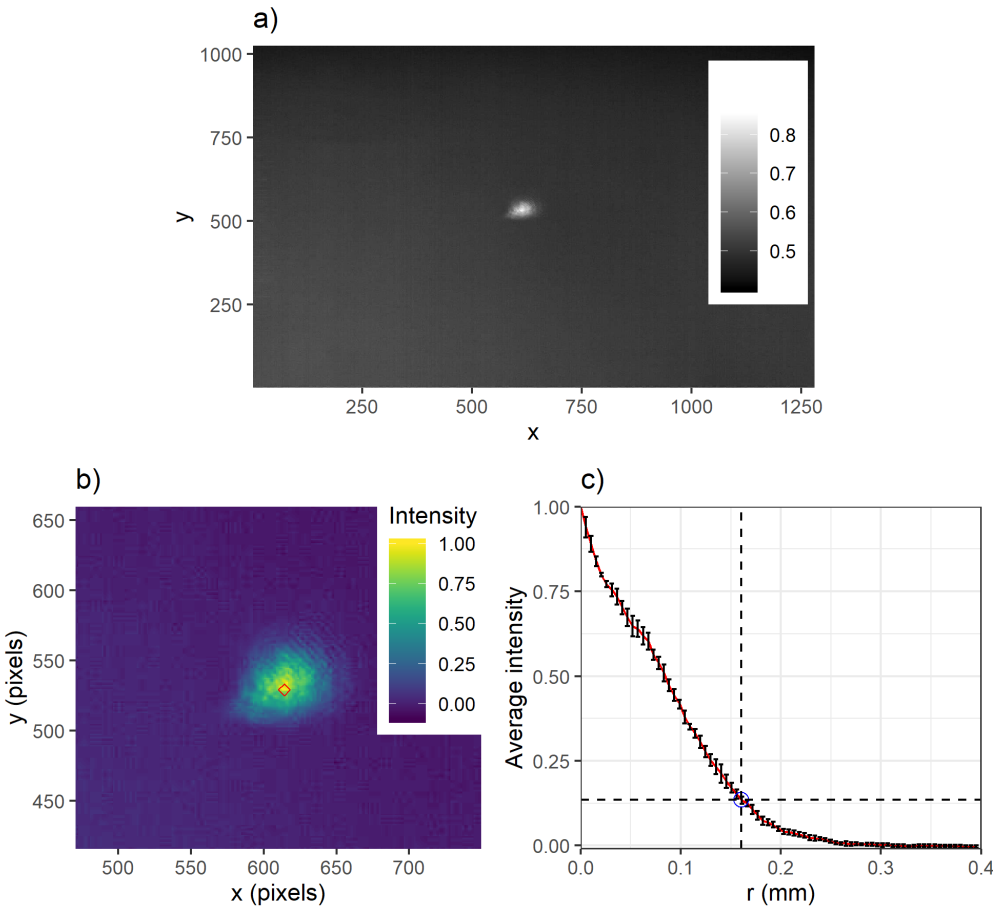


Figure 3.6: a) CCD camera image of the Millennia V laser spot at the PL measurement stage. b) Normalized intensity of the laser spot image with the highest-intensity point indicated by the red diamond and c) average intensity with radial distance from the point of maximum intensity. The dashed lines indicate the radius where the intensity falls below $1/e^2$, which is taken to be the laser spot size.

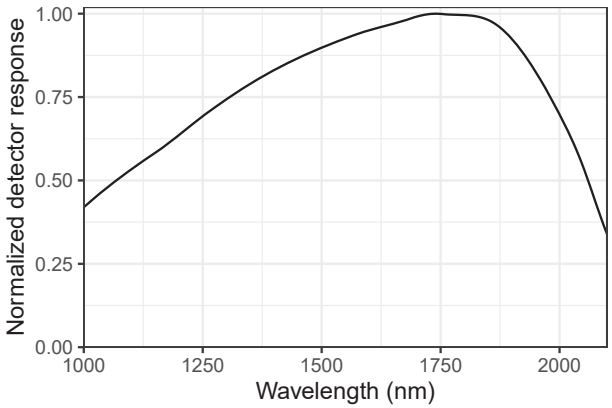


Figure 3.7: Normalized detector response for the Hamamatsu G7754-01 extended InGaAs detector (based on data supplied by Hamamatsu).

($r = \sqrt{(x - x_{max})^2 + (y - y_{max})^2}$), with a bin width of 1 pixel. The average intensity of the pixels in each radial bin, and its standard deviation, with distance r from the centre of the spot are shown in Fig. 3.6c. The relationship between the distance in pixels and mm was calculated from the imaging area (6.66 mm x 5.32 mm) and resolution (1280 x 1024 px) of the camera given in the data sheet, which shows that pixels had a width and height of 5.2 $\times 10^{-3}$ mm. As shown in Fig. 3.6, the radius in mm at which the intensity of the Millennia V laser falls below $1/e^2$ of the maximum is 0.161 mm. Assuming the laser spot size does not change with laser intensity, this allows the intensity of the laser to be calculated from the total incident power.

3.4.2 Spectral corrections

The primary purpose of performing PL measurements on SiGeSn is to determine at which energies band-to-band transitions occur, in order to gain an understanding of the band structure of SiGeSn and determine its bandgap. Thus, it is often useful to plot PL spectra in terms of energy, while the raw data measured is in the form of signal intensity per unit wavelength while scanning through wavelengths. When converting PL spectra from units of wavelength (e.g. nm) to units of energy (e.g. eV), it is not sufficient to simply transform the x-axis using $E = hc/\lambda$; it is also necessary to transform the measured intensity, in order to preserve the total intensity of signal measured (the signal integrated over the wavelength or energy range). In order to preserve the total intensity, we must have:

$$\begin{aligned} I(\lambda)d\lambda &= I(E)dE \\ I(E) &= I(\lambda)\frac{d\lambda}{dE} \end{aligned} \tag{3.7}$$

which, using $E = \frac{hc}{\lambda} \Rightarrow dE = -\frac{hc}{\lambda^2}d\lambda$, gives:

$$I(E) = \frac{\lambda^2}{hc}I(\lambda) \tag{3.8}$$

In addition, a spectral correction is made to correct the PL signal for the response of the extended InGaAs detector (see Fig. 3.7), by dividing the signal at every wavelength by the normalized detector response at that wavelength.

3.5 FTIR reflection and transmission measurements

Transmission and reflection measurements were carried out using a Bruker Vertex 70 Fourier-transform infrared spectroscopy (FTIR) system fitted with a Hyperion 2000 microscope setup. The microscope setup allows light to be directed from below the sample towards the detectors, to measure transmission, or from the same side as the detectors, to measure reflection. Rather than scanning through wavelengths monochromatically and measuring the reflection and transmission (and thus the absorption) at each point, FTIR measurements are made by directing a beam composed of many different frequencies towards the sample. Using an interferometer with a varying optical path length, the frequency composition of the incident spectrum is varied. The amount of light transmitted or reflected is measured by a detector. By varying the optical path length and thus the incident spectrum the transmission/reflection for many incident spectra can be measured. This produces an interferogram relating the mirror position or optical path length in the interferometer to the intensity of light of all wavelengths incident on the detector. A spectrum of the reflection or transmission against the wavelength can then be obtained through a Fourier transform. On the Bruker tool, the Fourier transform is done automatically by the measurement software. In order to measure the absolute reflection and transmission of the SiGeSn samples, references for unity transmission and absorption must be used; for transmission, this is simply the transmission of air (i.e. no sample is placed in the measurement setup), while for reflection, an aluminium mirror was used as a reference. To calculate the absolute reflection or transmission, the R or T measurement of the sample is simply divided by that of the reference.

The (NIR) and mid-infrared (MIR) absorptivity (equal to emissivity through Kirchhoff's law) for the silicon heterojunction (SHJ cells discussed in Section 6.2 samples was measured by Dr. Diego Alonso-Álvarez using the same Bruker Vertex FTIR stystem, with a gold-coated integrating sphere and a liquid nitrogen-cooled HgCdTe detector from Infrared Associates Inc.

3.6 Electrical measurements

External quantum efficiency (EQE) and current-voltage (IV) measurements of ultra-thin GaAs devices (Section 6.1.6) were performed to characterize solar cell performance. IV measurements under an AM0 spectrum were performed using a TS-Space Systems Unisim Compact dual-source solar simulator, which incorporates a quartz-halogen (QH) and metal-halide gas-discharge HMI lamp, used in conjunction with filters to obtain a close match to the solar spectrum. Both an AM0 (space) and AM1.5G (terrestrial) spectrum can be simulated by changing the filters used. The current-voltage characteristic is measured by scanning through voltages using a Keithley 236 Source-Meter unit (SMU).

EQE measurements were performed using Xe and quartz-halogen light sources, dispersed through a 0.3-m spectrometer using a microscope objective to focus the incident light. The photocurrent from the devices was recorded using standard lock-in techniques using an Ametek 7230 lock-in amplifier, with reference values at each wavelength determined using a calibrated Si photodiode.

3.7 Differential evolution

Although many different techniques are used to simulate the behaviour of solar cells, depending on the focus of the model and the structure being considered, a recurring problem in designing the most efficient devices

is the large parameter space available. For instance, for a multi-junction solar cell, the materials used in each layer, the thickness of each layer (including window layers, tunnel junctions, and the n- and p-type regions within each sub-cell) and the doping levels will affect the final performance of the device. For a cell with advanced light-trapping structures such as a diffraction grating, the materials used, thickness and period of the grating, as well as the feature sizes could all be varied during fabrication. This means that a flexible way of defining 'black-box' or derivative-free optimization problems is a powerful tool in solar cell design. For a derivative-free optimization problem, the functional form of the value to be optimized is not known so the problem cannot be solved analytically; this is generally the case when designing a solar cell and optimizing e.g. the photogenerated current.

One method for solving such black-box optimization problems is Differential Evolution (DE), a type of evolutionary algorithm, originally presented by Storn & Price [158]. The specific implementation used in this work was the open-source Python package yabox [159, 160]. In DE, a population of vectors corresponding to the input parameters of the model to be optimized (e.g. layer thicknesses, grating dimensions) is generated, the fitness of each population is checked, and then the population is 'mutated' in such a way that the traits of the more successful members of the population are more likely to survive. This is repeated a number of times, generating new populations with improving fitness with each iteration.

New populations at each iteration of the algorithm are generated through a combination of *mutation* and *recombination*. The initial population is generated by sampling randomly from a uniform distribution between the lower and upper bound specified for each parameter, creating a population of vectors (the standard population size used by yabox is five times the number of parameters to be optimized). Each vector is used as input for the objective function to be optimized to calculate its fitness, and the population is then mutated to generate new trial vectors which may replace the vectors currently in the population if they have a better fitness. To generate a mutated vector, three vectors are chosen randomly from the existing population and a new vector of parameters, $\mathbf{x_{mut}}$, is calculated as:

$$\mathbf{x_{mut}} = \mathbf{x_{r,1}} + m(\mathbf{x_{r,2}} - \mathbf{x_{r,3}}) \tag{3.9}$$

where $\mathbf{x_r}$ are the randomly chosen parameter vectors, and m is the mutation factor: a larger m will generally lead to a larger search radius around the current population of vectors, but may slow down convergence towards a solution[3]. Now, a target vector in the existing population undergoes recombination with this mutated vector; for each entry of the vector, we decide with some probability p whether the entry in the target vector is replaced with that of the mutated vector. This gives us the new trial vector. The fitness of the trial vector is evaluated, and if it performs better than the target vector in the existing population, the target vector is replaced. This process is repeated for every vector of parameters in the population; during each iteration, some of the vectors will be replaced by mutated vectors with a better performance. Over multiple iterations, the whole population will converge towards a solution. The mutation/crossover scheme described here is often referred to as 'rand/1/bin'; the other vectors used to generate the mutated vectors are chosen randomly from the current population, and only one vector difference is used in eq. 3.9 to generate the mutated vectors ('rand/1'). The 'bin' refers to the crossover scheme being binomial since the number of vector entries which are replaced will follow a binomial distribution. Alternative schemes for both the mutation and crossover exist, for instance 'best/2/exp'; rather than choosing three random vectors from the population to generate the mutated vectors, the best-performing vector can always be chosen.

[3]At this point, entries in the vector which fall outside the allowed upper and lower bounds for that parameter may be generated; in this implementation, these values are simply clipped (set to either the lower or upper bound of that parameter).

More than one vector difference can be used, and the crossover can be performed in different ways, with the most well-known alternative being the exponential method. These mutation and crossover techniques can be combined in different ways, with different methods performing better depending on the situation. Although there is little theoretical research guiding the choice of mutation/crossover scheme and other parameters (such as mutation factor and crossover probability) depending on the type of problem being considered, it was found empirically that this differential evolution algorithm performs very well for the design of optical structures by comparing against results from brute-force grid searching optimizations (see Section 6.1.4 for an example).

These techniques were used to optimize multi-junction cells using SiGeSn sub-cells (Section 5.5), ultra-thin cell designs (Section 6.1), and for fitting photoreflectance data of the SiGeSn samples to the combined interference/critical point model (Section 5.2), showing that this optimization method is a promising and flexible tool for solar cell design.

Chapter 4

Development of optical modelling tools

This chapter will discuss the extensive work undertaken over the course of the PhD to improve the existing optical modelling capabilities of Solcore, an integrated solar cell modelling Python package developed at Imperial College, and work undertaken to develop a new, completely open-source optical modelling tool (RayFlare), which allows users to access different optical methods and combine multiple methods across a single structure in a flexible way. A large range of optical modelling tools (the transfer matrix method (TMM), rigorous coupled-wave analysis (RCWA), ray-tracing, and combinations of these methods) were either expanded and made more accessible, or implemented from scratch. The interfaces to RCWA and TMM solvers, allowing multi-wavelength calculations of convenient quantities such as reflection, transmission, absorption per layer and depth-dependent absorption profiles can be used to define any structure, including with the user's own material data as discussed in Section 4.1.4, and therefore have wide applicability for optical simulations beyond solar cells. Convenient methods for importing the optical constants of materials (either from measurement or external databases) and data visualization were developed to aid with the optical design of solar cells. Both Solcore and RayFlare are available as open-source Python packages [161, 162].

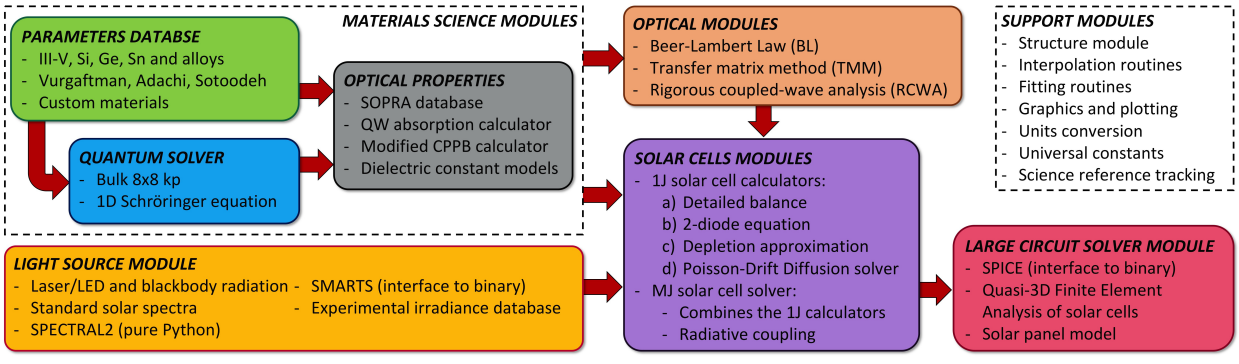


Figure 4.1: Overall structure and workflow of Solcore. From [161].

4.1 Solcore

Solcore is a modular, Python3-based package for modelling many aspects of solar cells, with capabilities from predicting the limiting efficiency of a cell based on the detailed balance method to simulating realistic structures involving multi-layers with interference, quantum wells, or regular scattering layers [128]. The structure and modules of Solcore are summarized in Fig. 4.1. This section will detail contributions I have made to Solcore, specifically to its optical modelling capabilities (TMM and RCWA) and materials database.

4.1.1 Transfer-matrix method

Solcore's transfer matrix method (TMM) capability is based on a vectorized, expanded version of code from the existing tmm package [91]. Vectorization refers to the process where rather than processing elements individually (e.g. by looping through wavelengths, for this example), array elements are processed simultaneously by using vector and matrix operations in a suitable programming language such as MATLAB or Python. This generally leads to faster execution of equivalent code. The original tmm package performs both coherent and (partially) incoherent calculations, but can only perform calculations for one wavelength at a time, while the new version was vectorized for the coherent calculations by Dr. Diego Alonso-Álvarez, while I implemented the vectorized version of the partially incoherent calculations. Solcore automatically passes the relevant wavelength-dependent optical constants and layer thicknesses to calculate total reflection, transmission and absorption, absorption per layer, and depth-dependent absorption. The latter is necessary to calculate the depth-dependent carrier generation rate, which is necessary for the more realistic electrical solvers (the depletion approximation and Poisson drift-diffusion method). Improvements I have made to the code include changes to prevent overflow issues in Python (which cause e.g. infinite, or negative, absorption to be calculated erroneously), methods to allow the polarization and incidence angle of the incident light to be set by the user in Solcore, and the ability to treat one or more layers within a structure incoherently, including the calculation of absorption profiles in structures containing both coherent and incoherent layers. These new capabilities were used extensively for the work on distributed Bragg reflectors in multi-junction solar cells in Section 6.3. The ability to treat incoherent layers is useful when one or more layers in a structure are very thick compared to the wavelength of light; in this case, absorption in the layer can be described by the Beer-Lambert law and phase information leading to thin-film interference is lost. Treating a very thick layer coherently leads to very narrow interference fringes (see Fig. 4.2a) which are generally not observed in measurements. The incoherent treatment of thick layers is the same principle which allows the use of the angular matrix method which forms the basis of the new optical modelling package RayFlare, as discussed in Section 4.2.

Figures 4.2 and 4.3 illustrate the capabilities of the solver in terms of partially coherent structures and variation of the incidence angle. The structure considered in both cases is a very simple three-layer stack of (top to bottom) 500 nm GaInP/30 µm GaAs/10 µm Ge. In Fig. 4.2a, many very narrow oscillations are visible in the reflection and absorption spectra; it is likely that these would not be measured in a real reflection/transmission measurement, both due to limited wavelength resolution in measurements and due to light losing coherence when travelling long distances (compared to its wavelength) inside the GaAs and Ge layers structure. In Fig. 4.2b, the thickest (middle) layer is treated incoherently, resulting in the disappearance of the very narrow interference fringes. Fig. 4.3 shows the reflection, absorption and transmission values of the same structures for s and p-polarized light incident at 45°. The behaviour of unpolarized light, such as sunlight, in wave-optical simulations is usually calculated by taking the average

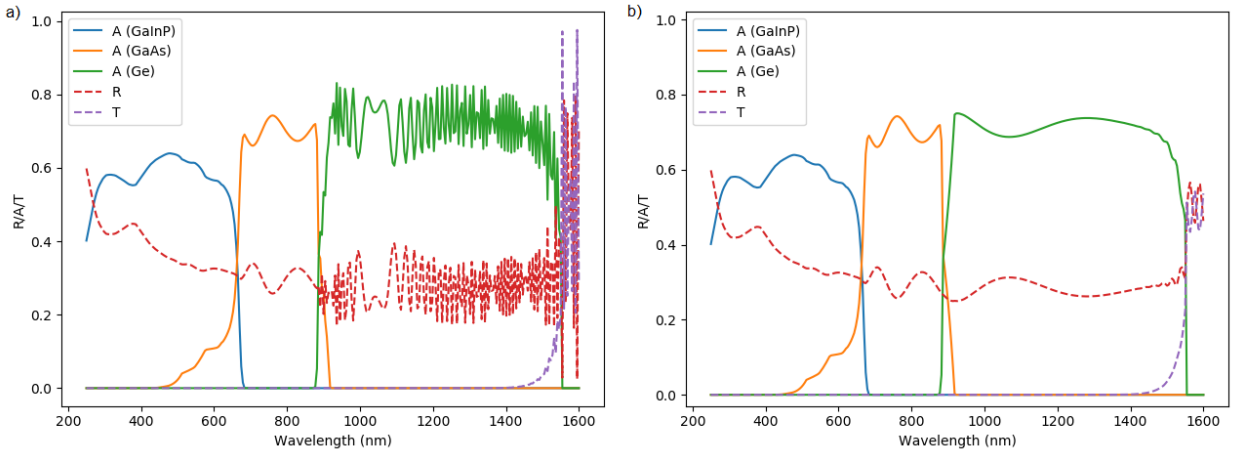


Figure 4.2: The total reflection and transmission, and absorption per layer of the GaInP/GaAs/Ge stack, when a) all the layers are treated coherently and b) when the middle GaAs layer is treated incoherently (i.e. phase information within this layer is ignored). The light is normally incident in both cases.

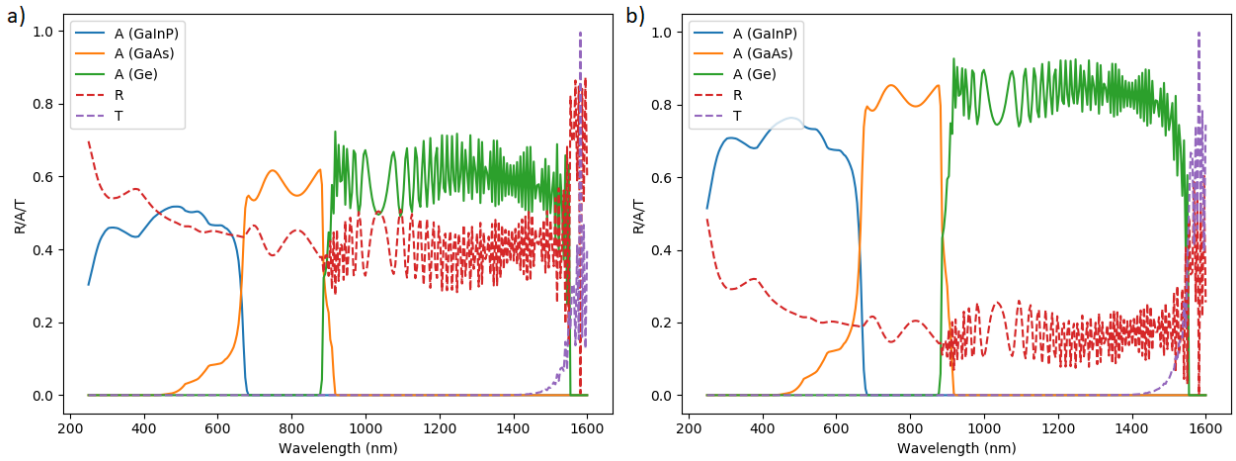


Figure 4.3: The total reflection and transmission, and absorption per layer in the GaInP/GaAs/Ge stack for a) s-polarized and b) p- polarized light. The light is incident at 45°, and all layers are treated coherently.

of the s and p-polarized cases (for normal incidence, there is no difference between s and p polarization).

4.1.2 Rigorous coupled-wave analysis

To further extend the types of structures which can be modelled in Solcore, an interface to the rigorous coupled-wave analysis (RCWA) Maxwell solver S^4 was added. S^4 was developed at Stanford University and is an implementation of RCWA, also sometimes referred to as the Fourier Modal Method (FMM), which solves the linear Maxwell's equations in structures containing 2D periodicity (the theory of RCWA is discussed in more detail in Section 2.3.3). S^4 is mostly C-based, with an interface to Python allowing its functions to be called from Python scripts. To make S^4 compatible with Solcore, I made modifications to its base code to make it compatible with Python3 rather than Python2, and to incorporate improvements to the code made by other users [163]. Structures in S^4 are defined by creating a layer stack of the desired materials, including a unit cell which can feature combinations of shapes, with built-in functions to add

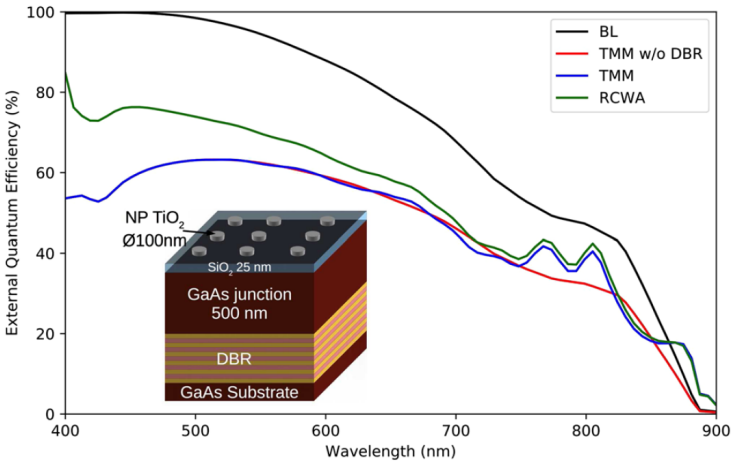


Figure 4.4: Comparison of the quantum efficiency of a thin GaAs solar cell with a distributed Bragg reflector (DBR) behind the cell and an array of TiO_2 nanoparticles (NP) on top, calculated using the three optical solvers in Solcore. The BL model ignores the NP and the DBR and does not include the front surface reflection, overestimating the result at all wavelengths. TMM correctly accounts for the reflection and the DBR but cannot model the effect of diffraction due to the NP layer. RCWA takes into account scattering from the NP, although it is significantly more time consuming. Figure from [128].

rectangles, circles, ellipsoids, or a general polygon with any number of vertices. Solcore's Layer and Junction classes are used to define these layers in the new implementation, in which each layer's composition can be modified by adding any number of the allowed shapes made of a specified Solcore material. Each layer is assumed to be infinitely periodic in the x and y directions, and uniform in the z direction. A unit cell must be defined for the whole structure (using the size attribute in the user options), and each shape is placed at a specified location (and, where relevant, angular orientation) in the unit cell; as many shapes as necessary can be added, supplied as a list of dictionaries with the relevant parameters for each shape. An example for each type of shape supported by S^4 is shown in Listing C.1 in Appendix C. The size of the unit cell in the x and y directions and the base size of the unit cell must be given in nm. The number of Fourier components used in the calculation [141] must also be specified; this is done using the orders attribute in the user options passed to the solver of choice.

4.1.3 Comparison of optical models

The different optical models in Solcore are suitable for different types of structures. The Beer-Lambert (BL) model does not include front surface reflection, unless it is externally specified, but is extremely fast and may be suitable for material stacks where the layers are optically thick (especially if the front surface reflectivity is specified by the user, e.g. from measured data, which can be taken into account by Solcore if supplied by the user). The transfer matrix model (TMM) deals with multi-layer interference correctly, and can be used at multiple incidence angles and either s, p, or unpolarized light. The most recent version can also treat one or more layers in a stack incoherently by ignoring phase information within that layer. Finally, the RCWA capability integrated in Solcore through its interface with S^4 is the most advanced solver, capable of dealing with periodic structures. For any multi-layer structures without diffracting layers, it gives the same results as the TMM solver. However, as the number of diffraction orders used in the calculation increases, the computation time can become very significant. In addition, the code is not vectorized (unlike the TMM

code). The number of diffraction orders necessary for the calculation to converge depends on the structure and wavelengths being considered.

Fig. 4.4 shows the simulated EQE of a thin GaAs cell with various light-trapping structures, using the different optical solvers available in Solcore. The structure is a relatively thin (500 nm) GaAs cell, with TiO_2 nanoparticles (NPs) on the front and a distributed Bragg reflector (DBR) consisting of 10 GaAs/AlAs bilayers at the back of the cell. The NP array is made up of disks 50 nm in height, with 100 nm diameter and arranged in a square pattern with a period of 400 nm. A DBR is a selective reflector, in this case designed to reflect light with wavelengths around 800 nm, close to the bandgap of GaAs where transmission losses would be highest. Fig. 4.4 shows that the simplest model, the BL law, does not give any front-surface reflection, with all the light absorbed at short wavelengths. At longer wavelengths, there is some transmission into the GaAs substrate; although absorption in the DBR will be calculated, the interference effects which lead to wavelength-selective reflection are ignored by the BL model. The TMM model with the DBR removed from the structure shows a similar profile to the BL EQE, but is significantly lower due to reflection at the front surface. When the DBR is included, two clear new peaks in the EQE calculated using the TMM are observed. Finally, when the full structure is modelled using RCWA, these peaks due to the DBR remain but the EQE at all wavelengths is increased, due to an anti-reflection effect from the NPs and increased path length in the GaAs cell due to diffraction effects. This clearly demonstrates the different capabilities and of the different optical solvers.

4.1.4 Use of custom materials

While Solcore has an extensive built-in database of materials commonly used in (inorganic) solar cells, it is frequently necessary when working with new or uncommon materials to define various properties of materials not currently in the database. Furthermore, as discussed in Section 4.3, it is very important to use accurate optical constants when simulating realistic structures, so it may be desirable to add custom material data (e.g. optical constants measured experimentally) for use with Solcore. Finally, there are existing, extensive databases containing data from the literature, such as refractiveindex.info [164]. In order to simplify the process of using custom material data, I adapted Solcore to make it possible to add new materials to the database, either from a user's own data or from the refractiveindex.info database. These materials only need to be defined once, and can then be used in the same way as a built-in Solcore database material.

The code in Listing C.2 shows how the custom materials capability is set up in Solcore's user configuration, and then how a custom material can be defined from three files, 'SiGeSn_n.txt', 'SiGeSn_k.txt' and 'SiGeSn_params.txt', respectively listing the real and imaginary parts of the refractive index n and κ against wavelength (in m) and any other parameters (mobilities, bandgap, etc.). It is also possible to define an 'optical-only' material with only the first two files. The plot generated in the final few lines of the code is shown in Fig. 4.5.

Although it is possible to simply download data from refractiveindex.info, and define new materials in the way described above, this is laborious if multiple materials are required. Therefore, a method was implemented which automatically takes the required n and κ data from the refractiveindex.info database, which can be used directly with Solcore's standard material function, as outlined in the code snippet in Listing C.3. This searches the database for "Ag" (silver) and defines materials based on four different sources, as well as the SOPRA database included with Solcore. Fig. 4.6 plots the n and κ data from these different sources. Being able to easily compare different optical constant sources is very useful to compare the effect of any discrepancies, as discussed in Section 4.3.

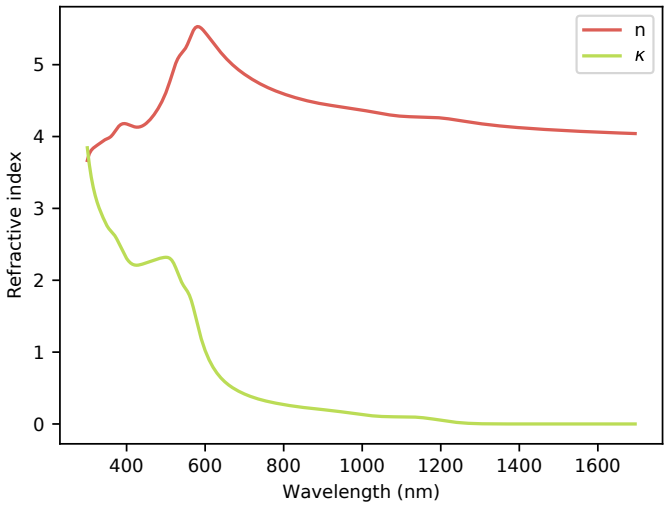


Figure 4.5: The optical constants of one of the SiGeSn samples, as measured through spectroscopic ellipsometry (see Section 5.2).

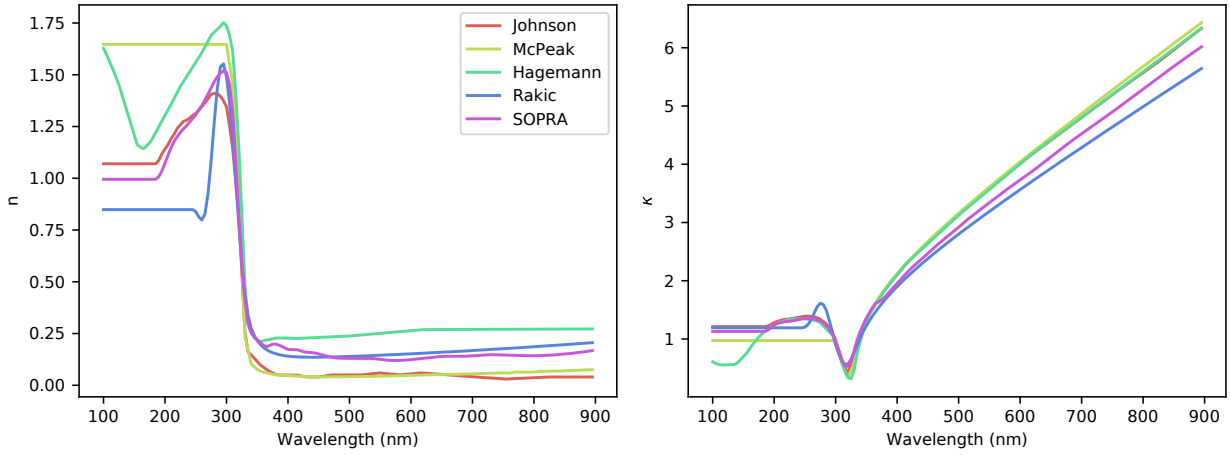


Figure 4.6: A selection of a) the real part n and b) the imaginary part κ of the refractive index for silver from different sources, pulled into Solcore from the refractiveindex.info database.

4.2 Integrating coherent and incoherent models: RayFlare

Accurate and efficient optical modelling of different types of structures (planar vs. structured layers, random vs. periodic structures, nano vs. micro-scale or larger) requires the use of different computational methods. Although in principle most problems can be solved by the most sophisticated type of solver available (in the case of the types of optical simulations we are considering, a full Maxwell solver), this is often not computationally efficient and can be less insightful than using a method with appropriate simplifications for the structure being considered. For instance, modelling micron-sized pyramids with a Maxwell solver such as RCWA or FDTD (finite-difference time-domain), or using RCWA to calculate the effect of a distributed Bragg reflector (DBR) made of planar layers, is possible and should yield correct results but is both computationally slow compared to a more physically appropriate method (e.g. ray-tracing and TMM, respectively, for the examples given), and does not generally lend additional insight into the physical processes that choosing a suitable simpler model would not. Especially if the problem being considered has an optimization aspect, requiring the simulation of many different structures, it is important to choose a modelling method which can accurately describe the relevant structure but is not unnecessarily computationally intensive. The development of RayFlare began due to a desire to integrate the various optical modelling codes developed and adapted for different types of problems over the course of the PhD into a single user-friendly Python package, which can be used to solve a wide range of optical problems by implementing ray-tracing, TMM, RCWA, simple Beer-Lambert law absorption, analytic models for surface scattering (e.g. perfect mirrors or Lambertian scattering) and an angular matrix formalism [99, 86]. The angular matrix formalism allows coupling of surfaces treated with the same or different optical methods across a thick, incoherent layer. By using Solcore's material system and database, and ability to define new materials easily (as discussed in the previous section) it thus becomes possible to model the wavelength-dependent optical behaviour of a wide variety of structures including structures involving planar layers of any thickness, structures with diffraction gratings, or structures with larger-scale textures such as pyramids. Combining e.g. a structure with pyramids on one side and a diffraction grating on the other is possible through the matrix framework, and comparison with idealized cases such as a perfect mirror or Lambertian scattering is easy and fast.

The matrix framework used is similar to OPTOS [86, 99] as discussed in Section 1.5.1. It divides the optical structure into three parts: the front surface, the bulk, and the back surface[1]. The front and back interfaces may be made up of several layers, or be textured, as long as there is a way to calculate the reflection and transmission for different angles of incidence, as well as (if relevant) the absorption in each layer of the interface. The matrix method itself is straightforward, and essentially amounts to matrix multiplication. For both interfaces, using any suitable optical method (e.g. TMM, ray-tracing, RCWA, or analytical expressions), a matrix must be constructed which describes how light incident on the interfaces is redistributed into other angles, or absorbed. In two dimensions, with a non-absorbing interface, this matrix will relate some polar angle θ_{in} to one or more θ_{out}, with the matrix elements describing what fraction of incident light is directed into each outgoing angle. This can be expanded to three dimensions by including an azimuthal angle ϕ [86]. The angular matrix framework and structures of the matrices in 2D, specifically using an integrated ray-tracing/TMM approach, are illustrated in Fig. 4.7. The ray-tracer takes the probabilities of reflection and transmission from an angle- and wavelength-dependent TMM calculation, to account for the multi-layer structure of the front surface of a realistic solar cell. The OPTOS framework has been expanded since its initial publication to include absorption in surface layers [165]; this ability was also developed independently

[1]The formalism could also be expanded to a stack with multiple interfaces and several 'bulk' materials, though this has not yet been implemented.

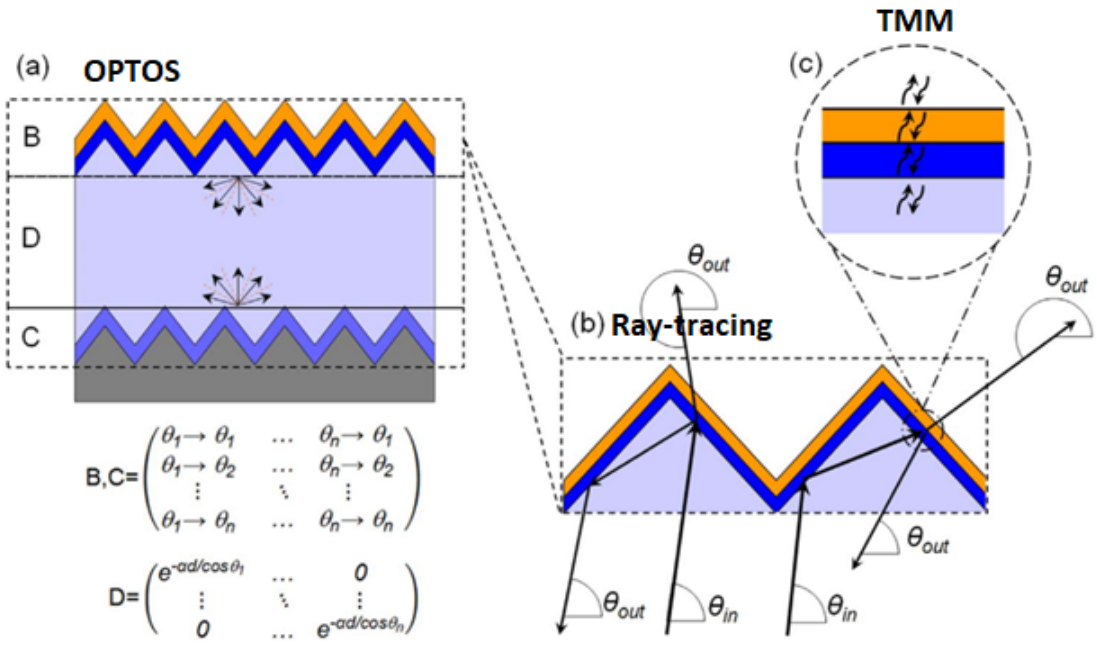


Figure 4.7: Schematic of the angular matrix framework, specifically when used with the integrated ray-tracing/TMM method, showing a) the function of the matrices B, C and D; b) how the matrix B could be calculated through ray-tracing; and c) how the TMM can be used with the ray-tracer to calculate reflection, absorption and transmission for a multi-layer surface. From [126].

as part of RayFlare over the course of the PhD approximately simultaneously [102]. While the existing matrix frameworks as discussed in Section 1.5.1 provide methods for combining different surface textures, there is no existing open-source modelling package which combines the angular matrix method with the actual generation of the matrices describing the redistribution at each interface. OPTOS provides only the matrix multiplication for calculating absorption in the bulk layers, but the matrices have to be computed and stored in the correct format by the user using external methods, while GenPro4 [98] is a proprietary software which combines the matrix approach with the generation of matrices but does not include an RCWA solver or other method for calculating diffraction from wavelength-scale periodic structures. The aim of RayFlare is to provide a free, open-source solution integrating both the generation of the matrices and the matrix multiplication to generate useful results, as well as tools for visualizing the outputs and matrices generated.

This section describes the work undertaken so far in developing the integrated optical modelling package RayFlare. The new ray-tracing implementation, developed specifically for RayFlare, is discussed first, followed by the description of the matrix method and validation of the various methods contained within RayFlare.

4.2.1 Ray-tracing

The ray-tracer used was written in Python3 specifically for use with RayFlare. The basis of the ray-tracer is the definition of a surface in terms of the Delaunay triangulation of a set of (x, y, z) points which define a surface, and the intersection of rays (directed lines) with those triangular planes. The surface could be very simple, such as regular V-grooves or pyramids (see Fig. 4.11a), or a more complicated surface based on e.g.

an AFM scan of a real surface structure.

The equations for a point on a line $\mathbf{l}$ (i.e. a ray) and a triangular plane $\mathbf{p}$ (i.e. one of the planes defining the surface) can be expressed in parametric form as:

$$\begin{aligned} \mathbf{l} &= \mathbf{l_a} + \mathbf{d}t \\ \mathbf{p} &= \mathbf{p}_0 + \mathbf{p}_{01}u + \mathbf{p}_{02}v \end{aligned} \tag{4.1}$$

where $\mathbf{d}$ is a vector pointing in the ray's direction of travel. The meaning of the symbols relating to the line-plane intersection is shown in Fig. 4.8a. Setting the RHS of both equations in eq. 4.1 equal to one another (which occurs at the intersection of the line $\mathbf{l}$ and the plane $\mathbf{p}$) and rearranging, the following matrix equation can be found:

$$[\mathbf{l}_a - \mathbf{p}_0] = \begin{bmatrix} -\mathbf{d} & \mathbf{p}_{01} & \mathbf{p}_{02} \end{bmatrix} \begin{bmatrix} t \\ u \\ v \end{bmatrix} \tag{4.2}$$

Note that since $\mathbf{d}$, $\mathbf{p}_{01}$ and $\mathbf{p}_{02}$ are vectors, the first term on the RHS of this equation is a 3 by 3 matrix.

This matrix equation can be solved in the standard way, by inverting the matrix, which after rearranging and multiplying out gives:

$$\begin{aligned} t &= \frac{(\mathbf{p}_{01} \times \mathbf{p}_{02}) \cdot (\mathbf{r}_a - \mathbf{p}_0)}{-\mathbf{d} \cdot (\mathbf{p}_{01} \times \mathbf{p}_{02})} \\ u &= \frac{(\mathbf{p}_{02} \times -\mathbf{d}) \cdot (\mathbf{r}_a - \mathbf{p}_0)}{-\mathbf{d} \cdot (\mathbf{p}_{01} \times \mathbf{p}_{02})} \\ v &= \frac{(-\mathbf{d} \times \mathbf{p}_{01}) \cdot (\mathbf{r}_a - \mathbf{p}_0)}{-\mathbf{d} \cdot (\mathbf{p}_{01} \times \mathbf{p}_{02})} \end{aligned} \tag{4.3}$$

For the intersection of a triangular surface with corners at $\mathbf{p}_0$, $\mathbf{p}_1$ and $\mathbf{p}_2$, with a forward-travelling ray, the following must be satisfied:

- $t > 0$, since the ray is travelling forward; $t < 0$ means the intersection point lies behind the point of origin of the ray
- $u > 0$ and $v > 0$ for the point to lie inside the triangle
- $u + v \leq 1$ for the point to lie inside the triangle

This calculation is straightforward to carry out for all the triangles which define a surface; however, looping through each surface and checking whether the ray intersects with it is computationally inefficient. For a complicated surface, such as one defined by an AFM scan, there may be hundreds or thousands of individual triangles; even for a single square-based pyramid, there are four surfaces to check. Thus, vectorizing this calculation so that for any given line, all surfaces can be checked at once using matrix operations will lead to much faster code. This can be done by defining matrices P_0, P_1 and P_2 which contain the p_0, p_1, and p_2 points of all the surfaces in the triangulation, and matrix versions of $\mathbf{d}$ and $\mathbf{r}_a$:

$$P_0 = \begin{bmatrix} \mathbf{p}_{0,I} \\ \mathbf{p}_{0,II} \\ \vdots \\ \mathbf{p}_{0,N} \end{bmatrix} \quad R_a = \begin{bmatrix} \mathbf{r}_a \\ \mathbf{r}_a \\ \vdots \\ \mathbf{r}_a \end{bmatrix} \quad D = \begin{bmatrix} \mathbf{d} \\ \mathbf{d} \\ \vdots \\ \mathbf{d} \end{bmatrix} \tag{4.4}$$

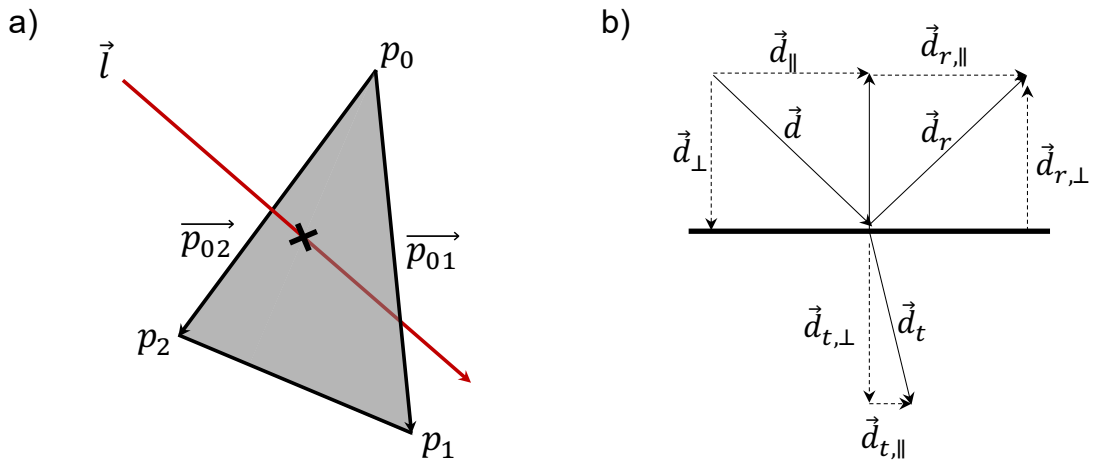


Figure 4.8: a) Intersection of a line with a finite, triangular plane. b) Reflection and transmission of a ray through an interface (in this case, from low to high refractive index).

where in the first equation, $\mathbf{p}_{0,I}$ refers to the p_0 coordinates of the first triangle in the surface triangulation, $\mathbf{p}_{0,II}$ refers to the second triangle, etc.

Eq. 4.3 has some vectors which appear multiple times. Matrix forms of these values can be computed once, then used in the calculation of matrix forms of t, u and v. The following quantities are defined:

$$C = \begin{bmatrix} (\mathbf{p}_{1,I} - \mathbf{p}_{0,I}) \times (\mathbf{p}_{2,I} - \mathbf{p}_{0,I}) \\ (\mathbf{p}_{1,II} - \mathbf{p}_{0,II}) \times (\mathbf{p}_{2,II} - \mathbf{p}_{0,II}) \\ \vdots \\ (\mathbf{p}_{1,N} - \mathbf{p}_{0,N}) \times (\mathbf{p}_{2,N} - \mathbf{p}_{0,N}) \end{bmatrix} = P_{01} \times P_{02} \tag{4.5}$$

C is a matrix with dimensions $(n_{\text{triangles}}, 3)$ and contains the cross products of $\mathbf{p}_{01}$ and $\mathbf{p}_{02}$ for each of the N triangles in the surface (one cross product per row). The '$\times$' symbol in the final expression is used to mean the row-wise cross product rather than the more standard cross or outer product. Note that because C depends exclusively on the surface itself and not on the incident ray, it can be computed before ray-tracing begins and stored for use in each call of the check_intersect function (see Listing 4.1). The vector version of the denominator factor common to the expressions of t, u and v is:

$$P_i = \frac{1}{\sum_j (-D \odot C)_{ij}} \tag{4.6}$$

P_i is a vector where the number of elements is equal to the number of triangles which define the surface. The '$\odot$' symbol is used to mean element-wise multiplication of the values in the matrix. The sum over the second matrix dimension j achieves the dot product per column (i.e. summing over the three dimensions after multiplying element-wise). This factor can be recognized as the denominator common to the expressions for t, u and v in eq. 4.3.

Finally, the matrix version of the $(\mathbf{r}_a - \mathbf{p}_0)$ factor common to t, u and v is defined simply as $X = R_a - P_0$.

Combining all this, and considering the relevant cross products and dot products, the vector versions of t, u and v can be written as:

$$
\begin{aligned}
t_i &= P_i \textstyle\sum_j (C \odot X)_{ij} \\
u_i &= P_i \textstyle\sum_j \left[(P_{02} \times -D) \odot X\right]_{ij} \\
v_i &= P_i \textstyle\sum_j \left[(-D \times P_{01}) \odot X\right]_{ij}
\end{aligned}
\tag{4.7}
$$

Note that throughout this section the use of indexing subscripts is *not* Einstein notation (summation of repeated indices is not implied – summation is explicitly denoted), but refers explicitly to which elements of the vectors should be multiplied together to give the ith element of t, u, and v. Computationally, all elements of t, u and v are calculated simultaneously using array multiplication in Python. Once t, u and v are computed, the conditions for intersection given above are checked simultaneously using logical 'and' statements to determine whether there is an intersection with each surface, resulting in a vector of 'True' and 'False' values with length equal to the number of triangles. Depending on the incident ray and surface, there may be more than one 'True' entry in the vector (the ray travelling in the forward direction can strike more than one triangle in the surface if allowed to continue travelling indefinitely); thus, if there are multiple intersections, the intersection with the minimum value of t is found, corresponding to the closest triangle. The location of the intersection is then given simply by $\mathbf{x} = \mathbf{r_a} + t_{min}\mathbf{d}$. The surface normal and thus the local angle of incidence between $\mathbf{d}$ and the surface normal are also calculated, since this is needed to calculate the reflection and transmission probabilities using either the Fresnel equations directly, or the TMM if a multi-layer surface is being considered.

The check_intersect function (Listing 4.1) implements the mathematical procedure as outlined, and forms the core of the ray-tracing algorithm. In order to treat a real structure, multiple auxiliary functions are needed, which define the triangulated surfaces, materials and implement scanning across the surface for a large number of rays. The reflection and refraction of light in three dimensions, with the correct wavelength-dependent refractive index of the material on each side of the surface, must also be implemented:

$$
\begin{aligned}
\vec{d_r} &= \vec{d} - 2\vec{d}_\perp = \vec{d} - 2\left(\vec{d}\cdot\vec{N}\right)\vec{N} \\
\vec{d}_{t,\parallel} &= \tfrac{n_0}{n_1}\vec{d}_\parallel = \tfrac{n_0}{n_1}\left(\vec{d} - \left(\vec{d}\cdot\vec{N}\right)\vec{N}\right) \\
\vec{d}_{t,\perp} &= -\sqrt{1 - \left|\vec{d}_{t,\parallel}\right|^2}\,\vec{N} \\
\vec{d_t} &= \vec{d}_\parallel + \vec{d}_\perp
\end{aligned}
\tag{4.8}
$$

which is shown schematically in Fig. 4.8b. $\vec{d}$ is the unit direction vector of the incoming ray, while $\vec{d_r}$ and $\vec{d_t}$ are the directions of the reflected and transmitted ray, respectively. $\vec{N}$ is the normal to the plane, pointing into the half-plane from which the ray $\vec{d}$ is entering. During reflection of the ray, the component of the ray perpendicular to the surface is flipped, while in transmission the component of the ray parallel to the surface obeys Snell's law ($n_0 \sin\theta_0 = n_1 \sin\theta_1$, or in vector notation $n_0\vec{d}_\parallel = n_1\vec{d}_{t,\parallel}$). The parallel ($\parallel$) and perpendicular ($\perp$) components are as indicated in Fig. 4.8b.

This describes a single interaction of the ray with a specific point of intersection with one triangular plane in the surface texture, but each ray must be tracked through the surface since in general a ray may interact with the same surface multiple times before being reflected or transmitted into the material above or below. Intersections with the surface texture inside one unit cell are checked until no further intersections are found; the ray is then translated back into the unit cell at the point where it would enter the next unit cell of the structure, assuming it is periodic in the x and y directions. This procedure is repeated until the ray is fully below (lower than the minimum point on the surface) or above (higher than the highest point on the surface) the triangulated surface. A diagram of a ray interacting with a square-based pyramid texture,

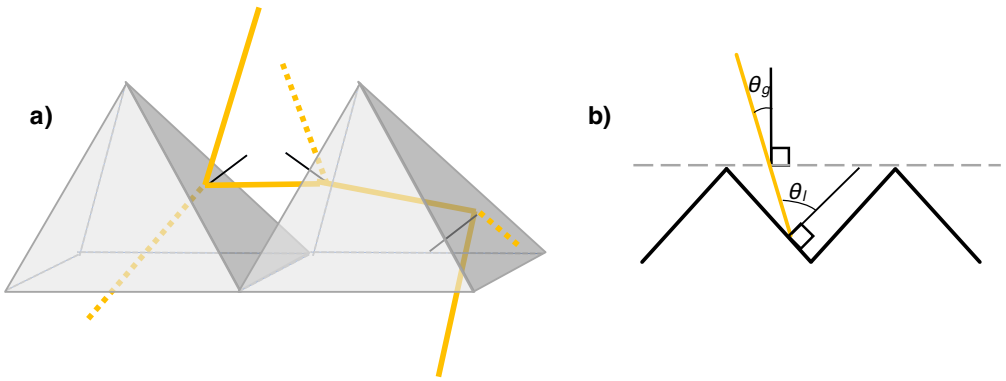


Figure 4.9: a) Schematic of three-dimensional ray-tracing for pyramids. b) Illustration of the meaning of the local angle of incidence θ_l and the global angle of incidence θ_g.

interacting with multiple interfaces, is shown in Fig. 4.9a. In order to accurately capture the behaviour of a surface, the unit cell defining the surface must be scanned, since a ray striking e.g. the top of a pyramid will behave differently to a ray which strikes the structure near the base. The reflection and transmission probabilities can be calculated directly from the optical constants of the interface materials using the Fresnel equations, or calculated through TMM (see Section 4.2.2).

Code Listing 4.1: The check_intersection function which forms the basis of RayFlare's ray-tracing algorithm.

```
def check_intersect(r_a, d, tri):

    D = np.tile(-d, (tri.size, 1))
    pref = 1 / np.sum(D * tri.crossP, axis=1)
    corner = r_a - tri.P_0s
    t = pref * np.sum(tri.crossP * corner, axis=1)
    u = pref * np.sum(np.cross(tri.P_2s - tri.P_0s, D) * corner, axis=1)
    v = pref * np.sum(np.cross(D, tri.P_1s - tri.P_0s) * corner, axis=1)

    which_intersect = (u + v <= 1) & (np.all(np.vstack((u, v)) >= -1e-10, axis=0)) & (t > 0)

    if sum(which_intersect) > 0:

        t = t[which_intersect]
        P0 = tri.P_0s[which_intersect]
        P1 = tri.P_1s[which_intersect]
        P2 = tri.P_2s[which_intersect]
        ind = np.argmin(t)
        t = min(t)

        intersn = r_a + t * d
        N = np.cross(P1[ind] - P0[ind], P2[ind] - P0[ind])
        N = N / np.linalg.norm(N)

        theta = atan(np.linalg.norm(np.cross(N, -d))/np.dot(N, -d)) # in radians, angle relative
            to plane
        return [intersn, theta, N]
    else:
        return False
```

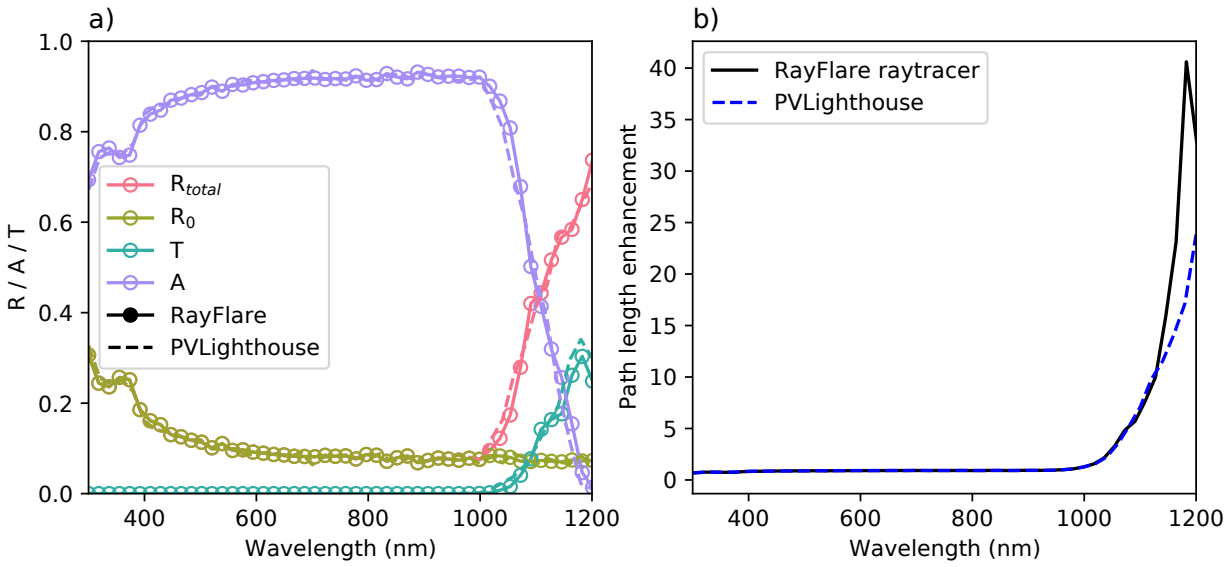


Figure 4.10: a) Comparison between the calculated reflection (total reflection and front surface reflection, R_0), transmission and absorption for a c-Si wafer, calculated using the widely-used PVLighthouse wafer ray-tracer [166] and the new Python3-based ray-tracer built for RayFlare. The structure considered is 300 µm of c-Si [129] with regular inverted pyramids with an elevation angle of 55° and base width 2 µm on the front surface. The rear surface is planar, and the surrounding medium is air. b) Comparison of the calculated path length enhancement using both methods.

Note that once an intersection has been found, before continuing to see if there are other intersections with the surface, the ray-tracer advances the ray by an infinitesimally small amount ($\mathbf{d} \times 10^{-9}$), otherwise the same intersection would immediately be found again. It is possible to use the ray-tracer in conjunction with the matrix method (Section 4.2.3) to calculate the angular redistribution of light at one interface, or to track the rays throughout the whole structure, interacting with the front and back surfaces until the ray is absorbed, transmitted, or reflected.

Model validation

To check if the ray-tracing algorithm is performing as expected, its results were compared to the widely-used PVLighthouse wafer ray-tracer [166], which is available as an online tool. Note that the matrix framework discussed below was not used in these simulations; ray-tracing was used to track the full path of rays through the structure. The same structures are defined in RayFlare and the PVLighthouse ray-tracer, consisting of a 300 µm thick Si wafer (optical constants in both cases were taken from [129]). The front surface of the wafer is textured with regular inverted pyramids with an opening angle of 55° while the rear of the cell is planar. The results in terms of total absorption, transmission, front surface reflection R_0, and total reflection calculated through both methods are shown in Fig. 4.10, showing very close agreement between both ray-tracing implementations. The total reflection includes the front surface reflection, i.e. light which is reflected during the first interaction of the incident light with the wafer, and escape reflection caused by rays which escape when light hits the front surface of the cell from the inside.

In addition, the results for the path length enhancement in an Si substrate patterned with random pyramids and regular pyramids depending on the substrate thickness are shown in Fig. 4.11. In both the

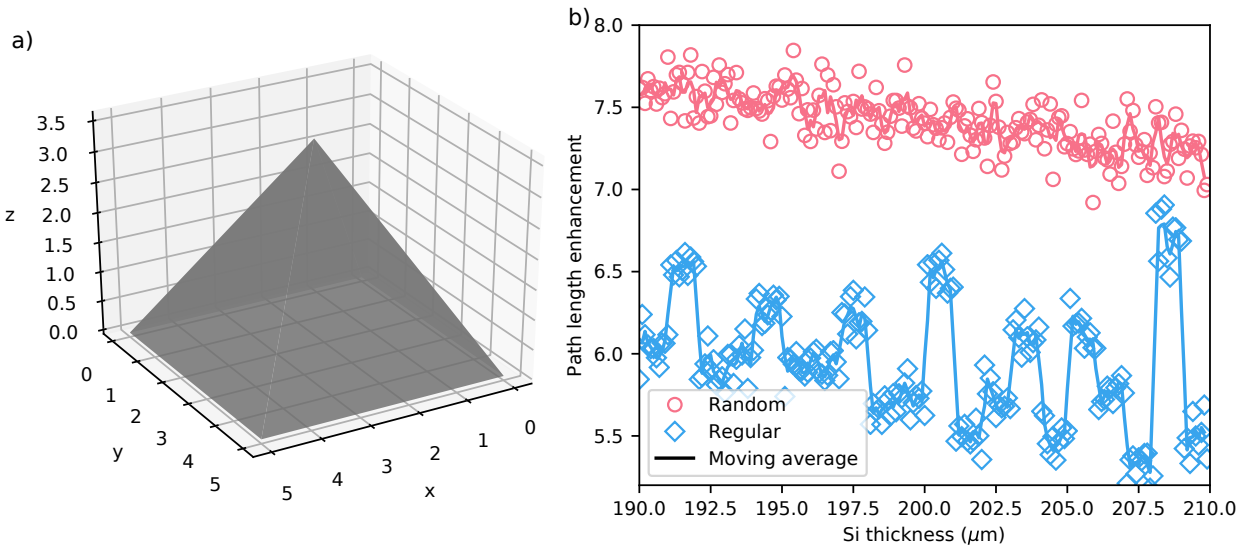


Figure 4.11: a) Example of a Delaunay triangulation surface object used for ray-tracing both regular and random pyramids. b) Comparison between the path length enhancement at 1100 nm compared to a single pass through a 200 µm Si substrate for structures with random (pink circles) and regular pyramids (blue diamonds) on the front surface, and a planar rear surface. The open symbols show the calculated data while the line shows a three-point moving average.

regular and random cases, the opening angle of the pyramids is 55°, the typical opening angle for chemically etched pyramids in Si. The size of the pyramids was set to 5 µm. The front surface is patterned with upright pyramids while the rear surface is planar. The triangulated surface used for both regular and random pyramids is shown in Fig. 4.11a; for the regular pyramids, the overall position in the unit cell is tracked while the ray makes passes inside the cell, preserving the location information of the ray. To simulate the effect of random pyramids, the same unit cell is used but the position of the ray is randomized before each interaction with the front or rear surface (the direction vector is kept at the value calculated during the previous surface interaction). The path length enhancement, depending on the Si thickness, at incident wavelength 1100 nm (close to the bandgap of Si) is shown in Fig. 4.11b. Fig. 4.11b shows that the path length enhancement for the regular pyramids is significantly lower than for the random pyramids. This is due to increased escape reflection through the front surface due to the relationship between the location on a pyramid at which the light enters the cell and the corresponding point on a pyramid which it will hit after traversing the cell. For truly random pyramids, the ray should be equally likely to encounter any (x, y) position of the unit cell with no correlation to its previous interaction with the surface, while for regular pyramids, there is a clear geometric relationship between the face of the pyramid the ray strikes while entering the cell and the face it will strike after traversing the cell and reflecting from the planar back surface, as discussed in detail in [84]. This effect can enhance or reduce the light-trapping; if a ray strikes the equivalent face of a pyramid through which it was coupled into the structure, it will be totally internally reflected back into the cell, while if it strikes the opposite face, it is likely to couple straight out of the cell (the reflection probability below the critical angle at an Si/air interface is around 30%). The results here are consistent with the predictions in [84]: random pyramids on the front surface only, with a planar back surface, consistently perform better than regular pyramids in a square grid, and are not very sensitive to the substrate thickness except a general trend of increasing absorption as the thickness increases. Note that while the total absorption increases, the

path length enhancement – the ratio of the fraction of light absorbed in the structure with light-trapping to the fraction of light absorbed in a single pass of a planar cell, calculated through the Beer-Lambert law – actually decreases, as shown in Fig. 4.11b. As the cell gets thicker, less absorption enhancement can be gained from the light-trapping structures, as the light has an increasing probability of being absorbed in a single pass. The performance of regular pyramids is extremely sensitive to the thickness of the substrate, shown by the sharp oscillations in Fig. 4.11b. For regular pyramids, the predicted interval between substrate thicknesses at which the path length enhancement reaches a local maximum is predicted to be [84]:

$$\Delta W' = (d/2)\tan(\theta_1 + \theta_2) \tag{4.9}$$

where $\theta_1 = \cot^{-1}(\sqrt{2}) \approx 0.615$ and $\theta_2 = \sin^{-1}[(\cos\theta_1)/n_3] \approx 0.233$, giving $\Delta W' = 2.83$ µm for $d = 5$ µm, matching the peak spacing observed in Fig. 4.11b.

The fact that regular pyramids consistently perform worse than random pyramids seems somewhat counter-intuitive, since random pyramids must represent some average over many different regular structures, and thus there must be regular structures which outperform a random structure for any wafer thickness and pyramid size. However, as shown in [84], these optimal regular structures are not structures where the pyramids are on a regular square grid, but rather regular structures where the overall grid is periodically staggered.

To further illustrate the effectiveness of randomizing the ray direction before rays return to a surface with similar features, Fig 4.12 compares the absorption in Si at long wavelengths for multiple structures with either regular V-grooves, random pyramids, or regular pyramids on the front surface and V-grooves, a planar rear surface, a perfect mirror or a perfect Lambertian reflector (see Section 4.2.6) on the rear surface. In each case, the feature size (pyramid base width or spacing between groove maxima) is 5 µm and the elevation angle of the features is 55°, with a substrate thickness of 100 µm. This means the front surface reflection for normal incidence in all cases is very similar (around 10% for the wavelength range 800-1200 nm), as Fig. 4.12 demonstrates. However, the transmission through the back surface and escape reflection vary significantly depending on the combination of front and rear surfaces. A structure with V-grooves on both sides performs significantly better when the V-grooves on the two surfaces are perpendicular; in the crossed case, most rays reaching the back surface cannot couple straight out by striking an equivalent surface to the one they entered through, reducing transmission, and the direction of the rays is changed before they re-encounter the front surface, thus also reducing escape reflection compared to the parallel case. Similarly, random front surface pyramids significantly outperform regular pyramids; in this case, the difference is mainly due to a reduction in escape reflection, since transmission through the planar back surface is similar. Random pyramids or a Lambertian scattering back surface lead to more absorption, with the highest absorption at long wavelengths achieved in the structure with random front pyramids and a Lambertian rear surface.

The results of the ray-tracing results are stochastic, as demonstrated by the fluctuations visible in the results shown in this section; a summary of the convergence of the ray-tracing for different numbers of rays and scanning points on the surface is shown in Appendix D.

4.2.2 Ray-tracing with integrated TMM

RayFlare can calculate the probability of reflection and transmission in the ray-tracer directly using the Fresnel equations; however, the probabilities can also be calculated using TMM if there are multiple surface layers, one or more of which may be absorbing. To be a useful approximation, the thickness of the surface

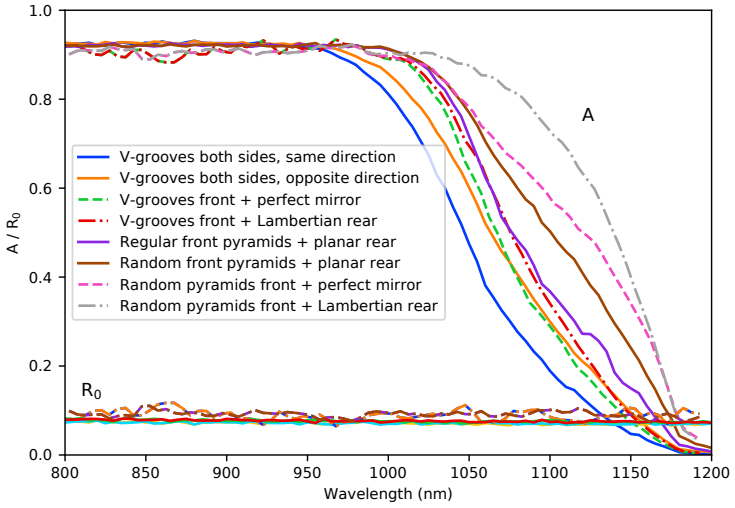


Figure 4.12: Comparison of the bulk absorption and front surface reflection R_0 for different structures with increasingly Lambertian behaviour.

textures should be thinner than the lateral dimensions of the surface texture (Fig. 4.7).

Computationally, it was found to be much faster to use the TMM to pre-compute lookup-tables with reflection, transmission and absorption probabilities which can be used as-needed by the ray-tracer, rather than doing individual TMM calculations each time those probabilities are needed. The TMM capabilities of RayFlare are based on the existing methods implemented in Solcore (Section 4.1.1), which are vectorized over wavelengths, and thus pre-computing the probabilities for a large number of incidence angles and the desired wavelength values is relatively fast (taking a few seconds or minutes on a normal computer depending on the structure) compared to computing individual probabilities as-needed, especially for a large number of rays. The downside is that these large arrays must be stored, as discussed in Section 4.2.7.

4.2.3 Matrix framework for multi-scale optical calculations

As discussed in the introduction to this section, it is not always appropriate to treat an optical structure with a single optical modelling method, for example because of diverging length scales (e.g. a diffraction grating with a period of hundreds of nanometres in a cell with a thickness of hundreds of microns). This is where the angular matrix method comes in; by calculating matrices which describe how incoming light is redistributed into outgoing directions by one interface of a structure (or absorbed in interface layers), optical methods can be combined across a single structure. The power fraction in each angular bin, $P(\theta_i, \phi_j)$, at any point within the simulation is represented as a vector $\vec{v}$:

$$\vec{v} = \begin{pmatrix} P(\theta_1, \phi_1) \\ P(\theta_1, \phi_2) \\ \vdots \\ P(\theta_2, \phi_1) \\ \vdots \\ P(\theta_m, \phi_n) \end{pmatrix} = \begin{pmatrix} 1 \\ 0 \\ \vdots \\ 0 \\ \vdots \\ 0 \end{pmatrix} \tag{4.10}$$

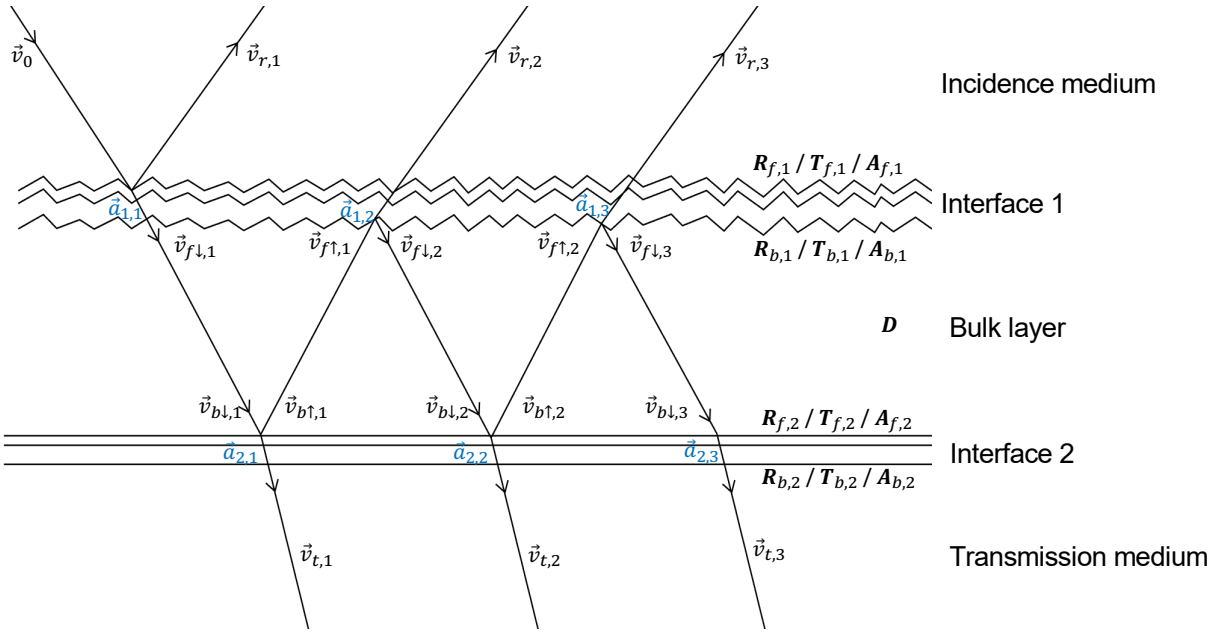


Figure 4.13: Schematic showing the labelling conventions used in RayFlare.

The length of the vector is l, the total number of angle bins (combinations of θ and ϕ). The specific example for $\vec{v}$ shown on the right-hand side of eq. 4.10 is for light incident from $\theta = 0°$ which has not yet interacted with any texture. Often, this is the form $\vec{v_0}$, the vector representing the incident light, will take. The discretization of θ and ϕ used here is the one proposed for the three-dimensional implementation of OPTOS [165]. The polar angle bins have equal $\sin(\theta)$ spacing; this means the $\mathbf{k}$ vector of light projected onto the surface planes has uniform spacing [99]. The azimuthal angle spacing is equidistant, and the number of azimuthal angle bins for any polar angle bin is given by $N_{\text{azimuth}} = \lceil c_{\text{azimuth}} \cdot r_{\text{polar}} \rceil$, where r is the index of the polar angle bin (starting from $r = 1$ for the $\theta = 0$ bin), $\lceil\rceil$ denotes rounding up the nearest integer, and $c_{azimuth}$ is a number between 0 and 1 which describes how fine the discretization should be. This discretization method means that the size of the angle bins when projected onto the plane in which the surfaces lie is approximately equal for all bins. The value of $c_{azimuth}$ used for all results presented in the thesis is 1/4, demonstrated to give accurate results while reducing computation time relative to using $c_{azimuth} = 1$ [86].

Fig. 4.13 shows an outline of how the propagation of light across a thick (compared to the wavelength of light) layer with front and rear textures is described by RayFlare. The $\vec{v}$ vectors, with length l, describe light propagating in the incidence or transmission medium, or within the structure, while the $\vec{a}$ vectors track the light absorbed in the interface layers. The $\vec{v_r}$ and $\vec{v_t}$ vectors track light which travels into the semi-infinite incidence and transmission media, respectively. Note that there is a difference between the meaning of the $\vec{v_f}/\vec{v_b}$ vectors inside the structure and the $\vec{v_r}/\vec{v_t}$ vectors outside the structure; the former track the total fraction of incident intensity left in the light propagating inside the structure over the course of the simulation, while the latter track how much power escapes from the structure at each interaction with the interface, and thus need to be summed over to give total reflection or transmission in each angular bin. The $\vec{a}$ vectors have length equal to the number of layers in the corresponding interface.

The $\mathbf{R}$ and $\mathbf{T}$ matrices describe the redistribution of light into other angular channels at each interface, either transmitted through the interface or reflected back into the same half-plane from which the light is

incident. The R and T labels clarify whether the matrix describes reflection or transmission through an interface, but could describe light incident from either the front or back of the texture; the subscripted 'f' or 'b' labels are used to distinguish incidence from the front and back respectively ('front' meaning the side of any interface closest to the incidence medium), while the subscripted number describes which interface the matrices describe. For instance, matrix $\mathbf{T_{b,1}}$ describes the angular redistribution when light incident from the inside of the structure onto the back of the front interface is transmitted into the incidence medium. For the 3D case, including azimuthal angle discretization, the matrices $\mathbf{R}$ and $\mathbf{T}$ take the form:

$$\mathbf{R}, \mathbf{T} = \begin{pmatrix} p(\{\theta_1,\phi_1\} \to \{\theta_1,\phi_1\}) & p(\{\theta_1,\phi_2\} \to \{\theta_1,\phi_1\}) & \dots & p(\{\theta_n,\phi_m\} \to \{\theta_1,\phi_1\}) \\ p(\{\theta_1,\phi_1\} \to \{\theta_1,\phi_2\}) & p(\{\theta_1,\phi_2\} \to \{\theta_1,\phi_2\}) & \dots & p(\{\theta_n,\phi_m\} \to \{\theta_1,\phi_2\}) \\ \vdots & \ddots & & \vdots \\ p(\{\theta_1,\phi_1\} \to \{\theta_n,\phi_m\}) & p(\{\theta_1,\phi_2\} \to \{\theta_n,\phi_m\}) & \dots & p(\{\theta_n,\phi_m\} \to \{\theta_n,\phi_m\}) \end{pmatrix} \tag{4.11}$$

where $p(\{\theta_i,\phi_j\} \to \{\theta_k,\phi_l\})$ is the probability that light incident from a direction in the $\{\theta_i,\phi_j\}$ bin is scattered into a direction in the $\{\theta_k,\phi_l\}$ bin.

The A matrices describing absorption take the form:

$$\mathbf{A} = \begin{pmatrix} p\left(\{\theta_1,\phi_1\} \to A_1\right) & p\left(\{\theta_1,\phi_2\} \to A_1\right) & \cdots & p\left(\{\theta_m,\phi_n\} \to A_1\right) \\ p\left(\{\theta_1,\phi_1\} \to A_2\right) & p\left(\{\theta_1,\phi_2\} \to A_2\right) & \cdots & p\left(\{\theta_m,\phi_n\} \to A_2\right) \\ \vdots & \vdots & \ddots & \vdots \\ p\left(\{\theta_1,\phi_1\} \to A_k\right) & p\left(\{\theta_1,\phi_2\} \to A_k\right) & \cdots & p\left(\{\theta_m,\phi_n\} \to A_k\right) \end{pmatrix} \tag{4.12}$$

Where $p\left(\{\theta_1,\phi_1\} \to A_1\right)$ is the probability that light incident from a direction that falls in the $\{\theta_1,\phi_1\}$ bin is absorbed in layer 1 of the interface. The dimensions of the $\mathbf{A_{f/b,i}}$ matrix depend on which interface it is describing; the number of columns is l, as for the $\mathbf{R}$ and $\mathbf{T}$ matrices, while the number of rows is equal to the number of layers in the interface with label i (thus the number of rows is interface-dependent, because not every interface has the same number of surface layers). In this labelling convention, and the code, 'layer 1' of an interface is always the layer at the front (closest to the incidence medium), and not necessarily the first layer the light encounters; light incident from inside the structure on the front surface would encounter the kth layer first.

Note that while Fig. 4.13 shows the light travelling through the structure as discrete rays to avoid confusion, light is generally scattered into multiple directions at each interface; the $\vec{v}$ vectors do not represent light travelling in a single direction, but keep track of the fraction of the incident intensity in each angular bin.

The definition of the angles θ and ϕ is somewhat ambiguous; Fig. 4.14 shows how light interacting with an interface with incident angles $\{\theta_1,\phi_1\}$ is scattered into outgoing angles $\{\theta_2,\phi_2\}$. θ is the polar angle from the positive z-direction, while ϕ is the azimuthal angle counter-clockwise from the x-axis (when viewed from the $z > 0$ half-plane). This coordinate system fully describes three-dimensional space with ranges $0 \leq \theta < \pi$ and $0 \leq \phi < 2\pi$. Keeping the same definition of θ and ϕ, the scattered ray travelling away from the first interaction in the $\{\theta_2,\phi_2\}$ direction will then be incident on a subsequent surface with polar angle $\theta_2' = \pi - \theta_2$ and azimuthal angle $\phi_2' = \pi + \phi_2$. The same coordinate system, with the z-axis pointing towards or into the incidence medium of the structure, is used for all interfaces. The transformation $\theta \to \pi - \theta$ and $\phi \to \pi + \phi$

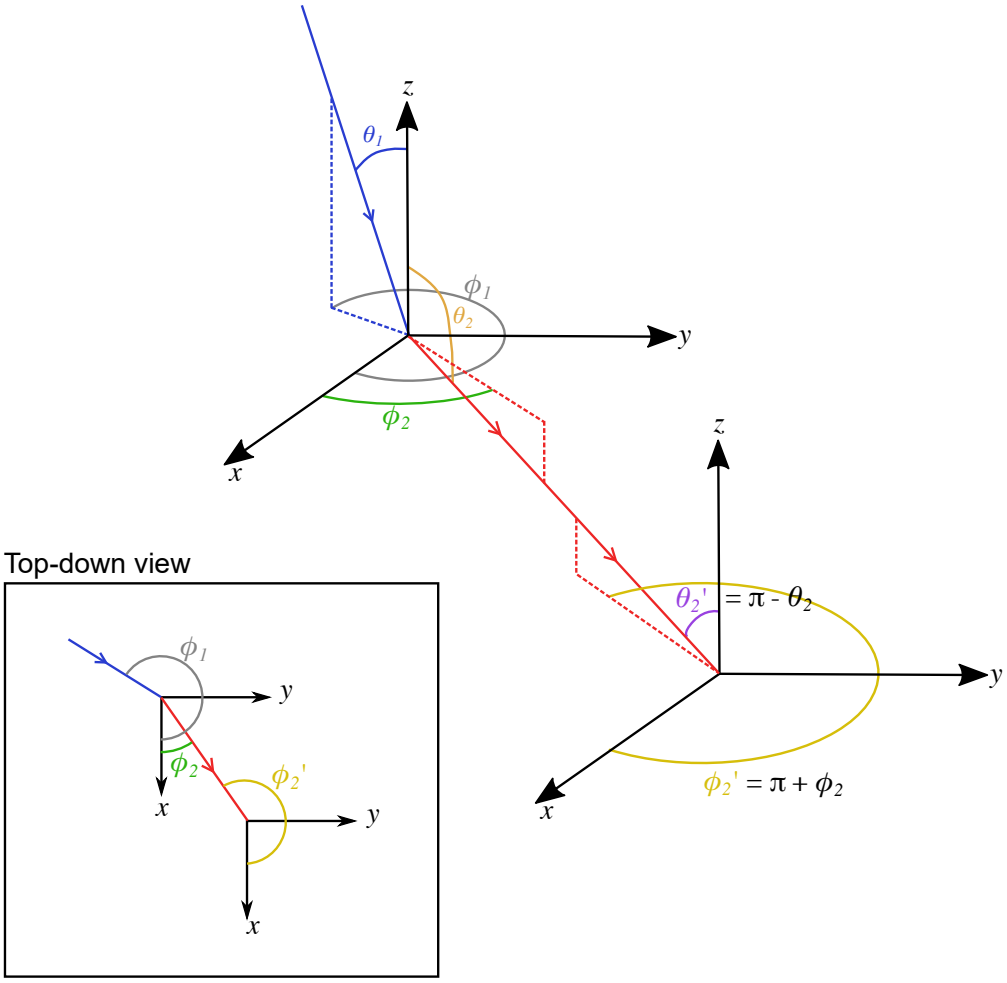


Figure 4.14: Schematic of the angle conventions used in RayFlare, and how they are transformed for incoming and outgoing light paths.

is applied to angles describing 'outgoing' directions to convert them into 'incoming' directions after each interaction with a surface (Fig. 4.14).[2]

Considering these definitions, it can be deduced that the **R** matrices describe light incident with some value of θ scattered so the outgoing direction (prior to a transformation into an 'incoming' vector) is in the same half-plane (so if $\theta < \pi/2$ before the interaction, it remains so after the interaction with the surface, and vice versa). The **T** matrices describe light where the value of θ is changed so the outgoing ray is travelling into the other half-plane. The attenuation of the intensity in the bulk, which in these simulations are assumed to be thick enough that interference effects within the bulk can be ignored, is described by matrix **D** using the Beer-Lambert absorption law:

[2]Applying this transformation often does not affect the results, as surfaces with mirror symmetry along the x and y axes, such as regular square-based pyramids or a square diffraction grating, are not affected by the transformations $\theta \rightarrow \pi - \theta$ and $\phi \rightarrow \pi + \phi$. However, implementing this transformation ensures the framework can be used for surfaces which do not exhibit such symmetry.

$$D = \begin{bmatrix} e^{-\alpha d/|\cos\theta_1|} & 0 & \dots & 0 \\ 0 & \ddots & & 0 \\ 0 & \vdots & \vdots & 0 \\ 0 & \dots & 0 & e^{-\alpha d/|\cos\theta_m|} \end{bmatrix}$$

The absolute value sign ensures that it does not matter whether the **D** matrix is applied before or after the transformation from outgoing to incoming direction, since $\cos(\pi - x) = -\cos(x)$. There may be multiple identical diagonal entries for each θ, depending on how many corresponding ϕ channels there are. The matrix **D** has the same dimensions as **R** and **T**. Note that the $\mathbf{R_{b,1}}$ and $\mathbf{R_{f,2}}$ matrices are equivalent to the **B** and **C** matrices, respectively, in the OPTOS formalism [99]; the labelling of the **D** matrix in Fig. 4.13 is unchanged from OPTOS.

After each surface interaction or pass through the bulk of the structure, the power remaining as a fraction of the incident power can be calculated by adding up all the entries in $\vec{v}$ inside the structure:

$$P = \sum_{m=1}^{l} \vec{v}_m \tag{4.13}$$

Note that the sum here is over all the angular bins, of which there are l. The initial total power sums to one: $\sum_{m=1}^{l} (\vec{v_0})_m = 1$. With reference to Fig. 4.13 for the vector and matrix labelling, the absorption, reflection and transmission can be calculated iteratively as follows:

First interaction with front surface:

$$\begin{aligned} \vec{v}_{f\downarrow,1} &= \mathbf{T_{f,1}}\vec{v}_0 \\ \vec{v}_{r,1} &= \mathbf{R_{f,1}}\vec{v}_0 \\ \vec{a}_{1,1} &= \mathbf{A_{f,1}}\vec{v}_0 \end{aligned} \tag{4.14}$$

Iterative calculation:

$$\begin{aligned} \vec{v}_{b\downarrow,i} &= \mathbf{D}\ \vec{v}_{f\downarrow,i} \\ \vec{a}_{2,i} &= \mathbf{A_{f,2}}\ \vec{v}_{b\downarrow,i} \\ \vec{v}_{t,i} &= \mathbf{T_{f,2}}\ \vec{v}_{b\downarrow,i} \\ \vec{v}_{b\uparrow,i} &= \mathbf{R_{f,2}}\ \vec{v}_{b\downarrow,i} \\ \vec{v}_{f\uparrow,i} &= \mathbf{D}\ v_{b\uparrow,i} \\ \vec{a}_{1,i+1} &= \mathbf{A_{b,1}}\ \vec{v}_{f\uparrow,i} \\ \vec{v}_{r,i+1} &= \mathbf{T_{b,1}}\ \vec{v}_{f\uparrow,i} \\ v_{f\downarrow,i+1} &= \mathbf{R_{b,1}}\ v_{f\uparrow,i} \\ &\vdots \end{aligned} \tag{4.15}$$

This iterative calculation can be repeated until the power remaining in the vector $\vec{v}_{f/b}$ describing light travelling inside the structure is below a certain threshold defined by the user, i.e. all the light has been

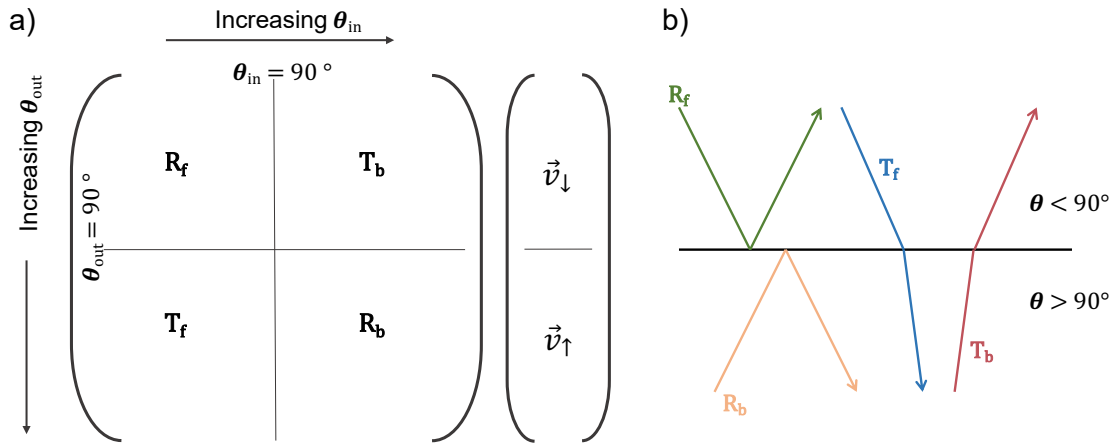


Figure 4.15: Schematic of a) the layout of the redistribution matrices for each surface and the angular vector $\vec{v}$ and b) the corresponding processes at the interface.

absorbed, transmitted, or reflected. At this point, all the relevant information will be stored in the $\vec{v}$ and $\vec{a}$ vectors. Although other values may be of interest, some of the most commonly-used quantities can be calculated as:

Calculating absorption in the bulk:

$$\begin{aligned} A_{\downarrow,i} &= \sum_l \vec{v}_{f\downarrow,i} - \sum_l \vec{v}_{b\downarrow,i} \\ A_{\uparrow,i} &= \sum_l \vec{v}_{b\uparrow.i} - \sum_l \vec{v}_{f\uparrow,i} \\ A_{total} &= \sum_i (A_{\downarrow,i} + A_{\uparrow,i}) \end{aligned} \tag{4.16}$$

Calculating absorption per layer in the interfaces:

$$\begin{aligned} \vec{a}_1 &= \sum_i \vec{a}_{1,i} \\ \vec{a}_2 &= \sum_i \vec{a}_{2,i} \end{aligned}$$

Calculating reflection and transmission per angular bin:

$$\begin{aligned} \mathbf{R}(\theta,\phi) &= \sum_i \vec{v}_{r,i} \\ \mathbf{T}(\theta,\phi) &= \sum_i \vec{v}_{t,i} \end{aligned} \tag{4.17}$$

Calculating total reflection and transmission:

$$\begin{aligned} R_{\text{total}} &= \sum_l \mathbf{R}\,(\theta,\phi) \\ T_{\text{total}} &= \sum_l \mathbf{T}\,(\theta,\phi) \end{aligned}$$

The relationship of the different matrices $\mathbf{R_f}$, $\mathbf{T_b}$, $\mathbf{T_f}$ and $\mathbf{R_b}$ to values of θ for the ray before and after interacting with a surface are shown in Fig. 4.15. $\mathbf{R_f}$ and $\mathbf{T_f}$ affect only downward-travelling rays ($\theta_{in} < \pi/2$), while $\mathbf{R_b}$ and $\mathbf{T_b}$ affect only upward travelling rays ($\theta_{in} > \pi/2$). The $\mathbf{R}$ matrices will redistribute light into the same half-plane while the $\mathbf{T}$ matrices will redistribute light into the other half-plane. Computationally, this means that if full matrices and vectors with $0 \leq \theta \leq \pi$ are used, three-quarters of the matrices and half of the vectors $\vec{v}$ will, by definition, be empty during any given matrix multiplication. Thus, only the relevant non-zero parts of the matrices and vectors are actually multiplied. The matrices $\mathbf{R_{b,2}}$, $\mathbf{T_{b,2}}$ and $\mathbf{A_{b,2}}$, corresponding to incidence from the back on the rear surface of the cell, are not automatically computed, since it is assumed no light will enter the structure from the semi-infinite transmission medium.

The iterative nature of the calculations means that in addition to the values shown above, more complex metrics can be tracked, e.g. how much of the incident power is absorbed on each pass of the bulk; the effect of direct reflection R_0 (due to the first interaction of the incident light with the front surface of the cell) and escape reflection (due to light escaping into the incidence medium during subsequent interactions with the front surface); or how much light is absorbed in the front interface layers due to light incident from outside vs. inside the cell. Note that the dependence on wavelength of each of the matrices has not been made explicit so far to simplify the description of the model, but in fact the iterative calculation is carried out simultaneously for all wavelengths using three-dimensional arrays with dimensions wavelength, index of the incoming angles, and index of the outgoing angles or absorbing layers (the Python package xarray is used to deal with the high-dimensional arrays).

A key advantage of the matrix approach to optical modelling problems is that although changing either of the surfaces means that the relevant $\mathbf{R}$, $\mathbf{T}$ and $\mathbf{A}$ matrices must be recalculated using an appropriate method, repeating the simulation with a different bulk thickness requires very little additional simulation time as only matrix $\mathbf{D}$ has to be recalculated, which is computationally trivial. If only one of the surfaces is changed, only the matrices for that surface need to be recalculated, rather than for the whole structure. This is especially useful when comparing realistic structures with idealized textures (Section 4.2.6); comparing the performance of a realistic back reflector or scatterer with that of a perfect mirror does not require re-computing the behaviour of the whole structure, and is very fast because these matrices are trivial to calculate.

4.2.4 Absorption in individual layers

Including absorption in the surface textures, in addition to bulk absorption and reflection/transmission at the interfaces is a natural extension of the angular matrix framework; instead of light being redistributed into other angles, it can be redistributed into a vector which describes absorption in each layer. This extension was also developed for the OPTOS method [165], but was conceptualized and developed independently for the RayFlare framework.

The ray-tracing method, whether used with the Fresnel equations or a lookup-table with values calculated through TMM, is a Monte Carlo method and therefore inherently stochastic; rays can be reflected, absorbed, or transmitted with some probability, depending on the structure being considered, the wavelength, and the point of incidence on the surface. If lookup-tables for an interface with multiple layers are used, the total probability of the light being absorbed anywhere in the stack is found by adding up the fraction of incident light absorbed in each layer. It is not necessary to choose which layer the absorption takes place in stochastically, since these probabilities are calculated exactly from the TMM; the choice of reflection, transmission or absorption is made stochastically, but the distribution of absorbed photons between the

layers can be done exactly based on the relative probabilities. Thus, if a ray is absorbed, RayFlare checks in the lookup-table what the probability of absorption per layer is (for the correct wavelength, side of approach, polarization and local incidence angle) and stores this information. At the end of the simulation, a matrix can then be generated relating the global incidence angle in terms of θ and ϕ bins to the probability of absorption in each layer; the intensity of absorbed rays is divided between the layers exactly based on the relative probability of absorption in that layer. However, because the absorption probabilities per layer are determined analytically using TMM while the fraction of rays reflected and transmitted are calculated stochastically, the situation can arise that (e.g. for a two-layer stack) $R + T + A_{\text{layer 1}} + A_{\text{layer 2}} \neq 1$. Thus, when generating the final matrices at the end of the simulation for each wavelength, the total number of rays which are not reflected or transmitted (i.e. must therefore have been absorbed) is stored, so that the fraction of absorbed rays A is known for each global incidence angle. This is then used to scale the absorption fractions per layer, so that $\sum_{i=1}^{n_{\text{layers}}} A_i \equiv A$.

Absorption profiles

When using the combined TMM/ray-tracing approach, it is possible to calculate absorption profiles within the surface layers by considering the local incidence angle and using existing TMM methods to generate absorption profiles. The absorption profile at a depth z in a coherent layer in a TMM calculation can be expressed analytically as [91]:

$$a(z) = A_1 e^{2z\,\mathrm{Im}(k_z)} + A_2 e^{-2z\,\mathrm{Im}(k_z)} + A_3 e^{2iz\,\mathrm{Re}(k_z)} + A_3^* e^{-2iz\,\mathrm{Re}(k_z)} \tag{4.18}$$

where $k_z = 2\pi n \cos\theta/\lambda_{vac}$ is the z-component of the wavevector $\vec{k}$. Eq. 4.18 can be found by calculating $-d(\mathbf{P}\cdot\hat{\mathbf{z}})/dz$, the negative of the derivative with respect to the z position of the z-component of the time-averaged Poynting vector $\mathbf{P} = \frac{1}{2}\,\mathrm{Re}\left[(\mathbf{E}^* \times \mathbf{H})\right]$. Physically, A_1 describes the intensity of the backward-travelling wave in the layer, A_2 describes the intensity of the forward-travelling wave, and A_3 describes interference between these waves. A_1, A_2 and A_3 depend on the layer structure under consideration and the wavelength. Note that if we consider a structure in which interference can be ignored, the expression for $a(z)$ at normal incidence simplifies to $a(z) = A_2 e^{-2z(2\pi\kappa)/\lambda_{vac}} = A_2 e^{-\alpha z}$, which is the negative of the first derivative with respect to z of the Beer-Lambert law ($I = I_0 e^{-\alpha z}$ with $A_2 = \alpha I_0$), as expected.

When the TMM lookup-tables are generated, the relevant parameters (A_1, A_2, A_3, and k_z) used to calculate the absorption profile for light incident on the layer stack from a specific (local) angle are stored along with the reflection, transmission, and absorption probabilities. A_1 and A_2 are, by definition, real, while k_z and A_3 are generally complex numbers for absorbing layers. During the ray-tracing process, the local incidence angle for each ray which gets absorbed must be stored if the absorption profile is to be calculated, so the correct values of the absorption profile parameters can be used (the difference between the overall angle of incidence on the surface and the local incidence angle is shown in Fig. 4.9b).

There is an added complication related to the issue discussed above for calculating absorption per layer in the combined TMM/ray-tracing approach; since the absorption fraction per layer has to be scaled to ensure that $R + A + T = 1$ for each global incidence angle, it follows that A_1, A_2 and A_3 must also be scaled accordingly. In addition, the data in the R, A and T redistribution matrices is in terms of global incidence angle, while the absorption profile depends on the local incidence angle. Thus, it is necessary to know the relationship between the global incidence angle and the local incidence angle for rays which were absorbed. Therefore, similar to the scaling to account for previous absorption, we must also scale the absorption profiles

to account for how much of a contribution each local angle makes. For regular textures like pyramids, clearly a global incidence angle will relate to only a small number of local incidence angles.

Although the intensity incident on the surface at each interaction can only be determined during the full matrix calculation, the relationship between the global and local incidence angle and thus the scaling required for A_1, A_2 and A_3 is known after ray-tracing, before the matrix calculation takes place. During the ray-tracing procedure, the relationship between the global incidence angle and the local incidence angle for rays which are absorbed is recorded in a matrix, with rows describing the local incidence angle bins and columns describing the global incident angle bin (in terms of both θ and ϕ as discussed above). Thus the dimension of this matrix is $(n_{theta\ bins}, n_{angle\ bins})$. The global/local angle matrix is used to scale A_1, A_2 and A_3 for each global incidence angle. Thus, we end up with a very large multi-dimensional matrix storing the values of A_1, A_2, A_3 and k_z for each layer and for each local angle per global incidence angle. This can then be used to generate a depth-dependent profile by using equation 4.18 for each local angle with a non-zero contribution, and then adding all the local angle contributions at each wavelength. The final result is a matrix with the different z positions along the rows, and the different global incidence angles along the columns.

Finally, this matrix is scaled so that the integrated total of all these contributions is consistent with the R and T probabilities. This final matrix can be used just like the R, T and A matrices; when multiplying a $\vec{v}$ vector, this gives the resulting absorption profile from that interaction with the surface. At the end of the matrix multiplication, all these contributions can be added up to come up with an overall absorption profile. Care must be taken to take into account how absorption profiles generated for front incidence and rear incidence are added together, since the light encounters the structure from the opposite direction, so the absorption profiles for rear incidence must be flipped.

4.2.5 Absorbing incidence media

In absorbing incidence media, the meaning of the incidence angle θ becomes somewhat ambiguous, as discussed in Section 2.3.1. This can be understood by considering the wavevector $\vec{k}$ of a plane wave. For a general plane wave (assuming without loss of generality that we are in the $x-z$ plane – see Fig. 4.14 for the angle convention):

$$\vec{k} = \frac{2\pi(n+i\kappa)}{\lambda}(\sin\tilde{\theta}, 0, \cos\tilde{\theta}) \tag{4.19}$$

Where the complex refractive index $\tilde{n}$ is expressed explicitly in terms of its real and imaginary parts. If $\kappa = 0$ (non-absorbing medium), the meaning of the angle θ is clear; it is the angle from the normal at which the light is travelling. But if we have $\kappa \neq 0$, this meaning becomes less clear. Specifically, $\tilde{n}\sin\tilde{\theta}$ will not be a real number if θ is a real number; this implies that there is dissipation of power in the direction parallel to the incident medium, since the x-component of the wavevector is not real, and therefore this cannot be an infinite plane wave. So $\tilde{n}\sin\tilde{\theta}$ must be real for a plane wave, and if $\tilde{n}$ is complex, this means $\sin\tilde{\theta}$ must be complex, and thus $\tilde{\theta}$ must be complex. This is equivalent to saying Snell's law ($n_0\sin\theta_0 = n_1\sin\theta_1$) holds even for interfaces where one or both of the media are absorbing. Although it is possible to deduce a relationship between the direction from which power is incident, a useful definition within the RayFlare matrix framework, and the complex angle $\tilde{\theta}$ (see Appendix B), this has not currently been implemented in RayFlare; instead, the much simpler assumption that $\kappa = 0$ for all incidence media has been made. This means that for light incident from inside the bulk structure, $\kappa = 0$ is set to zero. The justification for this

simplification is as follows:

- To be treated correctly within the RayFlare framework, the 'bulk' layer must be thick relative to the wavelength.
- If the bulk is thick relative to the wavelength and has high κ, then a large fraction of the light entering the bulk will be absorbed before ever encountering the back surface; so while the high incidence-angle entries[3] in the redistribution matrix for the rear surface, and back of the front surface, may not be accurate, this will not affect the overall results because a negligible fraction of the light encounters those surfaces at the problematic wavelengths.
- If the bulk has low κ, meaning the light may make many passes through the bulk before being absorbed and the high incidence-angle entries in the matrix become relevant (e.g. in an indirect semiconductor or glass), the angle at which power is travelling and the angle θ will be very similar since κ is close to zero.

Further work is needed to assess how much these assumptions affect modelling results, and whether implementing a more rigorous treatment of the complex angles as outlined in Appendix B is beneficial.

4.2.6 Ideal cases

To explore fundamental limits to light trapping or compare the performance of a device design with theory, it is useful to include a convenient way of generating matrices for several cases where the optical behaviour can be calculated analytically. Two cases used frequently in investigations of the performance of light-trapping structures (see Section 1.5.1) have so far been included in RayFlare: a perfect mirror and an ideal Lambertian scatterer. The perfect mirror case is straightforward: light hitting the interface at a polar angle θ and azimuthal angle ϕ is scattered into outgoing direction $\{\theta, \phi + \pi\}$. 100% reflectivity at all wavelengths is assumed, so the redistribution matrix is identical for all wavelengths, with a single entry equal to '1' per row and column of the matrix, with the location of the '1' entry describing the change in angle.

A perfectly Lambertian scatterer is an ideal diffuse reflector, having the same radiance (radiant flux per unit projected solid angle) regardless of the viewing angle. As the viewing angle increases from the normal, the projected area of the emitting surface appears to decrease proportional to $\cos\theta$, and thus the radiant flux should also decrease in order to maintain the same radiant flux. The power reflected into a polar angle bin with angle θ and width $d\theta$ can be written as:

$$dP \propto \cos(\theta) d\theta$$

The azimuthal dependence, ϕ, has been ignored; it is clear from the symmetry of the coordinate system and the requirement of an ideal diffuse reflector that the power should be divided evenly between the ϕ bins, which are of equal size for any given θ. The total power (summing over ϕ bins), as a fraction of incoming power, scattered into the bin at θ with a width of $d\theta$ is thus given by $\cos\theta d\theta$, with the final matrix normalized so that each column (corresponding to each incoming direction) sums to 1.

[3]The discrepancy between the angle from which power can be taken to be incident and the (real part of) the complex angle θ increases at higher angles of incidence, and with higher values of κ, as shown in Fig. B.1.

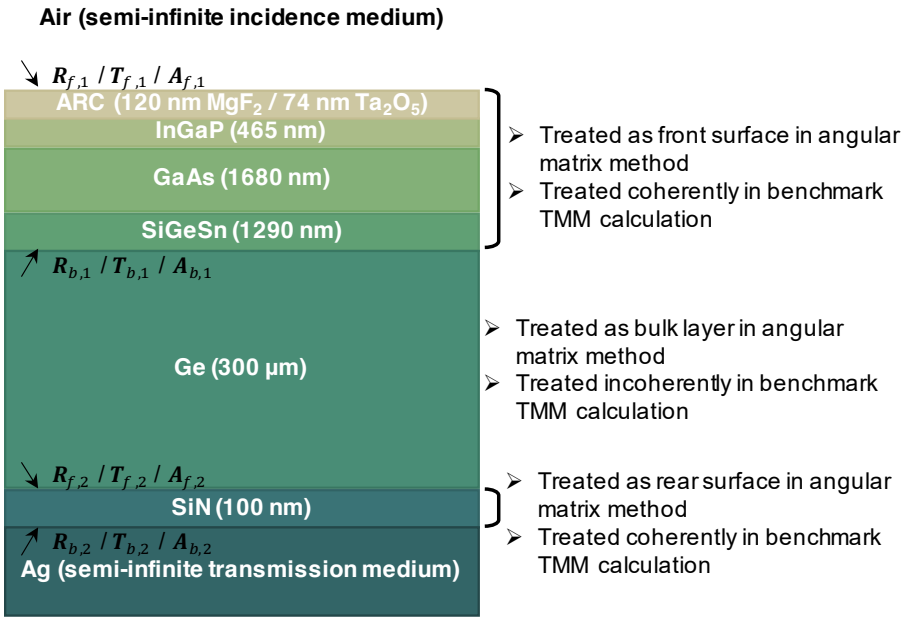


Figure 4.16: The four-junction solar cell optical structure used for validation of the RayFlare angular matrix model. The treatment of the layers in both RayFlare and the TMM reference calculation, done using Solcore's existing TMM implementation, is indicated. The labels $R_{f,1}$, $T_{f,1}$ etc. refer to the labels used in Fig. 4.13 for the angular matrices.

4.2.7 Storing information

For many structures commonly used in solar cells, such as pyramids or gratings, light will be scattered into specific directions according to its incidence angle, rather than being scattered across all possible outgoing directions (although this is not the case for randomly scattering structures or perfect Lambertian scattering). This means that the redistribution matrices are often extremely sparse, i.e. the vast majority of matrix entries is equal to zero; thus the matrices are stored in a sparse matrix format using the Python package sparse. A sparse matrix format stores a list of locations at which the matrix *is not* equal to zero, and the values at those indices, rather than storing each matrix entry explicitly. This significantly reduces the storage space required since typically a large number of matrices are generated during a simulation over a range of wavelengths.

In the case of perfect Lambertian scattering, where all the matrix elements describing reflection are non-zero and the scattering is assumed to be the same at all wavelengths, only a single matrix is stored as opposed to one matrix per wavelength to save storage space. The largest files which need to be stored are those for the TMM lookup-tables (Section 4.2.2), and those storing the parameters for calculating absorption profiles (Section 4.2.4); these multi-dimensional matrices are stored in NetCDF format using the xarray package.

4.2.8 Matrix method validation

In order to confirm if the matrix multiplication and methods for populating the redistribution matrices are working as expected, a planar multi-layer structure with a thick, incoherent layer can be considered. Such a structure can be modelled using the TMM method from Solcore directly, using the ability to treat layers incoherently, or by using the angular matrix framework with redistribution matrices calculated through

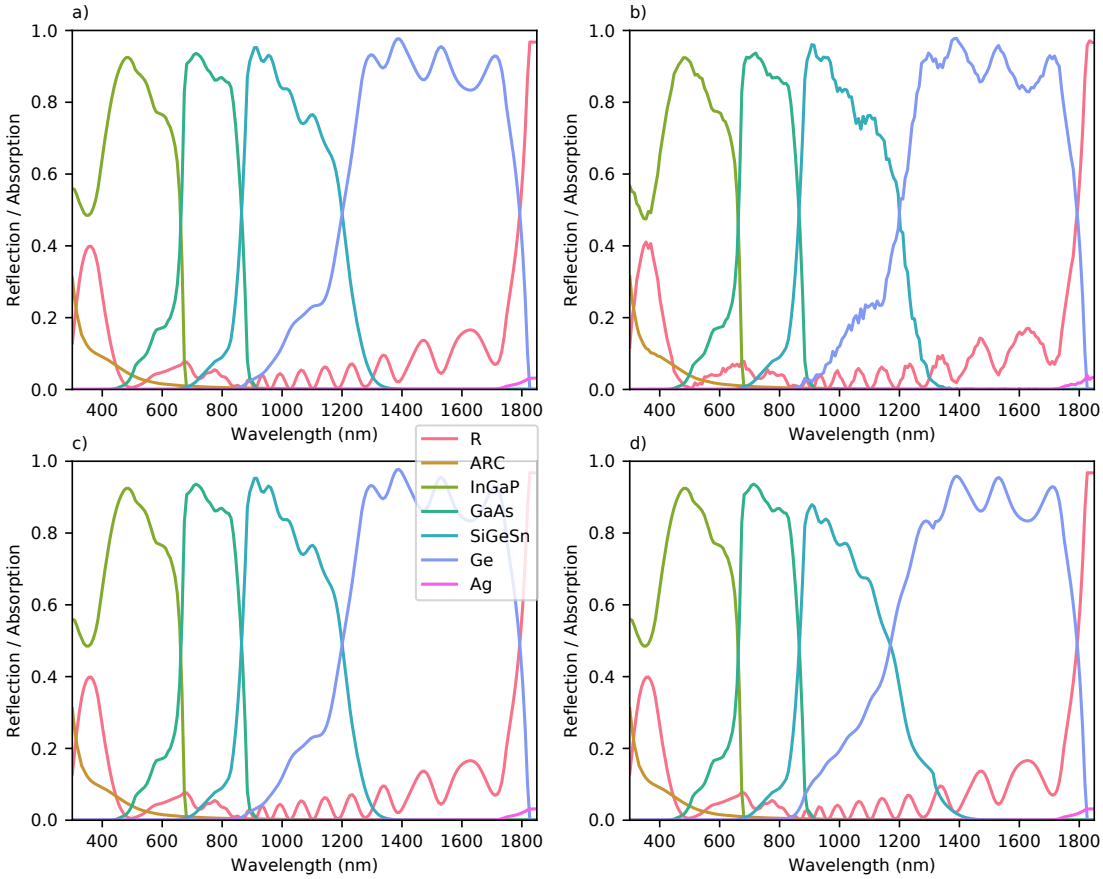


Figure 4.17: Calculated reflection, absorption per layer and transmission in a 4J solar cell-like optical structure for normally-incident unpolarized light, calculated using the RayFlare matrix multiplication framework and a) a TMM model, b) a ray-tracing model with TMM lookup-tables and c) an RCWA model to populate the redistribution matrices. d) shows the expected result, calculated using Solcore's TMM model (separate from RayFlare).

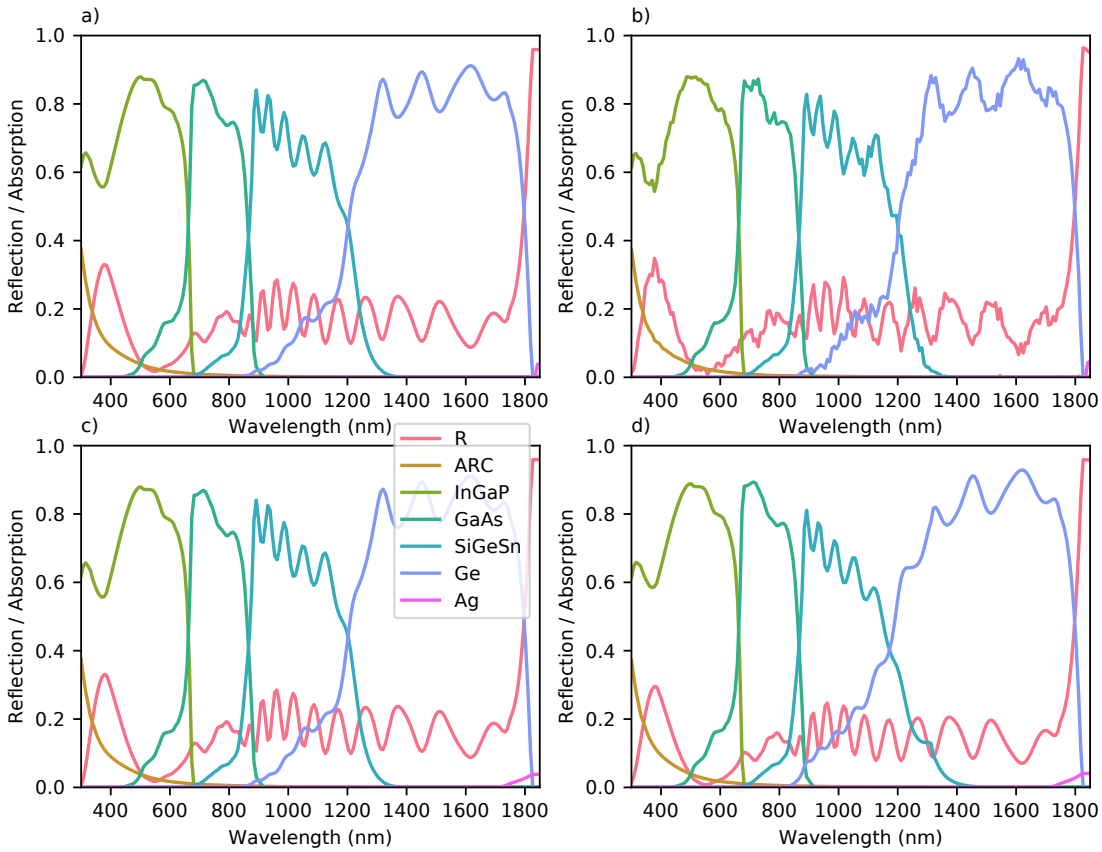


Figure 4.18: Calculated reflection, absorption per layer and transmission in a 4J solar cell-like optical structure with p-polarized light incident at 70° from the surface normal, calculated using the RayFlare matrix multiplication framework and a) a TMM model, b) a ray-tracing model with TMM lookup-tables and c) an RCWA model to populate the redistribution matrices. d) shows the expected result, calculated using Solcore's TMM model (separate from RayFlare).

TMM, ray-tracing in combination with a TMM lookup-table, or RCWA. As discussed previously, using ray-tracing or RCWA to calculate reflection, absorption and transmission through planar layers does not offer additional insight beyond that from a TMM calculation, but choosing a structure which can be modelled using all these methods allows a simple check of the angular binning method used in each, and the matrix multiplication itself.

The structure considered for the angular matrix model validation, and validation of the ray-tracing, TMM and RCWA methods as they are implemented to generate the redistribution matrices, is shown in Fig. 4.16. This structure is based on the optimized layer structure for a 4J solar cell with a SiGeSn sub-cell (Section 5.5). Using Solcore's TMM method, this structure is simply a Solcore layer stack with the thick Ge layer treated incoherently. In the RayFlare matrix method, this Ge layer is the bulk medium described by the matrix $\mathbf{D}$ and the thinner layers (MgF_2, Ta_2O_5, GaInP, GaAs and SiGeSn) form the front interface (this is also shown in Fig. 4.16). When the TMM and RCWA methods are specified in RayFlare, the reflection, absorption and transmission of these three layers is calculated by treating them as a coherent stack with an infinite transmission medium made of Ge, and the matrix method is used to couple this behaviour to the back surface. If ray-tracing is specified, a lookup-table is first generated using TMM. Clearly, there is much

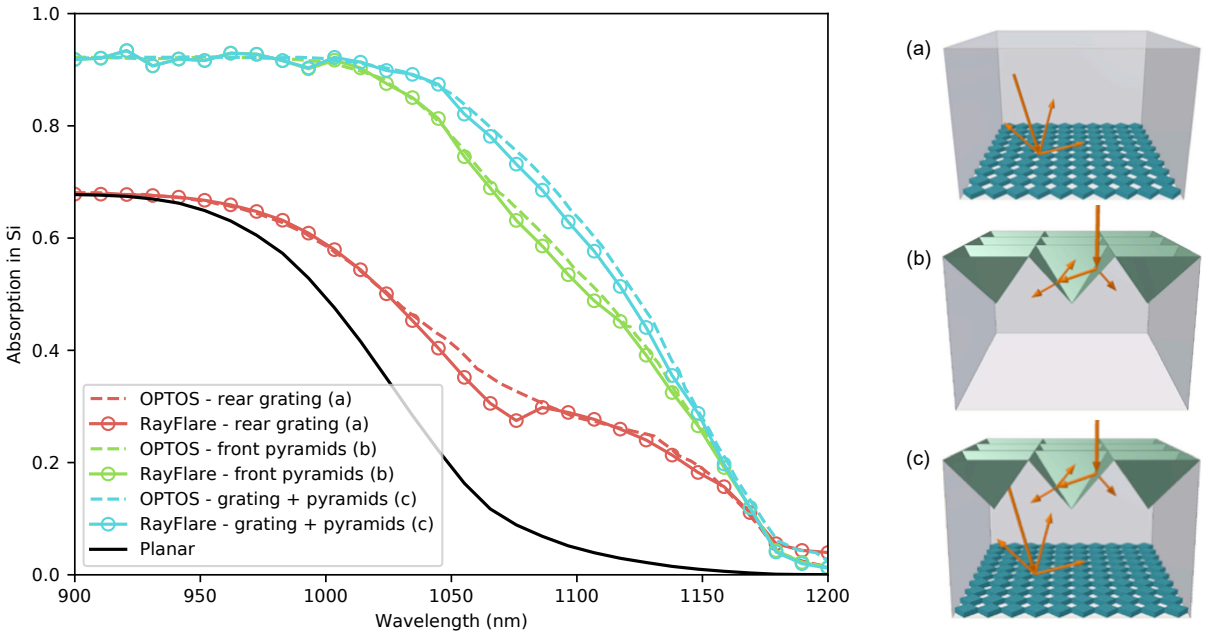


Figure 4.19: Comparison of absorption in 200 µm of bulk Si calculated using RayFlare (solid lines with open circles) and OPTOS (dashed lines) for (a) a structure with a planar front surface and a crossed diffraction grating at the rear (red lines), (b) a structure with inverted pyramids on the front of the structure and a planar rear surface (green lines) and (c) an Si layer with both structures, inverted pyramids on the front surface and a diffraction grating on the rear surface (blue lines). Schematics of the structures, reproduced from [86], are shown on the right.

redundancy between these methods, but the aim is to demonstrate the correct functioning of each method individually, and the connections between them. The optical behaviour of this structure was calculated at several angles of incidence, and for unpolarized, s and p-polarized light, using the four methods listed above. The comparison for normally incident, unpolarized light is shown in Fig. 4.17, showing that the results match extremely closely; the only deviation observed are the noisy oscillations in the result calculated through ray-tracing, due to the stochastic nature of this method. Results for p-polarized light incident at a glancing angle of 70° from the normal is shown in Fig. 4.18. Results for s-polarization and unpolarized light at non-zero incidence angles were also checked extensively to make sure the different methods were consistent.

To validate the performance of RayFlare for more complex structures, Fig. 4.19 compares the output of RayFlare with the results of OPTOS as reported in [86]. Three structures are considered, each with the bulk layer consisting of 200 µm of c-Si; (a) a structure with a planar front and crossed diffraction grating with period 1000 nm on the rear, (b) a structure with a planar rear surface and regular inverted pyramids (opening angle 55°) on the front and (c) a structure with pyramids on the front and a grating on the rear. The final structure uses the matrices for the front surface calculated for structure (a) and the matrix for the rear calculated for structure (b), so no additional time-consuming simulations are needed. There is a close match between the simulations in all cases. The dip in absorption in structure (a) around 1075 nm appears more pronounced in the RayFlare simulation, likely due to different RCWA methods being used with different numbers of Fourier orders (the number of orders used was not reported in the OPTOS paper). Fig. 4.20 shows the redistribution matrices (summarized over all the azimuthal angles ϕ) for light incident from inside the structure on the front surface pyramids, and for the rear-side diffraction grating.

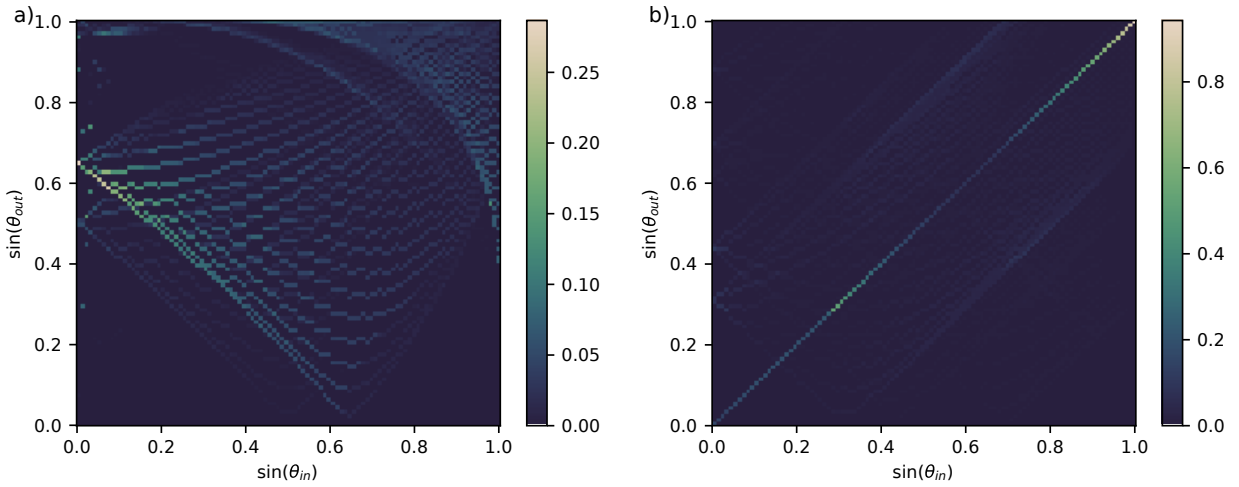


Figure 4.20: Reflection angular redistribution matrices, summarized per polar angle θ, for light with vacuum wavelength 1100 nm incident on a) inverted pyramids and b) a crossed diffraction grating with period of 1 µm. In both cases, incidence from inside the cell structure (Si) is considered. Note that the pyramids are inverted when considered from the outside of the cell, so the rays traced will actually encounter upright pyramids when incident from the silicon.

Table 4.1: Layer structure of the perovskite/Si tandem cell. The layer thicknesses and materials are taken from [97]. The sources for optical constant data for each material is also given.

Material	**Role**	**Thickness (nm)**	**Optical constant source**
MgF_2		100	[167]
IZO		110	[168] $r(O_2) = 0.10\%$, annealed
SnO_2		10	$n = 2$
C_{60}		15	[169]
LiF		1	[128]
Perovskite		440	[170]*
Spiro-TTB		12	$n = 1.65$
a-Si (n-type)		6.5	measured† [171]
a-Si (intrinsic)		6.5	measured [171]
c-Si		260,000	[129]
a-Si (intrinsic)		6.5	measured [171]
a-Si (p-type)		6.5	measured [171]
ITO		240	measured [171]
Ag		semi-infinite	[119]

* = The optical constants for the perovskite were based on the data for the films deposited with a 10% evaporation rate of CsBr to PbI_2 and a ratio of 1:2 FAI to FABr in the spin-coated solution, designated as 'CsBr 10%, 1:2' in the source [170], which is listed as having a bandgap of 1.65 eV. The best cell performance in [97] was actually achieved with a CsBr/PbI_2 perovskite layer with a slightly lower bandgap of 1.6 eV. The optical constants used in the simulation were constructed by taking the optical constants of the 1.65 eV bandgap material and shifting the n and k values down by 0.05 eV over the full wavelength range.
† = measured through spectroscopic ellipsometry at Imperial by Dr. Diego Alonso Álvarez.

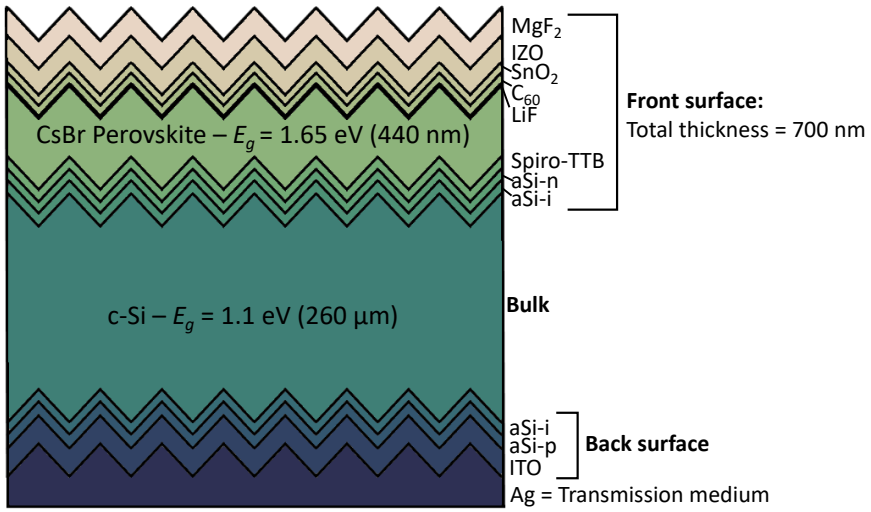


Figure 4.21: Structure of the perovskite/Si tandem cell structure. The incidence medium is air, with $n = 1$, while the semi-infinite transmission medium is silver. The front surface includes the perovskite, while the bulk material in RayFlare is the thick c-Si layer.

4.2.9 Application of integrated optical modelling

A useful application of the RayFlare framework is studying the effect of thin-film layers deposited conformally onto a surface texture, e.g. pyramids. An example of an application of such a structure in PV is a perovskite on silicon tandem cell, currently a device structure generating a large amount of research interest. One possible device structure involves depositing the relatively thin perovskite layer, and the necessary contacting and anti-reflection coating layers, conformally onto the pyramid structure of the Si, such as the device presented in Sahli et al. [97]. This preserves the well-optimized and effective use of pyramids to reduce front surface reflection and increase the path length of light in the silicon cell and increase absorption. The structure from [97] is shown in Fig. 4.21, with the details of the layer structure and the source of the optical constants used in these simulations shown in Table 4.1. The layer thicknesses in the stack are as reported in [97].

This structure was modelled using RayFlare's combined TMM/ray-tracing approach to calculate the redistribution matrices for each surface, with the Si as the bulk coupling medium across which the angular matrix method is applied. The overall result, with absorption in each layer, reflection, and transmission into the Ag substrate, is shown in Fig. 4.22. Examples of the matrices generated by RayFlare using the integrated ray-tracing/TMM lookup-table approach are shown in Fig. 4.23, showing the redistribution matrix for reflection and transmission of light incident from inside the cell on the front pyramidal surface. The TMM lookup-tables used during ray-tracing for the front surface are shown in Fig. 4.24, for light incident from outside the cell (left column) and inside the cell (right column). Fig. 4.24a shows that front surface reflection is low except at extremely glancing incidence angles[4], with some visible Fabry-Perot oscillations. In Fig. 4.24c and e we see low transmission and high absorption, respectively, at wavelengths below the bandgap of the perovskite (≈ 700 nm), where most incident light is absorbed in the surface layers, and high transmission into the Si bulk at wavelengths above the bandgap. For rear incidence, we can clearly see the effect of total

[4]For normally incident light incident on a surface with regular pyramids with elevation angle 55°, the only possible local angle of incidence is 35°; however, because generating the lookup-tables is fast, the full angular space is considered.

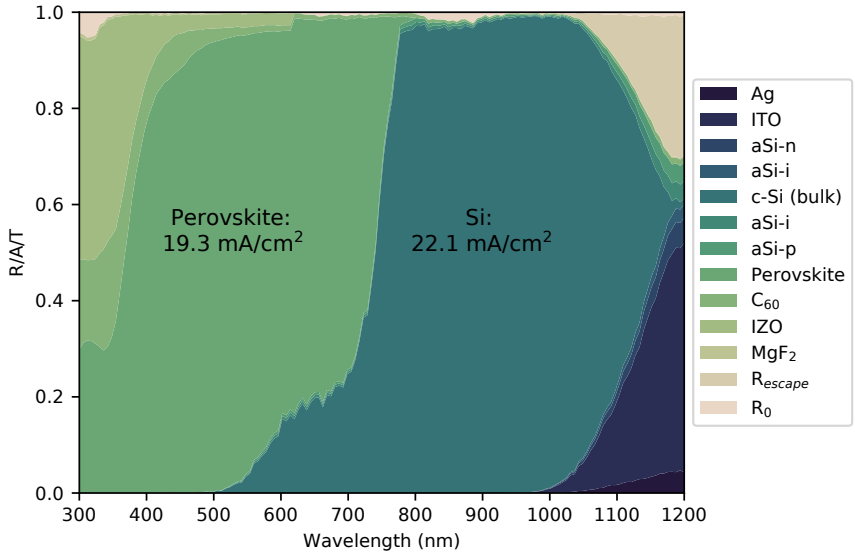


Figure 4.22: Reflection (direct and escape), absorption per layer, and transmission into the Ag substrate calculated using RayFlare for the perovskite/Si tandem cell structure shown in Fig. 4.21. The photogenerated currents are shown, calculated using eq. 2.38 from the AM1.5G solar spectrum. The front and rear surfaces were described using the integrated TMM/ray-tracing framework.

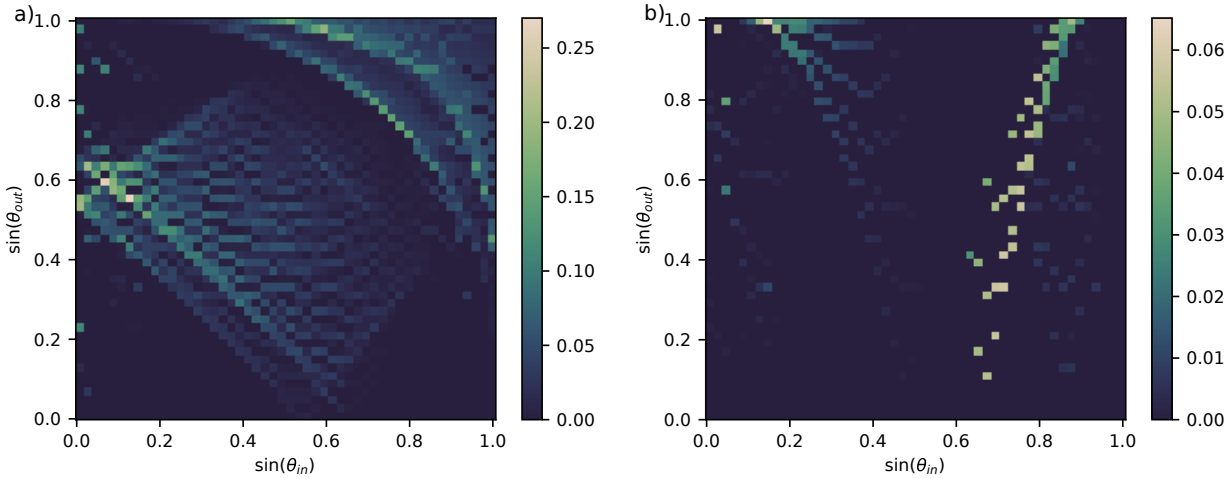


Figure 4.23: Examples of redistribution matrices calculated for the perovskite/Si tandem cell calculated using 100 incident/outgoing bins for the polar angle θ with azimuthal discretization $c_{azimuth} = 0.25$. These matrices describe a) reflection back into the cell and b) transmission into the incidence medium (air) for light which is incident from inside the Si on the pyramidal front surface. These matrices are summarized per θ bin (all the azimuthal ϕ bins are added together and normalized).

internal reflection in Fig. 4.24d, showing no transmission out of the cell into air above incidence angle of $\approx 15°$ (with the exact value of the critical angle depending on the refractive index of the layers and thus the wavelength). Light incident from inside the cell can also be absorbed in the front surface layers (Fig. 4.24f).

Fig. 4.25 shows escape reflection (light transmitted through the front Si surface from inside the cell) and absorption in the bulk during the first 25 interactions with the surface (for the reflection) or passes through the cell (for the absorption). At short wavelength, all the light is absorbed before reaching the front surface again, escape reflection is low, and absorption in a single pass in the Si is high. As the wavelength increases, light is able to make more passes through the cell without being absorbed, leading to increased escape reflection through the front surface as the light has an increasing number of chances to be transmitted out of the cell as the number of interactions with the front surface increases close to the bandgap of Si. These values are calculated from the $\vec{v}$ vectors.

Fig. 4.26a shows the absorption profile in the front surface layers of the structure, calculated as outlined in Section 4.2.4, at three different incident wavelengths. At short wavelengths, there is considerable parasitic absorption in the IZO layer, and the absorption profile at the start of the perovskite layer is very sharp as α is high at short wavelengths. At an intermediate wavelength of 540 nm, closer to the bandgap of the perovskite layer, the absorption profile is more extended throughout the layer, and thin-film interference is clearly visible. At long wavelengths, almost no light is absorbed in the deposited layers, and light is instead able to reach the c-Si cell.

Fig. 4.26b shows the effect of replacing the textured back surface of the Si cell with a perfect mirror, or keeping the texture the same and increasing the Si thickness to 360 µm (from 280 µm), on the long-wavelength absorption in the Si bulk. A perfect mirror actually performs slightly worse than the realistic structure; this is because the real back surface is already a good reflector due to the silver deposited on the rear, and in addition randomizes the ray directions further so behaves more 'Lambertianly' than the perfect mirror, which reflects but does not scatter light into more oblique angles. As expected, increasing the c-Si thickness increases the absorption near the bandgap. Both of these results are extremely quick to calculate; the first case requires only the matrices for the rear surface to be changed to the trivial matrix for a perfect mirror (see Section 4.2.6), while changing the bulk thickness only requires the matrix $\mathbf{D}$ to be changed, which uses only straightforward Beer-Lambert calculations.

4.2.10 Planned further work

Multiple relatively simple improvements to RayFlare could significantly decrease computation time. For ray-tracing, automatically checking the convergence as rays are traced and terminating the process at each wavelength once some sufficiently small standard deviation or confidence interval (adjustable by the user) has been reached prevents an unnecessarily large number of rays being traced for e.g. a simple interface or at wavelengths where the bulk is highly absorbing. For the matrix framework, populating the matrices can be time-consuming depending on the surfaces and methods chosen, and depending on the wavelength, some matrix entries may not be important; for instance, at wavelengths where the bulk material is very highly absorbing, the entries for the interaction with the rear surface, or for interaction with light encountering the front surface from inside the cell are not needed since no light will reach these surfaces at these wavelengths. Even for weaker bulk absorption, if the front surface scatters only into specific angles during the first interaction of light with the surface (e.g. a pyramidal surface), only the entries corresponding to angles into which the light will be scattered in the bulk need to be calculated for the rear surface redistribution matrices, as long as the light is able to make less than three passes through the cell (i.e. it does not reach the front

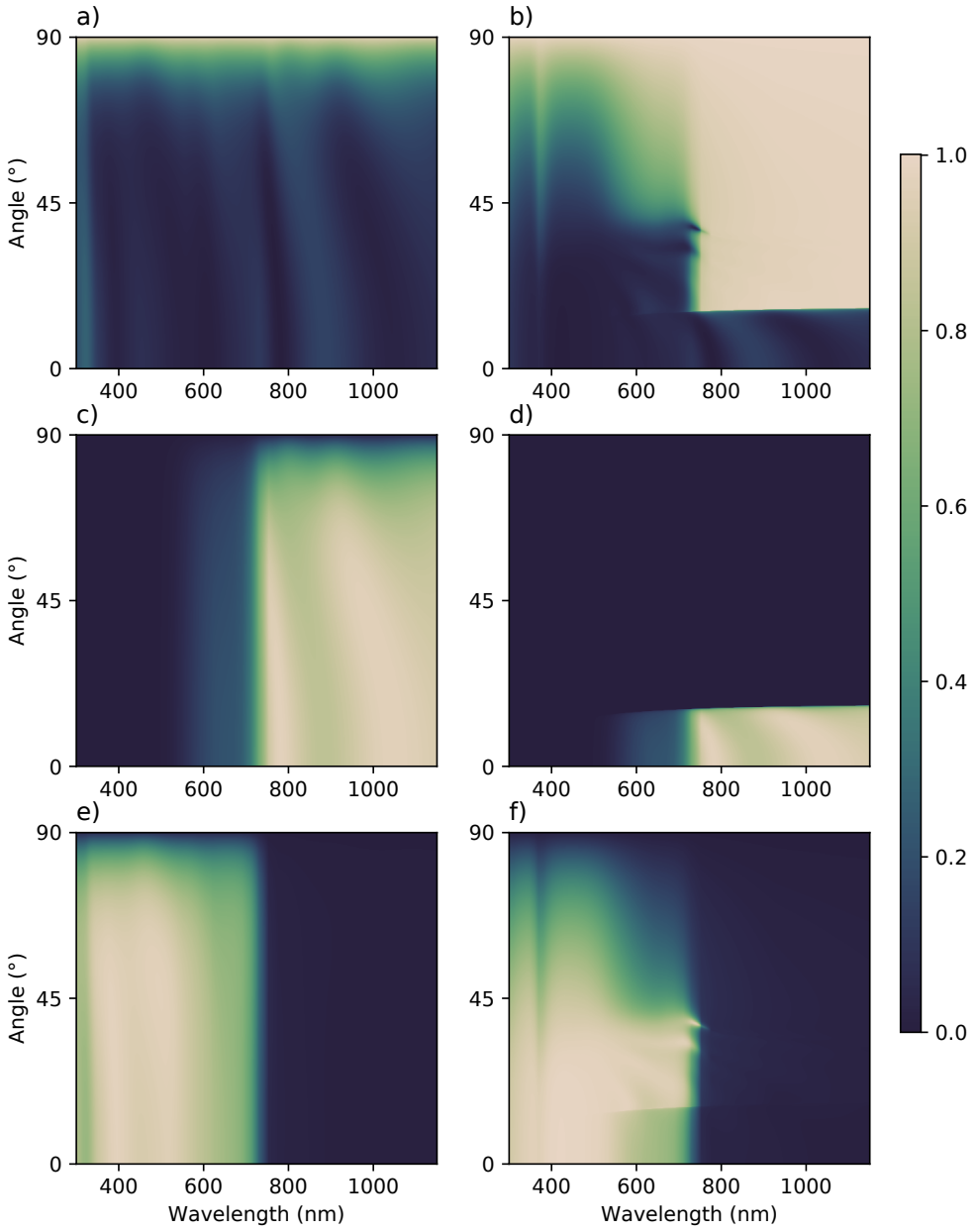


Figure 4.24: Example of the lookup-tables produced by RayFlare, in this case for the front surface of the perovskite/Si structure in Fig. 4.21; this information is used by the ray-tracing algorithm. The plots show incidence angle and wavelength dependence for the probability of: a) Reflection for front incidence (from air); b) reflection for rear incidence (from Si); c) transmission for front incidence (from air); d) transmission for rear incidence (from air); e) total absorption in the surface layers for front incidence; f) total absorption in the surface layers for rear incidence.

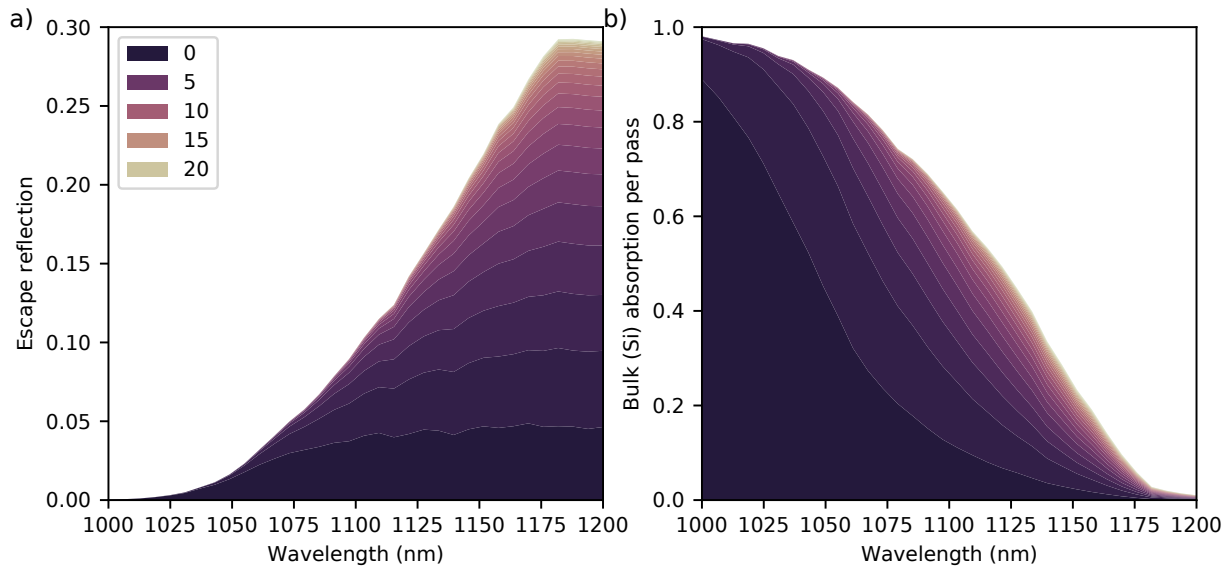


Figure 4.25: a) Escape reflection per interaction with the front surface and b) absorption in the bulk Si per pass for the perovskite/Si structure. The different colours represent the contribution of each pass/interaction, as shown in the legend.

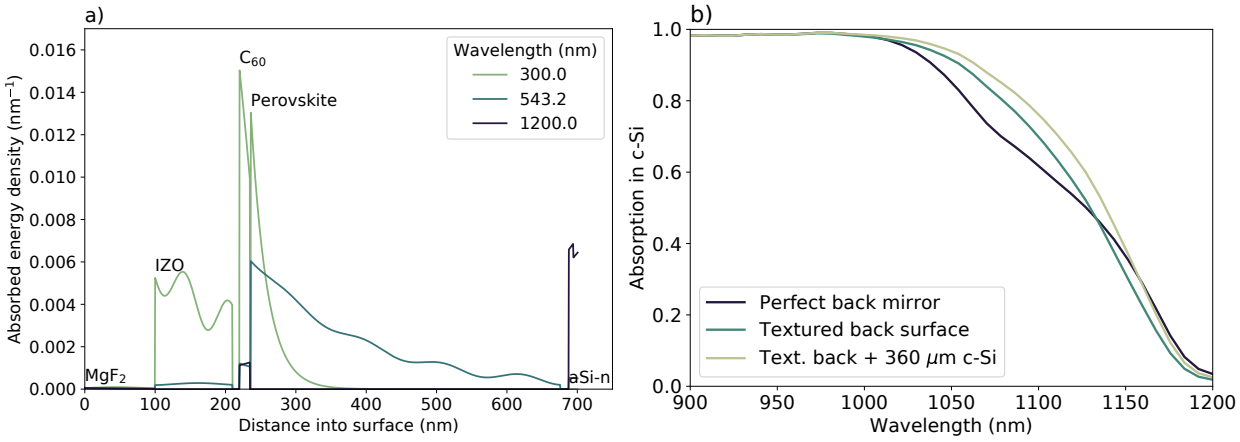


Figure 4.26: a) Absorption profile in the surface layers deposited on the pyramidal c-Si surface of the structure in Fig. 4.21 at three different wavelengths. b) Comparison of the absorption in Si at long wavelengths for the original textured back surface, a perfect mirror, or the original textured surface with an increase in the c-Si thickness.

surface again after interacting with the rear surface). If the rear surface is planar, this further reduces the number of matrix entries which have to be calculated. The ray-tracing and rigorous coupled-wave analysis modules, which can be slow due to their computational intensity, already support parallel implementation to calculate results for different wavelengths simultaneously on different threads; further improvements to the code speed can be made by running the computation using CPU (central processing unit) or GPU (graphics processing unit) acceleration, e.g. through the Python package numba.

RayFlare shares functionality with the optical modelling side of Solcore; in addition to the matrix framework, structures using any of the optical modelling methods (TMM, ray-tracing, ray-tracing with TMM or RCWA) for the full stack can also be defined. All these methods allow absorption profiles to be calculated, which allow a generation profile to be generated for Solcore's electrical solvers. An absorption profile can also be calculated using the matrix framework. Therefore, an easy way for RayFlare to interface with Solcore, and generate absorption profiles which can be used directly by Solcore's electrical solvers, will expand both the optical methods available for use with Solcore and allow direct use of the results of RayFlare in electrical models.

4.3 The effect of optical constants on modelling results

Arrays of metal nanoparticles [110], other diffracting structures using metal grids [111] or perforated films [112], and randomly arranged scattering nanoparticles [113, 114] have all been investigated as methods for improving absorption in solar cells using plasmonic and diffraction effects [109, 83, 82]. Optical simulations are key in developing, analysing and optimizing novel concepts for light-trapping architectures. In such structures, absorption in metal layers is usually parasitic, and thus in order to accurately predict solar cell performance (e.g. quantum efficiency and short-circuit current) it is critical to accurately quantify absorption in the target layer and in any parasitically absorbing layers. This is especially important for structures with front-surface metallic features or ultra-thin structures such as those discussed in Section 1.5.2.

A complicating factor in obtaining accurate simulation results is the uncertainty regarding the appropriate optical constants for commonly used metals such as gold, silver and titanium. The optical constants of nominally the same metal can vary depending on deposition process (e.g. bulk, evaporated, sputtered), sample thickness and other factors, leading different sources to report significantly different optical constants for the same material. These differences between sources may be exacerbated by instrumental error or the modelling approaches used to fit experimental data. Even metals grown by nominally similar methods can have different optical properties [172, 173], and optical constant measurements may be affected by metal thickness and possible effects from surface layers; some metals will oxidise or tarnish if exposed to air, and interfaces between different materials may not be perfect. For instance, detrimental optical effects from a porous interface between silver and zinc oxide have been observed [174], and the incorporation of oxygen into aluminium nanodisks during growth affects their optical constants and plasmonic properties [173]. Further processing steps required to produce a functional device, such as sintering, may also cause the formation of complex compounds at metal interfaces which are generally not taken into account in optical simulations.

There appears to be a bias towards the use of optical constants which give the most optimal results with little indication that these are the most appropriate data available; this was discussed in [119] for the case of silver optical constant data from Johnson & Christy [175]. This data has low extinction coefficient κ (and thus low absorption) and a high localized surface plasmon quality factor (LSPQ) compared to other data sources (see Fig. 4.28). Despite the availability of newer data and the large instrumental error reported in [175], this data continues to be used in recently published simulation results (e.g. [111, 112, 113, 176, 177]). Similar issues can readily be observed for other common metals including gold and titanium by comparing literature values of the optical constants.

In this section, four commonly-used metals are considered: silver, aluminium, gold, and titanium. In order to assess how the use of different optical constants affects simulation results, several different data sets from literature are used to optimize a simple solar cell-like optical structure in terms of optimal disk size and period of a regular scattering nanodisk array on top of a thin absorbing GaAs layer. In the cases of three of the four metals (all expect Al), variation in optical constants taken from different literature sources in the wavelength region 300-900 nm lead to significantly different optimal nanodisk arrangements for maximum absorption in the GaAs layer and thus photogenerated current (J_{ph}), and the predicted performance for these optimal structures also diverges. Differences observed in the J_{ph}, which depends on the number of photons absorbed in the GaAs, are not always reflected similarly in the total absorption; the total absorption profile may remain similar while the distribution of absorption between GaAs and metal layers changes significantly. Thus, care must be taken when comparing simulation results to total absorption measurements of optical precursor structures [96, 111], since accurate prediction of total absorption does not necessarily mean accurate prediction of absorption in the photovoltaic layer. Comparing the simulated J_{ph} results obtained for different

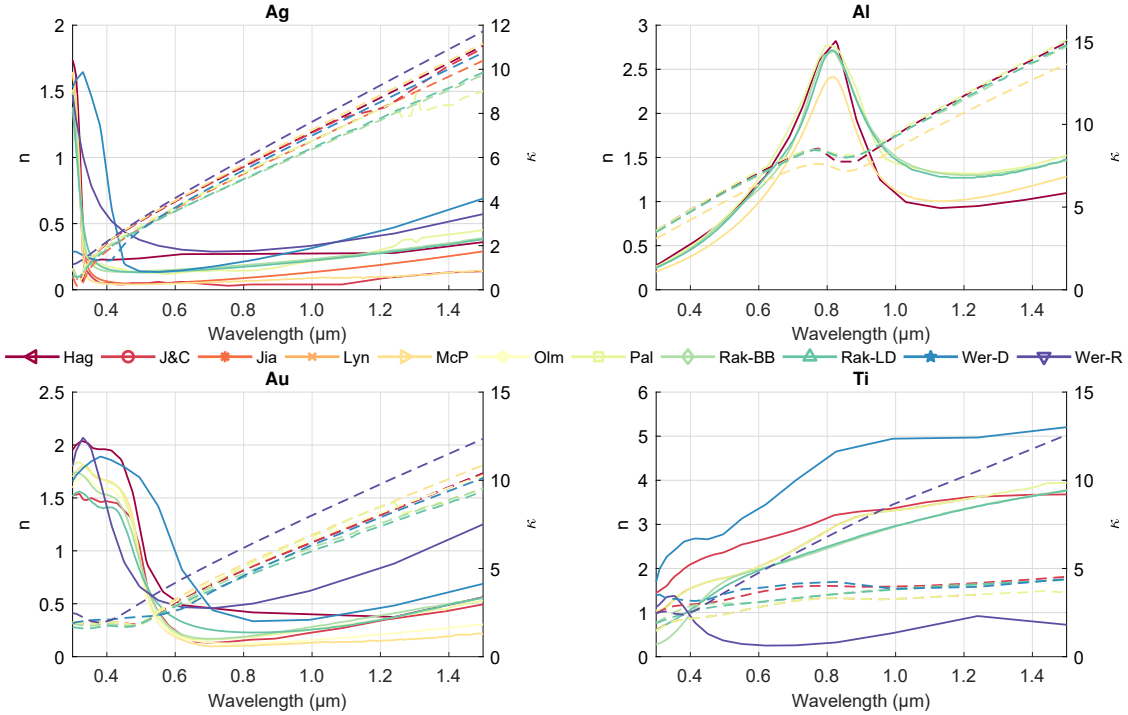


Figure 4.27: n (left axes, solid lines) and κ (right axes, dashed lines) for Ag, Al, Au and Ti, from different sources. Values were taken either directly from the published work (see Table 4.2) or from [164].

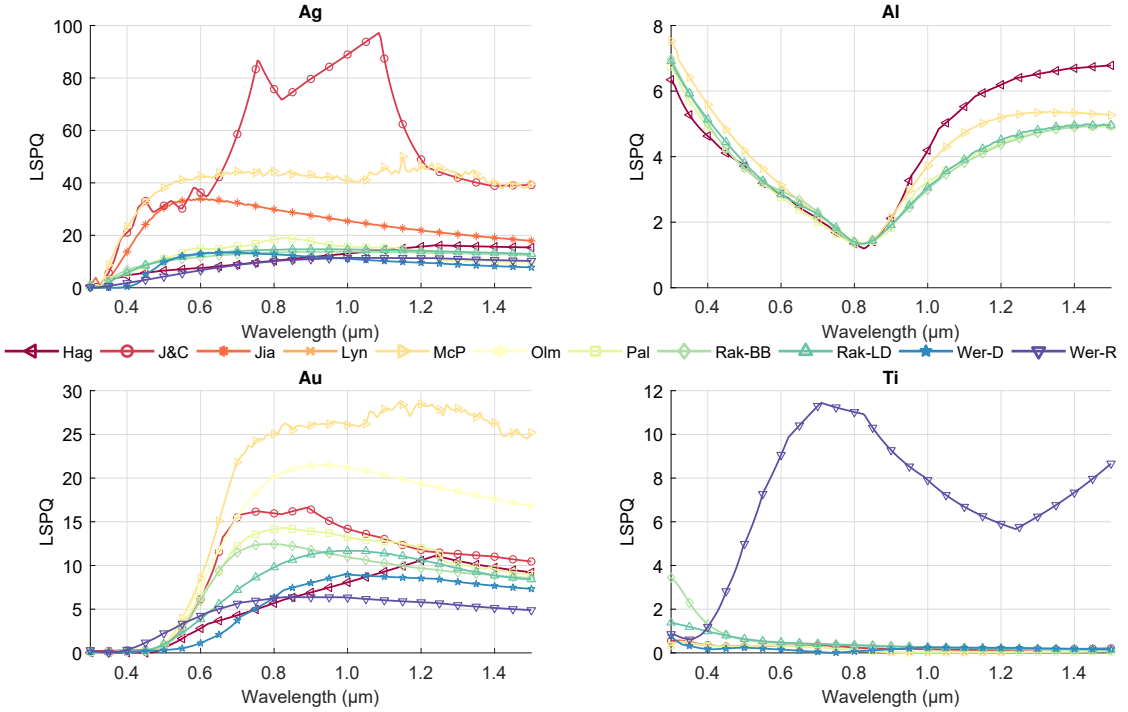


Figure 4.28: Localized surface plasmon quality factor, defined as $|n^2 - \kappa^2|/(2n\kappa)$ [119, 178].

Table 4.2: Sources used for optical constant data, the labels by which they are referred to throughout this section, which of the metals considered here can be found in each reference, and a brief summary of the method by which the optical constants were measured or modelled.

Reference	Label	Metals	Method
Hagemann et al. [180]	Hag	Al, Ag, Au	Transmittance measurements of vacuum-evaporated films/Kramers-Kronig analysis
Jiang et al. [119]	Jia	Ag	Variable-angle spectroscopic ellipsometry of overlayer-protected films
Johnson & Christy [175]	J&C	Ag, Au, Ti	Reflection and transmission measurements on vacuum evaporated films
Lynch et al. [181]	Lyn	Ti	Absorptivity/reflectivity measurements of polycrystalline Ti/Kramers-Kronig analysis
McPeak et al. [172]	McP	Ag, Al, Au	Variable-angle spectroscopic ellipsometry of template-stripped samples
Olmon et al. [182]	Olm	Au*	Variable-angle spectroscopic ellipsometry of evaporated gold
Palik [179]	Pal	Ag, Al, Au, Ti	Various
Rakić et al. [183]	Rak-BB	Ag, Al, Au, Ti	Brendel-Bormann model fit to available experimental data
Rakić et al. [183]	Rak-LD	Ag, Al, Au, Ti	Lorentz-Drude model fit to available experimental data
Werner et al. [184]	Wer-R	Ag, Au, Ti	Reflection electron energy-loss spectroscopy (REELS)
Werner et al.[184]	Wer-D	Ag, Au, Ti	Density functional theory (DFT) calculations

metal sources with the newly-defined spectral absorption enhancement factor (SAEF) shows this new figure of merit to be a good predictor of the absorption enhancement performance of metals.

4.3.1 Optical constant sources

Table 4.2 summarises the different sources used for the complex refractive index, $n + i\kappa$, of Ag, Al, Au and Ti, with references and the labels used to refer to each source throughout this section. Fig. 4.27 shows the refractive index n and extinction coefficient κ for each source. Not all sources have optical constant data for each of the metals considered here, and thus the number of data sets varies per metal (of course, more sources than those listed here are available). Although Palik's Handbook of Optical Constants [179] takes data from other publications, it is included here as a distinct source as it is very frequently cited and often the principal reference when optical constant data is required. For each source, the localized surface plasmon quality factor (LSPQ) for a sphere[5] was calculated; this is defined in terms of the dielectric function $\epsilon_1 + i\epsilon_2$ as [119, 178]:

$$\text{LSPQ} = \frac{-\epsilon_1}{\epsilon_2} = \frac{|n^2 - \kappa^2|}{2n\kappa} \tag{4.20}$$

in the region where ϵ_1 is negative (i.e. metallic). Broadly speaking, the field enhancement in a material depends on ϵ_1, while the absorption (loss) depends on ϵ_2, and thus the LSPQ provides a convenient, easily-calculated figure of merit to estimate the potential for different metals in light-trapping structures.

[5]The expression for the LSPQ depends on nanoparticle shape; it is given here for a sphere, as this is a commonly-used figure of merit, although the nanoparticles simulated here are disks rather than spheres. The use of disks was due to the additional computational intensity required for modelling spheres using RCWA, as a sphere must be built from multiple layers in the vertical direction, as opposed to the single layer necessary for a disk/pillar.

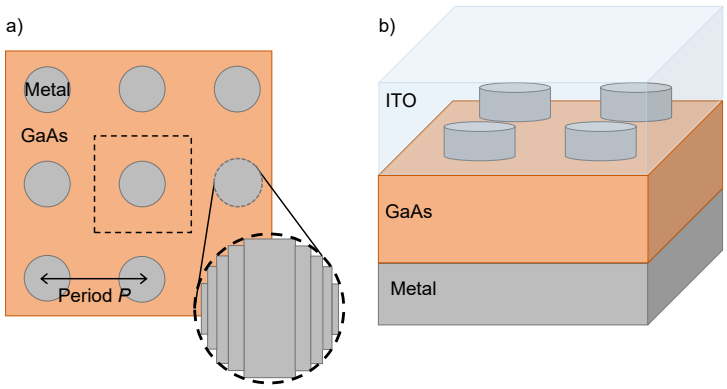


Figure 4.29: Schematic of the solar cell structure: a) Top-down view, with one unit cell outlined. The inset shows how the disks are built up in the RCWA method. b) Side view.

4.3.2 Simulated structures

To quantify the light-trapping benefit from a metallic nanostructure, we consider a considerably thinned-down single-junction GaAs cell with a thickness of 50 nm (the thickness of the active layer of a thin-film GaAs cell is normally on the order of 2 µm); this is so that the light-trapping can, in theory, have a significant benefit since the GaAs is optically thin and will suffer from high transmission loss. The GaAs is covered by 60 nm of ITO, which acts as an anti-reflection coating (ARC) and encapsulates the metal nanoparticles (NPs). The metal NPs are disk-shaped pillars, and are arranged in a square grid as shown in Fig. 4.29. The same optical constants are used for the GaAs [179] and ITO [185] throughout all simulations, while those of the metal are from the sources specified. The cell has a metal back reflector made of the same metal as the NPs, which is considered to be a semi-infinite transmission medium in the simulations. The metal coverage fraction is defined as:

$$C = \frac{\text{area covered by metal}}{\text{total area}} = \frac{\pi r^2}{P^2} \tag{4.21}$$

when the cell is viewed as in Fig. 4.29a, where r is the nanodisk radius and P is the array period. Thus the maximum coverage fraction before the disks start to overlap is $\pi/4 = 0.79$, when $r = P/2$.

4.3.3 Simulation method

In the test structure, photons can be absorbed in the ITO/NP layer, the GaAs, or the metal back mirror. The normal-incidence absorptivity $A(\lambda)$ in each case is the fraction of incident power absorbed in that layer at a given wavelength λ. The spectrally weighted absorption Abs in each layer is then given by:

$$\begin{aligned} Abs_{NP} &= \frac{\int \Phi(\lambda) A_{NP}(\lambda) d\lambda}{\int \Phi(\lambda) d\lambda} \\ Abs_{GaAs} &= \frac{\int \Phi(\lambda) A_{GaAs}(\lambda) d\lambda}{\int \Phi(\lambda) d\lambda} \\ Abs_{back} &= \frac{\int \Phi(\lambda) A_{back}(\lambda) d\lambda}{\int \Phi(\lambda) d\lambda} \end{aligned} \tag{4.22}$$

Where Φ is the spectral photon flux for a standard AM1.5G reference spectrum [15]. The total spectrally weighted absorption Abs_{total} is given by $Abs_{total} = Abs_{NP} + Abs_{GaAs} + Abs_{back}$. The photogenerated current (J_{ph}) values, used as the primary indicator of performance for the simulated structures in the subsequent sections, were calculated using:

$$J_{ph} = q \int \Phi(\lambda) A_{GaAs}(\lambda) d\lambda \tag{4.23}$$

Where q is the elementary charge. Only absorption in the GaAs leads to photocurrent; absorption in the NP layer or back reflector is parasitic. Note that the term photogenerated current (J_{ph}) is used here since transport and surface recombination are not taken into account in these simulations. If an IQE of 100% is assumed, then J_{ph} is equal to the short-circuit current J_{SC}. Simulations and J_{ph} calculations were carried out over the wavelength range 300-900 nm, since spectral photon flux in a standard AM1.5G spectrum below 300 nm and interband absorption above 900 nm in GaAs (which has a bandgap of $\approx$ 875 nm) are negligible.

To calculate the fraction of photons absorbed in each layer at each wavelength, the MATLAB-based GD-Calc (Grating Diffraction Calculator) [92], was used. This is an implementation of the RCWA method (Section 2.3.3) – note that this is a different implementation of the RCWA method than discussed in the first part of this chapter, where S^4 was used. In GD-Calc, only rectangular blocks can be used, so the nanodisks must be built up out of strips; the inset in Fig. 4.29a illustrates this using nine strips. Fig. 4.30a shows the convergence of the calculated J_{ph} with the number of Fourier orders and strips used for the circular disks for an example structure. The results in Section 4.3.5 were calculated using 441 total Fourier orders ($m_{max} = 21$) and 201 strips. Considering calculations with a larger number of Fourier orders, the maximum deviation seen from the calculated J_{ph} value using these parameters was 1%, observed for 625 Fourier orders and 51 strips, indicating that the use of 441 orders and 201 strips is sufficient. Fig. 4.30a also shows that as long as a sufficient number of Fourier orders are used, the choice of the number of strips does not significantly affect the calculated J_{ph}.

4.3.4 Optimization

A simple grid search was performed covering the full parameter space of metal coverage C and array period P using each set of optical constant values, to produce a full map of the predicted J_{ph}, such as those in Fig. 4.31. With the resolution chosen, this meant around 300 simulations had to be performed in each case, and thus a High Performance Computing cluster was used; on a normal laptop or desktop computer, each of these simulations may take hours. Single-core threads on Imperial's High-Performance Computing facility were used to run each simulation separately, since each simulation is independent and communication between the different nodes is not required. To reduce the parameter space, the height of the pillars (20 nm), ITO thickness (60 nm), and GaAs thickness (50 nm) were kept constant, while the period of the array and metal coverage (i.e. radius of the disks) were varied. Fig. 4.30b shows an example of calculated J_{ph} with varying disk height and ITO thickness for a structure using silver [119], showing that a disk height of around 20 nm and total ITO thickness (including the ITO between the metal disks) of around 60 nm are optimal. These optima will vary depending on the metal source and NP width/spacing, but were similar for several other arrangements and metals which were checked (with the exception of Ti, where generally the presence of any metal degrades the performance).

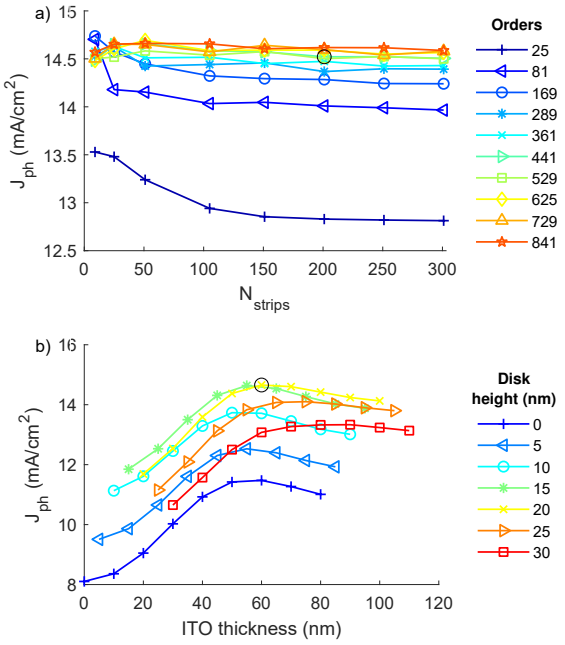


Figure 4.30: a) Calculated J_{ph} for a test structure as in Fig. 4.29 with nanodisk height 20 nm, ITO thickness 60 nm, GaAs thickness 50 nm, $P = 500$ nm and $C = 0.5$. The number of Fourier orders and strips to build up the disks (N_{strips}) is varied. The result for the number of orders and strips used to generate the results in Section 4.3.5 is circled in black. b) Calculated J_{ph} for the test structure with GaAs thickness 50 nm, $P = 500$ nm, $C = 0.5$ with different metal disk heights and ITO layer thicknesses. The result for the disk height and ITO thickness used to generate the results in Section 4.3.5 is circled. The metal optical constants used were those for silver from [119].

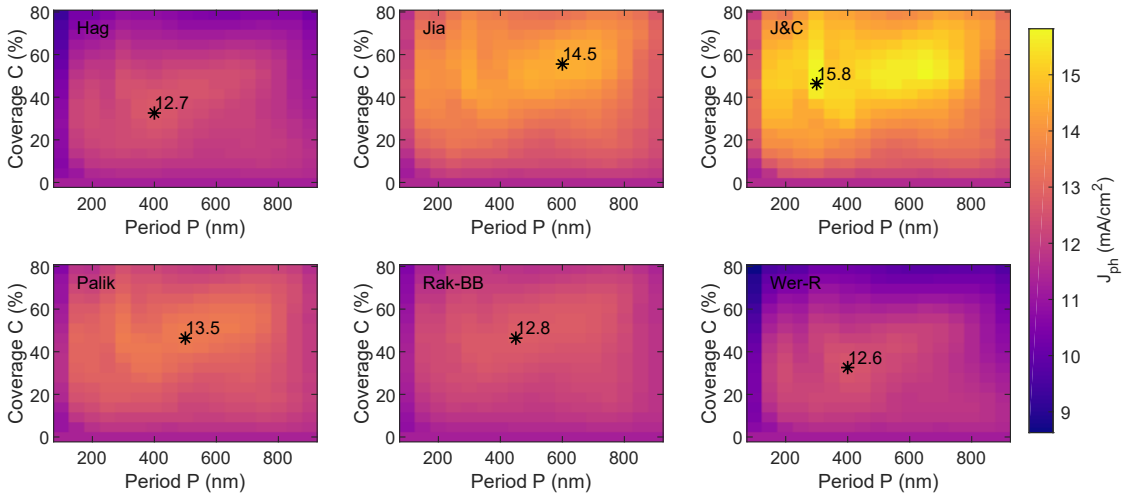


Figure 4.31: Predicted photogenerated current J_{ph} as a function of array period and metal coverage for the structure shown in Fig. 4.29 using six different sets of optical constant data for silver. The $*$ indicates the maximum J_{ph} (J_{max}), the value of which is labelled.

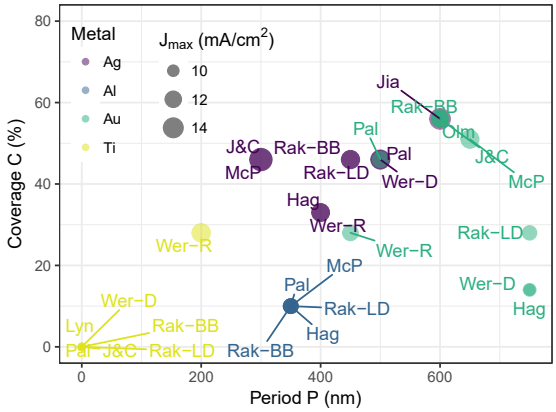


Figure 4.32: Location of the optimum configuration of nanodisks in terms of metal coverage and period for each optical constant source, corresponding to the points marked with $*$ for the illustrative plots in Fig. 4.31. The different colours indicate different metals, and the size of the point indicates the relative magnitude of each maximum photogenerated current J_{max}. The point (0, 0) (i.e. 0% metal coverage) means no nanoparticles are present, so the structure is GaAs with an ITO ARC and metal back mirror.

4.3.5 Results

Figures 4.27 and 4.28 shows the optical constants and LSPQ for the different sources, grouped by metal. With the exception of Ti, the optical constants (Fig. 4.27) for the same metal appear to follow the same trends, with apparently small deviations. However, these apparently small variations can lead to very large changes in the calculated LSPQ (Fig. 4.28). The J&C data is a clear outlier for silver, and McP gives the highest LSPQ for gold, although the other sources also vary considerably. Unlike the other metals considered, the optical constants and LSPQ for aluminium were consistent across sources up to around 900 nm. For Ti, both the complex refractive index and thus, unsurprisingly, the LSPQ vary strongly depending on source, with the Wer-R data having an LSPQ more than 25 times higher than any other source around 0.7 µm. Overall, silver and gold have higher LSPQ than aluminium and titanium.

The metal coverage and array period giving the maximum J_{ph}, J_{max}, for each source are shown in Fig. 4.32, and detailed results on the optimum for each source are given in Table 4.3. In each case, the optical constant source with the highest peak LSPQ also gives the highest optimum J_{ph}. The spread of optimal solutions predicted using different sources is evident for all metals except Al, although there are also coinciding points for Ag, Au and Ti. For Ti, six out of seven sources predict that an NP array of the type considered here does not offer any potential for J_{ph} improvement, while Wer-R predicts a 15% increase relative to the J_{ph} without NPs. To visualize the overall spread of results, Fig. 4.33 shows the results of all the simulations in terms of J_{ph} vs. metal coverage; for each source, the J_{ph} shows a clear trend, but these diverge significantly between sources for all metals except Al. Clearly, the choice of optical constant source has a significant effect when exploring possible arrangements for nanometallic structures in order to decide on an optimum for device fabrication.

Table 4.3 lists the optimal dimensions (grating period and metal disk coverage) for the nanodisk arrangement for each optical constant source. The overall optimum across all sources per metal is highlighted in bold. Table 4.4 shows the outcomes when this overall optimum arrangement is used to calculate the J_{ph} and Abs_{total} using the other optical constant sources for the same metal, reflecting a situation in which the structure is optimized using a specific set of optical constant data, which may not accurately predict

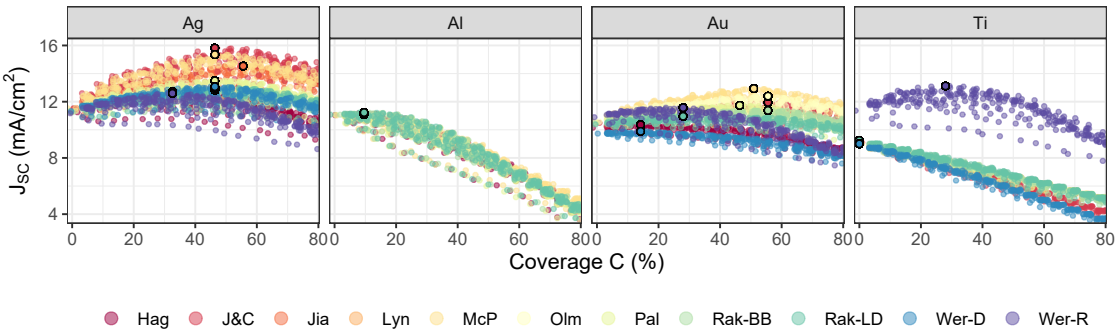


Figure 4.33: J_{ph} versus metal coverage C, showing the results of all the simulations (points are jittered slightly along the x-axis for visibility since C increases in discrete steps). Different colours represent different sources, and the point corresponding to J_{max} is outlined in black for each source (for Al, all these points coincide).

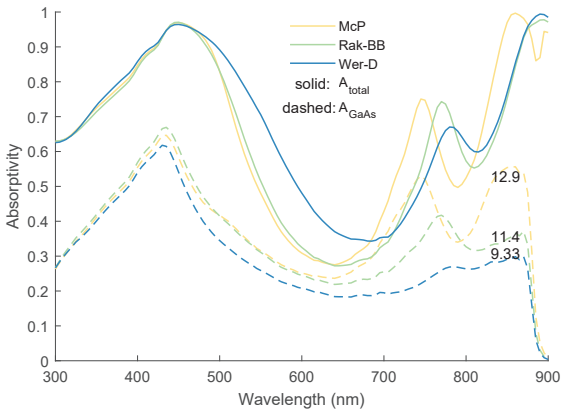


Figure 4.34: Absorptivity in the full structure (solid lines) and GaAs layer only (dashed lines) in the nanodisk structure with $C = 0.51$ and $P = 650$ nm using three different optical constant sources for Au. This is the arrangement which gives the overall maximum for gold when McP data is used. The labels indicate the predicted J_{ph} in mA/cm^2 due to absorption in the GaAs layer for each source.

Table 4.3: Detailed simulation results showing the J_{ph} without nanoparticles (J_0) and the optimal arrangement in terms of period P and metal coverage C leading to maximum photogenerated current J_{max}. The source giving the highest J_{max} is in bold for each metal. Also shown are the spectrally weighted absorption percentage *Abs* over the range 300-900 nm as defined in eq. 4.22 for the whole structure (total), GaAs layer, ITO + nanoparticle layer (NP) and the back reflector. The spectral absorption enhancement factor (SAEF) calculated for each source according to eq. 4.24 is shown in the final column.

Name	$\mathbf{J_0}$	$\mathbf{P_{opt}/C_{opt}}$	$\mathbf{J_{max}}$	**Spectral *Abs* (%)**				**SAEF**
				Total	**GaAs**	**NP**	**Back**	
Silver (Ag)								
Hag	11.3	400/0.33	12.7	58	41	9	7	208.09
Jia	11.5	600/0.56	14.5	57	45	9	3	802.81
J&C	**11.5**	**300/0.46**	**15.8**	**58**	**48**	**8**	**1**	**1144.1**
McP	11.6	300/0.46	15.4	58	47	9	2	1075.1
Pal	11.3	500/0.46	13.5	57	42	10	5	355.03
Rak-BB	11.3	450/0.46	12.8	57	41	10	5	303.35
Rak-LD	11.3	450/0.46	13.0	57	41	10	5	316.33
Wer-D	11.3	500/0.46	13.1	59	41	11	6	269.54
Wer-R	11.2	400/0.33	12.6	60	40	10	8	162.58
Aluminium (Al)								
Hag	11.0	350/0.10	11.2	62	38	6	18	111.42
McP	11.0	350/0.10	11.1	61	38	5	17	128.45
Pal	11.1	350/0.10	11.2	62	38	5	18	113.79
Rak-BB	11.1	350/0.10	11.2	62	38	5	18	118.26
Rak-LD	**11.1**	**350/0.10**	**11.2**	**62**	**38**	**5**	**18**	**118.97**
Gold (Au)								
Hag	10.1	750/0.14	10.4	56	35	5	16	61.913
J&C	10.5	600/0.56	12.0	63	37	16	10	178.1
McP	**10.6**	**650/0.51**	**12.9**	**63**	**39**	**14**	**9**	**249.49**
Olm	10.6	600/0.56	12.4	63	38	16	9	197.27
Pal	10.5	500/0.46	11.7	61	37	14	10	155.31
Rak-BB	10.4	600/0.56	11.4	62	35	16	11	143.73
Rak-LD	10.4	750/0.28	11.0	56	36	8	12	99.487
Wer-D	9.7	750/0.14	9.9	59	33	5	20	46.582
Wer-R	10.9	450/0.28	11.6	61	38	11	12	95.252
Titanium (Ti)								
J&C	9.1	0/0	9.1	73	32	1	39	11.176
Lyn	9.0	0/0	9.0	72	32	1	39	10.261
Pal	9.0	0/0	9.0	72	32	1	39	10.231
Rak-BB	9.2	0/0	9.2	69	33	1	36	29.741
Rak-LD	9.2	0/0	9.2	69	33	1	36	21.907
Wer-D	9.0	0/0	9.0	77	32	1	44	5.9927
Wer-R	**11.4**	**200/0.28**	**13.1**	**64**	**41**	**13**	**7**	**199.33**

Table 4.4: Best and worst outcomes, and the mean, using the nanodisk arrangements highlighted in Table 4.3 (i.e. those which give the highest overall J_{ph} in mA/cm^2 per metal out of all sources considered). Al is not included as there is no significant difference between sources.

Arrangement		**Best**			**Worst**		**Mean**
Ag	$P = 300$	J_{SC}	J&C	15.8	Wer-R	12.1	13.6
	$C = 0.46$	Abs_{total}		57.7		62.8	59.4
Au	$P = 650$	J_{SC}	McP	12.9	Wer-D	9.33	11.2
	$C = 0.51$	Abs_{total}		62.8		66.7	63.0
Ti	$P = 200$	J_{SC}	Wer-R	13.1	Wer-D	7.12	8.33
	$C = 0.28$	Abs_{total}		63.6		75.2	71.1

behaviour in a manufactured optical structure or device. For Ag, Au and Ti, the percentage reductions between the best J_{ph} and the mean are 14%, 15% and 36%, respectively, indicating that unless the actual optical constants of materials used in a device match those used in simulations very closely, the solar cell performance may be significantly different from simulated predictions.

Tables 4.3 and 4.4 also compare the calculated J_{ph} with the total spectrally weighted absorption in the structure, Abs_{total}. Only absorption in the GaAs produces photocurrent, whereas Abs_{total} considers all absorption in the structure, including in the ITO/NP layer and back reflector. Table 4.4 shows that while the J_{ph} predicted for identical NP arrangements using different optical constant sources varies considerably, the total spectral absorption Abs_{total} over the range 300-900 nm does not necessarily vary similarly. In fact, for the cases shown in Table 4.4, Abs_{total} actually *increases* slightly between the best and worst-case sources for J_{ph}, due to increased parasitic absorption in the metal layers. The similarity of the absorptivity spectrum is shown for three different Au sources in Fig. 4.34, for the NP arrangement which gives the overall maximum for gold when McP data is used. Although the proportion of photons absorbed in the GaAs layer varies, the overall absorption spectrum shows similar peaks for McP, Rak-BB and Wer-D data. The variation in the spectrally weighted absorption Abs_{total} is also much smaller than corresponding changes in J_{ph}; this has important implications when comparing simulation results to e.g. total absorption measurements of optical precursor structures [96, 111]. While the total absorption of a structure may match well with simulations, the absorption per layer and therefore J_{ph} may differ greatly between simulation and experiment depending on the optical constants used in the simulation.

4.3.6 Case study of impact on solar-cell modelling

As discussed in the introduction, many recently published simulation results continue to use silver data from J&C, which gives low parasitic absorption. An example is the multiresonant metallic nanogrid structure reported by Massiot et al. in [111]. This paper predicts a J_{ph} of 21.6 mA/cm^2 for an ultra-thin GaAs layer of 25 nm, using a biperiodic nanogrid of thickness 20 nm and period 500 nm (full details of the structure can be found in [111]). Fig. 4.35 shows calculated total absorption and absorption in the GaAs as reported in [111], and calculated using our RCWA implementation for three different optical constant sources. When using J&C data, the results both in terms of absorption profile and predicted J_{ph} (21 mA/cm^2) are very similar. However, using other sources significantly reduces the predicted J_{ph}. Jiang et al. [119] (labelled 'Jia' here) measured the optical constants of silver specifically to address the issue with the J&C data and provide new, realistic optical constants for evaporated silver; using these optical constants gives a J_{ph} 11% lower than that predicted in [111]. Other sources give even worse outcomes, with Hagemann data giving a predicted J_{ph} of only 14 mA/cm^2. All the data sources give similar resonant peaks to the J&C data in the total absorption spectrum, while the fraction absorbed in GaAs varies significantly. It should be noted that even the worst-case result shows impressive broadband absorption and a significantly enhanced J_{ph} compared to that of a similar structure without a metallic grating, which is around 10.5-11 mA/cm^2, depending on which optical constant data is used for the silver back reflector.

4.3.7 Origin of divergence

While the focus in this section is on investigating and quantifying the size of discrepancies between structures modelled using different optical constants, it is interesting to consider why the LSPQ, optimal arrangement of nanodisks, and predicted J_{ph} diverge, and how this is likely to impact the design of optical structures. In

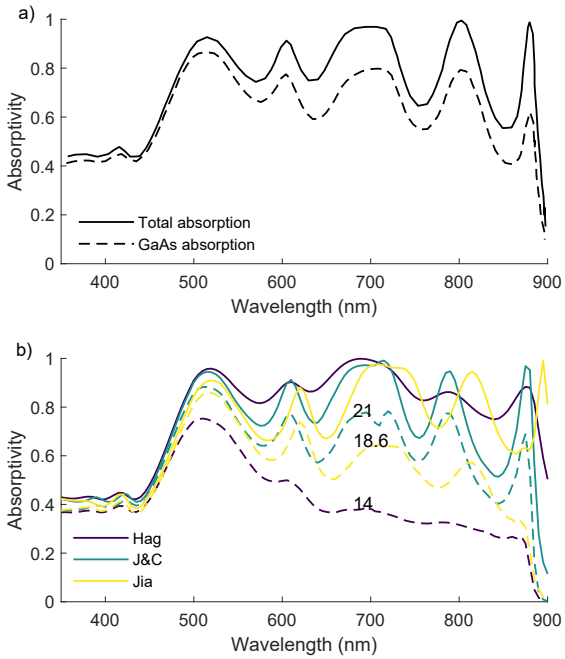


Figure 4.35: a) Calculated absorption in the total metal nanogrid + GaAs structure and in the GaAs layer only, as reported in [111]. b) Absorption for the same structure recalculated using our RCWA implementation for four different optical constant sources. The solid lines show total absorption while the dashed lines show absorption in the GaAs layer only. The labels indicate the predicted J_{ph} in mA/cm^2 due to absorption in the GaAs layer for each source.

the case of Ti, the LSPQ for six out of seven sources considered is < 4 over the full wavelength range 300-900 nm, indicating that it is unlikely to perform well in the test structures, which is also the result obtained in the simulations for these six sources: the best option is not using any Ti NPs. Only one source is a significant outlier, giving much higher LSPQ, and this would be an unlikely choice for use in a simulation as it is a new result measured in an unusual way (reflection electron energy loss spectroscopy). However, even for the six sources which show Ti to be a poor material for these applications, the actual optical constants vary significantly, indicating that it is difficult to measure them accurately. The most obvious explanation for this is the presence of a (complex) surface layer, such as a surface oxide or nitride, which is not accounted for accurately when interpreting experimental data of a surface-sensitive measurement such as ellipsometry or reflectance. However, this does not explain why the data for Al is consistent when it is well-known that Al in air will form a stable aluminium oxide layer; the oxidisation behaviour of Ti is more complex, with oxygen penetrating into grain boundaries and forming TiO_2 internally rather than simply forming a self-limiting surface oxide layer as is the case for Al. The amount of oxygen incorporated into Ti during the growth depends on factors including the deposition rate and the residual gases in the deposition chamber.

It appears that the J&C optical constants were impacted by silver tarnishing, as reported by Jiang et al. [119]. Jiang et al. were able to replicate the J&C results when performing measurements on unprotected silver, which showed clear surface layer effects. As discussed in the introduction, the method and exact experimental parameters under which a metal is grown can affect its optical constants [172], meaning not all the divergence between sources is due to surface layers or experimental error, but rather due to inherent variation of behaviour for metals deposited under non-indentical circumstances.

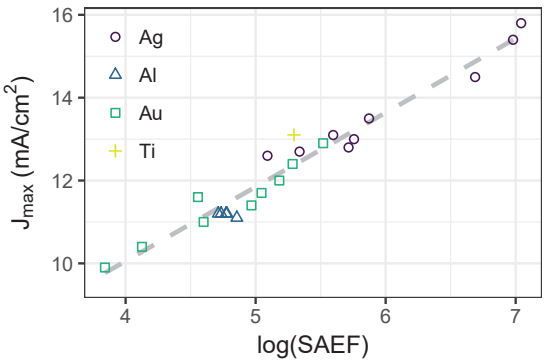


Figure 4.36: Maximum photogenerated current J_{max} obtained by optimizing the test structure for each set of optical constant data (as in Table 4.3), plotted against the logarithm of the spectral absorption enhancement factor (SAEF), with the straight line of best fit. Only structures which actually include metal NPs are plotted, so six out of seven Ti structures are excluded as the J_{ph} was obtained by not including any metal.

4.3.8 Defining the Spectral Absorption Enhancement Factor of metals

In order to compare the maximum J_{ph} obtained for each optical constant source, J_{max}, with a single figure of merit, we define the spectral absorption enhancement factor (SAEF):

$$\begin{aligned} \text{SAEF} &= \int_{300\text{ nm}}^{\lambda_g} \text{LSPQ}(\lambda)\Phi(\lambda)d\lambda \\ &= \int_{300\text{ nm}}^{\lambda_g} \frac{-\epsilon_1(\lambda)}{\epsilon_2(\lambda)}\Phi(\lambda)d\lambda \end{aligned} \tag{4.24}$$

where λ_g is the wavelength corresponding to the bandgap of the absorbing semiconductor (set to 875 nm here for GaAs). By defining a new figure of merit in this way, the LSPQ at each wavelength is weighted by the solar photon flux at that point, i.e. the relative usefulness of increasing absorption at that specific wavelength. Fig. 4.36 shows the maximum photogenerated current J_{max} for optimized structures, as in Table 4.3, against the logarithm of the SAEF calculated from the data shown in Fig. 4.28. There is a clear linear trend, showing that the SAEF is a useful quantity for comparing the expected absorption enhancement performance of a metal with a given set of optical constants without having to perform a large number of simulations to test different structures. It should be noted that the SAEF as defined here depends not only on the metal, but also the absorbing semiconductor; the upper limit of integration is determined by the bandgap of the absorbing material, as there is no utility in improving absorption at lower photon energies. The SAEF can be calculated straightforwardly from the optical constants of a metal and thus provides a much simpler method for predicting which materials will give the highest photocurrent enhancement, while finding J_{max} requires optimization using computationally intensive simulations.

When designing a solar cell structure, the SAEF could act as a useful guide in exploring different potential metals or optimizing deposition conditions for a given metal, since it can be calculated directly from optical constants measured through e.g. variable-angle spectroscopic ellipsometry (VASE). Measuring the optical constants and thus calculating the SAEF for metal films grown under different deposition conditions would allow optimization of the process, or at least the selection of the best available process and/or metal. The

metal with optical constants giving the highest SAEF can then be used as input for simulations to find the optimal NP dimensions and arrangement.

Further simulations are necessary to confirm whether the J_{ph} vs. SAEF trend holds for other NP arrangements and shapes, for different absorbers, or for metallic structures on the rear of the cell.

Chapter 5

Characterization of silicon-germanium-tin alloys

This chapter will detail the results of the structural and spectroscopic characterization of a range of SiGeSn samples, starting with composition, X-ray diffraction and surface microscopy measurements. The spectroscopic ellipsometry, photoreflectance, and absorption measurements which allow the direct transition energies to be measured are discussed, followed by photoluminescence measurements of the fundamental indirect bandgap. Finally, optimized multi-junction device designs based on the spectroscopic data, optimized using Solcore, are presented. The structural measurements discussed in the first section of this chapter were carried out by collaborators at the National University of Singapore, primarily by Dr. Sheau Wei Ong working in Prof. Eng Soon Tok's research group. The measurements discussed in the remainder of the chapter (photoluminescence, ellipsometry, FTIR measurements, photoreflectance) and the device simulations are my own work, with help from Dr. Michael Nielsen at UNSW Sydney for the photoreflectance measurements.

5.1 Structural measurements

The composition and lattice constants of the SiGeSn samples were characterized using SEM-EDX and XRD (rocking curve and reciprocal space mapping) measurements. Table 5.1 summarizes the sample structures, SiGeSn thickness from fits to ellipsometry data, the composition obtained through EDX measurements, and the predicted lattice constant through Vegard's law. Fig 5.1a shows the Si and Sn fractions of each sample; all samples lie somewhere between a 4.6:1 and 3.2:1 Si:Sn ratio, with the Set B samples having a lower ratio than the Set A samples. As shown in Fig. 5.1b, the Set B samples are more closely lattice-matched to Ge, while the Set A samples are more closely lattice-matched to GaAs. The line of best fit through all the sample compositions is a 4.2:1 Si:Sn ratio (the ratio which provides an exact lattice match to Ge according to Vegard's law is 3.7:1, as discussed in Section 1.4.2). Fig. 5.1b shows the maximum sample thickness (around 2 µm) compared to the critical thickness for epitaxial growth calculated through two different models, the well-known Matthews-Blakeslee formula [186], and the People & Bean model [187], the latter of which was developed to better describe the critical thickness of SiGe grown on Si. The Matthews-Blakeslee model considers the mechanical equilibrium of threading dislocations grown with the epitaxial layer to determine the onset of interfacial misfit dislocations. The People & Bean model differs from the Matthews-Blakeslee model in assuming that the critical layer thickness is determined solely by

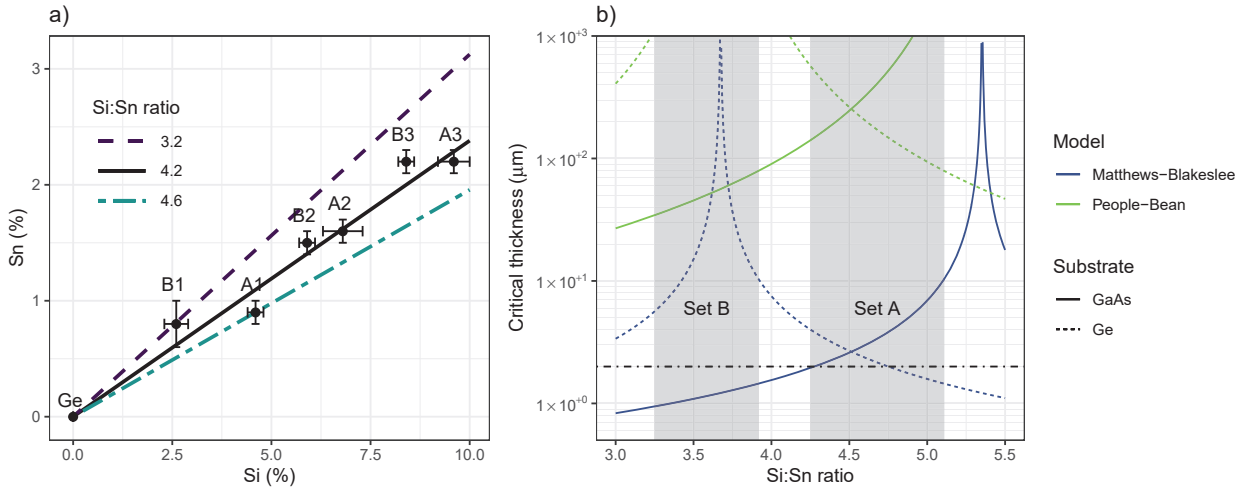


Figure 5.1: a) The Si:Sn ratio for each of the samples with composition measured through SEM-EDX. For Set B, only the thicker samples were measured. The error bars show the standard deviation from ten measurements of the same sample. b) Shows estimates of the critical thickness for epitaxial growth of SiGeSn on both Ge and GaAs substrates according to two different models (Matthews & Blakeslee [186] and People Bean [187]). The dash-dot horizontal line shows the approximate maximum thickness of the samples (2 µm) and the shaded areas show the range of measured Si:Sn ratios in the Set A (on GaAs) and Set B (on Ge) samples.

energy balance, occurring when the strain energy density is equal to the energy density associated with the dislocation-generating mechanism of minimum energy; the growing film is assumed to be initially free of threading dislocations. XRD measurements of GeSn grown on Ge substrates have shown that the People & Bean model also describes their critical thickness more accurately, predicting a higher value than Matthews-Blakeslee [188], although the exact thickness at which dislocations initially occur may be hard to determine through XRD measurements alone.

The Set B samples are grown on a Ge substrate with an $In_{0.012}Ga_{0.988}As$ buffer layer at the same lattice constant as Ge, while the Set A samples are grown on a GaAs substrate with a $\approx$ 60 nm buffer layer of Ge. The critical thickness calculated for Ge grown on GaAs is $\sim$ 1 µm according to the Matthews-Blakeslee formula, so it was assumed that the Ge buffer will be strained at the GaAs lattice constant. Thus, it is expected that the Set A samples will be strained to the GaAs lattice constant while the Set B samples will be strained to the Ge lattice constant. The Set B samples have a SiGeSn thickness lower than the critical thickness on Ge calculated through either of the critical thickness models, over the range of compositions observed for the Set B samples. The Set A samples have a critical thickness just below the Matthews-Blakeslee critical thickness on a GaAs substrate, and well below the People & Bean critical thickness. This indicates that even using the more conservative Matthews-Blakeslee estimate for the critical thickness, the SiGeSn layers for both sample sets should be strained to the substrate lattice constant, rather than relaxed.

Rocking curves and reciprocal space maps (RSMs) were measured around the (004) and (224) lattice points. Fig. 5.2a and b shows the RSM scans for sample A1; RSM data for all the Set A samples around both points is shown in Appendix G.1. Only the out-of-plane lattice constant can be observed in the (004) data, while the asymmetric (224) scan will contain contributions from both the in-plane and out-of-plane lattice constants. For samples A1 and A3, some spread around a single RSM peak is observed in both the (004) and (224) RSMs, but only a single clearly-defined peak is visible, indicating that the epi-layer is

Table 5.1: Sample structures, SiGeSn thickness (from SE fitting) d_{SiGeSn}, and composition of the SiGeSn measured through SEM-EDX for the SiGeSn samples. The composition values are the mean across ten measurements of each sample (the values in brackets are the standard deviation). The relaxed SiGeSn lattice constant a_{SiGeSn} is calculated according to Vegard's law (eq. 1.1) based on the compositions (the uncertainty is due to the error carried forwards from the composition measurements).

Sample	$\mathbf{d_{SiGeSn}}$ **(nm)**	**Structure**	**Composition**	$\mathbf{a_{SiGeSn}}$ **(Å)**
A1	1811	SiGeSn/Ge seed/GaAs subs.	4.6 (0.2) % Si, 0.9 (0.1) % Sn	5.65(4)
A2	1746	SiGeSn/Ge seed/GaAs subs.	6.8 (0.4) % Si, 1.6 (0.1) % Sn	5.65(5)
A3	1828	SiGeSn/Ge seed/GaAs subs.	9.6 (0.4) % Si, 2.2 (0.1) % Sn	5.65(4)
B1 (thin)	332	SiGeSn/InGaAs buffer/Ge subs.		5.65(8)
B2 (thin)	362	SiGeSn/InGaAs buffer/Ge subs.		5.65(7)
B3 (thin)	353	SiGeSn/InGaAs buffer/Ge subs.		5.65(7)
B1 (thick)	2073	SiGeSn/InGaAs buffer/Ge subs.	2.6 (0.3) % Si, 0.8 (0.2) % Sn	5.65(8)
B2 (thick)	2017	SiGeSn/InGaAs buffer/Ge subs.	5.9 (0.2) %Si, 1.5 (0.1) %Sn	5.65(7)
B3 (thick)	2036	SiGeSn/InGaAs buffer/Ge subs.	8.4 (0.2) %Si, 2.5 (0.1) %Sn	5.65(7)

very closely lattice-matched to the substrate. The peak broadening in reciprocal space at constant Q_x also indicates pseudomorphic (constant lattice constant) growth, with the in-plane lattice parameter strained to the substrate (GaAs) lattice constant. For sample A2, a clear split in the peak in the (004) RSM is observed, indicating that the epi-layer has a different out-of-plane lattice constant than the substrate, suggesting biaxial strain: the films have not relaxed. The XRD peaks correspond to lattice constants of 5.6537 Å and 5.6567 Å, with the former value being the GaAs lattice constant. This indicates that the relaxed lattice constant of sample A2 is larger than that of GaAs, causing in-plane compressive strain in the SiGeSn and expansion of the out-of-plane lattice constant. Assuming the in-plane lattice constant is pinned to that of GaAs, as indicated by the RSM in the (224) direction, and taking the Poisson ratio[1] of the SiGeSn to be 0.3 (a typical value used for Ge [187]), the relaxed lattice constant is calculated to be 5.6553 Å, in excellent agreement with the value of 5.655 Å calculated through Vegard's law using the composition measurements from SEM-EDX (see Table 5.1). Sample A2 was the Set A sample with the largest predicted deviation from the GaAs lattice constant through Vegard's law, and the only sample for which a clear second peak in the RSM can be observed. This indicates that the samples are closely lattice-matched to the substrates, with some strain.

The samples were also imaged using SEM and Nomarski microscopy. This shows the presence of defects, but no cross-hatching or features which indicate relaxation of the epitaxial layer. For Set B, only the thicker samples ($\approx$ 2000 nm) were measured in these structural measurements, and it was assumed that the corresponding thinner ($\approx$ 400 nm) SiGeSn layers have very similar compositions; this is corroborated by their extremely similar E_0 values from fits to the PR data (Section 5.2). The surfaces of both sets of samples show 'bubble' and 'pyramid'- like defects, as shown in Fig. 5.2c and d. Given the known difficulties of SiGeSn growth, especially regarding Sn incorporation, it is reasonable to assume these defects may be related to segregation of Sn during growth; however, additional EDX measurements comparing flat areas of the surface with the defect features do not indicate a measurably different composition within either of these feature types. The pyramid-type defects penetrate into the bulk of the material significantly, and appear to be the results of growth along a different crystal axis to the bulk film. The density of defects varies per sample (optical microscopy of all the samples is shown in Appendix G.1).

[1]The Poisson ratio describes the out-of-plane distortion for in-plane strain.

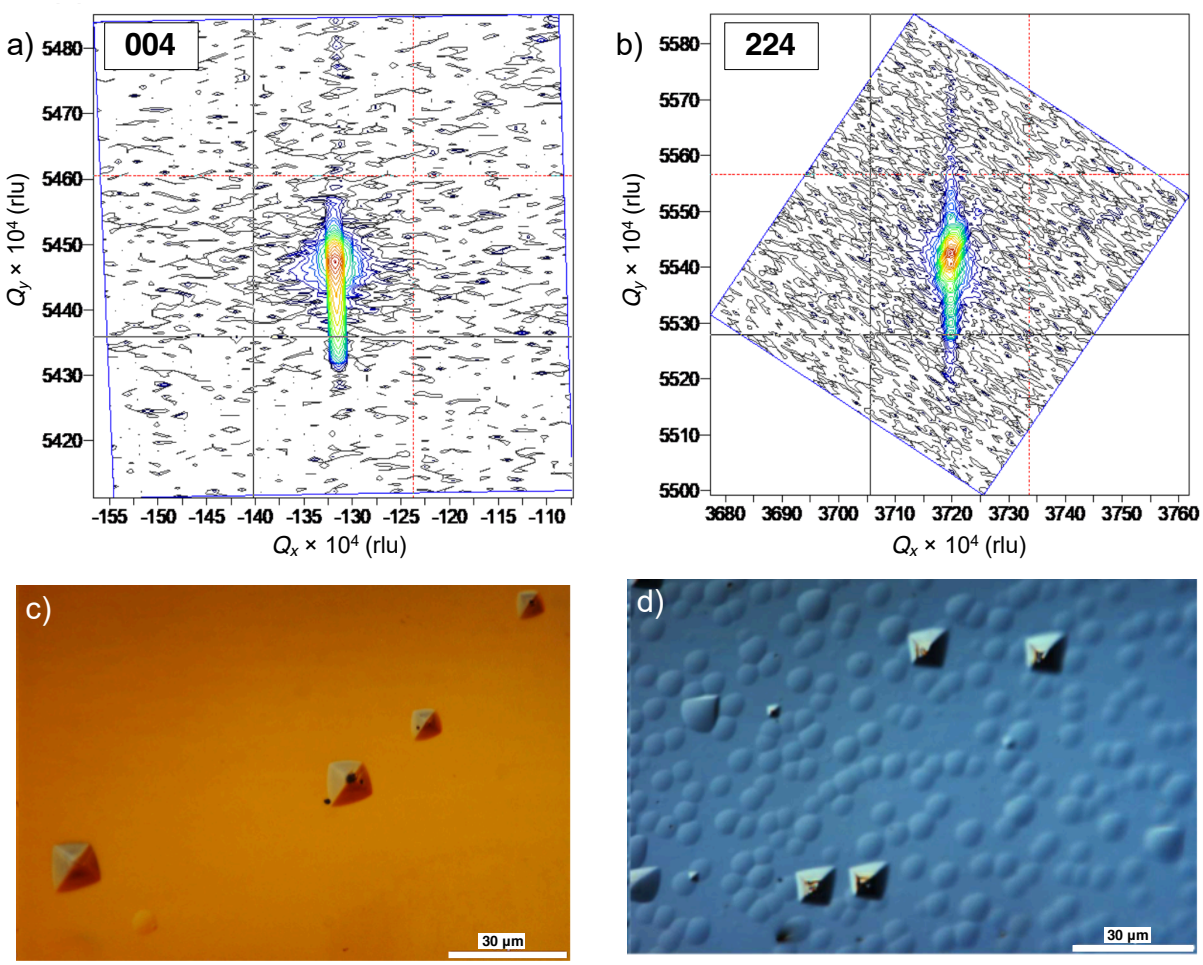


Figure 5.2: XRD reciprocal space maps and optical microscopy (OM) with polarizer and Nomarski prism. a) RSM measured around the (004) direction for sample A1. b) RSM measured around the (224) direction for sample A1. c) OM of the surface of sample A2 at 100× magnification. d) OM of the surface of sample A1 at 100× magnification.

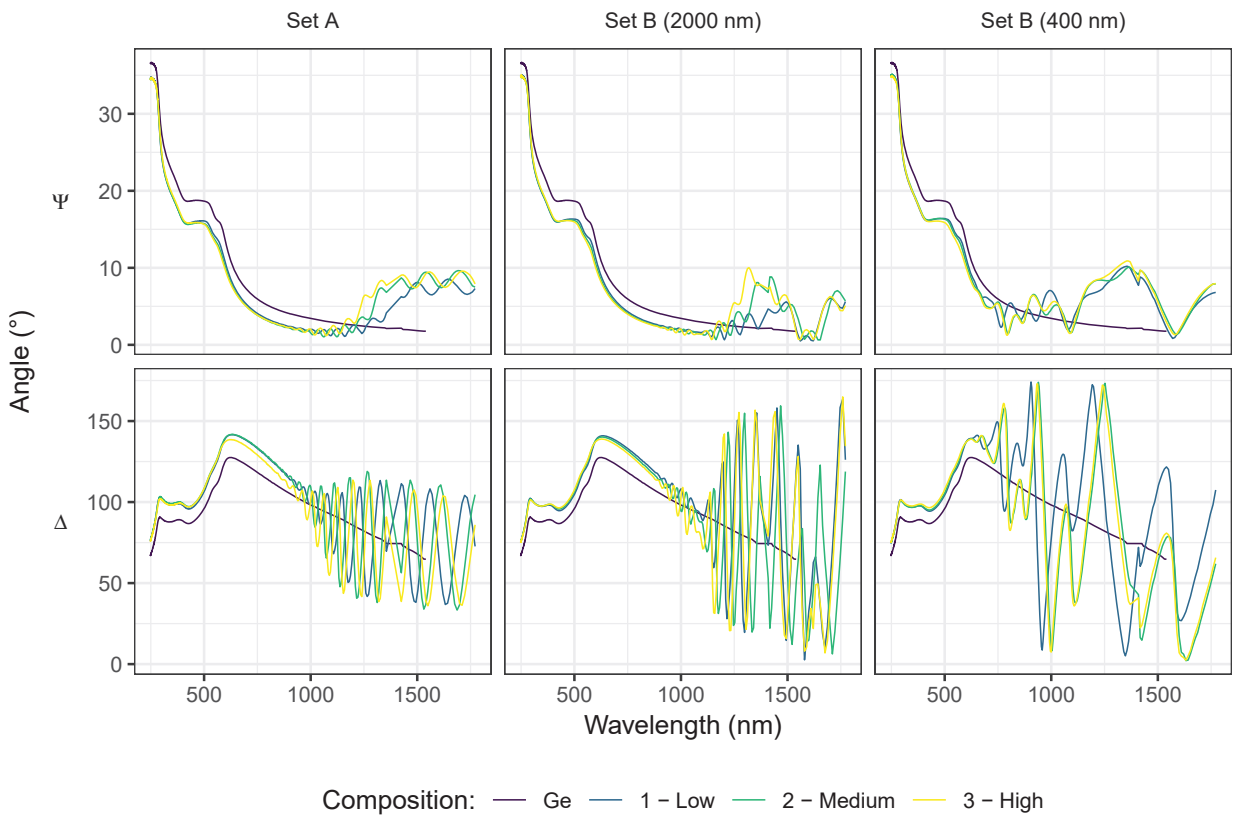


Figure 5.3: Ellipsometric angles Ψ and Δ for sample sets A and B, measured with incidence angle 77°. Data measured for a Ge substrate is shown for reference in each plot.

5.2 Investigation of the direct transitions

5.2.1 Spectroscopic ellipsometry results

Fig. 5.3 shows the ellipsometric data for a Ge substrate and samples from sets A and B. The pseudo-dielectric constants $\langle\tilde{\varepsilon}\rangle = \langle\varepsilon_1\rangle + i\langle\varepsilon_2\rangle$ are shown in Fig. 5.4. Both sets of samples show clear Fabry-Perot (thin-film) interference fringes in the SE data due to reflection at the SiGeSn/Ge seed layer/GaAs substrate interfaces (for Set A) or the SiGeSn/InGaAs buffer layer/Ge interfaces (for Set B). While the E_1 and $E_1 + \Delta_1$ features around 2 eV and higher-energy transitions are clearly visible, and show a blueshift with increasing Si/Sn content, the expected lower-energy features due to E_0 and $E_0 + \Delta_0$ are obscured by these interference fringes. The E_0 transition in Ge is important as it determines the direct absorption edge, but is relatively weak due to the small density of states as a result of the low effective mass in the Γ_7 CB involved in the E_0 and $E_0 + \Delta_0$ transitions [58]. In order to extract relevant transition energies from the data, a model taking into account the layer structure of the samples must be fitted to obtain the dielectric constants of just the SiGeSn layer using the method described in Section 3.2.2. Note that data for the Ge substrate sample is only shown up to 1550 nm (0.8 eV, the energy of the lowest-energy direct transition in Ge); beyond this wavelength, the signal is severely affected by depolarization (as discussed in Section 3.2) and is unreliable. The samples in Set A were similarly affected by depolarization at energies below the absorption edge of the SiGeSn, while the Set B samples did not show any significant depolarization effects.

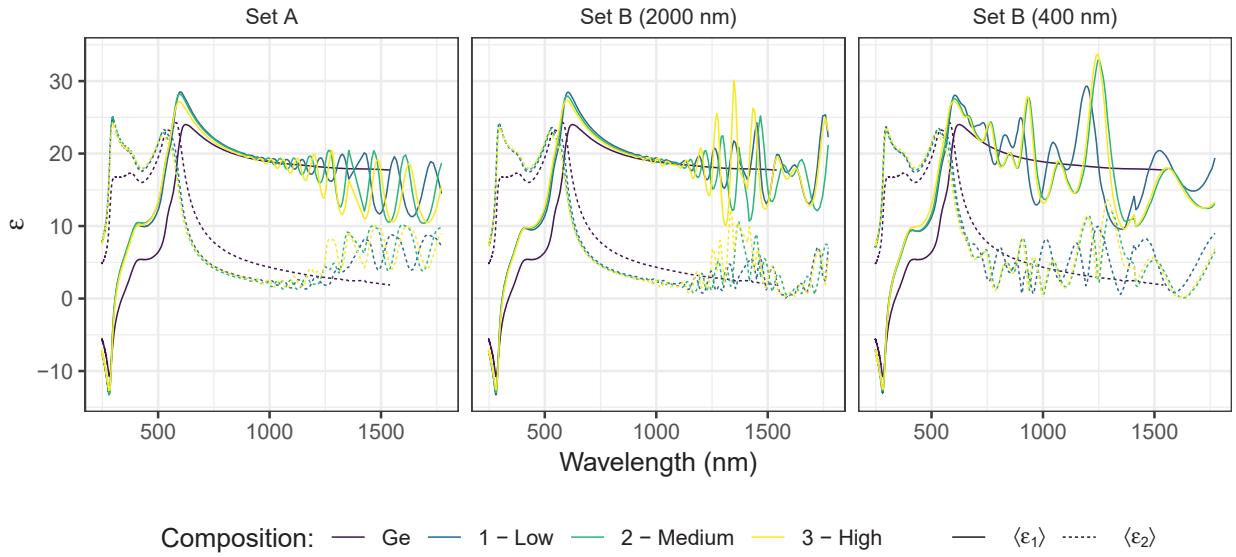


Figure 5.4: Real ($\langle\varepsilon_1\rangle$) and imaginary ($\langle\varepsilon_2\rangle$) parts of the pseudo-dielectric functions for samples sets A and B, calculated from the data in Fig. 5.3. Data from a Ge substrate is shown for reference in each plot.

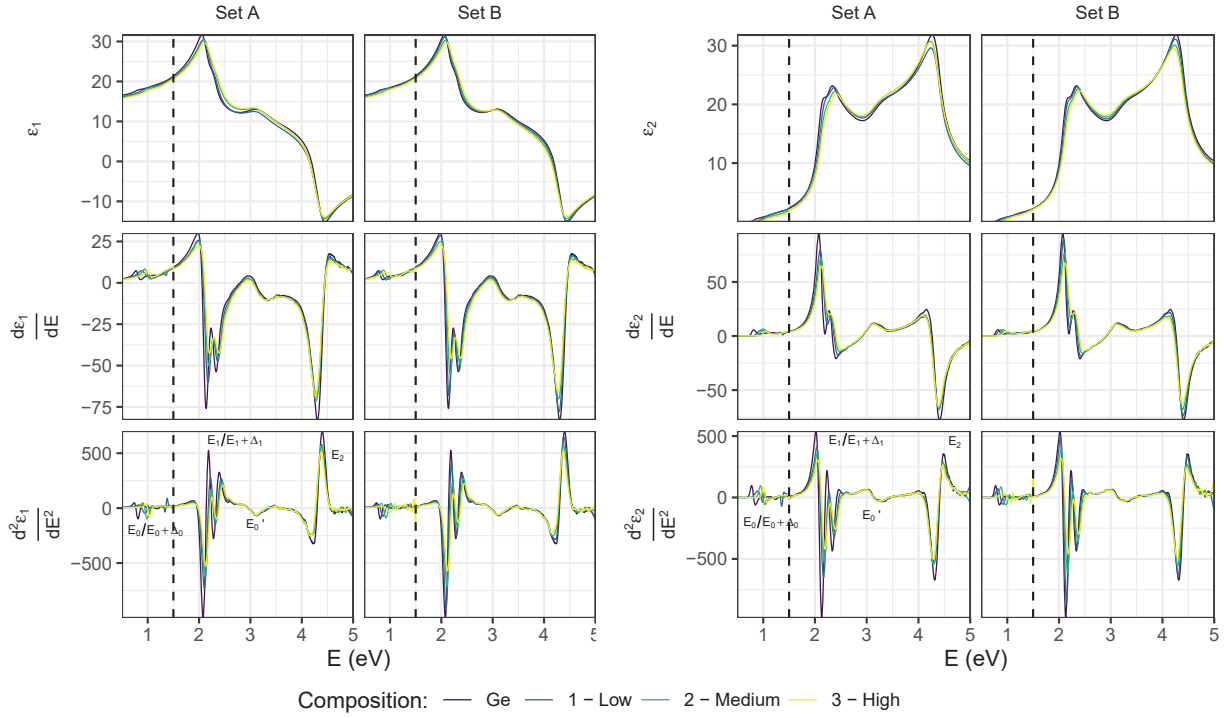


Figure 5.5: Real (ε_1) and imaginary (ε_2) parts of the dielectric functions from fits to the data in Fig. 5.3 for the different sample sets, and their first and second derivatives with respect to energy. Data for a Ge substrate is shown for reference in each plot. Data below 1.5 eV is from the parametric model fit, while data above 1.5 eV is from a point-by-point fit to the data; the dashed line in each plot indicates where the data is stitched together.

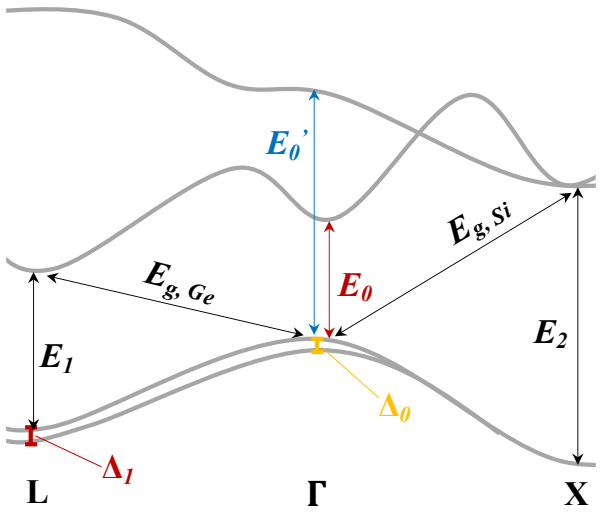


Figure 5.6: Simplified band structure of SiGeSn showing key indirect and direct transition energies in the band structure.

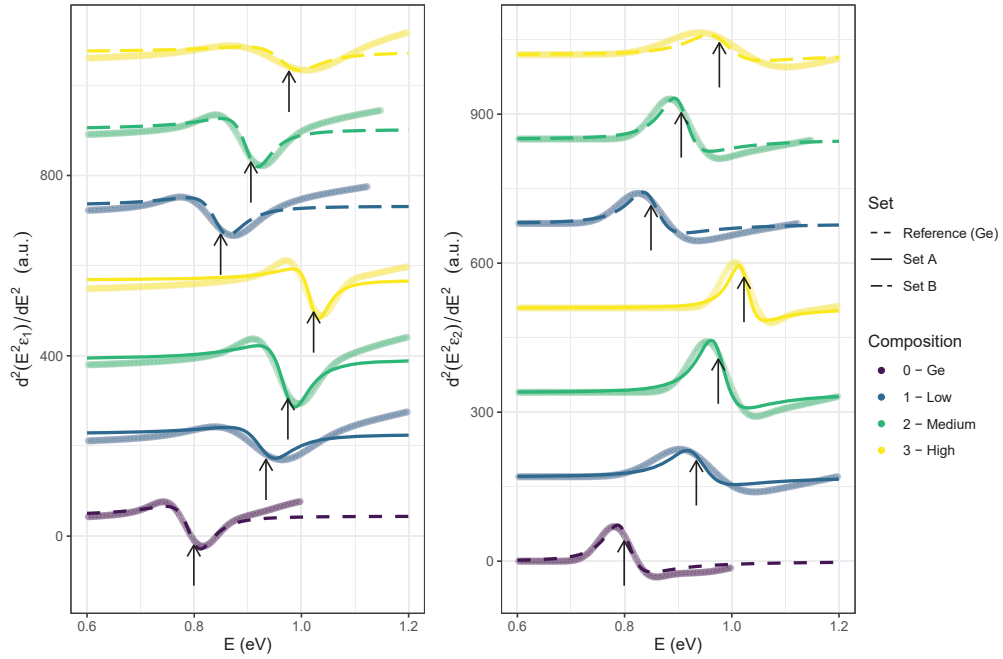


Figure 5.7: Fits of eq. 3.4 to the second derivative times E^2 of the real and imaginary parts of the dielectric function ($d(E^2\epsilon)/dE^2$) of a Ge reference sample and the SiGeSn samples around the E_0 critical point energy. The real and imaginary parts are fitted simultaneously to minimize the overall mean square error. The arrows indicate the fitted value of E_0.

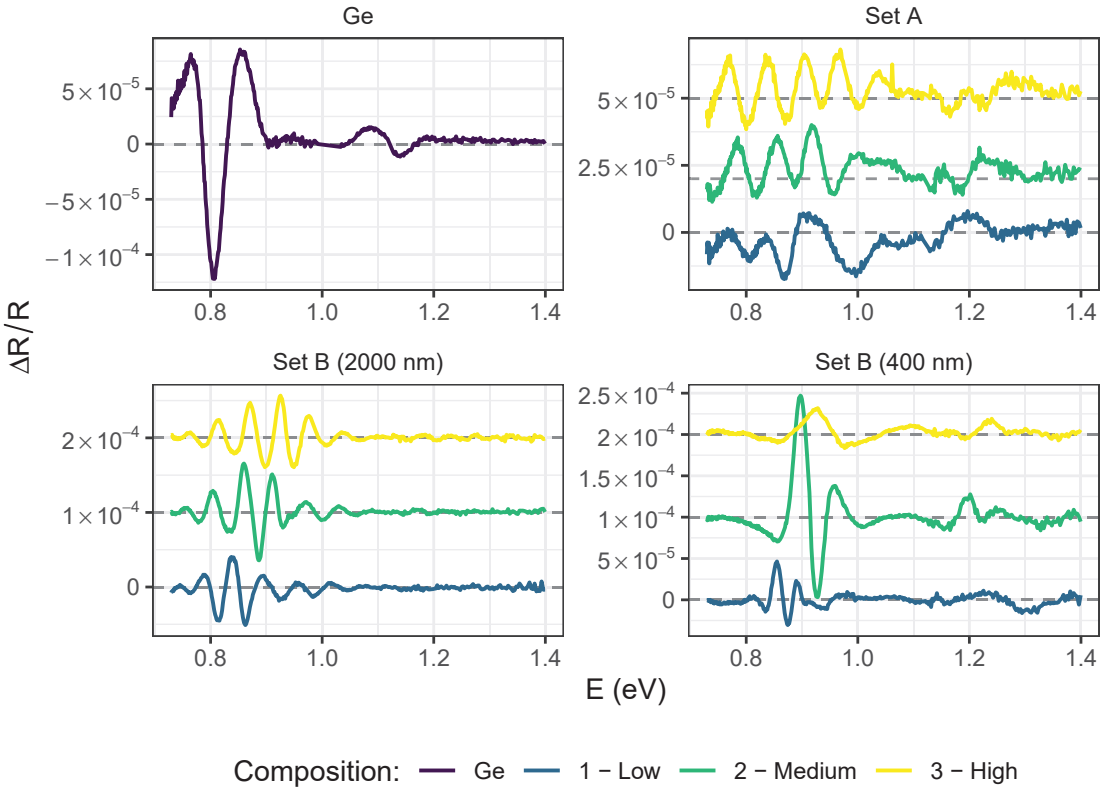


Figure 5.8: Photoreflectance measurements $\Delta R/R$ of a Ge substrate and the SiGeSn samples around the E_0 and $E_0 + \Delta_0$ energies. Data for the medium and high composition SiGeSn measurements is offset in the y-direction, with the offset relative to $y = 0$ indicated by the dashed lines.

Fig. 5.5 shows the real and imaginary part of the dielectric function fitted to the SiGeSn layer using the SE data, and their first and second derivatives. As discussed in Section 3.2.3, the exact location of the transition energies can be extracted from these derivatives (or more exactly in this case, the second derivative of the dielectric function multiplied by E^2, as discussed in Section 2.2.2); these sharp features are clearly visible in Fig. 5.5. As a reference for the meaning of the different transition energy labels used throughout this chapter, a simplified diagram of the Ge-like band structure used to describe these SiGeSn samples is shown in Fig. 5.6.

Fig. 5.7 shows the critical point fits according to eq. 3.4 for the E_0 features obtained from fitting optical constants to the SiGeSn samples. The phase was fixed to be the same for each composition, determined by the phase which gives the best fit overall ($-\pi/2$). For E_0, the parametric model fits were differentiated twice, while to fit the higher-energy critical points the point-by-point dielectric constant fit was used, as discussed in Section 3.2.2. The results for the critical point fits are summarized in Table 5.2 and shown in Fig. 5.12. Appendix F shows the results of the higher-energy critical point fits, and reports the other parameters fitted (strength, broadening and phase). These results are discussed further, in conjunction with the PR and PL fit results, in Section 5.4.

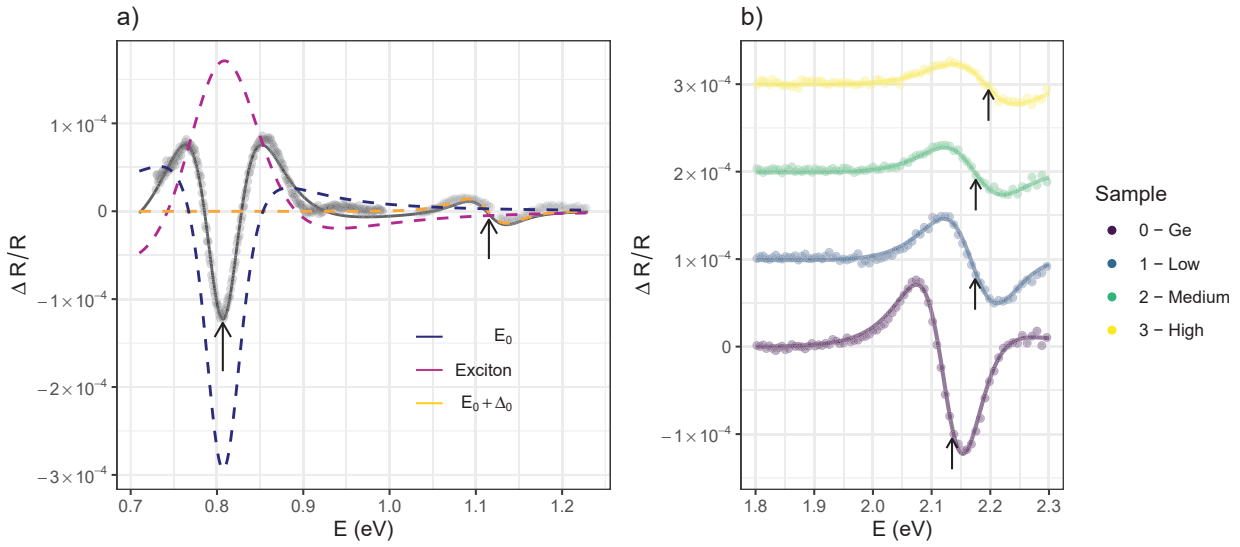


Figure 5.9: a) Fit (lines) to low-energy photoreflectance data (black circles) of a Ge substrate using eq 3.5. The solid black line shows the overall fit to the data while the dashed lines show the contributions of the individual peaks: the 3D M_0 E_0 and $E_0 + \Delta_0$ critical points, and the excitonic contribution to E_0. b) Fits of eq. 2.15 with $n = 3$ to the E_1 critical point for Ge and the SiGeSn samples from Set A. The data is cut off at 2.3 eV due to the 532 nm pump laser; thus, the $E_1 + \Delta_1$ peak cannot be observed.

5.2.2 Photoreflectance

Fig. 5.8 shows photoreflectance data of a Ge substrate, and samples from sets A and B (with two different SiGeSn thicknesses for Set B). The Ge clearly shows a feature with a sharp minimum at 0.8 eV, and another feature around 1.1 eV, corresponding to the expected E_0 and $E_0 + \Delta_0$ energies [58].

The Ge photoreflectance data was fitted to eq. 3.5, including critical points for E_0, the excitonic contribution close to E_0, and $E_0 + \Delta_0$. Previously reported exciton binding energy values for Ge are around 2 meV [189], and the exciton binding energy was fixed to this value during the fit. The resulting fit for Ge is shown in Fig. 5.9a. Eq 2.15 with $n = 3$ (for a 2D critical point) was used to fit the PR data in the range of the E_1 critical point for Ge and the Set A samples, as shown in Fig. 5.9b (the E_1 transition was not clearly visible in the photoreflectance data for the Set B samples).

Fitting the low-energy features of the SiGeSn samples was done using the combined interference/critical point model described in Section 3.3, which accounts for both the thin-film interference observed and the critical point feature in a self-consistent way. The resulting fits for all nine samples are shown in Fig. 5.10, showing the contributions of the interference and the excitonic, E_0, and $E_0 + \Delta_0$ critical point features. The full fitting results are given in Table F.3, and the values extracted for E_0 and $E_0 + \Delta_0$ are given in Table 5.2 and shown in Fig. 5.12.

5.2.3 Reflection and transmission measurements

Fig. 5.11 shows the reflection (R) and transmission (T) measured for Set A samples, and the calculated total absorption ($A = 1 - R - T$). Although the measured R and T seem reasonable, and show thin-film interference fringes which match the thickness of the samples fitted to ellipsometry data, the calculated absorption shows that below the expected bandgap, the absorption appears not to drop to zero, but rather

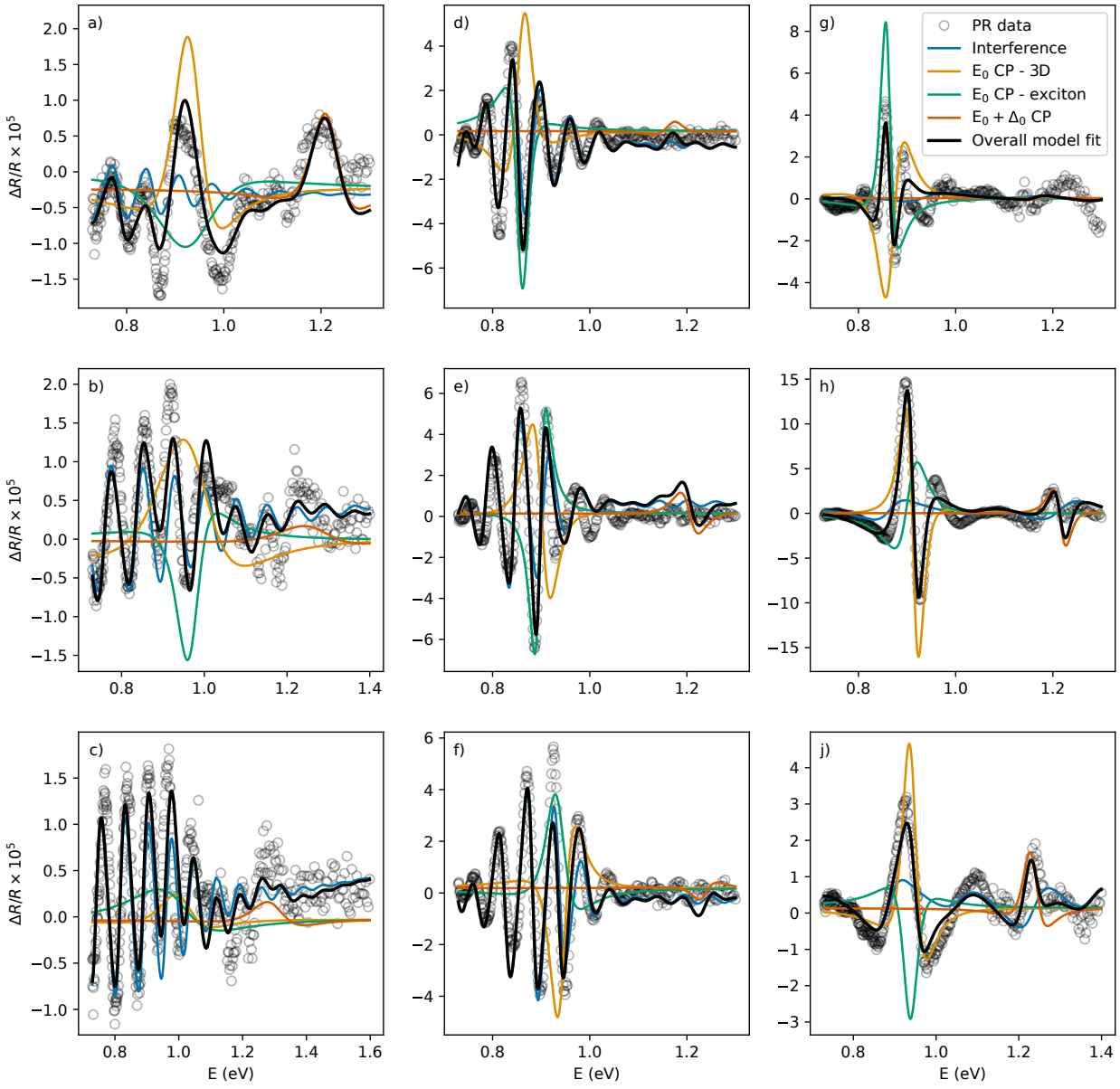


Figure 5.10: Fits to photoreflectance data for a)-c) Set A, d)-f) 2000 nm Set B samples and g)-j) 400 nm Set B samples. Samples in each set are in order of increasing Si/Sn composition (1 to 3). The overall model fit (black line) is shown in addition to contributions from thin-film interference, the E_0 critical point (plus excitonic contribution) and the $E_0 + \Delta_0$ critical point.

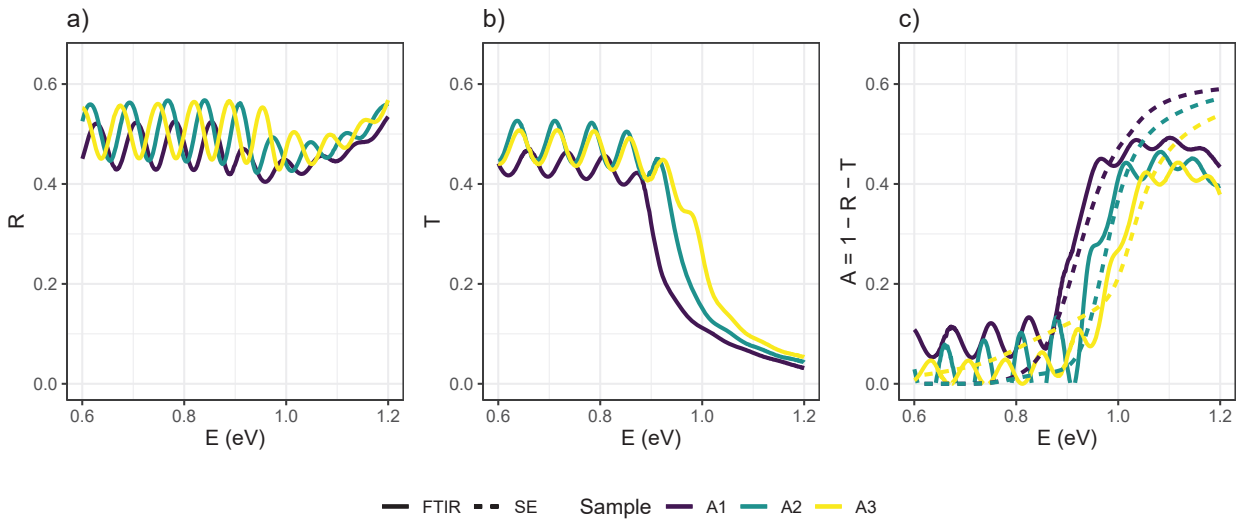


Figure 5.11: a) Reflection, b) transmission and c) total absorption calculated as $A = 1 - R - T$ of the Set A SiGeSn samples measured through FTIR. The modelled total absorption, based on optical constants determined through SE, is also shown in c) for each sample.

continues to oscillate. This is surprising, since the SiGeSn and the growth substrates are not highly doped, and thus low free-carrier absorption at energies close to the bandgap is expected. In addition, no high below-bandgap absorption is fitted to the ellipsometry data. It is likely that the observed non-zero absorption is due to incorrect normalisation of the reflection and/or transmission. It has been observed through optical microscopy, SEM, and TEM measurements that the surface of the samples is not perfectly smooth but rather has a high density of defects; these defects cause scattering of the incident light, so that rather than purely specular reflection/transmission there is a diffuse element. As the measurement uses a microscope setup rather than e.g. an integrating sphere, little of the scattered light will be collected, and thus the measured reflection/transmission will be lower than the true value. In addition, the 'bubble' and 'pyramid' features observed on the surface of the samples result in a slightly uneven layer thickness; since the reflection and transmission through the samples are not measured in exactly the same location on the sample, it is possible that slightly offset interference fringes corresponding to slightly different SiGeSn layer thicknesses cause the oscillations seen in the calculated total absorption.

However, despite the measurement issues for the reflection and transmission data, we can still clearly see an absorption edge consistent with a direct transition in all the samples, with the expected blueshifts in order of increasing Si/Sn composition. If the optical constants and thicknesses of all the layers are known, calculating R and T is straightforward computationally using the transfer matrix method (TMM). Thus, the absorption edge from the optical constants fitted to the ellipsometry data of each sample can be calculated using the TMM in Solcore and the layer structure in Fig. 3.1. Fig. 5.11c compares this predicted absorption edge to the A values measured using FTIR. This shows that apart from the oscillations observed in the FTIR data, likely due to the measurement issues discussed above, there is a good match between the two data sets for each sample, confirming the dominance of the direct transition E_0 in determining the absorption edge, and its blueshift with increasing Si/Sn composition. The absorption edge is dominated by the direct transition E_0, rather than by the fundamental indirect bandgap (shown to lie at lower energies through photoluminescence measurements in the next section).

5.2.4 Comparison of ellipsometry and photoreflectance results

Table 5.2 summarizes the centre energies fitted to the SE and PR data. With the exception of the E_1 energies of the Set A samples, the higher-energy features were obtained only from the SE data, while E_0 was determined from both the SE and PR data individually. For the SiGeSn samples, the difference between the two values for E_0 was $< 2\%$ for A1, A2, A3, B1 and B2. Sample B3 shows a slightly larger discrepancy between the two methods (3% difference); the PR gives 0.95 eV while the SE fits give 0.98 eV. For the Ge, and the two other thin samples B1 and B2 (less affected by interference fringes than the PR measurements of the thicker samples), the critical point centre energy fitted is close to the higher-energy minimum in the PR data (Fig. 5.8), while the E_0 value for B3 is shifted down in energy from that highest-energy minimum. As this feature in B3 is much broader than in the other samples, it is more likely to be significantly distorted by the wide interference fringes in the 400 nm samples, but comparison with the raw PR data indicates that the 0.98 eV E_0 energy obtained from the SE data does not seem unreasonable. The PR data and fits to the SE data show mostly good agreement, offering a validation of the SE data fitting method at low energies, since the E_0 transition energies cannot be observed or estimated directly from the SE data without fitting a model. The energy of the absorption edge is further confirmed by the reflection and transmission measurements as discussed in the previous section.

The E_1 values fitted to the photoreflectance data are consistently around 20 meV higher than the values fitted to the ellipsometry data (Table 5.2). The $E_1+\Delta_1$ transition is not visible in the photoreflectance data, due to the high-energy limit of the measurements around 2.3 eV due to the laser pump beam wavelength of 532 nm (although the lock-in amplifier is used to isolate reflectance signal from other signal, the laser intensity is so much higher than the reflectivity signal that even the small fraction of laser light which is observed drowns out the reflectance difference). In the SE data, E_1 and $E_1+\Delta_1$ can be clearly distinguished; it is likely that the fits to the PR data give higher energy since the fitting algorithm is attempting to fit the low-energy edge of $E_1+\Delta_1$ as well as the E_1 peak shape. It is not possible to fix the phase (as was done in the SE second-derivative fitting) for the PR data fits to obtain more consistent fit results, since the phase is an experimental parameter related to the lock-in amplifier which cannot be taken to be exactly the same between measurements. Thus, the SE values should be taken as more reliable; the SE-determined E_1 value (2.114 eV) for the Ge reference is in good agreement with the literature value (2.111 eV) [74].

Slightly different sample thicknesses were fitted to the ellipsometry data and using the photoreflectance model including thin-film interference, as shown in Table 5.3. For the ellipsometry fits, both the initial thickness obtained when the optical constants of Ge are used to fit the SiGeSn layer, and the final thickness after the optical constants of the SiGeSn layer are fitted are given. In each case, the final thickness is higher, and the difference between the initial and final thickness increases for the higher-composition SiGeSn samples; as the absorption edge of the SiGeSn shifts to higher energies, a thicker layer is needed to account for the amount of absorption consistent with the SE measurement, as expected. The thickness fits to the ellipsometry are robust, with multiple fits of the same sample with different starting parameters yielding very similar results; some thicknesses fitted to the PR data have a relatively large standard deviation, but this does not explain the difference in thickness. There does not appear to be a systematic deviation (e.g. one model consistently fitting a thicker layer) between the methods, and attempting to force the same thickness in both models gives poor fitting results, indicating there is some actual deviation in the thickness. The SE and PR measurements were performed on different pieces of the same 10 inch wafers, and the presence of some large-scale 'bubble' defects may explain the variation in thickness observed.

Table 5.3 also compares the E_0 energies obtained through PR fits, directly from the parametric model

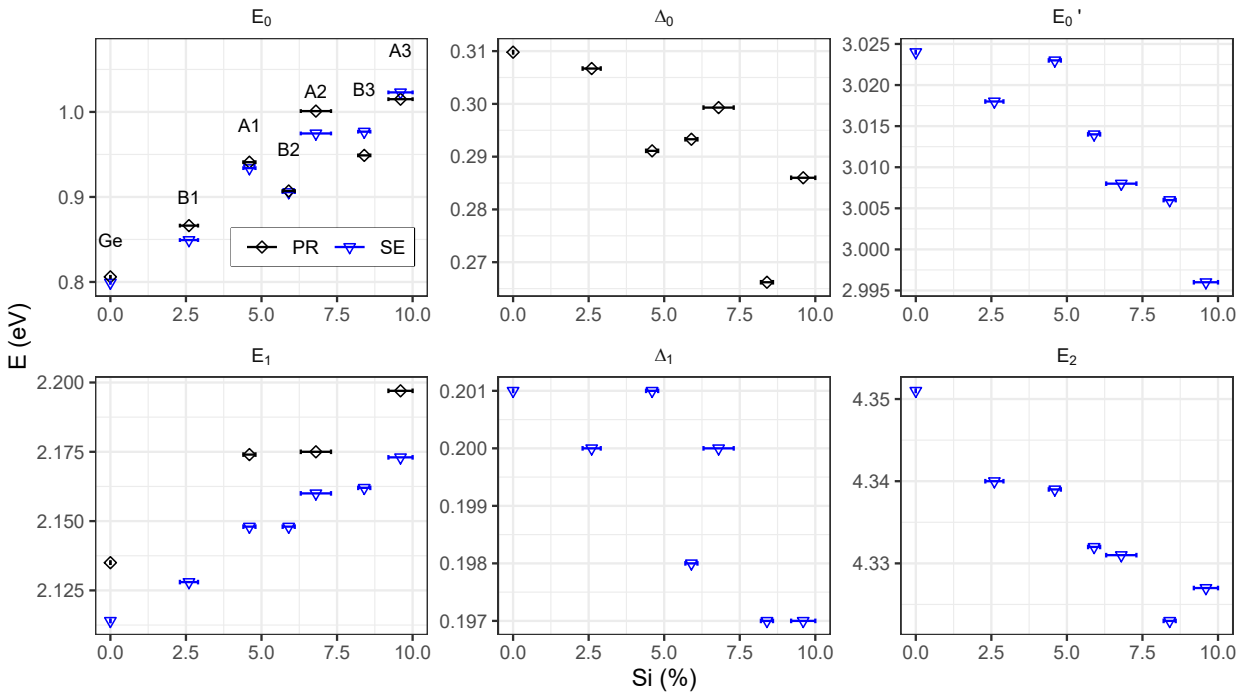


Figure 5.12: Summary of centre energies for the different direct transitions extracted from SE (blue triangles) and PR (black diamonds) data.

fit to the SE data, and from taking the second derivative of the dielectric function fitted to the SE data. As discussed in Section 3.2.2, for this type of parametric model the centre energy fitted to a peak may not be physically meaningful, but there is very good agreement between the parametric model centre energy and the E_0 value obtained through the second derivative.

5.3 Photoluminescence

Initial attempts to measure the PL of SiGeSn samples grown by IQE used samples grown directly on Ge substrates. Since Ge has a lower bandgap than SiGeSn, there is no energetic barrier for carriers excited in the SiGeSn layer (as shown in Fig. 1.11), which is relatively thin, to diffuse into the thick Ge substrate (especially if the quality of the epitaxial layer is high enough for sufficiently long carrier diffusion lengths). The carriers excited in the SiGeSn can then recombine in the Ge, and since the SiGeSn is almost completely transparent at the PL emission energies of Ge ($\approx$ 0.6-0.8 eV at room temperature), this results in PL from Ge being measured [70, 55]. The first PL attributed to SiGeSn measured during the PhD was from a sample including a thin (20 nm) layer of $Si_{0.2}Ge_{0.8}$ between the Ge substrate and the SiGeSn layer; since the $Si_{0.2}Ge_{0.8}$ has a higher bandgap than the SiGeSn around the compositions of interest, there is a barrier to carriers diffusing into the substrate (see Fig. 1.11b). Although the PL indicates that a large number of carriers are still able to reach the substrate, this sample showed an additional PL peak around 0.78 eV (at 12K) [70]. While the SiGe barrier allowed for proof of concept that including a higher-bandgap layer prevents carrier diffusion and allows PL to be measured, most of the PL detected still originated from the Ge layer due to the relatively small energetic barrier introduced by the SiGe; many carriers are still able to reach the

Table 5.2: Summary of centre energies fitted to model dielectric constants from SE and to PR data of SiGeSn and Ge samples. For the lower-energy critical points, results from SE and PR measurements are indicated – for the higher energy CPs (> 2.3 eV) all results are from SE measurements. For the Set B samples, the E_0 (PR) data from the thicker samples was used, though for each composition there was less than a 5 meV difference between the mean centre energy fitted to the thick and thin samples. All values are in eV.

Comp.	E_0 (SE)	E_0 (PR)	$E_0 + \Delta_0$ (PR)	E_1 (SE)	E_1 (PR)	$E_1 + \Delta_1$	E_0'	E_2
Ge	0.799	0.807	1.115	2.114	2.135	2.315	3.024	4.351
A1	0.934	0.941	1.225	2.148	2.174	2.349	3.011	4.339
A2	0.975	1.001	1.274	2.160	2.175	2.360	3.008	4.331
A3	1.023	1.015	1.309	2.173	2.197	2.370	3.002	4.327
B1	0.849	0.866	1.156	2.128		2.328	3.016	4.340
B2	0.906	0.907	1.199	2.148		2.346	3.007	4.332
B3	0.977	0.949	1.243	2.162		2.359	2.999	4.323

Table 5.3: Key parameters fitted to the photoreflectance and ellipsometry data. For the ellipsometry data, both the initial thickness fit obtained assuming the optical constants of the SiGeSn layer are equal to those of Ge, and the final fit after the optical constants of the layer are allowed to vary, are given. The values of E_0 obtained through both methods is also given; for the SE fits, the centre energy in the Psemi model fit is compared to the value obtained through fitting the second derivative of the dielectric function, showing good agreement. The values given for the photoreflectance data fit parameters are the mean of ten runs of the differential evolution fitting algorithm, with the standard deviation given in parentheses.

	Photoreflectance			**Ellipsometry**			
	d (nm)	E_0 (eV)	Δ_0 - PR (eV)	d - Ge fit (nm)	d - Final fit (nm)	Parametric E_0 (eV)	2nd deriv. E_0 (eV)
A1	1811 (40)	0.94 (0.007)	0.28 (0.01)	1753	1768	0.93	0.93
A2	1746 (6)	1.00 (0.02)	0.27 (0.02)	1825	1851	0.98	0.97
A3	1828 (2)	1.01 (0.002)	0.30 (0.01)	1842	1906	1.02	1.02
B1 - thin	332 (10)	0.87 (0.006)	0.29 (0.01)	334			
B1 - thick	2073 (20)	0.87 (0.003)	0.29 (0.01)	2029	2036	0.85	0.85
B2 - thin	362 (8)	0.91 (0.003)	0.30 (0.01)	363			
B2 - thick	2017 (40)	0.91 (0.02)	0.29 (0.01)	2084	2115	0.91	0.91
B3 - thin	353 (7)	0.95 (0.01)	0.29 (0.01)	359			
B3 - thick	2036 (50)	0.95 (0.008)	0.30 (0.01)	2035	2080	0.97	0.98

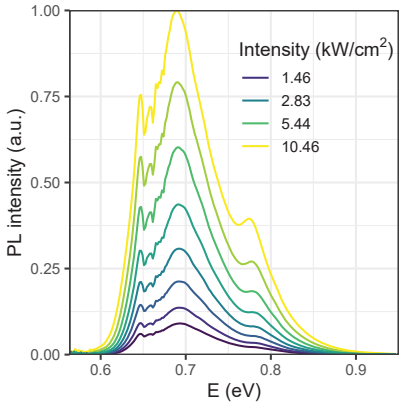


Figure 5.13: Power-dependent room-temperature PL of a piece of Ge substrate measured with incident laser intensity between 1.05 and 10.5 kW/cm^2.

Ge substrate. In addition, only a thin layer of SiGe can be grown without introducing dislocations related to lattice mismatch with the Ge substrate. Thus it was necessary to either grow samples on a different, higher-bandgap substrate, or to include a lattice-matched higher-bandgap layer between the Ge and SiGeSn. Thus, subsequent sample sets were grown on GaAs substrates or on Ge substrates which had been overgrown with a thin III-V barrier (InGaP or InGaAs). Initial samples with a lattice-matched, high-bandgap InGaP barrier had poor material quality and did not emit measurable PL; subsequent sample sets grown on GaAs substrates (Set A) and on Ge substrates with an $In_{0.012}Ga_{0.988}As$ barrier (Set B) did emit measurable PL, and are the focus of the results in the rest of this section.

5.3.1 Room-temperature power-dependence

Room-temperature photoluminescence was measured with incident powers between 100 mW and 3W, or 0.52-15.7 kW/cm^2 taking into account the laser spot size (Section 3.4), with the range of powers used for each sample depending on its luminescence intensity. A piece of Ge substrate was used for reference measurements, and has significantly higher PL intensity than any of the SiGeSn samples (around an order of magnitude higher both in terms of peak and integrated intensity compared to the SiGeSn sample with the highest intensity, A1, depending on the incident laser power). Due to the very different luminescence intensities, not all samples were measured at the same incident powers, but were divided into two groups: A1 and A3, which had the highest intensities out of the SiGeSn samples, and the Ge reference sample, were measured at power densities between 0.52 and 10.5 kW/cm^2. The four other samples were measured at powers between 5.23 and 15.7 kW/cm^2. The room-temperature power-dependent PL measurements are shown in Figures 5.13 for the Ge reference and 5.14 for the six SiGeSn samples. This data has been corrected for the response of the InGaAs detector. Only the thicker samples ($\approx$ 2000 nm SiGeSn) from set B are shown due to their higher luminescence intensity. Each sample shows multiple clear peaks; for Ge, the different PL peaks can be attributed to different phonon-assisted transitions [72], with the exception of the highest-energy peak around 0.78 eV which is attributed to the direct E_0 transition (0.8 eV).

Fig. 5.15 shows the variation of the integrated PL intensity (area under the curve) for all samples, integrated over the whole measurement range (0.62 eV to 1.10 eV/1125 nm to 2000 nm). The room temperature power dependence of the integrated PL intensity of all samples follow a power law of the form:

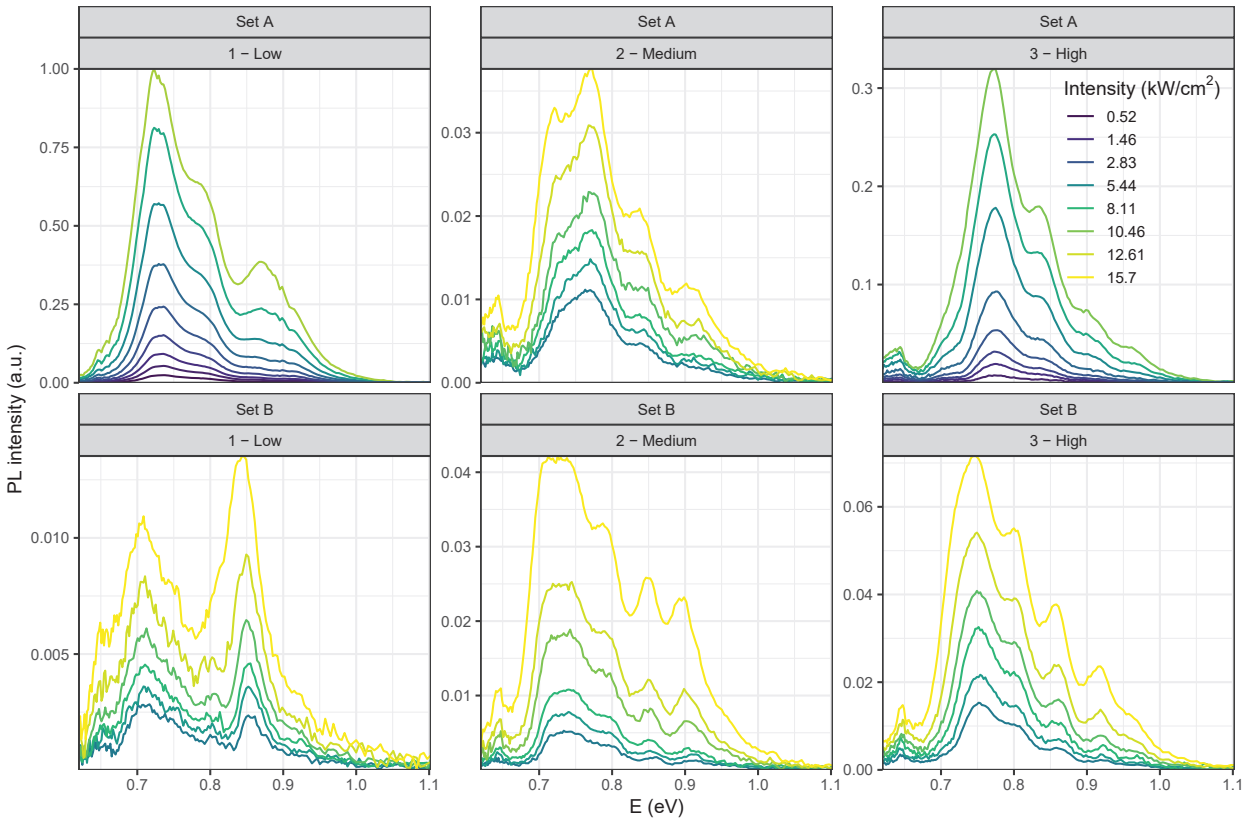


Figure 5.14: Power-dependent room-temperature PL of six SiGeSn samples. For the B series samples, this data is from samples with a thicker (≈ 2 µm) SiGeSn layer. Samples A1 and A3 had higher PL intensities at a given laser power than the other four samples, and were measured at incident laser intensities between 0.52 and 10.5 kW/cm^2. The four other samples were measured between 5.23 and 15.7 kW/cm^2.

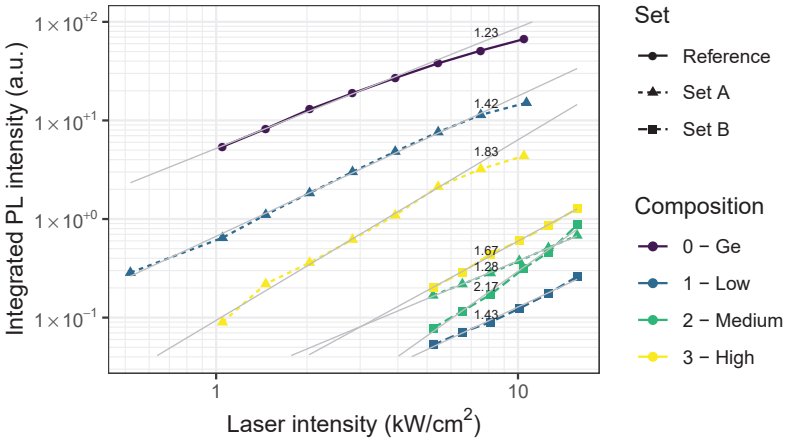


Figure 5.15: Variation of integrated room-temperature PL intensity over the whole measurement range (0.62 eV to 1.10 eV/1125 nm to 2000 nm) with incident laser intensity for each sample. The grey lines show fits to a power law (eq. 5.1); the number by each line is the fitted value of m. For the higher PL intensity samples (Ge, A1 and A3), only data for powers up to and including 2.83 kW/cm^2 was included as the dependence above these powers becomes visibly sub-linear on the log-log plot.

Table 5.4: Power law exponents fitted to the peak and integrated intensity of PL data for Ge and SiGeSn samples.

Sample	m_{int}	m_{peak}
Ge	1.22	1.20
A1	1.43	1.39
A2	1.28	1.11
A3	1.83	1.84
B1	1.43	1.53
B2	2.17	1.88
B3	1.67	1.38

Table 5.5: Summary of some parameters from this and previous work on Ge photoluminescence.

Reference	Power law exponent	Power densities	Temperature (K)
Lieten et al. [72]	2.02 (indirect)	0.008-0.128 kW/cm^2	9
Klingenstein & Schweizer [190]	1 (indirect), 1.6 (direct)	0.8-6.7 kW/cm^2	2
van Driel et al. [191]	not reported	0.05-10^5 kW/cm^2	174, 295
This work - 295 K	1.23 (indirect)	1.05-10.46 kW/cm^2	295
This work - 30 K	1.68 (indirect)	0.03-1.05 kW/cm^2	30

$$I_{PL} \propto I_{laser}^{m} \tag{5.1}$$

where I_{PL} is the integrated intensity of the PL signal and I_{laser} is the incident laser intensity (the peak intensity follows a similar power law behaviour for all samples) and m is a positive constant. The samples which showed higher PL intensities (Ge, A1 and A3) become sub-linear on a log-log plot at powers above $\approx$ 4 kW/cm^2, indicating that at higher powers there may be additional effects such as band-filling which affect the PL intensity. The power law fits shown in Fig. 5.15 are fitted to data for all the incident intensities for the lower-intensity samples (A2, B1, B2 and B3) and up to and including the measurements at 2.83 kW/cm^2 for the higher-intensity samples (Ge, A1 and A3).

While PL from all the samples follows a power law as expected, the variation of the exponent m between samples does not seem to correlate to an obvious parameter such as peak energy, composition or Si:Sn ratio, and lies between 1 and 2 for all the samples. The Ge substrate has an exponent of 1.23, which differs from values previously reported in the literature as summarized in Table 5.5; Lieten et al. [72] report a power law exponent of 2.02, relating to PL from the indirect transition, while Klingenstein & Schweizer [190] report an exponent of 1 for the indirect transition and 1.6 for the direct transition, with the latter measured at significantly higher laser intensities by around two orders of magnitude (Table 5.5). Both of these sets of measurements were taken at low temperature (9K and 2K respectively). Measurements of the Ge sample at 30 K (see Fig. 5.16) give an exponent of 1.66, higher than the room-temperature value of 1.23. The laser intensity used here for the low-temperature measurements is between those used by Lieten et al. and Klingenstein & Schweizer, and an intermediate value of the power law exponent is obtained. Considering the power-dependent data for Ge at room temperature shown here, and the exponents for the indirect transition obtained by Lieten at low laser intensity and by Klingenstein at high power, it appears that higher incident laser power decreases the exponent m while higher temperatures lead to higher m. This indicates that the behaviour of the Ge PL is quite consistent with that previously observed once variations of the exponent m with temperature and incident laser intensity are taken into account.

Schmidt et al. [192] formulated a general model to describe the dependence of the intensity of the near-

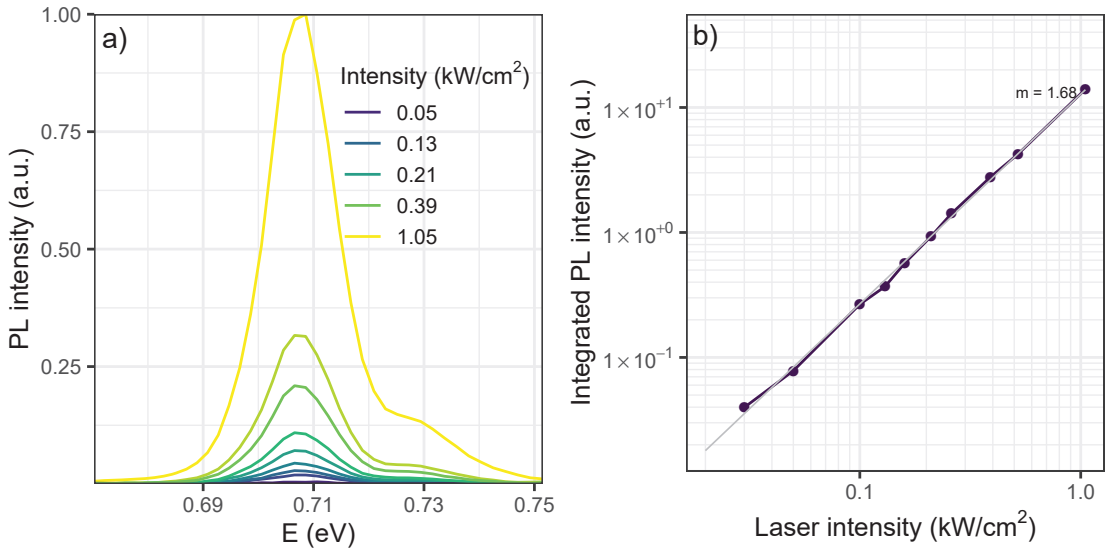


Figure 5.16: a) Low-temperature (30K) power-dependent PL measurements of the Ge substrate sample at laser intensities between 0.05 and 1.05 kW/cm^2 and b) integrated PL intensity vs. incident laser intensity of these measurements with a power law fit (eq. 5.1). The exponent m obtained is 1.68.

bandgap luminescence on the incident laser power by considering rate equations for carrier excitation and different recombination processes, including free and bound excitons and recombination involving donors and acceptors, and non-radiative processes; this model indicates that a value of m between 1 and 2 is consistent with interband radiative recombination, rather than transitions involving bound states (such as would occur with defects), indicating that the PL emitted by the Ge and SiGeSn samples at room temperature is consistent with radiative recombination in the bulk.

5.3.2 Peak fits

In order to determine the relative strength of the different peaks contributing to the PL data, and their individual power dependence, a combination of Gaussian (eq. 5.2) and Lorentzian (eq. 5.3) lineshapes were fitted to the data at each power for each sample:

$$I_G(E) = \frac{A}{\sigma\sqrt{2\pi}} e^{-\frac{1}{2}\left(\frac{E-E_i}{\sigma}\right)^2} \tag{5.2}$$

$$I_L(E) = \frac{A\gamma}{\pi} \frac{1}{(E-E_i)^2 + \gamma^2} \tag{5.3}$$

These peak shapes were chosen in order to fit the lineshapes observed; it was found that most of the peaks fit well to Gaussians, except for the highest-energy peaks (attributed to emission from the direct gap), which were fitted to Lorentzian lineshapes. The number of peaks to fit was determined through a combination of counting the visible peaks and fitting the data to find a suitable number of peaks. Fits to the data for each sample at the highest and lowest power are shown in Fig. 5.17. Table 5.6 lists the peak locations at low power for each of the samples, and offset between the peaks. The parameters fitted in each case were the centre energy of the peak (E_i), the broadening (standard deviation σ for the Gaussian distributions and scale parameter γ for the Lorentzian distribution), and the strength A, which corresponds to the area under

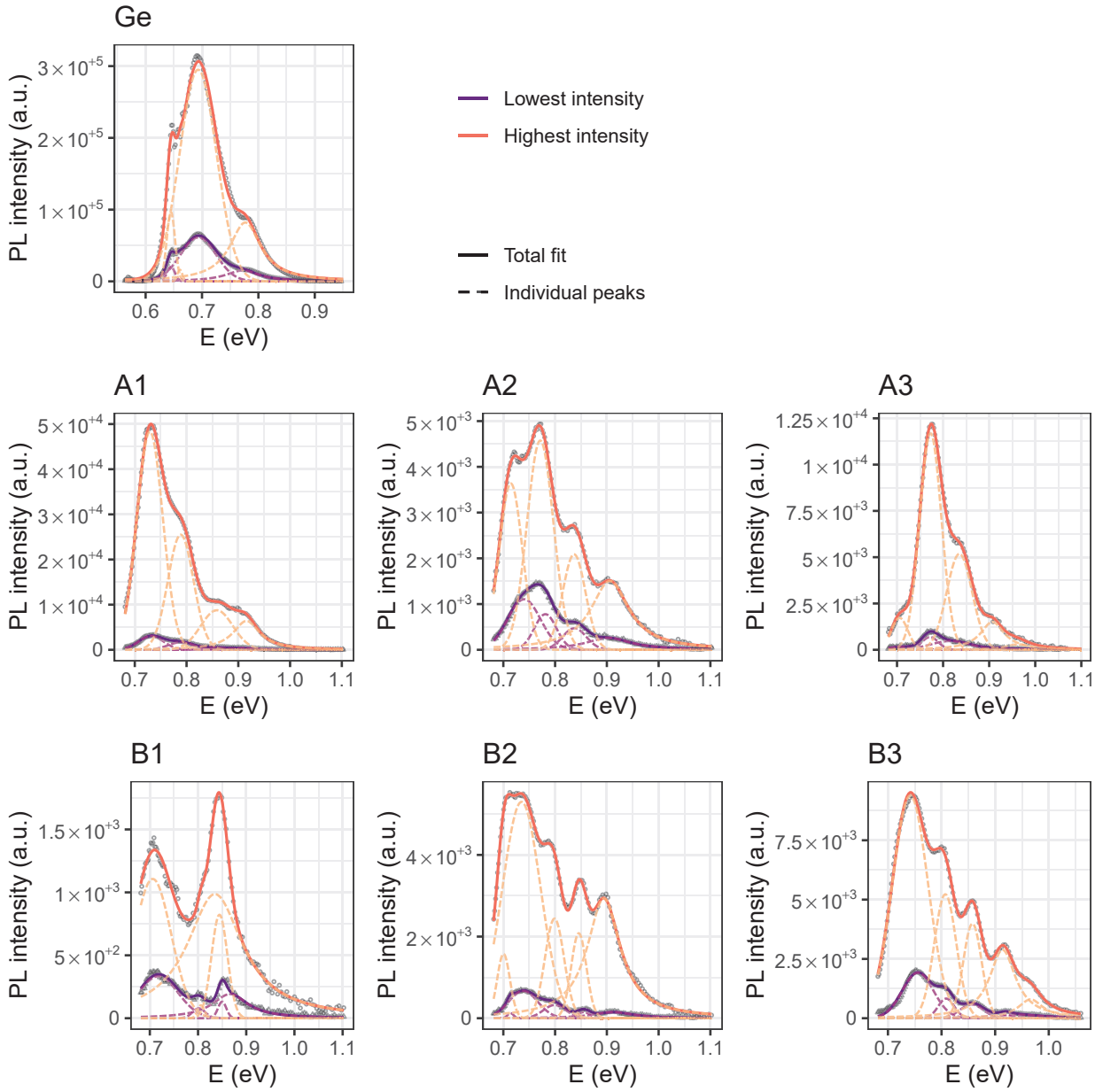


Figure 5.17: Illustration of the fits to power-dependent PL data using Gaussian and Lorentzian lineshapes. The lowest and highest power measured and the corresponding fits (total fit and individual peaks) are shown for each sample.

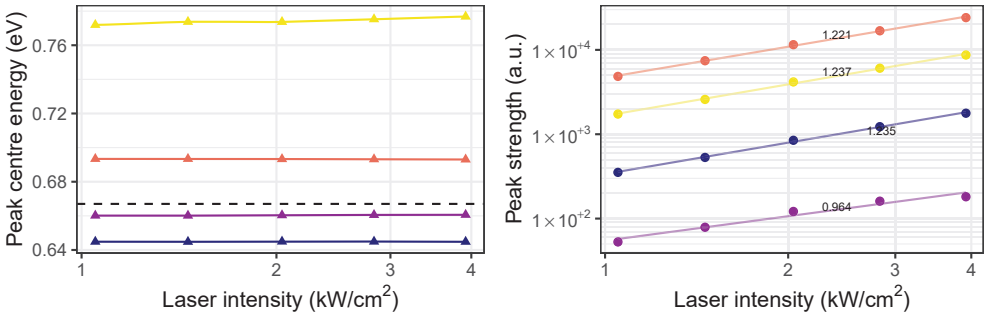


Figure 5.18: Dependence of fitted peak centre energy (left) and peak strength (right) on incident laser intensity for the three individual peaks fitted to Ge photoluminescence data. The numbers in the right-hand plot indicate the power law exponent of the peak strength (area under the peak). The dashed line in the left-hand plot shows the expected room-temperature bandgap of Ge (0.667 eV).

Table 5.6: Summary of the peaks observed in the room-temperature PL spectra of Ge and the SiGeSn samples, and the bandgap obtained from the data. The peak location in bold is the highest-intensity peak (corresponding to the fitted Gaussian with the largest strength parameter). The spacing between the peaks is given. The bandgap is calculated by assuming the highest-intensity peak corresponds to LA phonon absorption (27 meV) as it does in Ge. The bandgap shift, compared with theory[3] is also given.

Sample	**RT peak locations (meV)**	**Spacing (meV)**	**E_g (PL) (eV)**	**ΔE_g (PL) (meV)**	**ΔE_g (Theory) (meV)**
Ge	645 / 660 / **693** / 772	15 / 33 / 79	0.666	0	0
A1	**732** / 789 / 853 / 910	57 / 64 / 56	0.705	38	44
A2	**740** / 781 / 837 / 903	41 / 56 / 66	0.713	47	58
A3	708 / **772** / 826 / 911 / 976	64 / 54 / 85 / 66	0.745	79	74
B1	**717** / 803 / 856 / 863	86 / 53 / 7	0.690	23	26
B2	714 / **738** / 799 / 855 / 912	24 / 61 / 56 / 57	0.711	45	53
B3	**753** / 808 / 856 / 922 / 969	55 / 48 / 65 / 48	0.726	57	67

the peak.[2]

Figure 5.18 shows the variation of the fitted centre energy E_i and peak strength A for the individual peaks fitted to the Ge PL spectra (similar plots for the SiGeSn samples are shown in Appendix G.2). The expected room-temperature bandgap is also shown, showing that none of the individual peaks identified corresponds exactly to the bandgap; this is expected for an indirect semiconductor, since the photon emission must be mediated by a phonon and thus the energy of the photon emitted will be offset by the phonon energy (Fig. 2.3). The assignment of the Ge and SiGeSn peaks to different phonon-assisted transitions is discussed further in Section 5.3.4.

5.3.3 Temperature-dependence

Fig. 5.19 shows the PL signal of Ge at different temperatures. At low temperatures, the number of phonons in the lattice is low, making phonon absorption unlikely, and thus the observed PL takes place via phonon

[2]Fig. G.4 in Appendix G.2 shows the PL signal at low energies. The four samples with lower PL intensity show a peak around 0.645 eV/1922 nm, with similar intensities for each sample depending on the laser power. For instance, sample B3 has around 5 times the PL intensity of sample B1 (Fig. 5.14), yet the peaks around 0.645 eV are only around twice as intense, indicating that their source is some external source of background signal (with the remaining difference of intensity being due to the low-energy tail of the PL signal). For this reason, only data above 0.68 eV was used in fitting the PL signal (Fig. 5.17) of samples A2, B1, B2 and B3. For the three other samples the magnitude of this noise is small enough to be undetectable compared to the tail of the PL signal, so data over the full wavelength range was used.

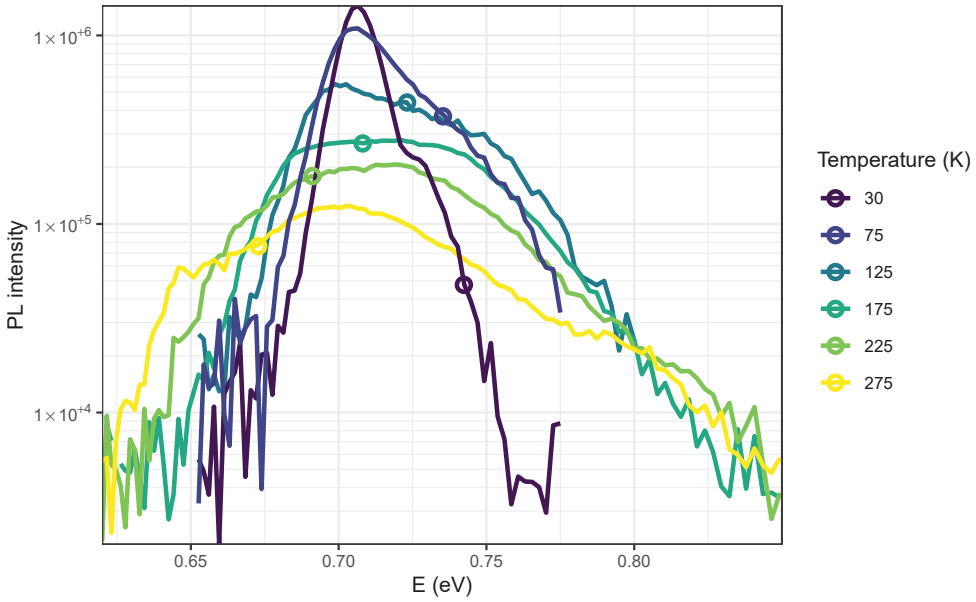


Figure 5.19: Temperature-dependent PL, on a logarithmic scale, of Ge measured at a laser intensity of 2.04 kW/cm^2. The open circles indicate the location of the expected bandgap at that temperature based on literature values.

emission and PL peak energies occur below the bandgap energy (see Fig. 2.3). At 30K, two peaks can be resolved: at 34 meV (the dominant peak) and at 26 meV below the predicted bandgap of 0.740 eV, corresponding to TO(L3) phonon emission (literature value 36 meV [49]) and LA(L2) phonon emission (literature value 27 meV). This is in good agreement with the observations in Lieten et al. [72], who also observe the dominant PL peak to be mediated through TO phonon emission at low temperatures, with the LA peak being the second-strongest.

As the temperature increases, an increasing number of PL peaks can be observed, as seen in Fig. 5.19; above $\approx$ 100K, peaks above the expected bandgap energy appear, corresponding to phonon absorption, and the TO phonon emission peak disappears (also consistent with Lieten et al.). Although the bandgap of Ge redshifts as the temperature increases, as is typical for an inorganic crystalline semiconductor, and the energy at which the maximum PL intensity occurs also redshifts, the high-energy edge of the PL signal is moving to higher energies as phonon absorption becomes more probable at higher temperatures. At room temperature, four peaks are observed, with Gaussians fitted at 0.645 eV, 0.660 eV, 0.694 eV and 0.772 eV (see Figs. 5.17 and 5.18). The highest-energy peak could be due to a multiple-phonon absorption, but is more likely due to the direct bandgap ($\Gamma_8^v \rightarrow \Gamma_7^c$) at 0.8 eV. The most intense peak, at 0.694 eV, lies 27 meV above the expected room-temperature bandgap of Ge (0.667 eV), which matches LA(L2) phonon absorption (literature value 27.4 meV). The secondary peak at 0.645, 22 meV below the expected bandgap, is closest in energy to LA(L2) phonon emission. The small peak just above this, at 0.660 eV, corresponds to emission of a TA(L3) phonon (literature value 7.7 meV).

Low-temperature PL (Fig. 5.20) of each of the Ge (Fig. 5.16) and SiGeSn (Fig. 5.20) samples shows a maximum of two distinguishable features for each sample. The PL peaks are blueshifted in the expected order from their composition, with the exception of sample B3, which peaks at a lower energy than sample B2. Temperature-dependent data between 30K and 275 K for each sample is shown in Appendix G.3.

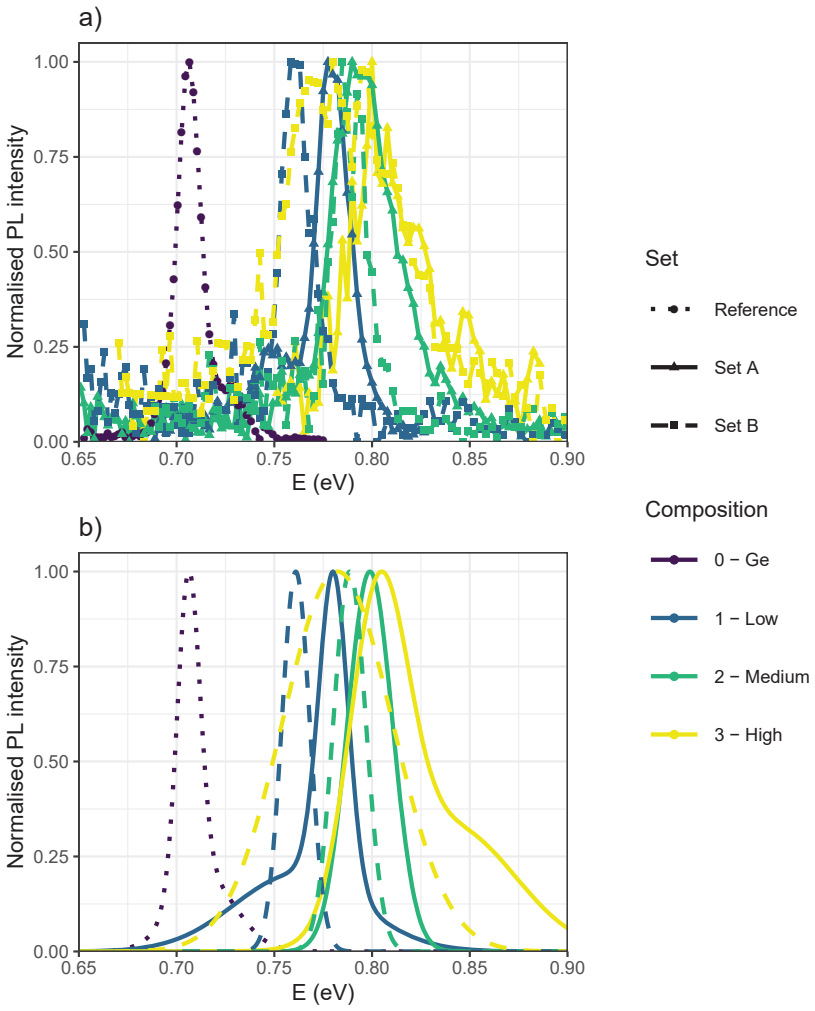


Figure 5.20: Low-temperature PL spectra of Ge and SiGeSn. a) shows the measured data while b) shows Gaussian fits to the data. All data was taken at 30K except for sample A3, where the 30K measurement was dominated by lower-energy defect-related PL; for this sample, data taken at 75K is shown instead.

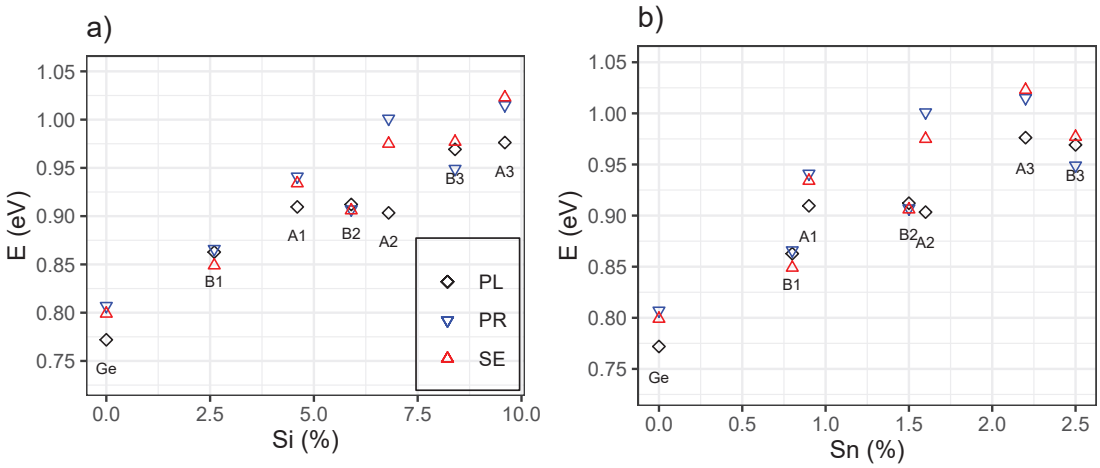


Figure 5.21: Centre energies fitted to Lorentzian lineshapes for the highest-energy peak in the room-temperature PL spectra for each sample (black solid circles) against a) the Si composition and b) the Sn composition of the samples. These are the centre energies fitted to data measured at the lowest laser intensity for each sample. The red upright triangles and blue inverted triangles show the direct transition energy E_0 obtained from SE and PR measurements, respectively, for comparison.

Samples A3 and B3 appear to be dominated by defect PL at low temperatures, deviating from the blueshift observed for the other samples. For sample B3, the PL signal appears to remain static between 225 K and 30 K, indicating that the low-temperature PL is likely due to a localized rather than bulk feature. At higher temperatures, carriers are able to escape localized traps due to their higher thermal energy [25]. The peak energy and shift from the Ge peak are given in Table 5.7. Two peaks can be distinguished in the 30K Ge PL spectrum, attributed to TO(L3) phonon emission and LA(L2) phonon emission, with the lower-energy TO peak having by far the larger intensity. For the SiGeSn samples, the shift from this peak was calculated assuming that the main peak in the 30K SiGeSn PL spectra also corresponds to the TO phonon emission (where multiple peaks are visible).

5.3.4 Assignment of PL peaks

Interpretation of the SiGeSn PL signal is hindered by the presence of multiple peaks for each sample. The origin of these peaks could be $\Gamma_8^v \rightarrow L_6^c$ (Ge-like) indirect transitions, $\Gamma_8^v \rightarrow X_5^c$ (Si-like) indirect transitions, direct $\Gamma_8^v \rightarrow \Gamma_7^c$ transitions (see Fig. 5.6), transitions involving localized states, or a combination thereof. The contribution of the indirect transitions can also consist of several peaks corresponding to different phonon-assisted transitions, as for Ge, or 'no-phonon' peaks which occur at the bandgap energy and occur through impurities [193]; such no-phonon contributions to the bandgap have been observed at low temperature in Ge [72]. PL could also be due to defect or localized states; SEM scans, surface microscopy scans, and cross-sectional TEM reveal obvious defects on both the surface and in the bulk of the SiGeSn samples. Theoretical calculations[3] indicate that the Si-like $\Gamma_8^v \rightarrow X_5^c$ transitions at the SiGeSn compositions considered lie above 1 eV, higher than the direct bandgap, making it unlikely that this transition contributes significantly to the PL of any of the SiGeSn samples. The low-temperature measurement of sample A3 clearly shows a power-

[3]Christopher A. Broderick (Tyndall National Institute, Cork, Ireland), personal communications, July 2020. These theoretical results are based on unfolded band structures from density functional theory (DFT) calculations performed for SiGeSn alloy compositions based on the values measured for the SiGeSn samples in this work.

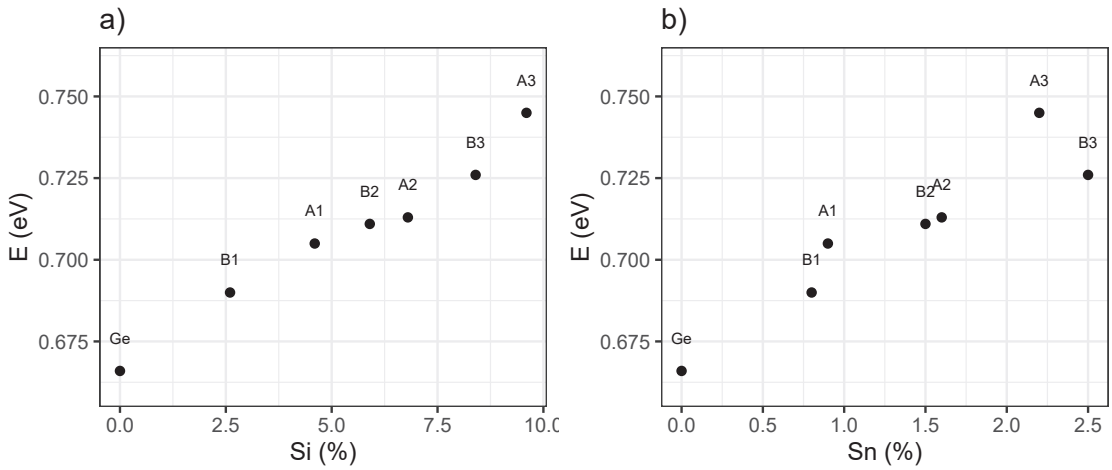


Figure 5.22: Indirect bandgaps estimated from photoluminescence data of the SiGeSn samples a) in terms of percentage Si composition and b) in terms of percentage Sn composition.

Table 5.7: Summary of low-temperature PL peak locations and shift relative to Ge for the SiGeSn samples, compared to the shift observed at room temperature. The shift estimate was calculated theoretically[3].

Sample	**LT peak locations (meV)**	**ΔE_{LT} (meV)**	**ΔE_{RT} (meV)**	**ΔE_{Theory} (meV)**
Ge	**706**/714	0	0	0
A1	762/**780**	74	38	44
A2	799	93	47	58
A3	**810**/848 *	104	79	74
B1	761	55	23	26
B2	788	82	45	53
B3	782 †	76	57	63

*= The PL at 30K for this sample was dominated by defect PL; this energy is calculated by considering the data at 75K and adding an appropriate Varshni shift based on the temperature-dependent behaviour of Ge.
† = The temperature-dependent PL of this sample (Appendix G.3) indicates that this is likely PL due to a localized feature or defect.

dependent low-energy peak (Fig. G.7). The temperature-dependent behaviour of this sample is consistent with emission related to a localized state – the characteristic 'S-shape' in the energy at which maximum PL intensity occurs is observed. At low temperatures, carriers are trapped in lower-energy defect states, and these features dominate the PL spectrum; as the temperature increases and carriers gain more energy, they are able to escape and PL from the bulk is observed. Exciting the samples at higher laser power reduces the temperature at which carriers are able to escape, as the defect states become filled with carriers [25]; this power-dependent behaviour was also observed for sample A3. Sample B3 also shows evidence of PL from a localized feature at low temperature. However, as discussed above, the power dependence of the room-temperature PL signal indicates that PL from radiative recombination of free carriers is being observed.

Thus, the most likely origin of the multiple PL peaks in the SiGeSn PL data at room temperature is the presence of multiple phonon-assisted transitions from the L point in the CB to the Γ point in the VB, in combination with emission from the direct gap occurring at the high-energy tail of the PL spectra. Fig. 5.21 shows the centre energy of the highest-energy peak fitted to the PL data of each of the SiGeSn samples compared to the E_0 values obtained through SE and PR measurements of the direct transition E_0, showing

a clear correlation between the high-energy PL tail and the direct transition energy. For the indirect gap emissions, it is expected that none of the peaks in the PL correspond directly to the bandgap energy, as they will be offset by some phonon energy (with the phonon detected being lower in energy than the bandgap for phonon emission and higher in energy for phonon absorption). There is some difficulty in assigning the phonon peaks due to the large number of possible phonons, and the lack of information on how their energies will vary in the SiGeSn alloy.

There does not appear to be a direct correspondence between the peak offsets observed in the Ge reference which is consistent across the SiGeSn samples (see Table 5.6), which would simplify the process of identifying the corresponding phonons, and the samples have significantly different temperature-dependent behaviour. Therefore, the room-temperature bandgap of the SiGeSn samples was estimated by considering the highest-intensity peak in the Ge room-temperature PL spectrum, which was identified as an LA phonon absorption (27 meV above the bandgap energy) as discussed above. In order to make a consistent identification of the bandgap among samples without additional ambiguity due to the interpretation of different peaks, it was assumed that the highest-intensity peak for the SiGeSn samples was also due to the LA phonon with the same energy. The peak locations identified in the SiGeSn samples and the bandgap predicted from the most intense peak are summarized in Table 5.6, along with theoretical predictions[3] of the bandgap shift, which are in good agreement with the experimentally-obtained results. The values obtained in this way for the indirect gap are shown in Fig. 5.22, showing a blueshift with increasing Si/Sn content.

The low-temperature SiGeSn PL data shows a consistently larger blueshift relative to Ge than the data at room temperature, as shown in Table 5.7; by assuming that the strongest-intensity PL peak at room temperature corresponds to LA phonon absorption, and the strongest peak at 30 K corresponds to TO phonon emission, consistent with the measurements for Ge, a larger shift by between 20 and 46 meV is observed at low temperatures. This may be due to differing temperature-dependent behaviour (Si shows a larger Varshni shift than Ge with temperature [194]) or because the dominant room or low-temperature phonon interaction is not consistent between samples.

5.4 Summary of critical points and theory comparison

As expected from examination of the band structure/naive interpolation between the constituent elements and from more sophisticated theoretical calculations, the observed indirect bandgap E_g and lowest direct interband transition energy E_0 of SiGeSn shift to higher energies as the Si and Sn composition increase. A 1 eV E_0 transition can be achieved with $< 10\%$ Si and $< 3\%$ Sn with a Si:Sn ratio of around 4:1, while maintaining a good lattice match to Ge/$In_{0.012}Ga_{0.988}As$. At these compositions (close to that of samples A2, A3 and B3), E_g as obtained from PL measurements is 0.71-0.75 eV, indicating a 15-25 meV shift in E_0 with a 5-10 meV shift in E_g. Both E_g and E_0 show an effect from higher relative Sn composition in the set B samples, which have a lower Si:Sn ratio: these samples show less blueshift than the Set A samples (this can be seen clearly in Fig. 5.22b and Fig. 5.21b). The location of the direct absorption edge fitted to the SE and PR data (confirmed through reflection and transmission measurements) and the fundamental bandgap are the key optoelectronic parameters for the performance of SiGeSn in a solar cell; optimized devices based on the measurements presented in this chapter are modelled in the next section.

The E_1 and $E_1 + \Delta_1$ energies, around 2.2 and 2.3 eV respectively, also blueshift with increased Si/Sn composition as expected [44, 63], as shown in Fig. 5.12. Meanwhile, Δ_0, E_0' and E_2 redshift slightly (Fig. 5.12), as does the split-off energy Δ_1. The redshift of Δ_0 is reasonable, since the Δ_0 energy of Si (0.06 eV)

is significantly lower than that of Ge (0.30 eV). The reduction in E_0' matches previously reported results [44]. Although different sources report different values for the E_0' energies of Ge and Si [58], the values for Si are generally slightly higher by around 0.2 eV, yet we observe a slight redshift here; this could be due to the presence of α-Sn, which has a lower E_0 by ≈ 1 eV, outweighing the effect of the Si, and because what is treated here as a single transition is in fact made up of at least two contributing critical points, as discussed in Section 3.2.3. The reduction in E_2 is also consistent with previous literature results [54, 44], and expected from the lower E_2 energy of both Si and α-Sn compared to Ge. Note that values of Δ_0 were not fitted to the ellipsometry data; this contribution is relatively much weaker than that of E_0, which is already much weaker than the higher-energy transitions. It was not possible to obtain a reliable, unique fit to the $E_0 + \Delta_0$ critical point, so it was excluded from the second-derivative fits, and values for Δ_0 were obtained only from the PR data.

5.5 Device modelling

The ultimate aim of the SiGeSn material studies described in this thesis is to aid the design and fabrication of high-efficiency monolithic (lattice-matched) solar cells incorporating SiGeSn sub-cells. To this end, a number of different cell architectures were considered and optimized, shown schematically in Fig. 5.23. These devices were optimized using Solcore simulations, using the differential evolution algorithm incorporated into Solcore [160] as discussed in Section 3.7. For the 2J and 3J cell architectures, two versions of the cell design with low-composition SiGeSn (based on sample A1) and high-composition SiGeSn (based on sample A3) were considered[4]. The optical constants used in the simulations were from the Psemi parametric optical constant model fitted to SE data for the relevant sample (Fig. 5.5), while the bandgap was fixed manually at values estimated from the PL measurements as described in the previous section, at 0.705 eV and 0.745 eV for samples A1 and A3 respectively. Other material parameters for SiGeSn were taken to be the same as Ge, as these are not known for the samples discussed in this chapter, with the exception of the minority carrier diffusion lengths which were taken from [195]. An example script for the optimization of the 4J cell design is shown in Appendix G.4.

The optical behaviour of the cells was simulated using Solcore's built-in TMM capabilities as discussed in Section 2.3.1 and 4.1.1. The first step of the optimization in each case was to balance the predicted photogenerated current in each sub-cell, assuming the cells will be connected in series and thus the overall device will be current-limited by the sub-cell generating the lowest current. This purely optical simulation only requires the total reflection, transmission and absorption per layer to be calculated and is extremely fast, since the calculation is vectorized over wavelengths and no absorption profiles have to be calculated. This means a very large parameter space can be explored using differential evolution (DE) without unreasonable computation times. Normal incidence of unpolarized light was assumed, over a wavelength range from 280 nm up to a wavelength longer than the bandgap of the lowest-bandgap sub-cell. The values to optimize in the optical simulations are the total thickness of each of the sub-cells (not differentiating between the p and n-doped material layers, which are assumed to have the same optical constants) and the anti-reflection coating. For the 4J and 3J cells, the compositions of the III-V layers were fixed at $In_{0.5}Ga_{0.5}P$ and $In_{0.01}Ga_{0.99}As$, lattice-matched to Ge. In the case of the dual-junction cell using an AlGaAs top junction, the composition of the AlGaAs was also allowed to vary to determine the composition which leads to the highest 2J cell

[4]No version of the 4J cell with the lower-bandgap SiGeSn was considered, since the higher-bandgap SiGeSn already causes the Ge to be current-limiting as shown in Fig. 5.24b.

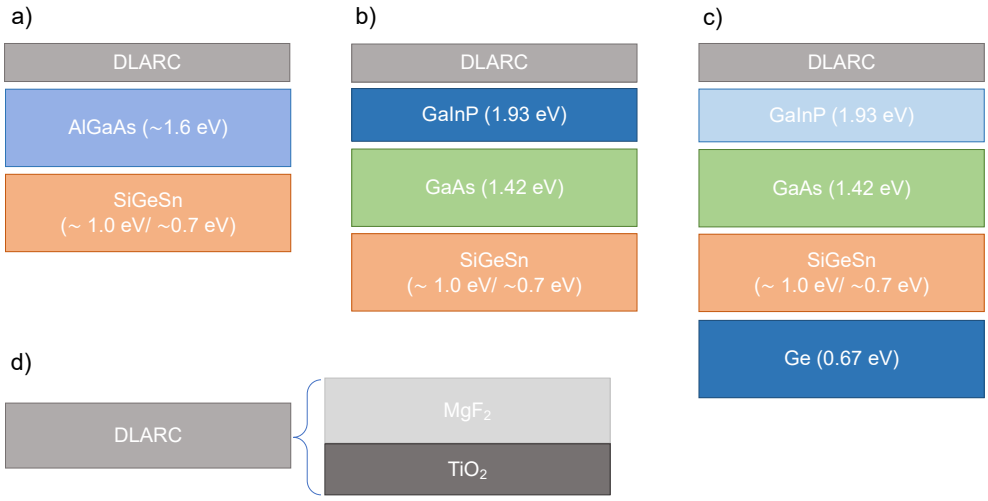


Figure 5.23: Structure of proposed device architectures for SiGeSn MJ solar cells for a) a two-junction device, b) a three-junction device and c) a four-junction device. d) Shows the structure of the double-layer anti-reflection coating used in each case.

efficiency with SiGeSn as the bottom cell. The bandgap of AlGaAs (an alloy of the III-V compounds AlAs and GaAs) is widely tuneable, with the lattice constant remaining almost constant (see Fig. 1.5). Although the bandgap becomes indirect at AlAs fractions of $\approx 45\%$, the AlGaAs composition region of interest lies in the region where the alloy has a direct bandgap around 1.6–1.7 eV. The thickness of the bottom sub-cell in each structure is not optimized; since this layer does not have to transmit any photons to a sub-cell underneath it, a thicker layer will have higher absorption, and the purely optical simulation would simply attempt to make this layer infinitely thick. The thickness of this cell was manually fixed to reasonable values in the electrical simulations. The optical simulations are also used to optimize the layer thicknesses for a double-layer anti-reflection coating (DLARC) made of MgF_2 and Ta_2O_5.

Once the approximate layer thicknesses necessary for current-matching are established, a second round of DE optimization is used to determine relative widths of the p and n-doped layers in each p-n junction, using the optimum total thickness from the optical-only simulations as the starting point to set the upper and lower bounds. Solcore's depletion approximation electrical solver (Section 2.4) was used for these simulations. The bandgap of the SiGeSn is set to values estimated from PL measurements; it is assumed that the voltage of the SiGeSn sub-cells will be determined by the lowest indirect bandgap as excited electrons thermalize to the lowest conduction band edge. The bounds for the total widths of the junctions, and the AlGaAs composition in the 2J cell simulations, were allowed to vary to 75% and 125% of the values determined through the optical simulations. The thickness of the highly-doped n-type emitter layers was allowed to vary between 30 nm and 300 nm. The doping levels of the p and n-layers were fixed at reasonable values, but could be optimized further. The thickness of both layers of the MgF_2/Ta_2O_5 DLARC were fixed at the optimum values obtained in the initial optical optimization.

The resulting optimized efficiencies are summarized in Table 5.8, and the simulated EQE and IV curves for each cell architecture are shown in Fig. 5.24. The cell performances shown in Fig. 5.24 are for cells under an AM1.5G solar spectrum without concentration. The best-performing devices are the 3J device with lower-composition SiGeSn and the 4J device with higher-composition SiGeSn, which both have predicted efficiencies of 35.7%. In the 4J cell, the Ge becomes slightly current-limiting, and the optimal device shows clear

Table 5.8: Efficiencies, open-circuit voltages (V_{OC}) and short-circuit currents (J_{SC}) for different cell designs incorporating SiGeSn sub-cells. The performance for simulations using a realistic SiGeSn bandgap based on measured values is compared to the performance of an equivalent device incorporating a theoretical direct bandgap material with the fundamental bandgap equal to the E_0 value, i.e. a direct semiconductor.

Design	**Measured $E_{g,indirect}$**			**$E_g = E_0$**			**% V loss**
	η (%)	V_{OC} (V)	J_{SC} (mA/cm^2)	η (%)	V_{OC} (V)	J_{SC} (mA/cm^2)	
4J	35.7	3.20	13.2	39.2	3.47	13.2	7.8
3J (A3)	35.4	2.91	14.1	39.1	3.18	14.1	8.5
3J (A1)	35.7	2.87	14.5	38.9	3.11	14.5	7.7
2J (A3)	30.4	1.67	21.6	36.1	1.94	21.6	13.9
2J (A1)	30.7	1.60	22.5	35.7	1.83	22.5	12.6

thinning of the SiGeSn junction to allow more light to reach the Ge junction. This reduces the cell current and efficiency; previously, maximizing absorption in the Ge cell of a 3J device has not been important for boosting device performance, as this junction overproduces current in the standard architecture as discussed in Section 1.3. Further investigation into how the photocurrent in the Ge cell can be boosted (e.g. through light-trapping) may yield further efficiency improvements. In the 3J device with similar efficiency, the SiGeSn actually noticeably over-produces current, giving slightly better efficiency than the other 3J architecture which is more closely current-matched. Although the 3J device with higher-composition SiGeSn (A3) has a higher voltage, this does not compensate for the slight loss of current. Overall, the 3J and 4J devices all give efficiencies of close to 36% while the 2J devices have efficiencies just over 30%.

It was assumed that the voltage of the SiGeSn sub-cells will be determined by the lowest indirect bandgap (estimated from room-temperature PL measurements) as excited electrons and holes thermalize to the lowest conduction and valence band edge, respectively. The predicted effect of this voltage loss is shown in Table 5.8, which compares the predicted efficiency of the cell structures with realistic values for the indirect bandgap to the efficiency of cells containing theoretical direct bandgap materials which otherwise have the same properties as SiGeSn. In the latter case, the fundamental bandgap is set explicitly to be equal to the E_0 values determined through ellipsometry and photoreflectance (0.94 eV and 1.02 eV for the A1 and A3 sample, respectively). These cells will have a higher voltage and thus a higher efficiency, while the current, which is dependent on the direct absorption edge for these thin-film cells, is not affected. Clearly, the overall performance of a multi-junction cell will generally be less affected by a reduction in the voltage of the SiGeSn sub-cell if the cell has a larger number of junctions, since the SiGeSn contributes a smaller fraction of the total voltage. Note that the cell structure was not re-optimized with the new voltage; the same structure obtained from the optimization with a more realistic bandgap was used with only the SiGeSn bandgap adjusted. The percentage point loss in efficiency lies between 5.6 p.p. for the 2J cell with high composition SiGeSn and 3 p.p. for the low composition 3J structure, or between 13.7 and 7.1% loss of output power. The structures with higher-composition SiGeSn suffer more voltage loss due to the larger energy difference between the indirect bandgap and the E_0 energy.

Although the 3J and 4J cells perform very similarly under 1 Sun simulations, the 4J cell begins to outperform the 3J devices under concentration. Efficiencies and voltages of each cell design (with the indirect bandgap assumed to be limiting the voltage) at 1× and 400× concentration are shown in Table 5.9. Under concentration, the voltage of all the cell designs increases (neglecting practical losses due to e.g. increased resistance in tunnel junctions at higher concentrations) due to a reduction in the Boltzmann loss (Section 1.5.2). Increasing the concentration reduces the Boltzmann loss and increases the voltage, with the

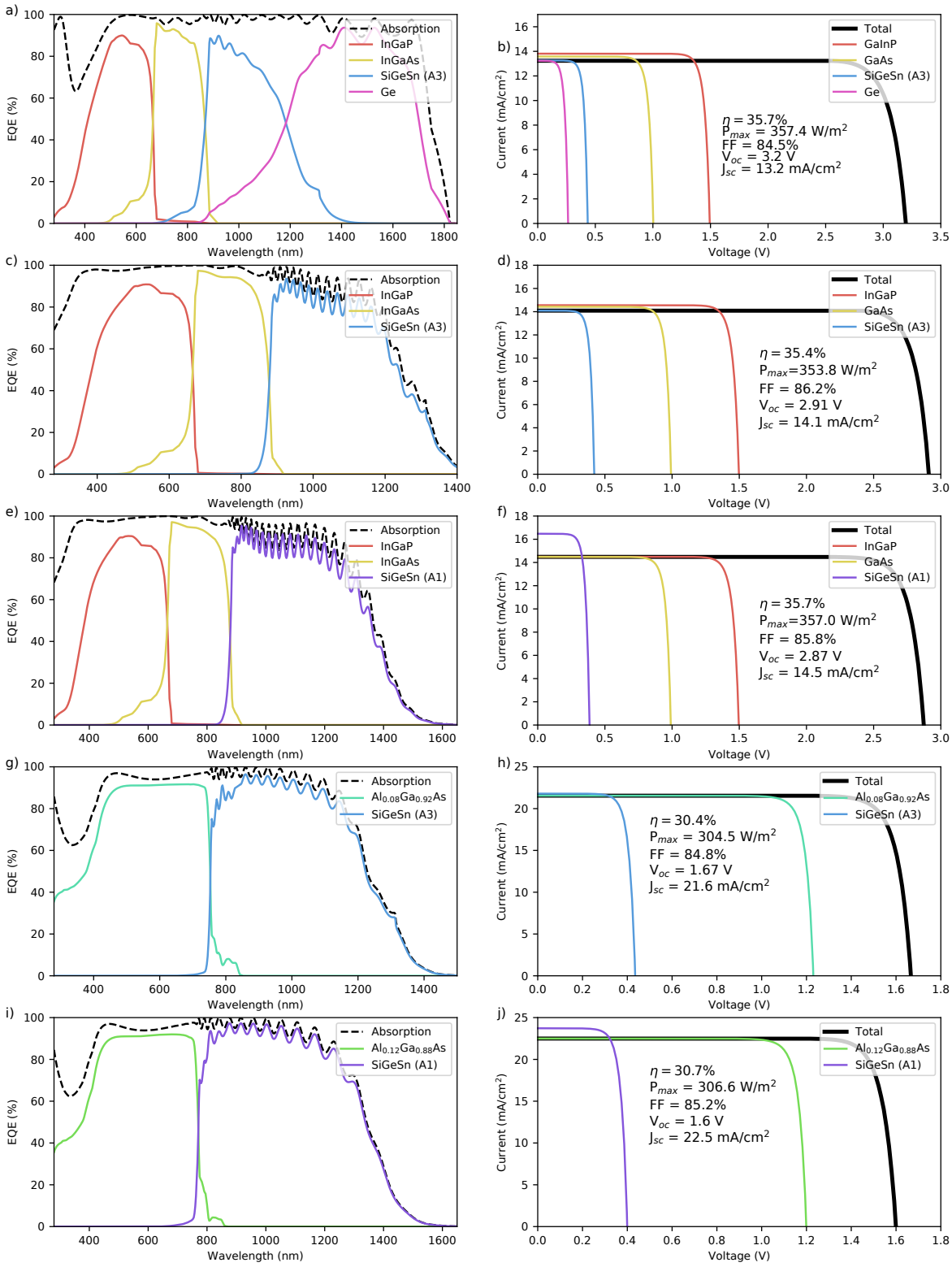


Figure 5.24: Simulated EQE and J-V curves under AM1.5G 1-Sun illumination for monolithic device architectures containing SiGeSn. a-b) a 4J InGaP/InGaAs/SiGeSn (A3)/Ge device; c-d) a 3J InGaP/InGaAs/SiGeSn (A3) device; e-f) a 3J InGaP/InGaAs/SiGeSn (A1) device; g-h) a 2J AlGaAs/SiGeSn (A3) device and i-j) a 2J AlGaAs/SiGeSn (A1) device.

Table 5.9: Comparison of the simulated SiGeSn devices under 1 Sun and 400 Sun concentration.

Design	**Concentration**			
	1 ×		**400** ×	
	V_{OC} (V)	η (%)	V_{OC} (V)	η (%)
4J (A3)	3.20	35.7	3.50	45.4
3J (A3)	2.91	35.4	3.42	43.5
3J (A1)	2.87	35.7	3.38	44.1
2J (A3)	1.67	30.4	1.99	37.9
2J (A1)	1.60	30.7	1.92	38.5

limit being maximum concentration (3640× for sunlight), where the solid angle of absorption and emission are equal. The short-circuit current of course also increases under concentration, but it increases linearly with concentration (e.g. doubling if the concentration doubles), and thus does not lead to an increase in efficiency. The 4J cell has a higher voltage and lower current than the 3J designs, and thus the improved voltage under concentration has a more significant effect on the 4J cell.

Compared to the standard GaInP/GaAs/Ge 3J architecture, the 3J device designs incorporating SiGeSn give a higher voltage (due to the higher indirect gap of SiGeSn), and could be manufactured to be lifted-off and used as thin-film devices, as the total thickness of the device layers for the optimized 3J and 2J cells is around 10 µm. The reduced current in the SiGeSn bottom cell compared to the Ge in the 'standard' 3J cell architecture does not reduce the device efficiency as the Ge generally overproduces current (Fig. 1.8); thus, these devices can maintain an overall current density very similar to the standard 3J device with an increased voltage. Thus, the 3J devices show an improvement in predicted efficiency compared to a similar Solcore device model for a typical 3J GaInP/GaAs/Ge cell (Fig. 1.8, with a simulated efficiency of 31.8%) and the record-efficiency devices of that type with a measured efficiency of 32% [196].

Chapter 6

Light management in advanced cell designs

This section will present optical modelling results for three different types of devices: an ultra-thin (circa 85 nm) GaAs cell for space applications, a silicon heterojunction cell for hybrid photovoltaic-thermal use, and spectrum-splitting triple-junction devices. While these device structures are targeted at very different applications, all have unique light-trapping needs, which require the use of specialized modelling approaches as discussed in Chapter 4. While Chapter 4 detailed the implementation and underlying theory behind the various strands of optical modelling code which were developed over the course of the PhD, this chapter demonstrates how these methods have been applied to solve research problems. The development of Solcore and RayFlare represents an advancement in the ease with which the optics of a wide range of solar cells can be modelled, made available to the community in the form of free, open-source Python packages. The devices in this chapter show the range of structures which can be investigated with these tools: the ultra-thin cells are modelled using RCWA, through the Python-based interface to S^4 developed as part of Solcore and RayFlare. The silicon heterojunction cells are modelled over a wide wavelength range spanning the visible to the mid-infrared using the angular matrix method and integrated ray-tracing/TMM to calculate the reflection, transmission and absorption at each interface using the RayFlare angular matrix framework and integrated ray-tracing/TMM. The spectrum-splitting devices use Solcore's improved TMM capabilities to model the effect of a distributed Bragg reflector (DBR) to selectively reflect certain wavelengths of light in a structure with both coherent and incoherent layers at non-normal incidence.

6.1 Ultra-thin GaAs solar cells

Ultra-thin III-V devices, with absorber layer thickness on the order of 100 nm or less – compared to several microns for commercial single-junction GaAs cells, and several hundreds of microns for commercial Si cells – are a promising avenue for developing more radiation-tolerant devices for space applications, in addition to increasing device flexibility, decreasing material use, and increasing specific power. For radiation tolerance, GaAs cells with absorber thickness 100 nm or less are especially interesting as they are expected to suffer little loss in the external quantum efficiency (EQE) due to current degradation with high radiation fluences for space power applications [108], since these cells are less sensitive to radiation-induced diffusion length degradation.

However, such ultra-thin layers of GaAs suffer from high transmission loss if no additional processing is done to improve light-trapping. Nanostructured diffracting arrays combining a metal and dielectric can boost absorption in the active layer, but must be designed carefully to balance parasitic absorption in the metal and maximise the benefit of reflection, diffraction and plasmonic effects due to the grating to increase absorption in the active layer, especially at wavelengths close to the bandgap of the photovoltaic material. Here, the design of metal/dielectric diffraction structures with hexagonal symmetry, to be used as a rear-side structured grating in an ultra-thin ($\approx$ 80 nm absorber layer) GaAs cell is discussed.

This section explores structures which can be fabricated using a pattern of hexagonally-arranged holes in SiN_x, followed by silver deposition to create a grating of silver disks in dielectric SiN_x. RCWA simulations are used to determine the optimal period and dimensions of the grating features. In addition, guided mode analysis, treating the structure as a waveguide, is used to investigate the origin of resonant features in the simulated absorption spectra. These structures could be fabricated through various methods, such as nanosphere lithography, or more conventional photo- or e-beam lithography techniques. Here, we consider structures fabricated through Displacement Talbot Lithography (DTL) [197, 198], which allows wafer-scale patterning of extremely regular structures with sub-micron features. There is considerable flexibility in the design space for metal/dielectric patterns which can be produced using DTL, and simulations are crucial in determining structures which most optimally increase the path length inside the cell while maintaining high rear-side reflectivity, low front surface reflection, and low parasitic absorption.

On-substrate precursor devices demonstrating good electrical performance have already been demonstrated, and the diode characteristics of these devices, which lack any light-trapping features, can be used to predict the expected electrical performance of the final structures including a dielectric/metal grating. Quantum efficiency measurements of the first round of processed devices with DTL-patterned SiN/Ag grating show evidence of diffraction leading to absorption enhancement in the GaAs, showing the potential of these device architectures. The device processing was done by Larkin Sayre in Dr. Louise Hirst's group at the University of Cambridge, while DTL to expose the grating took place in Dr. Philip Shields' group at the University of Bath. The electrical measurements and optical modelling are my own work.

6.1.1 Device growth and measurement

Samples were grown using molecular beam epitaxy (MBE) by IQE plc. on GaAs substrates. The targeted layer thicknesses are shown in Fig. 6.1a, and ellipsometry measurements showed the as-grown thicknesses (Fig. 6.1b) were within the 10% margin expected. The doping level of the GaAs in the p-n junction is 1 $\times$ 10^{18} cm^{-3}, using Be and Si as the p and n-type dopants respectively. Doping levels in the hole barrier, n-type contact and electron barrier are around 5 $\times$ 10^{18} cm^{-3} and the p-type contact is more highly doped at 10 $\times$ 10^{18} cm^{-3}.

The metal/dielectric grating is placed at the back of the structure with the aim of reducing parasitic absorption losses in the silver layer; any light which reaches the grating has already passed through the cell at least once. The final device design requires device processing followed by patterning of the nanostructured grating in an SiN_x layer using Displacement Talbot Lithography [197] to create a hexagonal array of holes in the SiN_x, deposition of a silver layer to complete the grating and for the back mirror, and finally lifting the device off by etching back the GaAs substrate and affixing the device to a mechanical substrate. The device structures and grating layout are shown in Fig. 6.1b and c.

To test device performance, fully front-contacted, on-wafer (Fig. 6.1a) devices with an area of 2.5 $\times$ 2.5 mm^2 were processed, without addition of the grating and lift-off from the substrate. These devices are

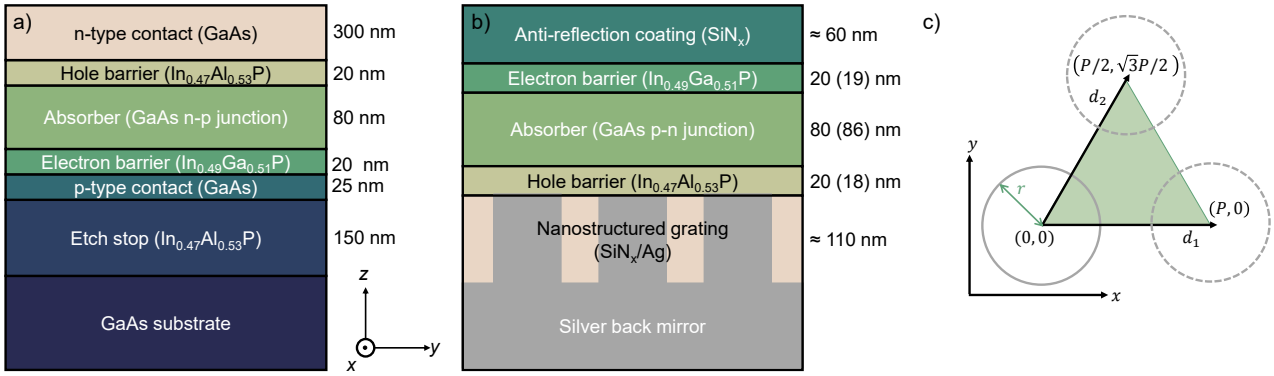


Figure 6.1: Schematic structures of a) the epitaxial wafer as grown, with target layer thicknesses, and b) the simulated device structure, also showing the coordinate axes x, y, and z used in the simulations relative to the device structure. The values in brackets in b) show the thicknesses of the epi-layers measured through ellipsometry (Appendix E), which are kept constant at these values in the simulations. c) Layout of the grating in the x-y plane: the lattice vectors $\mathbf{d_1}$ and $\mathbf{d_2}$ are shown, as well as their coordinates relative to the origin in one real space unit cell (shaded green) in terms of the grating period P. The location of the silver disks with radius r is shown; the solid line shows the disk belonging to the first unit cell, while the dashed line circles show those of subsequent unit cells removed by one lattice vector in the positive direction. This unit cell is assumed to repeat infinitely in the $\pm\mathbf{d_1}$ and $\pm\mathbf{d_2}$ directions for the simulations.

inverted relative to the final planned structures, but were used to measure the IV and EQE to check the device processing steps work as expected (Section 3.6). Expected absorption in the GaAs layer of these on-wafer devices was modelled using a transfer-matrix model (TMM) using Solcore (see Chapter 4.1), so that the IQE of the devices could be calculated by comparing calculated absorption and measured EQE. These IQE values were used to calculate predicted efficiencies for devices with light-trapping features. In addition, a first set of devices with grating structures was processed (see Section 6.1.6 for further details and results). For the measurements of the on-substrate devices, only a small area of the cell was illuminated during the EQE measurements and the loss is estimated at $< 2\%$. while for the ultra-thin cells with deposited grating structures, the whole cell area is illuminated by the solar simulator and the shading loss is estimated at 10%.

In order to obtain the optical constants of the key layers in the device structure to be used in the simulations, pieces of wafer with the structure shown in Fig. 6.1a were etched back selectively to expose different layers, down to the InAlP etch stop layer. This gave six samples for ellipsometry measurements (Section 3.2) with different top layers exposed. For each sample, the thicknesses of the layers and the optical constants of the top layer were fitted, starting from the sample with all layers except the InAlP etch stop removed through etching. By building up the layer model one material at a time starting with the thinnest sample, the thicknesses of all the layers and the optical constants of each material were obtained; the detailed results for each of the etched samples are given in Appendix E. The measured layer thicknesses were within the 10% range of the nominal values specified for the MBE process. A sample of 100 nm SiN_x deposited on Si in the same conditions which are used to fabricate the grating structures for the thin devices was measured to obtain optical constants for the SiN_x.

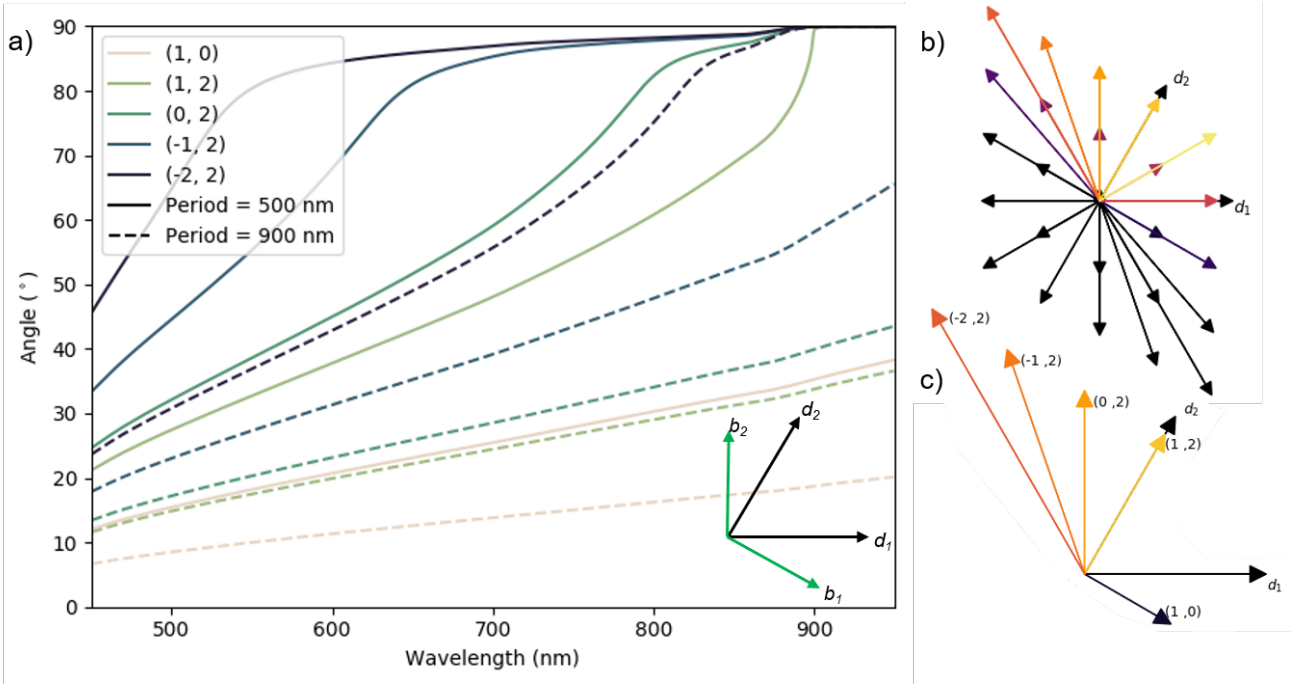


Figure 6.2: a) The directions, relative to the surface normal, at which different diffracted orders travel in GaAs. These directions depend on the period of the grating, and are shown for $P = 900$ nm and $P = 500$ nm. The direction of the lattice vectors $\vec{\mathbf{d}}$ and reciprocal lattice vectors $\vec{\mathbf{b}}$ are also shown. Note that the $\vec{\mathbf{d}}$ vectors were scaled down to unit length. b) Direction in real space of the 25 diffraction orders with m_1 and m_2 in the range [-2, 2]. c) Shows only the five unique orders from b), excluding (0, 0) which corresponds to specular reflection. The lattice vectors $\mathbf{d}$ are scaled in each diagram to have unit length.

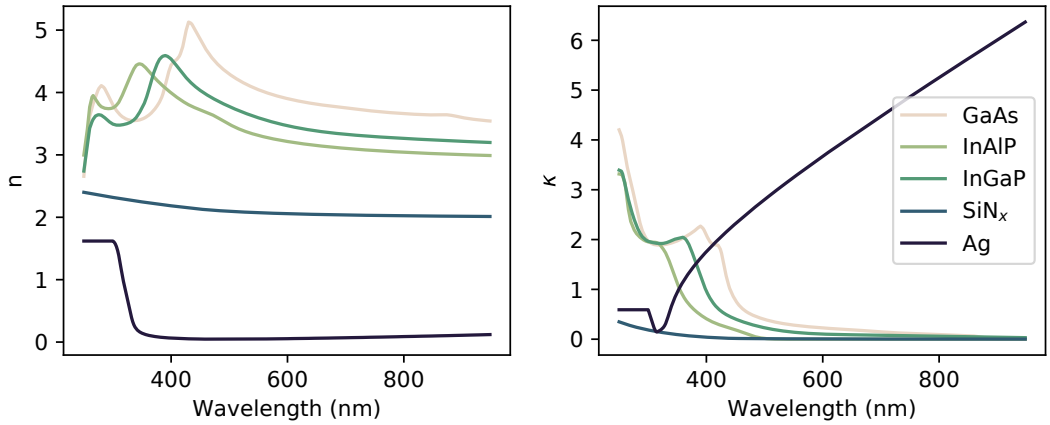


Figure 6.3: n and κ values for each material used in the simulations from fits to SE data, with the exception of the silver optical constants which are from [119]. Note that the data for Ag starts at 300 nm, and is assumed to be constant below this wavelength; this does not affect the simulation results since the III-V materials are very strongly absorbing at wavelengths < 300 nm, so no light reaches the Ag in the grating or back mirror.

6.1.2 RCWA simulations

The layer structure used for the RCWA optimization simulations is as given in Fig. 6.1b. The grating layout is shown in Fig. 6.1c, with unit vectors and relevant parameters indicated. A total of 43 diffraction orders were used, using circular lattice truncation which chooses the shortest possible G-vectors ($\vec{G} = m_1\mathbf{b_1} + m_2\mathbf{b_2}$). To find optimal grating structures, a grid search was performed, scanning through grating thicknesses and radius r of the disks in the hexagonal array at periods P of 500 nm, 600 nm and 700 nm (the period was varied in discrete steps to reflect the availability of existing masks for DTL). The thicknesses of the III-V layers, based on SE measurements, were kept fixed, and a simple single-layer anti-reflection coating made of 60 nm SiN$_x$ was included and kept at fixed thickness.

To analyse the origin of the resonant features and compare with the guided mode analysis, RCWA simulations spanning the range of grating periods 400-900 nm were carried out, keeping the grating thickness constant at 110 nm and the radius of the silver disks constant at $P/3$ (close to the optimum found during the first set of simulations for 500, 600 and 700 nm as discussed in Section 6.1.4). All simulations assumed normally-incident, unpolarized light.

To test the performance of the differential evolution (DE) optimization method (Section 3.7) for this problem, a similar optimization was carried out using this method. Comparing the results of the grid search against the computationally more efficient DE method indicates that the DE is capable of finding the overall maximum. The parameters optimized using DE, with allowed ranges given in brackets, are the disk radius (0-300 nm), the grating thickness (50-150 nm), the grating period (200-1000 nm) and the thickness of the SiN$_x$ ARC (20-150 nm).

6.1.3 Optical constants

The values of the optical constants obtained through fitting SE data of the etched samples are shown in Fig. 6.3, alongside the literature values used for Ag [119]. More detailed results of the ellipsometry fitting

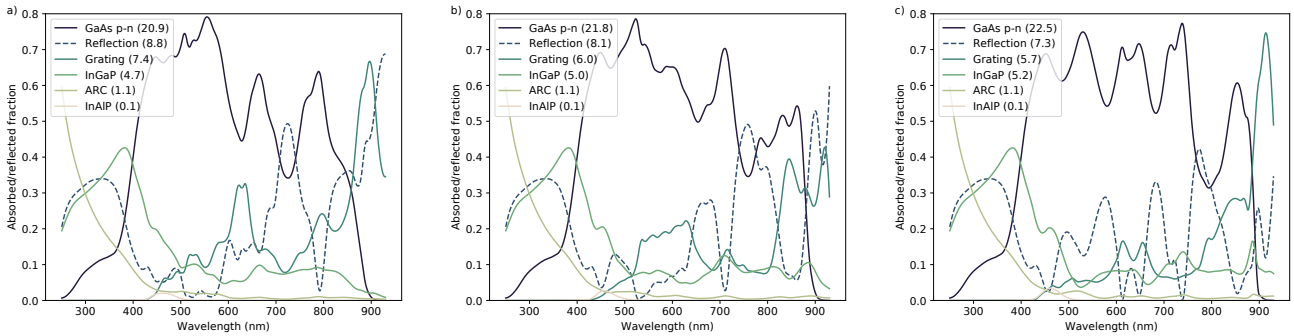


Figure 6.4: Absorption per layer, and reflection, for the structures with optimized grating with a) $P = 500$ nm, b) $P = 600$ nm and c) $P = 700$ nm. The numbers in brackets for the legend entries show the current which is generated in (or lost to) each layer/reflection.

procedure are given in Appendix E. The layer thicknesses from fitting SE data are the values shown in brackets in Fig. 6.1b. For all the layers, the measured thickness was close to the value targeted during growth, showing $< 10\%$ deviation. The fitted thicknesses, rather than the nominal values, were used to define the structures used in the RCWA and guided mode calculations.

6.1.4 Structure optimization

Grid search optimization

Optimization at $P = 500$ nm, 600 nm and 700 nm indicated that in each case, the ideal radius for the disks is close to one-third of the grating period; thus the percentage area coverage of silver and SiN_x for the optimum structures is constant at 40%. The optimum grating thickness varies slightly (100 nm for the 500 and 600 nm period gratings and 110 nm for the 700 nm period), but at grating thicknesses around 100 nm the photocurrent is not very sensitive to the exact thickness. The absorption per layer and reflectivity for the optimized structure at each P is shown in Fig. 6.4, in addition to the photogenerated current lost or generated in each layer. The 700 nm structure gives the highest photogenerated current in the GaAs at 22.5 mA/cm^2. The largest loss in each case is to reflection (which includes direct front surface reflection and light escaping through the front surface of the cell after one or more passes through the cell) followed by parasitic absorption in the grating. Additional simulations with more sophisticated ARC designs indicate that the simple, non-optimized ARC is not the main issue; it appears front surface reflection from the initial interaction of light with the cell is not the limiting factor, but rather light which escapes the cell on later passes. It is clear from Fig. 6.4 that in the wavelength range 550-900 nm, reflection is high away from the resonant peaks; where there is no efficient diffraction into guided modes, light is able to escape the cell. This effect is reduced somewhat by increasing the grating period from 500 nm to 700 nm, which gives more overlapping resonant peaks in this wavelength range, but cannot be avoided completely with this type of multi-resonant design. Absorption in the grid is expected due to the Ag content of the grating, but can also be seen as a transmission loss; since the grating is at the back of the cell, any light absorbed in the grating would likely have been lost through transmission if there was no light-trapping structure. At short wavelengths, there is high absorption in the InGaP electron barrier; although the simulations assumed that only light absorbed in the GaAs leads to useful photocurrent, the device results measured so far indicate

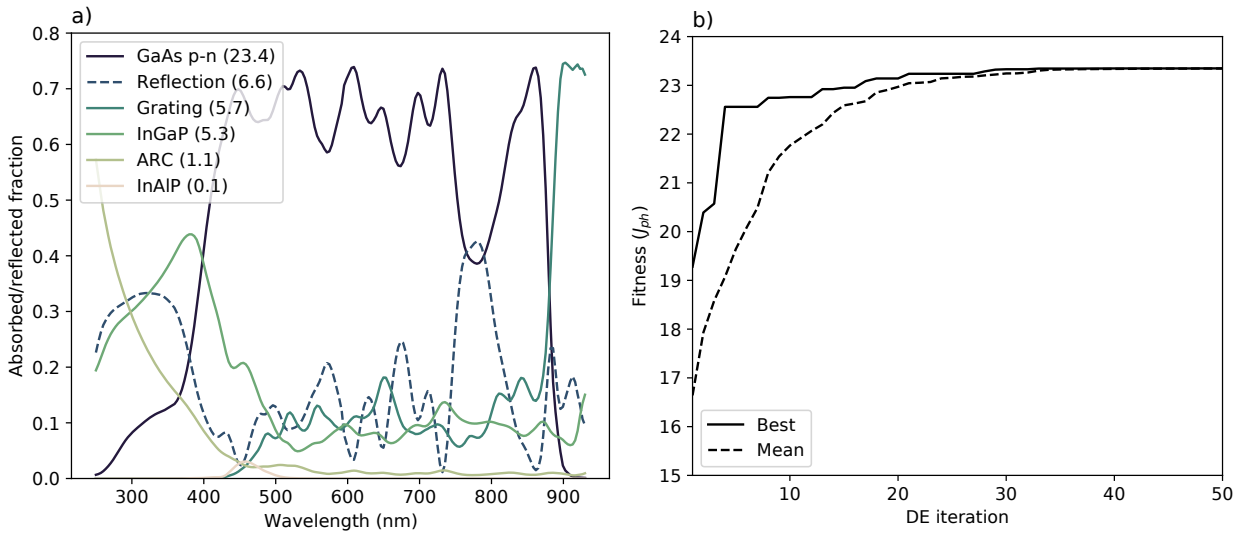


Figure 6.5: a) Absorption per layer and reflection for the ultra-thin GaAs cell optimized using differential evolution with $P = 685$ nm, $d_{\text{grating}} = 109$ nm and $r_{\text{disks}} = 251$ nm. b) Convergence of the differential evolution algorithm, using a population size of 20 sets of parameters for each iteration. The fitness (J_{ph}) of the best parameter set in the population and the mean of the population's fitness are shown.

that there is also very efficient collection of carriers from the InGaP (see Section 6.1.6).

Differential evolution optimization

The full grid search results give a useful opportunity to compare the performance of DE optimization. The absorption per layer and reflectivity for the structure optimized through DE are shown in Fig. 6.5a, in addition to the photogenerated current lost to or generated in each layer. The optimized structure has a period of 686 nm, a disk radius of 251 nm ($r/P = 0.37$), and a silver/SiN grating thickness of 110 nm. The thickness of the front surface ARC was also optimized in this case (during the grid search, it was fixed at 60 nm), giving a thickness of 58.6 nm. This result is in good agreement with the grid search; in that case, the best photocurrent was obtained for a period of 700 nm (as only discrete grating periods of 500, 600 and 700 nm were checked) with a disk size to period ratio of 0.33. The convergence of the differential evolution algorithm is shown in Fig. 6.5b, showing the fitness of the best population during each iteration and the mean performance of all the populations. The DE was run with 20 populations per iteration, meaning that over 50 iterations, a total of 1000 RCWA simulations are used to optimize the structure (as seen in Fig. 6.5b). In fact, good convergence has already been reached after around 35 iterations, or 700 simulations. For the grid search, the resolution is limited by the step size (for the results in Fig. 6.4, around 500 simulations were used to scan disk radii and grating thicknesses in steps of 10 nm). The differential evolution method does not have these resolution limitations, and also explored a much larger parameter space, showing that this optimization method is promising for such a computationally intensive problem with a large parameter space.

6.1.5 Guided mode analysis

For the guided mode analysis as explained in Section 2.3.2, the incident medium is air, while the guiding medium is taken to have a thickness equal to that of the III-V layers (123 nm) and optical constants equal

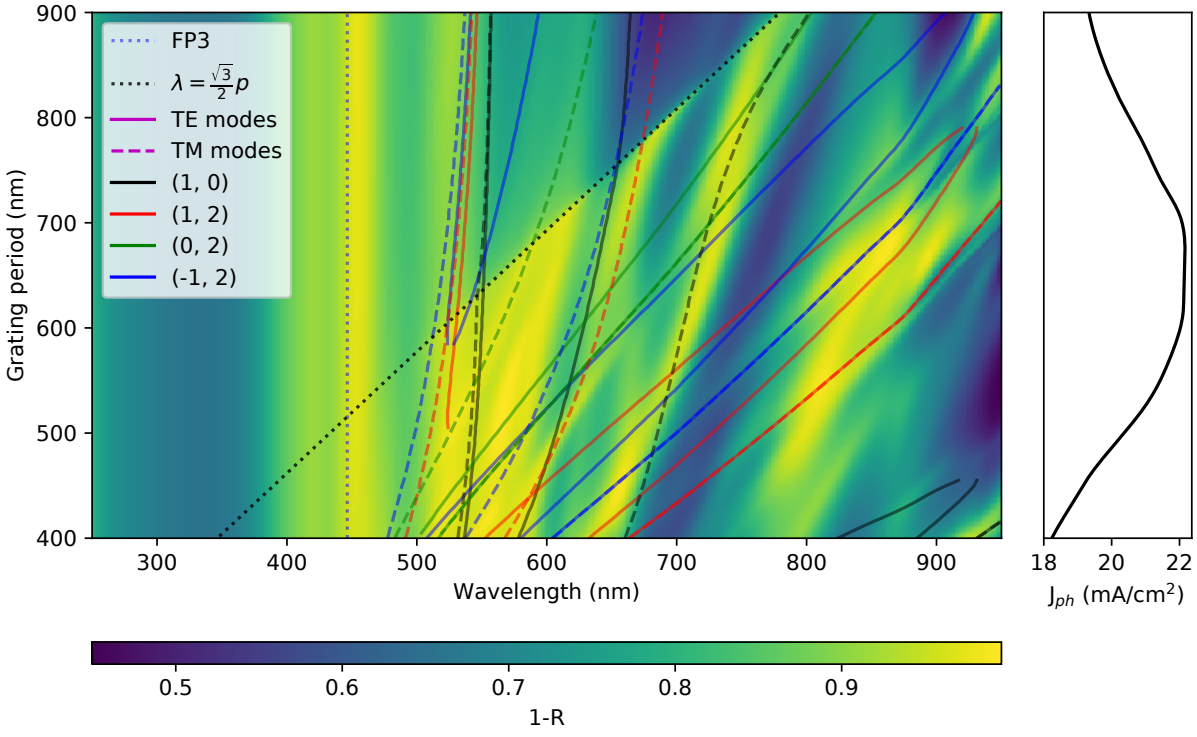


Figure 6.6: Values of $1 - R$ calculated using RCWA over wavelengths relevant for absorption in a GaAs cell, and TE (transverse electric) and TM (transverse magnetic) guided modes arising from diffraction into the allowed angles, over grating periods of 400-900 nm. The legend labels for the guided mode indicate the diffraction order (and thus the angle) the guided mode solution is associated with (see Fig. 6.2a). The radius of the silver disks is kept at $\frac{P}{3}$, close to the optimal values for grating periods 500-700 nm, which gives an area coverage of $\approx 40\%$ Ag in the Ag/SiN$_x$ grating. The J_{ph} in the GaAs, calculated using eq. 2.38 at each period, is plotted on the right-hand side. No diffracted orders can propagate in air below the line $\lambda = \frac{\sqrt{3}}{2}$, which is shown.

to the weighted average (by thickness) of the III-V layers. The bottom reflecting medium is taken to be a Ag/SiN_x metamaterial, with the optical constants given as a weighted average of those of Ag and SiN_x weighted by the fraction of the area covered by each.

RCWA calculations covering a range of grating periods P between 400 and 900 nm at relevant wavelengths for absorption in the GaAs cell, alongside allowed waveguide solutions calculated using the method described in Section 2.3.2, are shown in Fig. 6.6. The J_{ph}, calculated with eq. 2.38 using the simulated absorption in GaAs at each period, is also shown. While the agreement between the guided mode analysis and the values for $1 - R$ calculated using RCWA is not perfect, it is clear that the density of available modes does correspond to increased absorption observed in the RCWA-generated intensity plot, although most guided mode solutions do not match the intensity plot at all wavelengths. This indicates that the metamaterial description of the grating, and the assumption of a fixed thickness for the waveguide, are not sufficient to correctly describe the confinement of light in the cell at all wavelengths[1]. Note that not all the guided modes were plotted; there are several guided modes which mainly propagate at wavelengths below 500 nm, which are not visible in the RCWA calculations as the results here are dominated by front-surface reflection, high absorption at the front of the structure, and Fabry-Perot interference. No clear features corresponding to the guided modes arising from diffraction into the (2, -2) order are seen, so these solutions were also not plotted.

Considering the hexagonal symmetry of the grating, rearranging eq. 2.26 with the reciprocal lattice vectors for a hexagonal grating shows the vacuum wavelengths λ_0 at which orders can propagate is given by $\frac{\lambda_0}{n} \leqslant \frac{\sqrt{3}}{2}p$, with $n = 1$ for air/vacuum. This line is clearly visible in the simulated RCWA intensities in Fig. 6.6; above this line, at least one diffracted order can propagate in air, thus leading to higher values of R and lower values of $1 - R$.

The optimal period for the grating lies between 600 and 700 nm; the J_{ph} is not very sensitive to the exact period in this range. With a short grating period, many allowed guided modes are available but most of these propagate at wavelengths below 700 nm, which are less important for light-trapping. For periods above $\approx$ 700 nm, many of the available guided modes occur at wavelengths beyond the bandgap of GaAs, where absorption enhancement is not useful, and the larger grating period means diffracted light is also able to escape to the air at more wavelengths, increasing reflection.

6.1.6 Device measurements

On-substrate devices

EQE and IV results for the on-substrate test devices (which are inverted relative to the final envisioned device structure in Fig. 6.1b) are shown in Fig. 6.7. As expected, these devices have low EQE and thus low short-circuit current; this is expected as there is no anti-reflection coating, and thus front-surface reflection is high at all wavelengths, while transmission losses into the AlInP etch stop layer and GaAs substrate lead to further reduced EQE at longer wavelengths due to the extremely thin GaAs absorber layer. The measured EQE is very close to the absorption in the GaAs layer calculated using a TMM model in Solcore with the measured optical constants for the III-V layers. Around 370 nm, the EQE appears to slightly exceed the calculated absorption in GaAs, indicating there is some contribution to the current from the InGaP electron barrier at the front of the cell. Comparing the calculated absorption with the EQE gives internal quantum efficiencies (IQE) $>$ 85% over the wavelength range 350-820 nm. The overall efficiency of five measured

[1]It is possible to treat the waveguide in a more realistic way by using a full TMM model [199], rather than the simpler model of the asymmetrical waveguide.

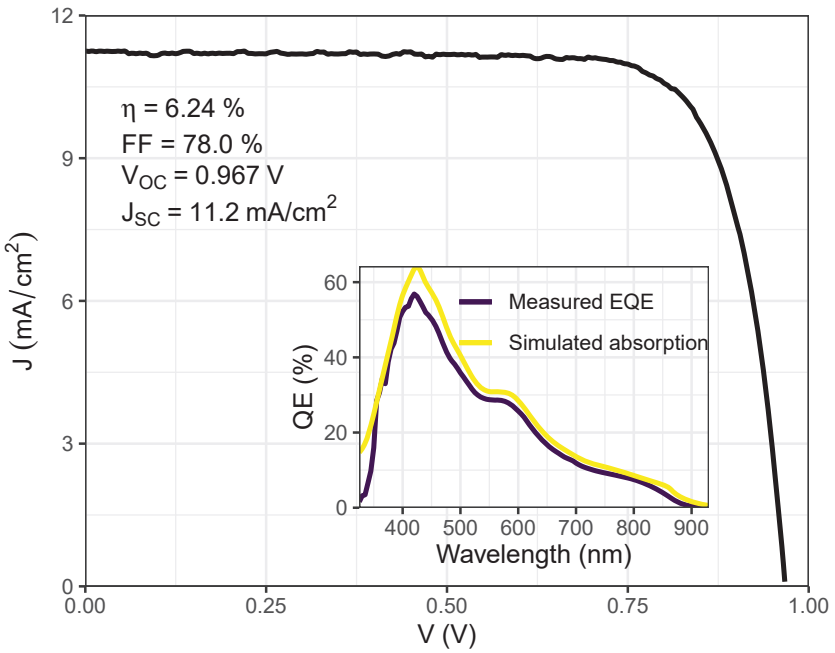


Figure 6.7: Light IV measurements under a simulated AM0 spectrum with the resulting efficiency η, fill factor, V_{oc} and J_{sc} for one of the on-substrate devices, and the EQE of the same device alongside simulated absorption in the GaAs layer for the on-substrate devices (inset).

devices with dimensions 2.5 x 2.5 mm^2 is 5.8 $\pm$ 0.4%, achieving good fill factors of 78 $\pm$ 1.0% and J_{sc} values of 10.8 $\pm$ 0.6 mA/cm^2 (six devices were measured, with one showing much lower V_{oc} and fill factor; this sample was excluded from these averages and standard deviations). The V_{oc} is 0.95 $\pm$ 0.02 V, below that expected for a high-quality thicker GaAs device (around 1.1 V for a high-quality device); this is expected, since the V_{oc} is related to the generated carrier density. In the devices with light-trapping structures, the increased absorption and carrier generation may thus lead to a higher V_{oc}. In addition, the relatively high doping of the GaAs in these devices appears to cause bandgap narrowing, reducing the V_{oc}; identical devices with doping levels of 10^{17} cm^{-3} rather than 10^{18} cm^{-3} in the p-n junction showed an improved V_{oc}.

Quantum efficiency measurement of processed devices

The first set of fully processed devices used a mask with period 500 nm to define the hexagonal grating. AFM and SEM measurements performed at the University of Cambridge showed that the holes etched in the SiN_x have a mean radius of 115 nm and a depth of 80 nm, while the total SiN thickness (measured through ellipsometry) is 103 nm. This indicates that the SiN_x was not etched all the way through during the fabrication process, meaning there is a planar layer of unetched SiN_x with a thickness of around 20 nm between the SiN_x/Ag grating and the InAlP hole barrier layer.

EQE measurements of these devices, performed at Cambridge, are shown in Fig. 6.8a, compared to the modelled absorption. The RCWA model used the dimensions measured for the grating thickness and disk radius, and assumes there is a 23 nm layer of planar SiN_x between the silver/dielectric grating (with thickness 80 nm) and the III-V materials. The EQE measurements show peaks between 500 and 950 nm which correspond to guided modes excited by the diffraction grating, although the peaks in absorption are

Table 6.1: Calculated photogenerated current J_{ph} for several structures, as well as predicted efficiencies η under an AM0 spectrum. Predicted efficiencies were calculated by shifting the light-IV curve for an on-substrate devices to values of the J_{sc} calculated through optical simulations. For structures with an optimized grating, the value of r/P is also given. The ideal double-pass absorption assumes zero front surface reflection ($A = 1 - e^{-2\alpha d}$) where $d = 86$ nm, the thickness of the GaAs layers, while the other structures all include a 60 nm SiN_x anti-reflection coating.

Structure	**Calculated J_{ph}** (mA/cm^2)	**Calculated J_{sc}** (mA/cm^2)	**r/P**	**η** (%)
On GaAs substrate	11.4	7.37	n/a	3.9
Lifted-off (air as substrate)	12	10.5	n/a	5.8
Planar Ag mirror as substrate	15.2	13.4	n/a	7.5
Best-performing grating ($P = 500$ nm)	20.8	18.2	0.33	10.4
Best-performing grating ($P = 600$ nm)	22.05	18.7	0.34	10.8
Best-performing grating ($P = 700$ nm)	22.5	19.2	0.33	11.1
Ideal double-pass	21.9	18.5	n/a	10.7

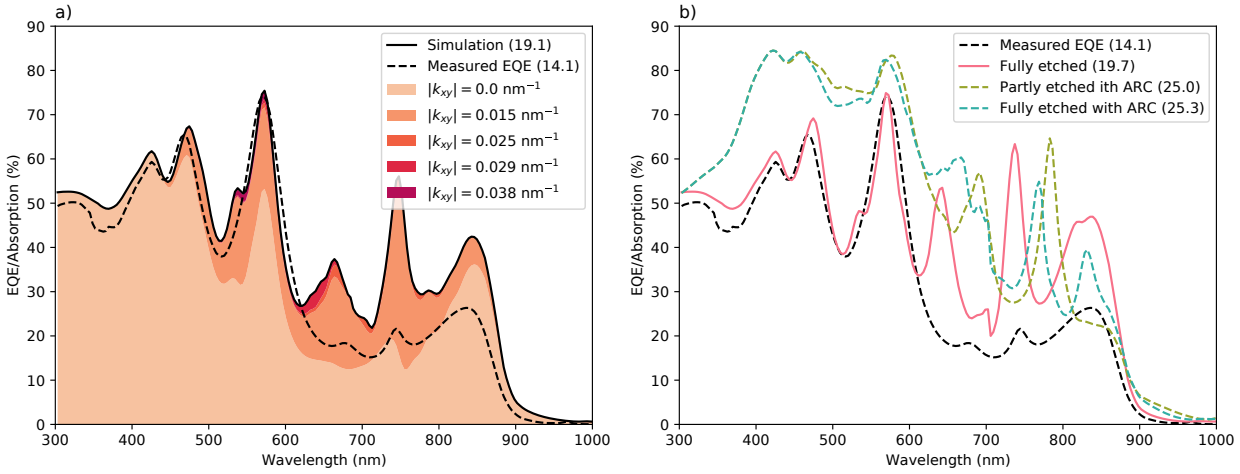


Figure 6.8: a) Comparison of the measured EQE for a lifted-off device with Ag/SiN_x grating and the modelled absorption for a structure corresponding to structural measurements of the devices. b) Comparison between the measured EQE, simulated EQE for a similar structure with the grating fully etched through the SiN layer, and both structures with an added anti-reflection coating (also simulations). The numbers in brackets in both plots give the photogenerated current in the GaAs and InGaP layers.

not as high as predicted from simulation based on the structure with a partially-etched grating. The model absorption plotted is the sum of absorption in the GaAs and the InGaP, assuming a uniform 10% loss due to contact shading, since the whole cell area was illuminated in these measurements. At short wavelengths, about 30% of the light is absorbed in the InGaP, but these EQE measurements indicate that almost all of the current from this layer is collected, showing excellent agreement between the combined simulated absorption in the GaAs and InGaP up to around 600 nm.

Fig. 6.8a shows the absorption in the GaAs/InGaP layers per diffraction order (defined by the in-plane magnitude of the wavevector $\mathbf{k}$); this shows that the measured EQE clearly has contributions due to diffracted orders, notably in the sharp peak around 570 nm. At long wavelengths, the measured EQE is lower than the theoretical prediction. This may be due to imperfections in the real structure leading to less efficient diffraction or electrical losses; the cause of this discrepancy is a matter of ongoing research. However, the very good match between measurement and theory at short wavelengths, and the qualitative match in the peaks above 600 nm, indicate that absorption enhancement using a metal/dielectric grating produced using DTL and the existing device process, including lifting off the thin cell, is achievable.

Despite the processing issues leading to a non-ideal grating, the DTL device already shows an improvement in the J_{SC}, from 11.2 mA/cm^2 for the planar device to 14.1 mA/cm^2. Fig. 6.8b shows the potential improvement in photogenerated current if the grating were fully etched (with the same disk radius and grating thickness as the fabricated device), and the benefit of adding a 70 nm Al_2O_3 ARC, with the latter predicted to improve the photocurrent by around 6 mA/cm^2. Such Al_2O_3 ARC layers will be used for the first set of devices.

6.1.7 Predicted efficiencies

Table 6.1 shows the calculated photogenerated currents for various structures, calculated through simulation using either TMM or RCWA, and predicted efficiencies. For the grating structures, the constant value of the optimized $\frac{r}{P}$ indicates an area coverage of about 40% silver gives the best absorption enhancement.

While the predicted efficiencies for the grating structures are not especially high for a GaAs cell, they are significantly improved compared to a thin cell without light trapping and are able to match or slightly exceed the values for ideal double-pass absorption. These efficiencies could be improved further by considering a more advanced anti-reflection coating; in addition, the V_{oc} may improve with the better light trapping of the devices with gratings due to higher generated carrier concentrations. Investigating other grating geometries with symmetry-breaking elements, which could be fabricated using DTL [200] could yield higher photogenerated current, as decreased grating symmetry leads to more unique diffraction orders and associated available guided modes.[2]

6.1.8 Conclusions

Using a grating of hexagonally arranged metallic disks in a dielectric, the predicted efficiency of an ultra-thin 86 nm GaAs solar cell can be increased by close to a factor of three compared to an on-substrate device. For cells targeted towards space applications, this indicates a promising pathway for developing much thinner GaAs cells with increased radiation tolerance and reduced need for protective cover glass. Using a waveguide analysis, the origin of resonant features and the approximate optimum period for a hexagonal grating can

[2]The efficiencies in Table 6.1 were calculated using the AM0 (space) spectrum. Efficiencies under an AM1.5 spectrum would be higher as there are fewer infrared photons which do not generate carriers in GaAs; the predicted efficiency of the cell with an optimized 700 nm grating is 13% under AM1.5.

be understood further. Precursor devices without light-trapping features show good IQE and fill factor, and excellent agreement with a TMM model for absorption. Processed devices with silver/dielectric gratings manufactured through Displacement Talbot Lithography show good quantitative agreement with RCWA simulations at short wavelengths, with qualitative agreement and clear evidence of absorption enhancement due to diffraction. Future work will focus on improving the quality of the grating and investigating different grating periods and arrangements to boost device performance further.

6.2 Emissivity of heterojunction devices in the infrared

As discussed in Section 1.5.3, the thermal emissivity of solar cells plays an important part in the operating temperature of a device. When designing a hybrid solar PV/thermal system, the aim is to capture as much of the heat as possible, and prevent it from being radiatively emitted. Recent work at Imperial College focused on determining the magnitude of the emissivity of aluminium back surface field (Al-BSF) c-Si solar cells, and investigating which layers in the cell cause their high emissivity (around 80% in the infrared). This work showed that most of the infrared emissivity in Al-BSF cells is mainly caused by the highly-doped back surface field and emitter layers. In the specific cell that was investigated, the thickness of the emitter layer and BSF are 55 nm and 4.3 µm respectively. The work in this section was done as part of further investigation into the emissivity of silicon solar cells, focusing on an alternative type of device: heterojunction (SHJ) cells [171]. Unlike Al-BSF cells, the SHJ cell lacks highly-doped layers, using ITO on the front and rear surfaces instead. (see Fig. 6.9). As such, these devices were expected to have low absorptivity and therefore emissivity in the infrared, below the bandgap of c-Si.

6.2.1 Methods & structures

The layer structure of the SHJ cell is shown in Fig. 6.9, with the layer thicknesses given in Table 6.2. The emissivities of two different cells (produced at Arizona State University in Dr. Stuart Bowden's group) were measured experimentally: a SHJ cell with an 80 nm layer of ITO on the front (Structure 1), and the same structure without the front ITO layer (Structure 2). The optical constants of the different types of amorphous silicon and ITO layers were obtained through fitting ellipsometry data (Section 3.2) and are shown in Fig. 6.11. The absorptivity/emissivity data was measured using a Bruker Vertex 70 Fourier-transform infrared spectroscopy (FTIR) system equipped with a gold-coated integrating sphere and a liquid nitrogen-cooled HgCdTe detector. The absorptivity measurements discussed in this section were done by Dr. Diego Alonso-Álvarez, while the ellipsometry over the full wavelength range was carried out by Lourdes Ferre Llin at the University of Glasgow.

For the absorptivity/emissivity simulations, the front and back surface are modelled as having upright, square-base pyramidal textures with an opening angle of 55° (the standard opening angle for randomly etched silicon pyramids). First, a lookup table is calculated using the TMM code which includes the reflection, transmission and absorption probabilities for a ray arriving at the relevant layer stack at a particular incidence angle and wavelength. The 3D ray-tracer uses this data by checking the local incidence angle (which is not the same as the overall incidence angle due to the surface texture) and looking up the relevant probabilities for each interaction of the ray with the surface, until the ray is finally reflected or transmitted. By scanning through incidence angles and across the surface texture in the x-y plane, the ray-tracer is used to build up the redistribution matrices for the front and back surfaces (using 12 million rays in total).

The pyramidal structure on these samples is random, but the surface structure used in the simulations is regular. Tucher et al. [86] demonstrated by comparing simulation and experiment that because the angular matrix method does not preserve position information of the rays between interactions with the front and back surfaces, the results of an angular matrix calculation using redistribution matrices for regular pyramids matches more closely with the experimental results for random pyramids. The front surface stack sitting on the pyramidal Si surface is the intrinsic a-Si, p+ a-Si, and finally the ITO layer (only for Structure 1), as shown in Fig. 6.10a. The stack sitting on the rear pyramidal Si surface is intrinsic a-Si, n+ a-Si and the ITO-IR (see Fig. 6.10b). Note that the front and back ITO do not have the same optical properties, as they

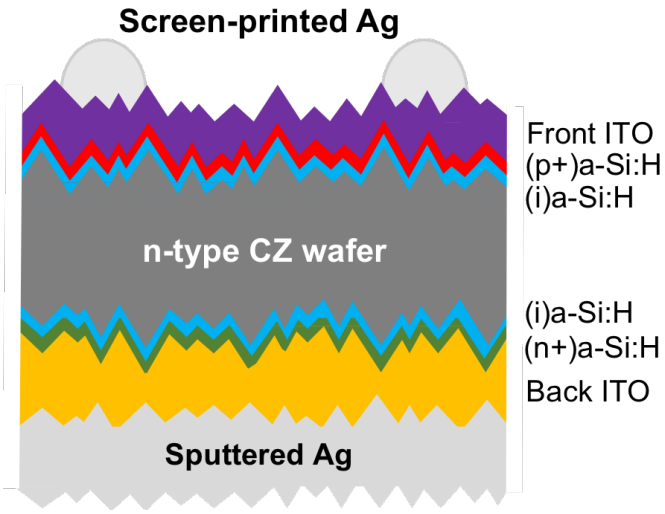


Figure 6.9: Structure of a silicon heterojunction solar cell.

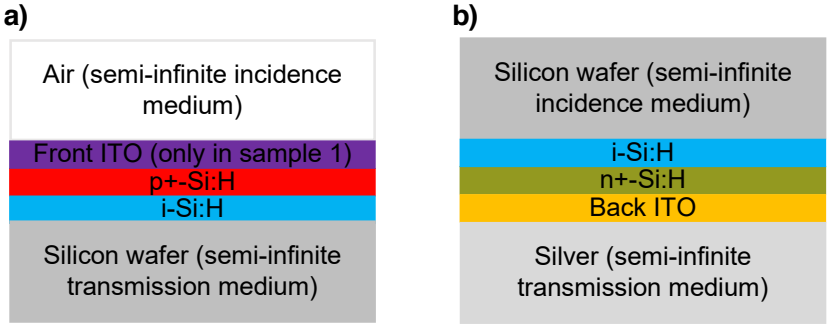


Figure 6.10: The layers used to calculate R, A and T probabilities using TMM for a) the front surface and b) the rear surface

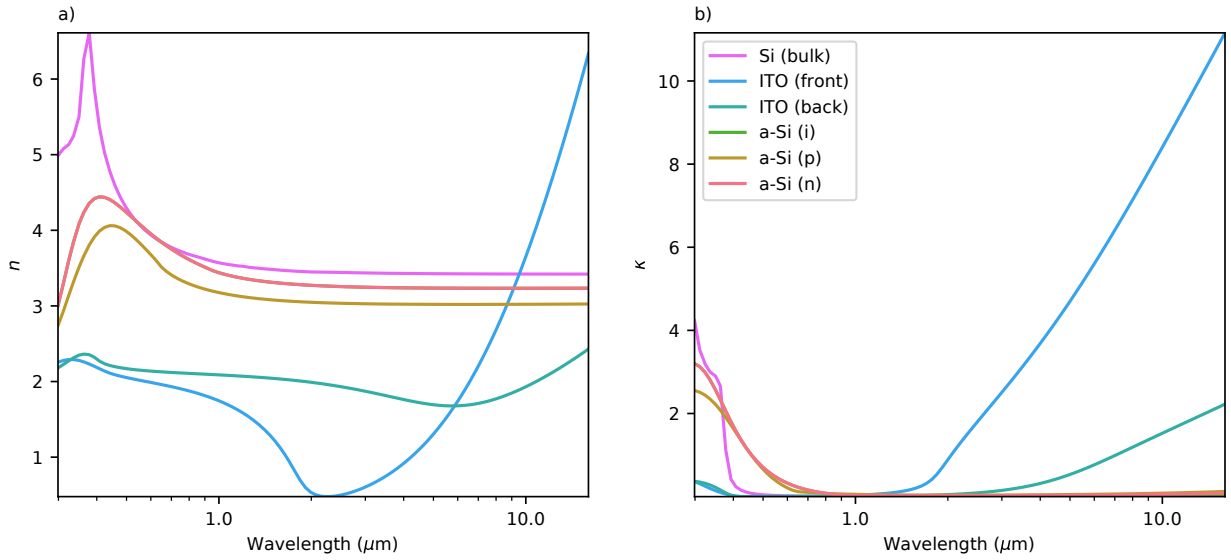


Figure 6.11: a) Real part n and b) imaginary part κ of the refractive index for the layers in the silicon heterojunction cell, obtained through fits to ellipsometry data.

Table 6.2: Layer thicknesses in the SHJ structure shown in Fig. 6.9, and the optical constant sources for each layer.

Layer	**Thickness**	**Source for optical constants**
Si wafer	170 µm	[129] (short wavelengths) and [201] (long wavelengths)
Front ITO	80 nm*	Ellipsometry
p+-Si:H	6-7 nm	Ellipsometry
i-Si:H	6-7 nm	Ellipsometry
n+-Si:H	6-7 nm	Ellipsometry
Back ITO	240 nm	Ellipsometry
Ag	240 nm	[202]

* = this layer is only present in Structure 1.

have different doping levels. The silver on the back stack is the semi-infinite transmission medium in the calculations, although the silver layer on the real cells is only 240 nm thick; silver is highly absorbing, and photons which enter it will be absorbed within the first few tens of nanometres. Thus, treating this layer as semi-infinite does not affect the simulation results.

6.2.2 Results

The results of the absorptivity simulations and measurements are shown in Fig. 6.12. Looking at the wavelength range which is relevant for photovoltaic function (≈ 1.1 µm and below), removing the front ITO clearly reduces absorption in the c-Si and will thus degrade solar cell performance. Removal of the front ITO leads to slightly lower emissivity just below the c-Si bandgap, but in the long wavelength range, the total emissivity rises and is equal to or higher than the cell with front ITO. This is somewhat surprising as the main source of absorption/emission below the bandgap of c-Si for Structure 1 (Fig. 6.12a) is the front stack, in which the ITO is the thickest and most highly absorbing layer. Intuitively, it seems that removing this layer would reduce the overall emissivity of the cell; however, this is not the case, as shown in Fig. 6.12b.

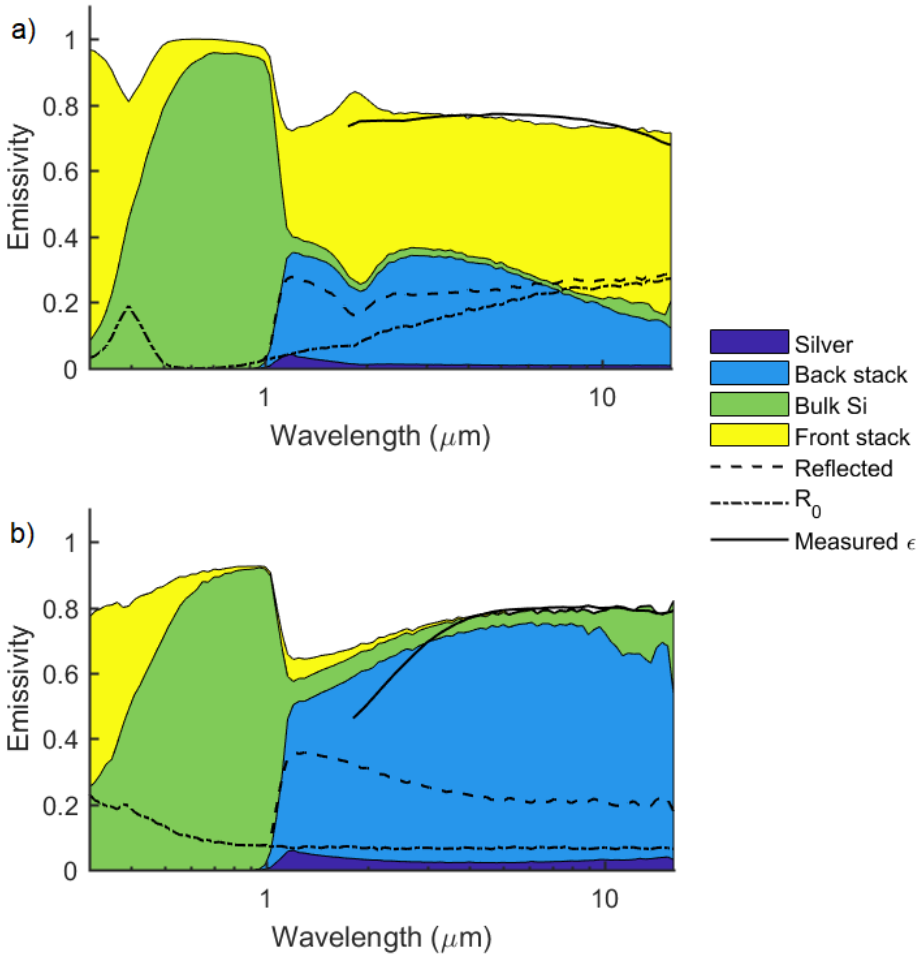


Figure 6.12: Modelled emissivity results for a) an SHJ cell with 80nm of ITO on the front surface (Structure 1) and b) the SHJ cell without the front ITO (Structure 2). The contributions to the emissivity of the different part of the cells (front, bulk, back and Ag) are shown, as well as the front surface reflectivity (R_0) and the total power reflected.

Although the absorption in the front stack is now almost zero, the absorption in the back stack has increased significantly. In both cases, the absorption in the c-Si silicon wafer is low below the bandgap (as expected). When the front stack becomes mostly transparent, light is still trapped very well inside the texture due to the pyramidal structures, and gets absorbed in the back texture after one or more passes through the cell; in the cell with ITO on the front, far fewer photons have a chance to reach the back stack, but if the front stack is removed, most photons are eventually absorbed in the back stack. Although the extinction coefficient κ of the ITO-IR on the back of the cell is about an order of magnitude lower than that of the front ITO in the > 1 µm wavelength range, the back ITO layer is thicker, and the absorption is non-negligible. The effective light-trapping in the structure due to the pyramidal surfaces means that the light may have many interactions with this layer, increasing its likelihood of being absorbed.

The plots in Fig. 6.12 distinguish between the total reflected power, i.e. all the light which is travelling backwards at the end of the simulation, and R_0, the light which is reflected during the first interaction of the light with the front surface. The total reflection can be higher than R_0 if light can make at least two passes through the bulk, and some light escapes through the front surface upon subsequent interactions with it. Thus, at short wavelengths, where all the light is absorbed in one or two passes, $R_0 = R_{total}$, while $R_{total} > R_0$ at longer wavelengths where the cell is more transparent. For the cell with ITO, R_0 increases with wavelength and contributes to a slight reduction in emissivity, while for the cell without ITO it stays very constant at $< 10\%$ for wavelengths > 1 µm. This means that more light enters the cell without ITO at longer wavelengths (R_0 is lower), but a significant fraction ($> 10\%$) escapes the cell on subsequent interactions with the front surface.

In both cases, the simulations correctly reproduce the trend in the measured absorption data at long wavelengths. There is a noticeable discrepancy between experimental and modelled data in the 2-4 µm wavelength range, i.e. at wavelengths above the bandgap of c-Si but before the onset of free carrier absorption in Si. These differences are likely related to the uncertainty in the determination of the values of κ for c-Si when these are extremely small and thus difficult to measure. The data used in the simulations for the bulk Si is constructed from literature sources, using published data for Si with a similar doping level at long wavelengths [201] and thus the exact extinction coefficient at intermediate wavelengths may not be exactly the same as the Si in the cells. Because the light may make many passes through the cell, a small difference in the absorption coefficient can affect the simulation results quite significantly.

6.2.3 Designing low-emissivity cells

Fig. 6.13 shows two alternative optical designs, with different ITO layer thicknesses. Both have 70 nm of ITO on the back surface, significantly reduced from 240 nm. Fig. 6.13a, showing the results for a structure with 70 nm of ITO on the front surface, shows reduced emissivity compared to Structure 1; absorption in the front stack is more or less the same (the only change is the ITO thickness changing from 80 nm to 70 nm), while the thickness of the back ITO is reduced, and thus absorption is reduced. Increasing the thickness of the front ITO gives even lower emissivity, perhaps counter-intuitively, as this front stack was initially highly absorbing. Fig. 6.13b shows the lowest emissivity, for a structure with 160 nm of ITO on the front. The low absorption seems to be mainly due to high R_0; the surface reflectivity of the cell is significantly affected by the front surface ITO thickness. While this structure has low emissivity, it also shows reduced absorption in the Si at the wavelengths relevant for photovoltaics (< 1.1 µm) compared to the other cell designs, which will lead to a reduced efficiency of the solar cell.

These results show that designing a structure with high absorption in the relevant wavelength range for

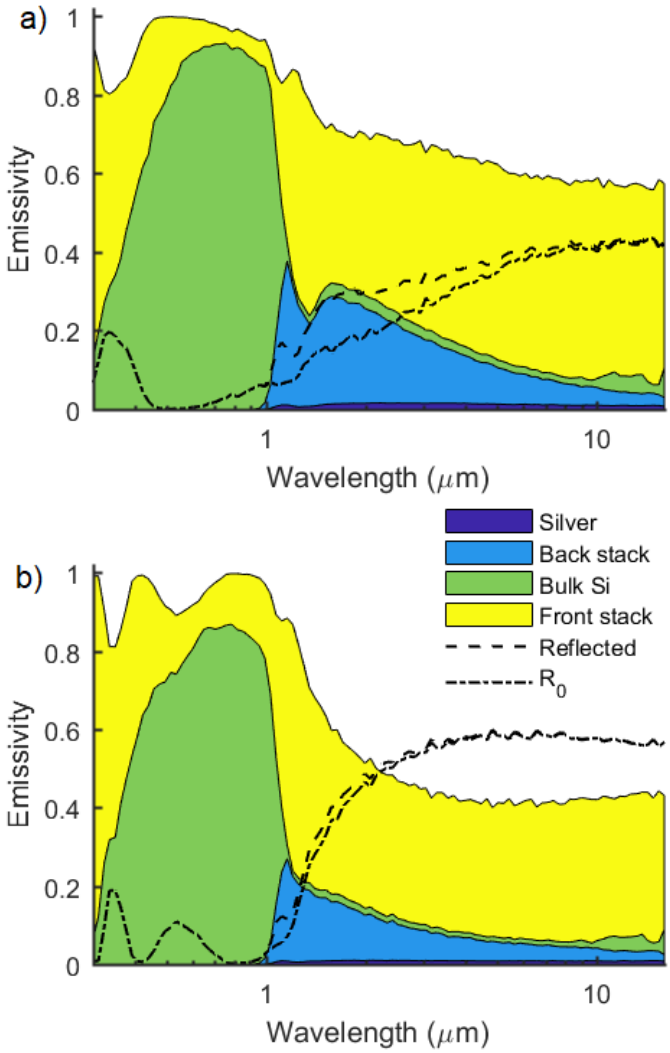


Figure 6.13: Modelled emissivity results for a) a SHJ cell with 70nm of ITO on the front surface and b) a SHJ cell with 160 nm of ITO on the front surface. Both cells have 70 nm of back ITO. The contributions to the emissivity of the different part of the cells (front, bulk, back and Ag) are shown, as well as the front surface reflectivity (R_0) and the total power reflected.

photovoltaic operation and low emissivity in the infrared is not trivial; both the nature of the doped layers and their thicknesses must be carefully tuned, and thin-film interference effects in the surface textures play an important role. The exact extinction coefficient of the layers, which tends to be very doping-dependent in the infrared also plays an important role.

6.3 Application of Solcore to spectrum-splitting multi-junction cell design

A spectrum-splitting solar cell is a device in which some part of the solar spectrum which cannot be used by a cell is purposely reflected away from the cell, for instance onto a second device which can use this part of the solar spectrum. The motivation for using a spectrum-splitting design with a triple-junction device is that in a 'standard' 3J cell, due to the combination of bandgaps, the Ge cell overproduces current compared to the middle and top cells, as discussed in Section 1.3. Since the cells are connected in series in a monolithic design, this overproduced current cannot be used, as under a standard AM1.5 solar spectrum the middle cell (InGaAs) is current-limiting.

The overproduction of current in the Ge sub-cell is illustrated in Fig 6.16b and 6.18b for lattice-matched and metamorphic AzurSpace solar cells, respectively. The current overproduction is more significant in the lattice-matched cell, since the metamorphic cell is specifically designed to improve current-matching by increasing the fraction of InAs in the middle junction and the fraction of InP in the top junction. This lowers the bandgap of the InGaAs and InGaP slightly, meaning that more current can be generated in those junctions and fewer photons are able to reach the Ge. Changing the alloy composition means the cell is no longer lattice-matched, so grading layers must be included between the Ge and InGaAs layers to accomodate the change of lattice constant.

If some light in the wavelength range above ≈ 950 nm (below the bandgap of GaAs) but below ≈ 1130 nm (the bandgap of Si) can be selectively reflected before reaching the Ge, the performance of the 3J cell will not suffer but the reflected light, which is otherwise wasted, can be directed onto a second solar cell (an obvious choice for the second solar cell in a practical application is an Si cell, due to their low cost). However, we do not want to take any current (photons) away from the middle or top cells. Earlier work by collaborators at UNSW illustrated this spectrum-splitting concept by using a separately manufactured dielectric filter on top of the cell to reflect part of the solar spectrum onto an Si cell[203] (see Fig. 6.14). However, rather than using an expensive, separate dielectric filter, it is also possible to incorporate the reflector into the solar cell stack during epitaxial growth by inserting a distributed Bragg reflector (DBR) below the GaAs cell, as shown in Fig. 6.15.

Solcore's improved TMM capability (Section 4.1.1) was used to model spectrum-splitting triple-junction solar cells designed by collaborators at UNSW [204]. The basic structure is based on commercially-available AzurSpace triple-junction cells, designed to operate under 800× concentration. The additional element is an integrated selective reflector, a DBR, which reflects specific infrared wavelengths which are then directed onto an Si cell (see Fig. 6.15), with the ultimate aim being to exceed 50% overall efficiency. Several triple-junction devices involving spectrum-splitting distributed Bragg reflectors (DBR) were designed by Dr. Yajie Jiang at UNSW through purely optical simulations; based on these designs, Solcore simulations for the full systems (triple-junction cell plus Si cell) were constructed.

6.3.1 Cell designs

A number of cell designs were considered, with DBR structures with a different number of layers; here, the reference structures, based on AzurSpace lattice-matched (LM) and metamorphic (MM) cells, and the best-performing DBR designs for the LM and MM case are shown. Full results for all the cell designs can be found in [204]. To calculate the overall efficiency, Solcore first calculates reflection, transmission, and total and depth-dependent absorption in the 3J cell with light incident at a 45° angle; this information is

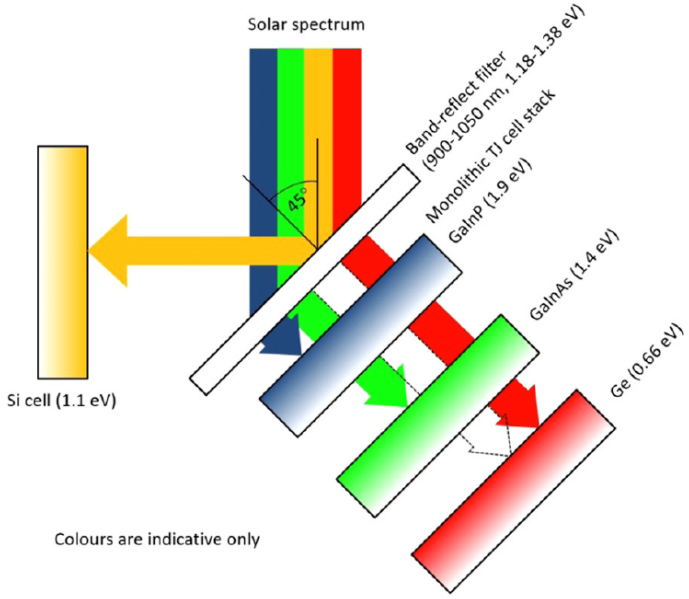


Figure 6.14: Schematic of a spectrum-splitting setup design with a selectively reflecting dielectric filter in front of the 3J cell. From [204]. A DBR can be incorporated into the solar cell instead of this separate filter.

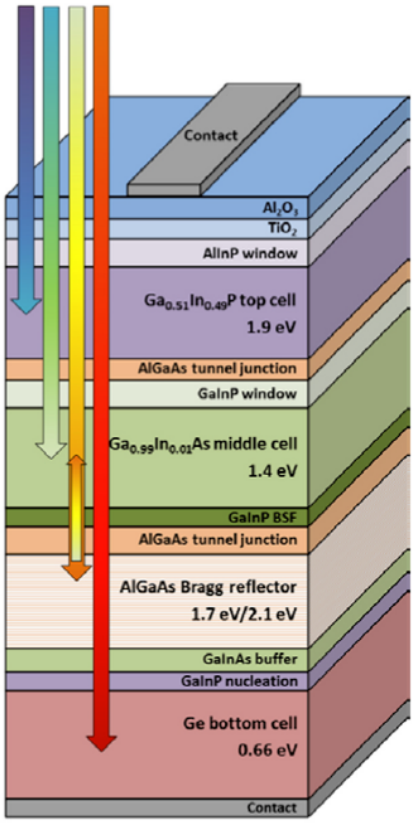


Figure 6.15: Schematic of the lattice-matched 3J cell structure. From [204].

Table 6.3: The sub-cell short-circuit currents and efficiencies of the different 3J cell designs, and the Si cell and total efficiencies for the spectrum-splitting designs. The results for the 'standard' cell are calculated at normal incidence at 800× concentration, reflecting how these cells would be used in a standard concentrator setup. The results for the modified cells with spectrum-splitting DBRs are calculated at an incidence angle of 45°, so the effective concentration is reduced to $800/\sqrt{2}$ (since Solcore calculates results per unit area). In each case, the sub-cell current results are divided by the effective concentration, so they are scaled to 1 Sun illumination.

Device structure	InGaP J_{SC} (mA/cm^2)	InGaAs J_{SC} (mA/cm^2)	Ge J_{SC} (mA/cm^2)	3J η (%)	Si η (%)	Total η (%)
Original LM TJSC (1×16 bilayer DBR) @ 0°	12.5	11.9	17.7	39.8	n/a	39.8
LM TJSC (3×16 bilayers) @ 45°	13.2	12.8	12.6	40.8	4.46	45.2
Original MM TJSC (no DBR) @ 0°	13.6	12.7	16.5	40.1	n/a	40.1
MM TJSC (2×16-bilayer DBR + 8-trilayer buffer) @ 45°	13.4	13.0	13.3	39.6	3.45	43.1

fed into the electrical solver (using the depletion approximation [145] in this case) which calculates the EQE and light IV curves under an AM1.5D spectrum at 800 × concentration, and thus the efficiency of the 3J structure. The AM1.5D spectrum includes only direct sunlight, since concentrator cells cannot make use of diffuse sunlight like large-area flat-plate PV. In order to calculate the efficiency of the silicon cell onto which the reflected light is directed, its incident spectrum needs to be defined; this is given by the reflectivity of the 3J cell multiplied by the incident spectrum at each wavelength, taking into account the concentration of the incident spectrum. This information is used to define a new, custom spectrum in Solcore, which is used to calculate the efficiency of an Si cell. The Si cell was specified using measured EQE from a high-quality concentrator Si cell [205]. The simulations are carried out for unpolarized light; computationally, this means repeating the TMM calculations for both s and p-polarized light and averaging the result. Since the final layer of the cell (the Ge sub-cell base layer) is, at 30 µm, very thick compared to the wavelength of light considered, it was treated incoherently in the calculations (see Section 4.1.1); this is both to speed up the calculation, but is also physically more accurate, as treating the layer coherently results in thin-film oscillations with an extremely small period in the wavelength, which are not observed in measurements.

6.3.2 Results

The AzurSpace LM cell already incorporates a DBR made of 16 bilayers of AlGaAs of varying compositions under the InGaAs junction (see Fig. 6.15), to maximise the current in the middle cell (usually the current-limiting cell in this type of 3J architecture) by reflecting light near the bandgap of GaAs. The EQE and light IV of the cell are shown in Fig. 6.16. Due to the DBR, there is already a significant spike in the reflectance around 900 nm, as shown in Fig. 6.16c.

The optimized LM structure incorporates a 3 × 16 bilayer AlGaAs DBR, optimized to reflect light at slightly longer wavelengths than the DBR in the original cell. This is to avoid the atmospheric absorption band at 950 nm, as there are few photons in that part of the terrestrial solar spectrum to be reflected onto the Si cell. Fig. 6.17 shows the results of the electrical solver, assuming light incident at 45°. The light reflected onto the Si cell (see Fig. 6.17c) gives an additional 4.5% efficiency relative to the power in the concentrated AM1.5G spectrum, thus increasing the total efficiency of the system by 5.4 percentage points.

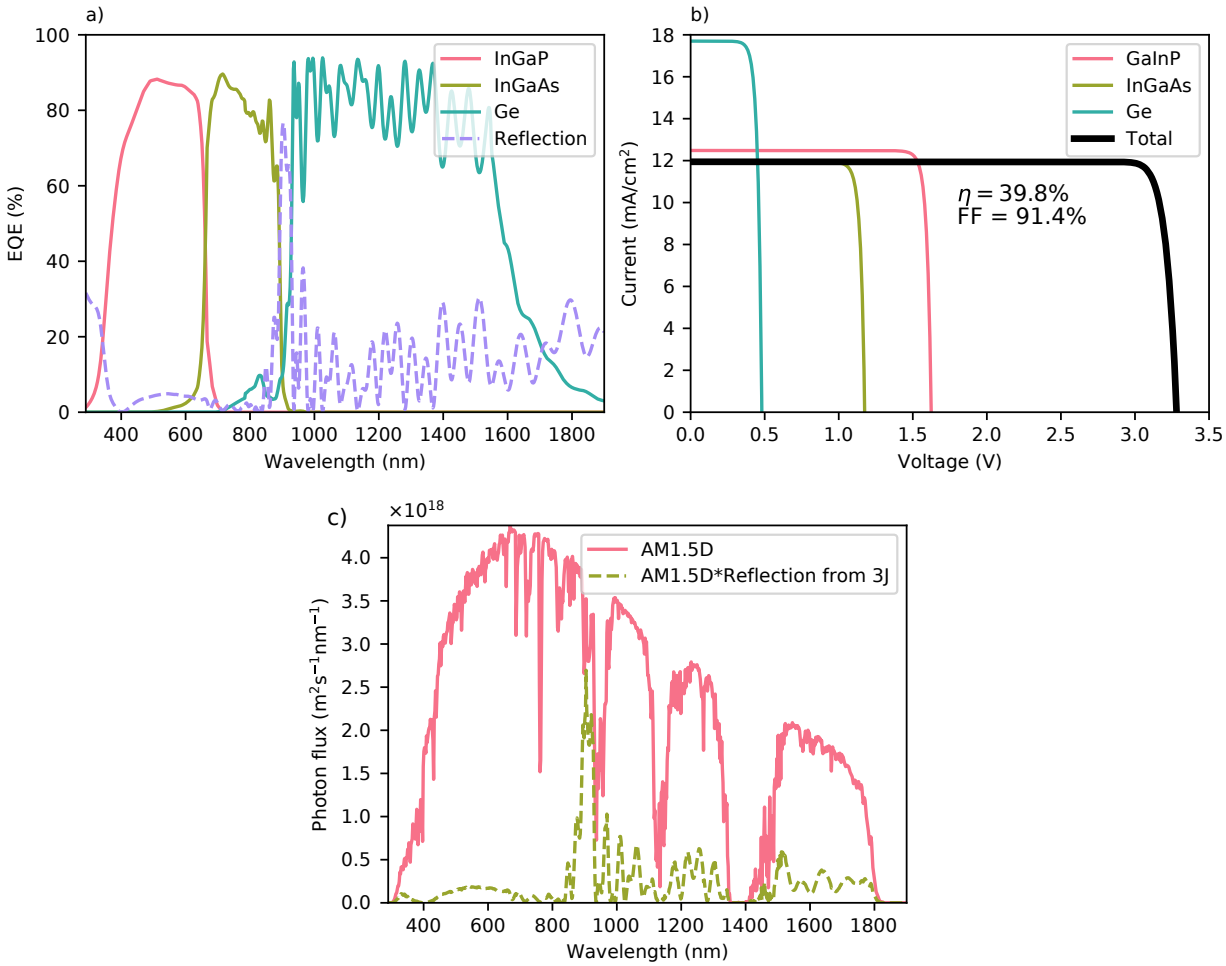


Figure 6.16: a) The EQE and b) the light IV of the standard 3J LM cell modelled at normal incidence. The sub-cell currents are shown divided by the concentration (800×). The efficiency and fill factor are also shown. c) The AM1.5G solar photon flux (divided by the concentration), and the spectrum reflected (solar photon flux × reflectivity of the 3J cell at normal incidence) from the standard LM 3J cell.

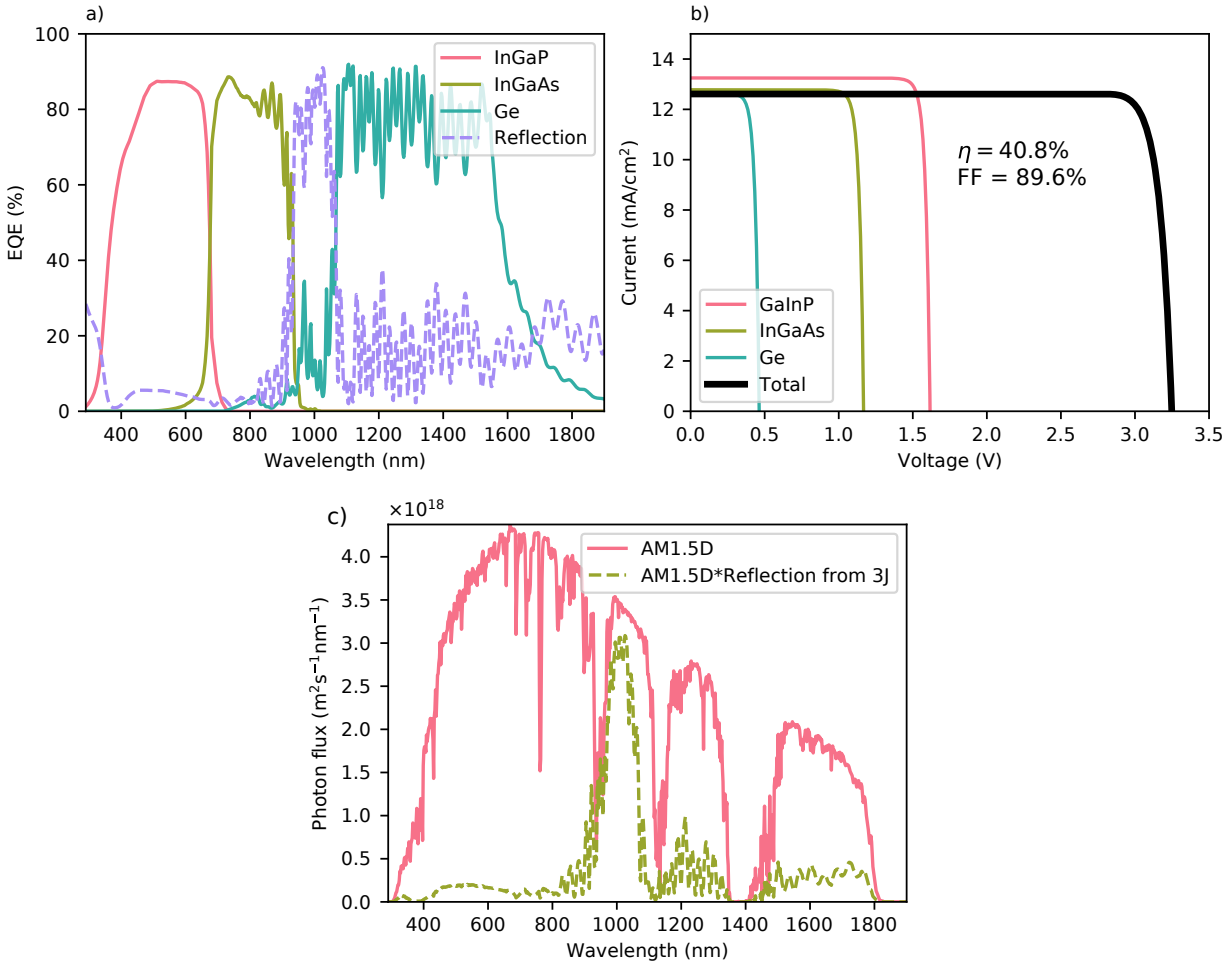


Figure 6.17: a) The EQE and b) the light IV of the 3J LM cell with spectrum-splitting DBR modelled at 45° incidence. The sub-cell currents are shown divided by the concentration ($800/\sqrt{2}$). The efficiency and fill factor are also shown. c) The AM1.5G solar photon flux (divided by the concentration), and the spectrum reflected onto the Si cell (solar photon flux × reflectivity of the 3J cell at 45° incidence) from the LM 3J cell with spectrum-splitting DBR.

The current in the Ge sub-cell has decreased by 5 mA/cm^2 (Table 6.3) compared to the standard 3J design, bringing the current in line with the other two sub-cells.

Since the MM structure already has improved current-matching compared to the LM cell, it does not include a DBR. Unlike the standard 3J LM cell, there is thus no clear peak in the reflectance before the insertion of a spectrum-splitting DBR, as shown in Fig. 6.18c. In the MM structure, the top two cells are grown at a slightly different lattice constant to Ge, and to accommodate this, an 8-step buffer layer of graded InGaAs compositions is grown between the Ge and InGaAs cell. This means the Ge sub-cell does not overproduce current as significantly as in the LM cell (see Table 6.3). Designing the spectrum-splitting DBR here is complicated by the fact that the change in lattice constant must still be accommodated with a combined DBR/grading buffer. The full, optimized DBR + buffer layer structures are shown in Figures 7 and 8 in [204]. The best efficiency was obtained using a 2 $\times$ 16-bilayer DBR + 8-trilayer buffer, with EQE and IV results shown in Fig. 6.19. The spectrum reflected onto the Si cell is shown in Fig. 6.19c. The efficiency is slightly reduced compared to the original MM cell (by half a percentage point) due to increased front surface reflection at more oblique incidence, but the total efficiency of the 3J + Si cell system is 3 percentage points higher than the original MM cell.

Although the original LM cell performs worse than the MM design, these simulations show that it is actually more suited to the spectrum-splitting application, since a large number of photons in the long wavelength range can be directed onto an Si cell without the Ge cell becoming current-limiting. Further work in this area is being carried out using the Solcore's differential evolution capabilities, developed over the course of the PhD, to design DBR layers with high selective reflectivity and overall device structures to be grown.

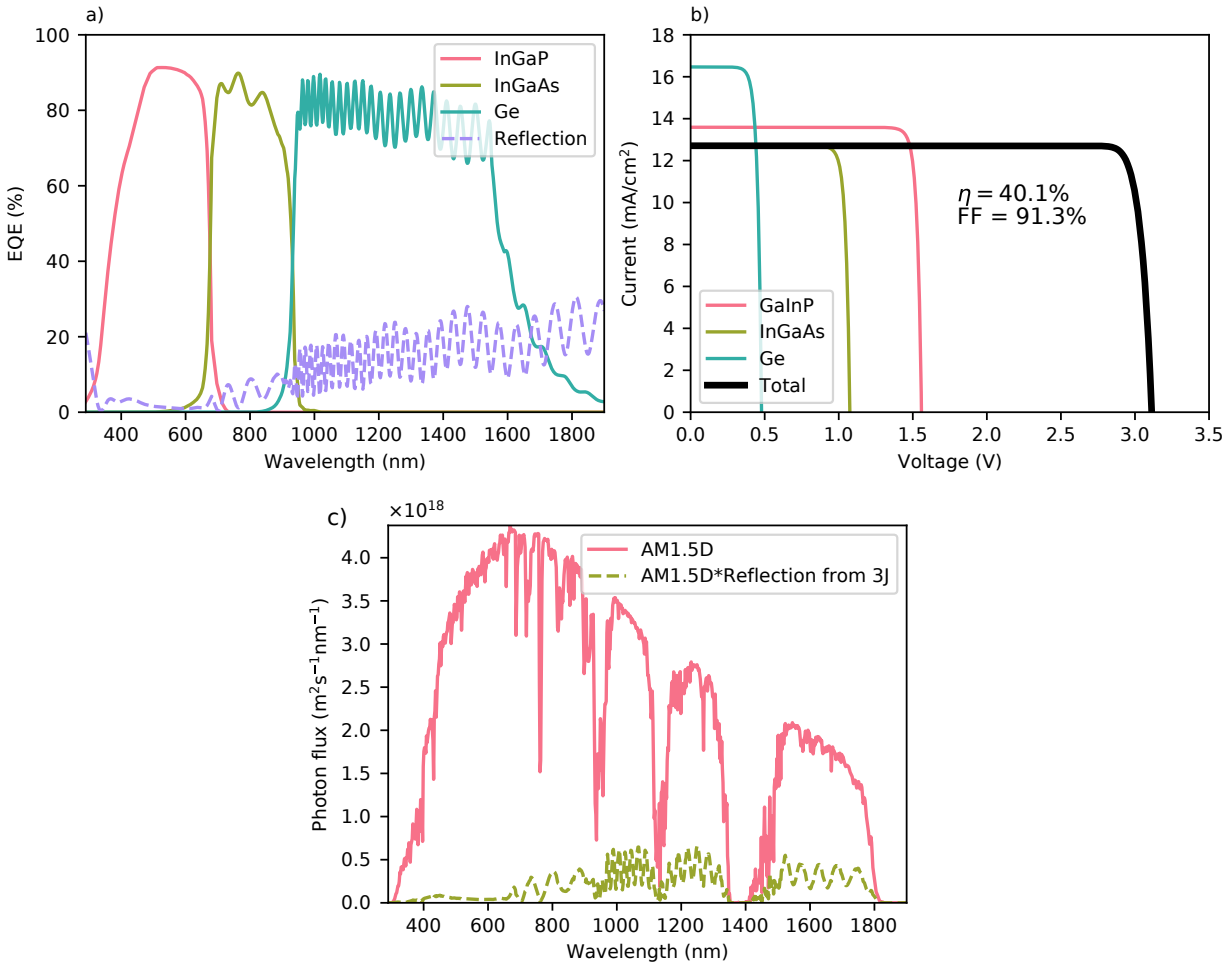


Figure 6.18: a) The EQE and b) the light IV of the standard 3J MM cell modelled at normal incidence. The sub-cell currents are shown divided by the concentration (800). The efficiency and fill factor are also shown. c) The AM1.5G solar photon flux (divided by the concentration), and the spectrum reflected (solar photon flux $\times$ reflectivity of the 3J cell at normal incidence) from the standard MM 3J cell.

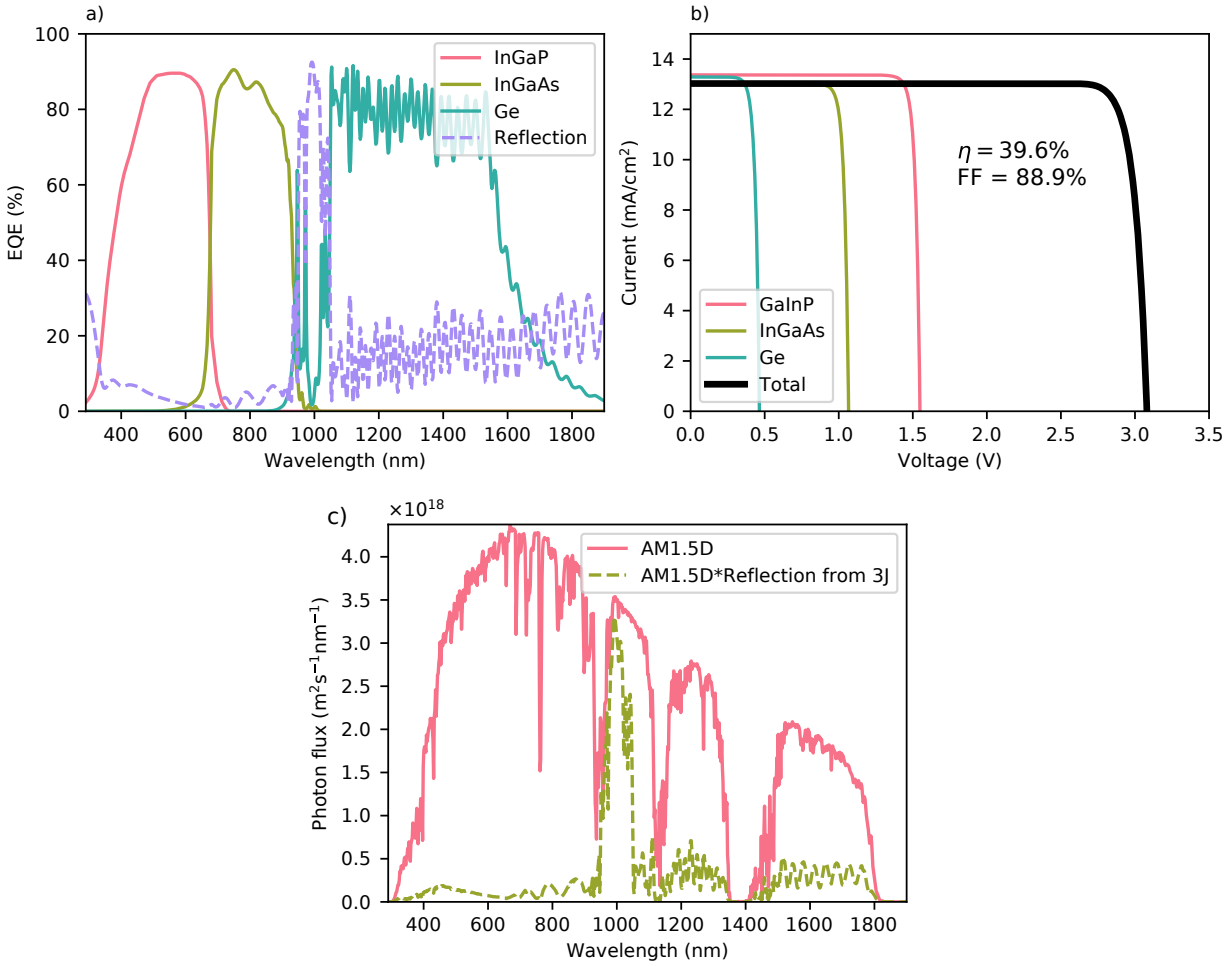


Figure 6.19: a) The EQE and b) the light IV of the 3J MM cell with spectrum-splitting DBR modelled at 45° incidence. The sub-cell currents are shown divided by the concentration ($800/\sqrt{2}$). The efficiency and fill factor are also shown. c) The AM1.5G solar photon flux (divided by the concentration), and the spectrum reflected onto the Si cell (solar photon flux × reflectivity of the 3J cell at 45° incidence) from the MM 3J cell with spectrum-splitting DBR.

Chapter 7

Conclusions

Improving the efficiency of solar cells requires the identification and growth of high-quality semiconductor materials and careful design of the overall device architecture. Chapter 5 detailed the results of extensive material study of SiGeSn, a candidate material to fill the niche for an absorber with a 1 eV absorption edge at the same lattice constant as Ge and GaAs, for use in multi-junction solar cells. Choosing the optimal combination of bandgaps for a multi-junction cell is necessary for another key aspect of the device design: optimizing absorption in the photovoltaic layers, whether that is distributing the absorption of the solar spectrum between sub-cells to achieve current-matching in a multi-junction cell, or maximizing the absorption in a single-junction cell (such as an ultra-thin GaAs device or a textured silicon solar cell). Chapter 4 outlined the development of integrated optical modelling tools in Solcore and RayFlare, which enable research into a wide range of device architectures, such as those presented in Chapter 6.

7.1 Development of optical modelling tools

Chapter 4 covered the wide range of optical modelling methods which have been developed and implemented over the course of the PhD. The transfer matrix method capability of the existing solar cell modelling package Solcore was expanded to allow for incoherent calculations and variation of the angle and polarization of the incident light, and the materials-related functionality of Solcore was expanded to allow users to add their own materials to the database easily. A new Python interface with the RCWA Maxwell solver S^4 was implemented, to make wavelength-dependent calculations of useful values such as reflection, transmission, absorption per layer and absorption profiles possible for structures containing wavelength-scale periodic features. A new ray-tracer was implemented in Python, capable of calculating reflection, absorption and transmission probabilities directly through the Fresnel equations or in conjunction with the TMM method for multi-layer interfaces. All these methods were integrated with an angular matrix framework in the new Python package RayFlare, which makes it possible to combine multiple modelling methods for a single structure. These methods have been validated against existing models and previously-published results, showing excellent agreement. Both Solcore [161] and RayFlare [162] are fully open-source and available as Python packages.

The improvement of RayFlare and Solcore, as well as the compatibility between the two packages, is an ongoing project. Specific improvements to RayFlare include using statistical methods to improve the speed of the ray-tracing and angular matrix algorithms. Speed improvements to computationally intensive parts

of the code (such as the RCWA and ray-tracing algorithm) may also be possible through CPU or GPU acceleration. As both packages are open-source and open to outside contributions and updates to the code, the aim is for development of the packages to be in part guided by other users and contributors.

The results of optical simulations are affected significantly by the exact optical constants used for the materials; this is especially important for structures containing metallic scattering layers such as diffraction gratings. This effect was quantified, showing that the use of inaccurate optical constants can lead to an incorrect optimal structure being identified in optimization problems. Thus, obtaining realistic data for metallic optical constants is key to matching experiment and simulation. This provides a strong motivation for researchers to obtain optical constants of the metal films produced in their own facilities prior to designing a light-trapping structure, since the optical constants of metals will vary depending on the deposition method. Where direct determination of the optical constants is not possible, due caution must be taken to use alternative data that corresponds well to the expected deposition conditions. Following the investigation of the effect of differing optical constants on the effectiveness of a metal/dielectric grating, a new figure of merit, the Spectral Absorption Enhancement Factor (SAEF), has been proposed which predicts the suitability of a metal film for light-trapping applications. The SAEF can be determined directly from a metal's optical constants using a simple analytical expression, and has been found to correlate well with the photocurrent enhancement expected when that metal is used in an optimized light-trapping structure, as determined by rigorous simulations. This finding is useful for researchers and technologists, since it guides material choice, and allows deposition processes to be optimized without the need to repeatedly perform nano-fabrication and/or optical simulations for each deposition iteration.

Further work in this area will focus on investigating whether the correlation between the SAEF and optimized photocurrent holds true for other device structures and materials (e.g. a grating on the rear of the cell rather than the front, different grating symmetry and layout, different absorber thicknesses, and different metal/dielectric combinations in the grating).

7.2 Application of SiGeSn to multi-junction cells

SiGeSn is a promising candidate material for solar cells and other optoelectronic applications, with previous experimental and theoretical results indicating that a direct transition energy at 1 eV can be achieved with $< 10\%$ Si and $< 3\%$ Sn, with the resulting alloy being lattice-matched to Ge. The results of spectroscopic measurements presented in Chapter 5 confirm these results, showing E_0 energies between 0.85 and 1.02 eV for alloys with compositions of 2.6-9.6% Si and 0.8-2.5% Sn. Photoreflectance and spectroscopic ellipsometry were used to measure the lowest direct transition energy E_0, in both cases using a critical point fitting approach. The two methods gave transition energy values in good agreement with each other, and clearly show a blueshift of the key transitions determining the absorption edge with increasing Si and Sn composition. A novel method for fitting the photoreflectance data was developed to extract values of E_0 and $E_0 + \Delta_0$ from the raw data, incorporating both the critical points due to van Hove singularities in the band structure and thin-film interference effects due to modulations of the refractive index. Ellipsometry was also used to examine the higher-energy direct transitions, showing good agreement with previously-published results.

Photoluminescence measurements were used to investigate the lower-energy indirect transitions, showing evidence of multiple phonon peaks, as observed in the PL of pure germanium, and demonstrating photoluminescence of SiGeSn grown on Ge and GaAs substrates for the first time. Identifying the strongest PL peak by analogy with the luminescence spectrum of germanium, increases in the fundamental bandgap of

40-80 meV from the Ge bandgap of 0.67 eV at room temperature were observed. Therefore, the SiGeSn alloy compositions considered here remain fundamentally indirect, although absorption is dominated by the lowest available direct transition (E_0) which was shown to be tuneable to $\approx$ 1 eV, useful for a range of multi-junction device architectures.

Finally, the information on optical constants and the location of the fundamental bandgap extracted from these extensive spectroscopic measurements were used to inform device models, optimized using differential evolution. These models are useful for predicting realistic limiting efficiencies for multi-junction devices containing high-quality epitaxial SiGeSn. Device designs for two, three and four-junction cells were presented, showing efficiencies over 30% under 1 Sun illumination in all cases. The triple junction cell architectures ($In_{0.5}Ga_{0.5}P/In_{0.01}Ga_{0.99}As$/SiGeSn) show a possible improvement of around 4 percentage points over the well-established $In_{0.5}Ga_{0.5}P/In_{0.01}Ga_{0.99}As$/Ge triple-junction cell through an increase in the voltage.

Further work will focus on the growth and processing of epitaxial structures for single and multi-junction cells, initially involving InGaAs and InGaP, and characterizing the electrical performance of these devices.

7.3 Optical design of advanced devices

The modelling techniques developed and implemented over the course of the PhD have enabled the investigation of a wide range of cell architectures, from ultra-thin devices ($<$ 100 nm) with diffraction gratings to silicon devices hundreds of microns thick, which were discussed in Chapter 6.

A combination of RCWA simulations and guided mode analysis was used to optimize a hexagonal grating of silver disks in dielectric silicon nitride, predicting that the photocurrent of ultra-thin ($<$ 100 nm) GaAs solar cells can be more than doubled compared to a cell without light-trapping. The power of differential evolution as a tool for optimizing optical structures was demonstrated by comparing its results to a grid search. Electrical measurements of on-substrate devices and the proof-of-concept devices incorporating a silver/dielectric grating show a good match with the optical simulations. Despite some remaining processing issues, the device with a grating produced through Displacement Talbot Lithography already shows an enhanced photocurrent compared to the planar device. Work to deposit anti-reflection coatings and complete electrical measurements of the devices with gratings is ongoing, in addition to further simulation and theory work to understand the principles behind optimal grating design within the constraints of available photolithography methods suitable for large-area patterning.

Controlling the emissivity of solar cells is key to their temperature regulation. In a hybrid thermal-PV system, where the aim is to generate electricity and capture heat from the solar cell, a low emissivity in the infrared is desirable to maximize the amount of heat which can be extracted. The RayFlare angular matrix formalism was used to calculate the effects of pyramidal textures with thin-film layers on the light-trapping in a silicon heterojunction solar cell over a wavelength range from the UV to the mid-infrared, showing excellent agreement with experimental results. The model results shed light on which layers lead to high emissivity, which cannot be determined from the experiments alone, showing that due to the efficient light-trapping in the cell even layers with low absorption coefficients can contribute significantly to the total absorption.

Finally, Solcore was used to model spectrum-splitting triple-junction solar cells incorporating distributed Bragg reflectors which reflect part of the solar spectrum onto a separate Si cell. Using a part of the solar spectrum which is normally wasted in conventional triple-junction cell architectures, these systems can achieve efficiencies over 45% under 800$\times$ solar concentration, with a boost of up to 5 percentage points compared to the triple-junction cell by itself. Work is currently ongoing to design spectrum-splitting structures which

will be fabricated, so that the full spectrum-splitting setup with an Si cell can be tested experimentally. These structures are being designed using Solcore's optical models and differential evolution, implemented over the course of the PhD.

Bibliography

[1] International Energy Agency IEA. *World energy balances and statistics – Data services - IEA*. 2020. URL: https://www.iea.org/subscribe-to-data-services/world-energy-balances-and-statistics (visited on 08/03/2020).

[2] IRENA (International Renewable Energy Agency). *Renewable capacity highlights (31 March 2020)*. Tech. rep. 2020.

[3] Ngai Lam Alvin Chan, Helen E. Brindley, and Nicholas John Ekins-Daukes. "Impact of individual atmospheric parameters on CPV system power, energy yield and cost of energy". In: *Progress in Photovoltaics: Research and Applications* 22.10 (Oct. 2014), pp. 1080–1095. ISSN: 10627995. DOI: 10.1002/pip.2376.

[4] Michael Woodhouse et al. *Crystalline Silicon Photovoltaic Module Manufacturing Costs and Sustainable Pricing: 1H 2018 Benchmark and Cost Reduction Roadmap*. 2019. URL: https://www.nrel.gov/docs/fy19osti/72134.pdf (visited on 09/28/2020).

[5] Martin A. Green et al. "Solar cell efficiency tables (Version 55)". In: *Progress in Photovoltaics: Research and Applications* 28.1 (Jan. 2020), pp. 3–15. ISSN: 1062-7995. DOI: 10.1002/pip.3228.

[6] Louise C. Hirst and Nicholas J. Ekins-Daukes. "Fundamental losses in solar cells". In: *Progress in Photovoltaics: Research and Applications* 19.3 (May 2011), pp. 286–293. ISSN: 10627995. DOI: 10.1002/pip.1024. arXiv: 1303.4604.

[7] Brendan M. Kayes et al. "27.6% Conversion efficiency, a new record for single-junction solar cells under 1 sun illumination". In: *Conference Record of the IEEE Photovoltaic Specialists Conference* (2011), pp. 000004–000008. ISSN: 01608371. DOI: 10.1109/PVSC.2011.6185831.

[8] William Shockley and Hans J. Queisser. "Detailed balance limit of efficiency of p-n junction solar cells". In: *Journal of Applied Physics* 32.3 (1961), pp. 510–519. ISSN: 00218979. DOI: 10.1063/1.1736034.

[9] Y Okada et al. "Intermediate band solar cells: Recent progress and future directions". In: *Applied Physics Reviews* 2.2 (June 2015), p. 021302. ISSN: 1931-9401. DOI: 10.1063/1.4916561.

[10] Anthony Vaquero-Stainer et al. "Semiconductor nanostructure quantum ratchet for high efficiency solar cells". In: *Communications Physics* 1.1 (Dec. 2018), p. 7. ISSN: 2399-3650. DOI: 10.1038/s42005-018-0007-6.

[11] Roland B Piper et al. "Kinetic insight into bimolecular upconversion: experiment and simulation". In: *RSC Adv.* 4.16 (2014), pp. 8059–8063. ISSN: 2046-2069. DOI: 10.1039/C3RA46953K.

[12] Louise C Hirst et al. “Hot Carriers in Quantum Wells for Photovoltaic Efficiency Enhancement”. In: *IEEE Journal of Photovoltaics* 4.1 (Jan. 2014), pp. 244–252. ISSN: 2156-3381. DOI: 10.1109/JPHOTOV.2013.2289321.

[13] James A R Dimmock et al. “A metallic hot-carrier photovoltaic device”. In: *Semiconductor Science and Technology* 34.6 (June 2019), p. 064001. ISSN: 0268-1242. DOI: 10.1088/1361-6641/ab1222.

[14] Octavi E Semonin et al. “Peak External Photocurrent Quantum Efficiency Exceeding 100% via MEG in a Quantum Dot Solar Cell”. In: *Science* 334.6062 (Dec. 2011), pp. 1530–1533. ISSN: 0036-8075. DOI: 10.1126/science.1209845.

[15] NREL. *Reference Solar Spectral Irradiance: Air Mass 1.5*. URL: http://rredc.nrel.gov/solar/spectra/am1.5/ (visited on 08/04/2017).

[16] Xing Sheng et al. “High efficiency quadruple junction, four-terminal solar cells and modules by transfer printing”. In: *2014 IEEE 40th Photovoltaic Specialist Conference, PVSC 2014* (2014), pp. 3605–3607. DOI: 10.1109/PVSC.2014.6924886.

[17] A De Vos. “Detailed balance limit of the efficiency of tandem solar cells”. In: *Journal of Physics D: Applied Physics* 13.5 (1980), pp. 839–846. ISSN: 0022-3727. DOI: 10.1088/0022-3727/13/5/018.

[18] John F. Geisz et al. “Six-junction III–V solar cells with 47.1% conversion efficiency under 143 Suns concentration”. In: *Nature Energy* 5.4 (Apr. 2020), pp. 326–335. ISSN: 20587546. DOI: 10.1038/s41560-020-0598-5.

[19] D. J. Friedman, Sarah R. Kurtz, and J. F. Geisz. “Analysis of the GaInP/GaAs/1-eV/Ge cell and related structures for terrestrial concentrator application”. In: *Conference Record of the IEEE Photovoltaic Specialists Conference* May (2002), pp. 856–859. ISSN: 01608371. DOI: 10.1109/pvsc.2002.1190714.

[20] R. R. King et al. “Band-Gap-Engineered Architectures for High-Efficiency Multijunction Concentrator Solar Cells”. In: *24th European Photovoltaic Solar Energy Conference and Exhibition* (2009), pp. 1–7. DOI: 10.4229/24thEUPVSEC2009-1AO.5.2.

[21] M. Stan et al. “High-efficiency quadruple junction solar cells using OMVPE with inverted metamorphic device structures”. In: *Journal of Crystal Growth* 312.8 (2010), pp. 1370–1374. ISSN: 00220248. DOI: 10.1016/j.jcrysgro.2009.10.059.

[22] Thomas N D Tibbits et al. “New Efficiency Frontiers With Wafer-Bonded Multi-Junction Solar Cells”. In: *29th European PV Solar Energy Conference* September (2014), p. 4. DOI: 10.4229/EUPVSEC20142014-4CP.2.1.

[23] Vijit Sabnis, Homan Yuen, and Mike Wiemer. “High-efficiency multijunction solar cells employing dilute nitrides”. In: *8th International Conference on Concentrating Photovoltaic Systems*. Vol. 14. 2012. 2012, pp. 14–19. ISBN: 9780735410862. DOI: 10.1063/1.4753823.

[24] T Thomas et al. “Requirements for a GaAsBi 1 eV sub-cell in a GaAs-based multi-junction solar cell”. In: *Semiconductor Science and Technology* 30.9 (2015), p. 094010. ISSN: 0268-1242. DOI: 10.1088/0268-1242/30/9/094010.

[25] Tom Wilson et al. “Assessing the Nature of the Distribution of Localised States in Bulk GaAsBi”. In: *Scientific Reports* 8.1 (2018), p. 6457. ISSN: 2045-2322. DOI: 10.1038/s41598-018-24696-2.

[26] A J Ptak et al. “Defects in GaInNAs: What We’ve Learned So Far”. In: *NCPV and Solar Program Review Meeting Proceedings* May (2003), pp. 202–205.

[27] G. Sun, R. A. Soref, and H. H. Cheng. “Design of an electrically pumped SiGeSn/GeSn/SiGeSn double-heterostructure midinfrared laser”. In: *Journal of Applied Physics* 108.3 (2010). ISSN: 00218979. DOI: 10.1063/1.3467766.

[28] Yiyin Zhou et al. “Investigation of SiGeSn/GeSn/SiGeSn Quantum Well Structures and Optically Pumped Lasers on Si”. In: *2019 Conference on Lasers and Electro-Optics, CLEO 2019 - Proceedings* 1.c (2019), pp. 2019–2020. DOI: 10.23919/CLEO.2019.8750134.

[29] Yan-yan Fang et al. “Molecular-Based Synthetic Approach to New Group IV Materials for High-Efficiency, Low-Cost Solar Cells and Si-Based Optoelectronics”. In: *Journal of the American Chemical Society* 130.47 (Nov. 2008), pp. 16095–16102. ISSN: 0002-7863. DOI: 10.1021/ja806636c.

[30] Cecilia I. Ventura et al. “Electronic structure of Ge 1 − x − y Si x Sn y ternary alloys for multijunction solar cells”. In: *Progress in Photovoltaics: Research and Applications* 23.1 (Jan. 2015), pp. 112–118. ISSN: 10627995. DOI: 10.1002/pip.2405. arXiv: 1303.4604.

[31] Richard T Beeler et al. “Band Gap-Engineered Group-IV Optoelectronic Semiconductors, Photodiodes and Prototype Photovoltaic Devices”. In: *ECS Journal of Solid State Science and Technology* 2.9 (July 2013), Q172–Q177. ISSN: 2162-8769. DOI: 10.1149/2.034309jss.

[32] Richard T. Beeler et al. “GeSiSn photodiodes with 1 eV optical gaps grown on Si(100) and Ge(100) platforms”. In: *IEEE Journal of Photovoltaics* 2.4 (2012), pp. 434–440. ISSN: 21563381. DOI: 10.1109/JPHOTOV.2012.2206568.

[33] Nils von den Driesch et al. “SiGeSn Ternaries for Efficient Group IV Heterostructure Light Emitters”. In: *Small* 13.16 (Apr. 2017), p. 1603321. ISSN: 16136810. DOI: 10.1002/smll.201603321.

[34] S. Wirths, D. Buca, and S. Mantl. “Si-Ge-Sn alloys: From growth to applications”. In: *Progress in Crystal Growth and Characterization of Materials* 62.1 (2016), pp. 1–39. ISSN: 09608974. DOI: 10.1016/j.pcrysgrow.2015.11.001.

[35] Matthew Bauer et al. “Synthesis of ternary SiGeSn semiconductors on Si(100) via Sn xGe1-x buffer layers”. In: *Applied Physics Letters* 83.11 (Sept. 2003), pp. 2163–2165. ISSN: 00036951. DOI: 10.1063/1.1606104.

[36] Richard Soref et al. “Advances in SiGeSn technology”. In: *Journal of Materials Research* 22.12 (Dec. 2007), pp. 3281–3291. ISSN: 0884-2914. DOI: 10.1557/JMR.2007.0415.

[37] Radek Roucka et al. “Demonstrating Dilute-Tin Alloy SiGeSn for Use in Multijunction Photovoltaics: Single- and Multijunction Solar Cells with a 1.0-eV SiGeSn Junction”. In: *IEEE Journal of Photovoltaics* 6.4 (2016), pp. 1025–1030. ISSN: 21563381. DOI: 10.1109/JPHOTOV.2016.2559785.

[38] S. Wirths et al. “Band engineering and growth of tensile strained Ge/(Si)GeSn heterostructures for tunnel field effect transistors”. In: *Applied Physics Letters* 102.19 (May 2013), p. 192103. ISSN: 00036951. DOI: 10.1063/1.4805034.

[39] S. Wirths et al. “SiGeSn growth studies using reduced pressure chemical vapor deposition towards optoelectronic applications”. In: *Thin Solid Films* 557 (Apr. 2014), pp. 183–187. ISSN: 00406090. DOI: 10.1016/j.tsf.2013.10.078.

[40] S. Wirths et al. “Growth Studies of Doped SiGeSn/Strained Ge(Sn) Heterostructures”. In: *ECS Transactions* 64.6 (Aug. 2014), pp. 689–696. ISSN: 1938-6737. DOI: 10.1149/06406.0689ecst.

[41] Torsten Wendav et al. “Compositional dependence of the band-gap of Ge1-x-YSixSny alloys”. In: *Applied Physics Letters* 108.24 (2016). ISSN: 00036951. DOI: 10.1063/1.4953784.

[42] Inga A Fischer et al. “Optical critical points of Si x Ge 1− x − y Sn y alloys with high Si content”. In: *Semiconductor Science and Technology* 32.12 (Dec. 2017), p. 124004. ISSN: 0268-1242. DOI: 10.1088/1361-6641/aa95d3.

[43] Hai Lin et al. “Structural and optical characterization of SixGe1−x−ySny alloys grown by molecular beam epitaxy”. In: *Applied Physics Letters* 100.14 (2012), pp. 141904–141908. ISSN: 00036951. DOI: 10.1063/1.3701732.

[44] V. R. D’Costa et al. “Ternary GeSiSn alloys: New opportunities for strain and band gap engineering using group-IV semiconductors”. In: *Thin Solid Films* 518.9 (2010), pp. 2531–2537. ISSN: 00406090. DOI: 10.1016/j.tsf.2009.09.149.

[45] J. P. Fleurial and A. Borshchevky. “Si-Ge-Metal Ternary Phase Diagram Calculations”. In: *Journal of The Electrochemical Society* 137.9 (1990), p. 2928. ISSN: 00134651. DOI: 10.1149/1.2087101.

[46] Erich Kasper and Michael Oehme. “Germanium tin light emitters on silicon”. In: *Japanese Journal of Applied Physics* 54.4S (Apr. 2015), 04DG11. ISSN: 0021-4922. DOI: 10.7567/JJAP.54.04DG11.

[47] S. Mukherjee et al. “Short-range atomic ordering in nonequilibrium silicon-germanium-tin semiconductors”. In: *Physical Review B* 95.16 (2017), pp. 1–5. ISSN: 24699969. DOI: 10.1103/PhysRevB.95.161402.

[48] Junqi Xie et al. “Synthesis, stability range, and fundamental properties of Si-Ge-Sn semiconductors grown directly on Si(100) and Ge(100) platforms”. In: *Chemistry of Materials* 22.12 (2010), pp. 3779–3789. ISSN: 08974756. DOI: 10.1021/cm100915q.

[49] O. Madelung, U. Rössler, and M. Schulz, eds. *Group IV Elements, IV-IV and III-V Compounds. Part b - Electronic, Transport, Optical and Other Properties*. Vol. b. Landolt-Börnstein - Group III Condensed Matter. Berlin/Heidelberg: Springer-Verlag, 2002. ISBN: 3-540-42876-3. DOI: 10.1007/b80447.

[50] Richard A. Soref and Clive H. Perry. “Predicted band gap of the new semiconductor SiGeSn”. In: *Journal of Applied Physics* 69.1 (1991), pp. 539–541. ISSN: 00218979. DOI: 10.1063/1.347704.

[51] Pairot Moontragoon, Zoran Ikonić, and Paul Harrison. “Band structure calculations of Si-Ge-Sn alloys: achieving direct band gap materials”. In: *Semiconductor Science and Technology* 22.7 (2007), pp. 742–748. ISSN: 0268-1242. DOI: 10.1088/0268-1242/22/7/012.

[52] P. Moontragoon, R. A. Soref, and Z. Ikonic. “The direct and indirect bandgaps of unstrained Si xGe 1-x-ySn y and their photonic device applications”. In: *Journal of Applied Physics* 112.7 (2012). ISSN: 00218979. DOI: 10.1063/1.4757414.

[53] L. Vegard. “Die Konstitution der Mischkristalle und die Raumfüllung der Atome”. In: *Zeitschrift für Physik* 5.1 (Jan. 1921), pp. 17–26. ISSN: 1434-6001. DOI: 10.1007/BF01349680.

[54] P Aella et al. “Optical and structural properties of SixSnyGe1−x−y alloys”. In: *Applied Physics Letters* 84.6 (Feb. 2004), pp. 888–890. ISSN: 0003-6951. DOI: 10.1063/1.1645324.

[55] Liying Jiang et al. “Development of light emitting group IV ternary alloys on Si platforms for long wavelength optoelectronic applications”. In: *Chemistry of Materials* 26.8 (2014), pp. 2522–2531. ISSN: 15205002. DOI: 10.1021/cm403801b.

[56] Buguo Wang et al. “Comparison study of temperature dependent direct/indirect bandgap emissions of Ge 1-x-y Si x Sn y and Ge 1-y Sn y grown on Ge buffered Si”. In: *Thin Solid Films* 673.January (2019), pp. 63–71. ISSN: 00406090. DOI: 10.1016/j.tsf.2019.01.022.

[57] J. R. Sanchez-Perez et al. “Direct-bandgap light-emitting germanium in tensilely strained nanomembranes”. In: *Proceedings of the National Academy of Sciences* 108.47 (Nov. 2011), pp. 18893–18898. ISSN: 0027-8424. DOI: 10.1073/pnas.1107968108.

[58] Sadao Adachi. “Model dielectric constants of Si and Ge”. In: *Physical Review B* 38.18 (1988), pp. 12966–12976. ISSN: 01631829. DOI: 10.1103/PhysRevB.38.12966.

[59] Manuel Cardona, Kerry L. Shaklee, and Fred H. Pollak. “Electroreflectance at a semiconductor-electrolyte interface”. In: *Physical Review* 154.3 (1967), pp. 696–720. ISSN: 0031899X. DOI: 10.1103/PhysRev.154.696.

[60] Vijay R D’Costa et al. “Sn-alloying as a means of increasing the optical absorption of Ge at the C - and L -telecommunication bands”. In: *Semiconductor Science and Technology* 24.11 (2009), p. 115006. ISSN: 0268-1242. DOI: 10.1088/0268-1242/24/11/115006.

[61] Chi Xu et al. “Synthesis and optical properties of Sn-rich Ge1–x–ySixSny materials and devices”. In: *Thin Solid Films* 557 (Apr. 2014), pp. 177–182. ISSN: 00406090. DOI: 10.1016/j.tsf.2013.08.043.

[62] Richard Soref et al. “Advances in SiGeSn technology”. In: *Journal of Materials Research* 22.12 (2007), pp. 3281–3291. ISSN: 0884-2914. DOI: 10.1557/JMR.2007.0415.

[63] Chi Xu et al. “Compositional dependence of optical interband transition energies in GeSn and GeSiSn alloys”. In: *Solid State Electronics* 110 (2015), pp. 76–82. ISSN: 0038-1101. DOI: 10.1016/j.sse.2015.01.015.

[64] Bader Alharthi et al. “Study of material and optical properties of Si_xGe_1-x-ySn_y alloys for Si-based optoelectronic device applications”. In: *Optical Materials Express* 7.10 (2017), p. 3517. ISSN: 2159-3930. DOI: 10.1364/OME.7.003517.

[65] Vijay R. D’Costa et al. “Transferability of optical bowing parameters between binary and ternary group-IV alloys”. In: *Solid State Communications* 138.6 (2006), pp. 309–313. ISSN: 00381098. DOI: 10.1016/j.ssc.2006.02.023.

[66] Chi Xu et al. “Optical properties of Ge 1- x-y Si x Sn y alloys with y > x : Direct bandgaps beyond 1550 nm”. In: *Applied Physics Letters* 103.7 (Aug. 2013), p. 072111. ISSN: 0003-6951. DOI: 10.1063/1.4818673.

[67] J. D. Gallagher et al. “Fundamental band gap and direct-indirect crossover in Ge$_{1-x-y}$Si$_x$Sn$_y$ alloys”. In: *Applied Physics Letters* 103.20 (2013), p. 202104. ISSN: 00036951. DOI: 10.1063/1.4829621.

[68] Wei Du et al. “Investigation of optical transitions in a SiGeSn / GeSn / SiGeSn single quantum well structure”. In: 123102 (2017). DOI: 10.1063/1.4986341.

[69] Joe Margetis et al. “All group-IV SiGeSn/GeSn/SiGeSn QW laser on Si operating up to 90 K”. In: *Applied Physics Letters* 113.22 (Nov. 2018), p. 221104. ISSN: 00036951. DOI: 10.1063/1.5052563.

[70] Phoebe Pearce et al. “III-V Multi-Junction Solar Cells Utilising Group IV SiGeSn Alloys as a 1.0 eV Component Sub-Cell”. In: *33rd European Photovoltaic Solar Energy Conference and Exhibition*. Amsterdam, 2017, pp. 1248–1252. DOI: 10.4229/EUPVSEC20172017-4CV.4.5.

[71] R. T. Beeler et al. “Compositional dependence of the absorption edge and dark currents in Ge 1− x − y Si x Sn y /Ge(100) photodetectors grown via ultra-low-temperature epitaxy of Ge 4 H 10 , Si 4 H 10 , and SnD 4”. In: *Applied Physics Letters* 101.22 (Nov. 2012), p. 221111. ISSN: 0003-6951. DOI: 10.1063/1.4768217.

[72] R. R. Lieten et al. “Photoluminescence of bulk germanium”. In: *Physical Review B - Condensed Matter and Materials Physics* 86.3 (2012), pp. 1–5. ISSN: 10980121. DOI: 10.1103/PhysRevB.86.035204.

[73] L Jiang et al. “Compositional dependence of the direct and indirect band gaps in Ge 1− y Sn y alloys from room temperature photoluminescence: implications for the indirect to direct gap crossover in intrinsic and n -type materials”. In: *Semiconductor Science and Technology* 29.11 (2014), p. 115028. ISSN: 0268-1242. DOI: 10.1088/0268-1242/29/11/115028.

[74] L. Vina, S. Logothetidis, and M. Cardona. “Temperature dependence of the dielectric function of germanium”. In: *Physical Review B* 30.4 (1984), pp. 1979–1991. ISSN: 01631829. DOI: 10.1103/PhysRevB.30.1979.

[75] Vijay R. D’Costa et al. “Optical critical points of thin-film Ge1−ySny alloys: A comparative Ge1−ySny/Ge1−xSix study”. In: *Physical Review B* 73.12 (Mar. 2006), p. 125207. ISSN: 1098-0121. DOI: 10.1103/PhysRevB.73.125207.

[76] Juan C Minano. “Optical confinement in photovoltaics”. In: *Physical Limitations to Photovoltaic Energy Conversion*. Bristol: Adam Hilger, 1990, pp. 50–83.

[77] A. Mellor et al. “Upper limits to absorption enhancement in thick solar cells using diffraction gratings”. In: *Progress in Photovoltaics: Research and Applications* 19.6 (Sept. 2011), pp. 676–687. ISSN: 10627995. DOI: 10.1002/pip.1086. arXiv: 1303.4604.

[78] E. Yablonovitch and G.D. Cody. “Intensity enhancement in textured optical sheets for solar cells”. In: *IEEE Transactions on Electron Devices* 29.2 (Feb. 1982), pp. 300–305. ISSN: 0018-9383. DOI: 10.1109/T-ED.1982.20700.

[79] Martin A. Green. “Lambertian light trapping in textured solar cells and light-emitting diodes: Analytical solutions”. In: *Progress in Photovoltaics: Research and Applications* 10.4 (2002), pp. 235–241. ISSN: 10627995. DOI: 10.1002/pip.404.

[80] A. Mellor et al. “Interstitial light-trapping design for multi-junction solar cells”. In: *Solar Energy Materials and Solar Cells* 159 (2017), pp. 212–218. ISSN: 09270248. DOI: 10.1016/j.solmat.2016.09.005.

[81] Corsin Battaglia et al. “Light Trapping in Solar Cells: Can Periodic Beat Random?” In: *ACS Nano* 6.3 (Mar. 2012), pp. 2790–2797. ISSN: 1936-0851. DOI: 10.1021/nn300287j.

[82] Kylie R. Catchpole et al. “Plasmonics and nanophotonics for photovoltaics”. In: *MRS Bulletin* 36.6 (2011), pp. 461–467. ISSN: 08837694. DOI: 10.1557/mrs.2011.132.

[83] Martin A. Green and Supriya Pillai. “Harnessing plasmonics for solar cells”. In: *Nature Photonics* 6.3 (2012), pp. 130–132. ISSN: 17494885. DOI: 10.1038/nphoton.2012.30.

[84] Patrick Campbell and Martin A. Green. “Light trapping properties of pyramidally textured surfaces”. In: *Journal of Applied Physics* 62.1 (1987), pp. 243–249. ISSN: 00218979. DOI: 10.1063/1.339189.

[85] R. Santbergen and R.J.C. van Zolingen. "The absorption factor of crystalline silicon PV cells: A numerical and experimental study". In: *Solar Energy Materials and Solar Cells* 92.4 (Apr. 2008), pp. 432–444. ISSN: 09270248. DOI: 10.1016/j.solmat.2007.10.005.

[86] Nico Tucher et al. "3D optical simulation formalism OPTOS for textured silicon solar cells". In: *Optics Express* 23.24 (2015), A1720. ISSN: 1094-4087. DOI: 10.1364/OE.23.0A1720.

[87] Peter Y. Yu and Manuel Cardona. *Fundamentals of Semiconductors*. Graduate Texts in Physics. Berlin, Heidelberg: Springer Berlin Heidelberg, 2010. ISBN: 978-3-642-00709-5. DOI: 10.1007/978-3-642-00710-1.

[88] Jessica R. Piper and Shanhui Fan. "Broadband Absorption Enhancement in Solar Cells with an Atomically Thin Active Layer". In: *ACS Photonics* 3.4 (Apr. 2016), pp. 571–577. ISSN: 2330-4022. DOI: 10.1021/acsphotonics.5b00510.

[89] O. Isabella et al. "Advanced light trapping scheme in decoupled front and rear textured thin-film silicon solar cells". In: *Solar Energy* 162.October 2017 (2018), pp. 344–356. ISSN: 0038092X. DOI: 10.1016/j.solener.2018.01.040.

[90] Stéphane Collin and Maxime Giteau. "New limits for light-trapping with multi-resonant absorption". In: *2018 IEEE 7th World Conference on Photovoltaic Energy Conversion, WCPEC 2018 - A Joint Conference of 45th IEEE PVSC, 28th PVSEC and 34th EU PVSEC*. Institute of Electrical and Electronics Engineers Inc., Nov. 2018, pp. 3460–3462. ISBN: 9781538685297. DOI: 10.1109/PVSC.2018.8547477.

[91] Steven J. Byrnes. "Multilayer optical calculations". In: (Mar. 2016), pp. 1–20. arXiv: 1603.02720.

[92] K. C. Johnson. *GD-Calc_Intro.pdf*. 2005. URL: http://kjinnovation.com/GD-Calc.html.

[93] Liping Liu et al. "Heat dissipation performance of silicon solar cells by direct dielectric liquid immersion under intensified illuminations". In: *Solar Energy* 85.5 (May 2011), pp. 922–930. ISSN: 0038092X. DOI: 10.1016/j.solener.2011.02.007.

[94] Pochi Yeh. *Optical Waves in Layered Media*. John Wiley & Sons, 1988, pp. 308–316.

[95] Hung-Ling Chen et al. "A 19.9%-efficient ultrathin solar cell based on a 205-nm-thick GaAs absorber and a silver nanostructured back mirror". In: *Nature Energy* 4.September (2019). ISSN: 2058-7546. DOI: 10.1038/s41560-019-0434-y.

[96] Alexander Mellor et al. "Nanoimprinted diffraction gratings for crystalline silicon solar cells: implementation, characterization and simulation." In: *Optics express* 21 Suppl 2.March (2013), A295–304. ISSN: 1094-4087. DOI: 10.1364/OE.21.00A295.

[97] Florent Sahli et al. "Fully textured monolithic perovskite/silicon tandem solar cells with 25.2% power conversion efficiency". In: *Nature Materials* 17.9 (2018), pp. 820–826. ISSN: 14764660. DOI: 10.1038/s41563-018-0115-4.

[98] Rudi Santbergen et al. "GenPro4 Optical Model for Solar Cell Simulation and Its Application to Multijunction Solar Cells". In: *IEEE Journal of Photovoltaics* 7.3 (May 2017), pp. 919–926. ISSN: 2156-3381. DOI: 10.1109/JPHOTOV.2017.2669640.

[99] Johannes Eisenlohr et al. "Matrix formalism for light propagation and absorption in thick textured optical sheets". In: *Optics Express* 23.11 (2015), A502. ISSN: 1094-4087. DOI: 10.1364/OE.23.00A502.

[100] Yang Li et al. "Angular matrix framework for light trapping analysis of solar cells". In: *Optics Express* 23.24 (Nov. 2015), A1707. ISSN: 1094-4087. DOI: 10.1364/OE.23.0A1707.

[101] Benjamin Lipovšek, Janez Krč, and Marko Topič. "Optical model for thin-film photovoltaic devices with large surface textures at the front side". In: *Informacije MIDEM* 41.4 (2011), pp. 264–271. ISSN: 03529045.

[102] Phoebe Pearce and Nicholas Ekins-Daukes. "Open-source integrated optical modelling with RayFlare". In: *2019 IEEE 46th Photovoltaic Specialists Conference (PVSC)*. IEEE, June 2019, pp. 2627–2633. ISBN: 978-1-7281-0494-2. DOI: 10.1109/PVSC40753.2019.8980868.

[103] G.J. Bauhuis et al. "Thin film GaAs solar cells with increased quantum efficiency due to light reflection". In: *Solar Energy Materials and Solar Cells* 83.1 (June 2004), pp. 81–90. ISSN: 09270248. DOI: 10.1016/j.solmat.2003.11.030.

[104] J J Schermer et al. "High rate epitaxial lift-off of InGaP films from GaAs substrates". In: *Applied Physics Letters* 76.15 (Apr. 2000), pp. 2131–2133. ISSN: 0003-6951. DOI: 10.1063/1.126276.

[105] G.J. Bauhuis et al. "26.1% thin-film GaAs solar cell using epitaxial lift-off". In: *Solar Energy Materials and Solar Cells* 93.9 (Sept. 2009), pp. 1488–1491. ISSN: 09270248. DOI: 10.1016/j.solmat.2009.03.027.

[106] NREL. *Best Research-Cell Efficiences*. 2017. URL: http://www.nrel.gov/pv/assets/images/efficiency%7B%5C_%7Dchart.jpg (visited on 07/27/2020).

[107] M. A. Steiner et al. "Optical enhancement of the open-circuit voltage in high quality GaAs solar cells". In: *Journal of Applied Physics* 113.12 (2013). ISSN: 00218979. DOI: 10.1063/1.4798267.

[108] L. C. Hirst et al. "Intrinsic radiation tolerance of ultra-thin GaAs solar cells". In: *Applied Physics Letters* 109.3 (2016). ISSN: 00036951. DOI: 10.1063/1.4959784.

[109] Chuan Fei Guo et al. "Metallic nanostructures for light trapping in energy-harvesting devices". In: *Light: Science and Applications* 3.11 (2014), pp. 1–12. ISSN: 20477538. DOI: 10.1038/lsa.2014.42.

[110] Alexander Mellor et al. "Nanoparticle Scattering for Multijunction Solar Cells: The Tradeoff Between Absorption Enhancement and Transmission Loss". In: *IEEE Journal of Photovoltaics* 6.6 (Nov. 2016), pp. 1678–1687. ISSN: 2156-3381. DOI: 10.1109/JPHOTOV.2016.2601944.

[111] Inès Massiot et al. "Metal Nanogrid for Broadband Multiresonant Light-Harvesting in Ultrathin GaAs Layers". In: *ACS Photonics* 1.9 (2014), pp. 878–884. ISSN: 23304022. DOI: 10.1021/ph500168b.

[112] Yang Wang et al. "Metamaterial-plasmonic absorber structure for high efficiency amorphous silicon solar cells". In: *Nano Lett.* 12.1 (2012), pp. 440–445. ISSN: 15306984. DOI: 10.1021/nl203763k.

[113] T. V. Pfeiffer et al. "Plasmonic nanoparticle films for solar cell applications fabricated by size-selective aerosol deposition". In: *Energy Procedia* 60.C (2014), pp. 3–12. ISSN: 18766102. DOI: 10.1016/j.egypro.2014.12.335.

[114] Xu Guo et al. "A New Strategy of Lithography Based on Phase Separation of Polymer Blends". In: *Scientific Reports* 5 (2015), pp. 1–12. ISSN: 20452322. DOI: 10.1038/srep15947.

[115] Hairen Tan et al. "Improved light trapping in microcrystalline silicon solar cells by plasmonic back reflector with broad angular scattering and low parasitic absorption". In: *Applied Physics Letters* 102.15 (Apr. 2013), p. 153902. ISSN: 0003-6951. DOI: 10.1063/1.4802451.

[116] Hitoshi Sai et al. "Thin-film microcrystalline silicon solar cells: 11.9% efficiency and beyond". In: *Applied Physics Express* 11.2 (Feb. 2018), p. 022301. ISSN: 1882-0778. DOI: 10.7567/APEX.11.022301.

[117] Phoebe Pearce, Alexander Mellor, and Nicholas Ekins-Daukes. "The importance of accurate determination of optical constants for the design of nanometallic light-trapping structures". In: *Solar Energy Materials and Solar Cells* 191.November 2018 (Mar. 2018), pp. 133–140. ISSN: 09270248. DOI: 10.1016/j.solmat.2018.11.008.

[118] F.-J. Haug et al. "Plasmonic absorption in textured silver back reflectors of thin film solar cells". In: *Journal of Applied Physics* 104.6 (Sept. 2008), p. 064509. ISSN: 0021-8979. DOI: 10.1063/1.2981194.

[119] Yajie Jiang, Supriya Pillai, and Martin A. Green. "Realistic Silver Optical Constants for Plasmonics". In: *Scientific Reports* 6.1 (2016), p. 30605. ISSN: 2045-2322. DOI: 10.1038/srep30605.

[120] B. Marion. "Comparison of predictive models for photovoltaic module performance". In: *Conference Record of the IEEE Photovoltaic Specialists Conference*. 2008. ISBN: 9781424416417. DOI: 10.1109/PVSC.2008.4922586.

[121] Kenji Araki, Hisafumi Uozumi, and Masafumi Yamaguchi. "A simple passive cooling structure and its heat analysis for 500 X concentrator PV module". In: *Conference Record of the IEEE Photovoltaic Specialists Conference*. 2002, pp. 1568–1571. DOI: 10.1109/pvsc.2002.1190913.

[122] Aaswath P. Raman et al. "Passive radiative cooling below ambient air temperature under direct sunlight". In: *Nature* 515.7528 (Nov. 2014), pp. 540–544. ISSN: 14764687. DOI: 10.1038/nature13883.

[123] Joe S. Coventry. "Performance of a concentrating photovoltaic/thermal solar collector". In: *Solar Energy*. Vol. 78. 2. Pergamon, Feb. 2005, pp. 211–222. DOI: 10.1016/j.solener.2004.03.014.

[124] Denis G. Baranov et al. "Nanophotonic engineering of far-field thermal emitters". In: *Nature Materials* 18.9 (Sept. 2019), pp. 920–930. ISSN: 1476-1122. DOI: 10.1038/s41563-019-0363-y.

[125] A. Mellor et al. "Roadmap for the next-generation of hybrid photovoltaic-thermal solar energy collectors". In: *Solar Energy* 174 (Nov. 2018), pp. 386–398. ISSN: 0038-092X. DOI: 10.1016/J.SOLENER.2018.09.004.

[126] A Riverola et al. "Mid-infrared emissivity of crystalline silicon solar cells". In: *Solar Energy Material and Solar Cells* 174.July 2017 (2018), pp. 607–615. DOI: 10.1016/j.solmat.2017.10.002.

[127] Diego Alonso-Álvarez et al. "ITO and AZO films for low emissivity coatings in hybrid photovoltaic-thermal applications". In: *Solar Energy* 155 (2017), pp. 82–92. ISSN: 0038092X. DOI: 10.1016/j.solener.2017.06.033.

[128] D. Alonso-Álvarez et al. "Solcore: a multi-scale, Python-based library for modelling solar cells and semiconductor materials". In: *Journal of Computational Electronics* 17.3 (Sept. 2018), pp. 1099–1123. ISSN: 1569-8025. DOI: 10.1007/s10825-018-1171-3. arXiv: 1709.06741.

[129] Martin A. Green. "Self-consistent optical parameters of intrinsic silicon at 300 K including temperature coefficients". In: *Solar Energy Materials and Solar Cells* 92.11 (2008), pp. 1305–1310. ISSN: 09270248. DOI: 10.1016/j.solmat.2008.06.009.

[130] Timothy Nathan Nunley et al. "Optical constants of germanium and thermally grown germanium dioxide from 0.5 to 6.6eV via a multisample ellipsometry investigation". In: *Journal of Vacuum Science & Technology B, Nanotechnology and Microelectronics: Materials, Processing, Measurement, and Phenomena* 34.6 (Nov. 2016), p. 061205. ISSN: 2166-2746. DOI: 10.1116/1.4963075.

[131] D. E. Aspnes et al. "Optical properties of AlxGa1-x As". In: *Journal of Applied Physics* 60.2 (1986), pp. 754–767. ISSN: 00218979. DOI: 10.1063/1.337426.

[132] M S Dresselhaus. *Solid State Physics, Part II: Optical Properties of Solids*. 2001. URL: http://web.mit.edu/course/6/6.732/www/6.732-pt2.pdf.

[133] Giuseppe Grosso and Giuseppe Pastori Parravicini. *Solid State Physics*. Second. Academic Press, 2014. ISBN: 9780123850300.

[134] Sadao Adachi. "Optical Properties". In: *Physical Properties of III-V Semiconductor Compounds*. Vol. 2. Weinheim, FRG: Wiley-VCH Verlag GmbH & Co. KGaA, Jan. 2005. Chap. 8, pp. 135–192. DOI: 10.1002/352760281X.ch8.

[135] Sadao Adachi. "Optical dispersion relations for Si and Ge". In: *Journal of Applied Physics* 66.7 (1989), pp. 3224–3231. ISSN: 00218979. DOI: 10.1063/1.344140.

[136] Charles C. Kim et al. "Modeling the optical dielectric function of semiconductors: Extension of the critical-point parabolic-band approximation". In: *Physical Review B* 45.20 (1992), pp. 11749–11767. ISSN: 01631829. DOI: 10.1103/PhysRevB.45.11749.

[137] B Johs et al. "Development of a parametric optical constant model for Hg1−xCdxTe for control of composition by spectroscopic ellipsometry during MBE growth". In: *Thin Solid Films* 313 (1998), pp. 137–142. ISSN: 00406090. DOI: 10.1016/S0040-6090(97)00800-6.

[138] D.E. Aspnes. "Third-derivative modulation spectroscopy with low-field electroreflectance". In: *Surface Science* 37.1973 (June 1973), pp. 418–442. ISSN: 00396028. DOI: 10.1016/0039-6028(73)90337-3.

[139] Max Born and Emil Wolf. *Principles of Optics: Electromagnetic Theory of Propagation, Interference and Diffraction of Light*. Sixth Edit. Cambridge: Cambridge University Press, 1980.

[140] M G Moharam and T K Gaylord. "Rigorous coupled-wave analysis of planar-grating diffraction". In: 71.7 (1981).

[141] Victor Liu and Shanhui Fan. "S4: A free electromagnetic solver for layered periodic structures". In: *Computer Physics Communications* 183.10 (2012), pp. 2233–2244. ISSN: 00104655. DOI: 10.1016/j.cpc.2012.04.026.

[142] K. C. Johnson. *GD-Calc.pdf*. 2005. URL: http://kjinnovation.com/GD-Calc.html.

[143] Martin Weismann, Dominic F G Gallagher, and Nicolae C Panoiu. "Accurate near-field calculation in the rigorous coupled-wave analysis method". In: *Journal of Optics* 17.12 (Dec. 2015), p. 125612. ISSN: 2040-8978. DOI: 10.1088/2040-8978/17/12/125612.

[144] Claude E. Duchon. "Lanczos Filtering in One and Two Dimensions". In: *Journal of Applied Meteorology* 18.8 (Aug. 1979), pp. 1016–1022. ISSN: 0021-8952. DOI: 10.1175/1520-0450(1979)018<1016:LFIOAT>2.0.CO;2.

[145] Jenny Nelson. *The Physics of Solar Cells*. PUBLISHED BY IMPERIAL COLLEGE PRESS and DISTRIBUTED BY WORLD SCIENTIFIC PUBLISHING CO., May 2003. ISBN: 978-1-86094-340-9. DOI: 10.1142/p276.

[146] Thomas W. M. Wilson. "A Comprehensive Study of the Highly Lattice Mismatched Alloy GaAsBi for High Efficiency Photovoltaic Applications". PhD. Imperial College London, 2019.

[147] J.A. Woollam Co. *Guide to using WVASE Spectroscopic Ellipsometry Data Acquisition and Analysis Software*. Tech. rep. 2012.

[148] Rasheed M A Azzam. "Fresnel's interface reflection coefficients for the parallel and perpendicular polarizations: global properties and facts not found in your textbook". In: ed. by Dennis H. Goldstein and David B. Chenault. Sept. 1994, p. 120. ISBN: 0819415898. DOI: 10.1117/12.186660.

[149] James W Fleming. "Dispersion in GeO 2 -SiO 2 glasses". In: 23.24 (1984).

[150] J. D. Gallagher et al. "Compositional dependence of the bowing parameter for the direct and indirect band gaps in Ge1-ySny alloys". In: *Applied Physics Letters* 105.14 (2014), pp. 1–6. ISSN: 00036951. DOI: 10.1063/1.4897272.

[151] Timur V Elzhov et al. *minpack.lm: R Interface to the Levenberg-Marquardt Nonlinear Least-Squares Algorithm Found in MINPACK, Plus Support for Bounds*. 2016. URL: https://cran.r-project.org/package=minpack.lm.

[152] P. M. Amirtharaj, D. Chandler-Horowitz, and D. P. Bour. "Double Modulation and Selective Excitation Photoreflectance for Characterizing Highly Luminescent Semiconductor Structures and Samples with Poor Surface Morphology". In: *MRS Proceedings* 406 (Jan. 1995), p. 229. ISSN: 1946-4274. DOI: 10.1557/PROC-406-229.

[153] H Shen and M Dutta. "Franz – Keldysh oscillations in modulation spectroscopy Franz-Keldysh oscillations in modulation spectroscopy". In: 2151.1995 (2011). DOI: 10.1063/1.360131.

[154] D. Huang, D. Mui, and H. Morkoç. "Interference effects probed by photoreflectance spectroscopy". In: *Journal of Applied Physics* 66.1 (July 1989), pp. 358–361. ISSN: 0021-8979. DOI: 10.1063/1.343882.

[155] N. Kallergi et al. "Correlation of interference effects in photoreflectance spectra with GaAs homolayer thickness". In: *Journal of Applied Physics* 68.9 (Nov. 1990), pp. 4656–4661. ISSN: 0021-8979. DOI: 10.1063/1.346176.

[156] S Ghosh and B M Arora. "Interference effects in photoreflectance and contactless electroreflectance spectra of CdTe films grown on Si substrate". In: *Journal of Applied Physics* 81.10 (May 1997), pp. 6968–6974. ISSN: 0021-8979. DOI: 10.1063/1.365260.

[157] Diego Alonso-Álvarez. *Mordor: Python-based program to control lab equipment.* URL: https://github.com/qpv-research-group/mordor (visited on 08/08/2020).

[158] Rainer Storn and Kenneth Price. "Differential Evolution – A Simple and Efficient Heuristic for global Optimization over Continuous Spaces". In: *Journal of Global Optimization* 11.4 (1997), pp. 341–359. ISSN: 1573-2916. DOI: 10.1023/A:1008202821328.

[159] Pablo Rodriguez-Mier. *A tutorial on Differential Evolution with Python*. 2017. URL: https://pablormier.github.io/2017/09/05/a-tutorial-on-differential-evolution-with-python/ (visited on 07/01/2020).

[160] Pablo R. Mier. *pablormier/yabox*. 2020. DOI: 10.5281/zenodo.841089.

[161] Diego Alonso Álvarez et al. *Solcore*. 2020. URL: http://www.solcore.solar/.

[162] Phoebe Pearce. *RayFlare*. 2020. URL: https://github.com/qpv-research-group/rayflare.

[163] Victor Liu and Phoebe Pearce. *GitHub forked repository - phoebe-p/S4: Stanford Stratified Structure Solver - Electromagnetic simulator for layered periodic structures*. 2020. URL: https://github.com/phoebe-p/S4 (visited on 09/16/2020).

[164] Mikhail N Polyanskiy. *Refractive index database*. URL: https://refractiveindex.info.

[165] Nico Tucher et al. “Optical modeling of structured silicon-based tandem solar cells and module stacks”. In: *Optics Express* 26.18 (2018), A761. ISSN: 1094-4087. DOI: 10.1364/OE.26.00A761.

[166] PV Lighthouse. *Wafer ray tracer*. URL: https://www2.pvlighthouse.com.au/calculators/wafer%20ray%20tracer/wafer%20ray%20tracer.html (visited on 05/14/2020).

[167] Luis V. Rodríguez-de Marcos et al. “Self-consistent optical constants of MgF2, LaF3, and CeF3 films”. In: *Optical Materials Express* 7.3 (Mar. 2017), p. 989. ISSN: 2159-3930. DOI: 10.1364/OME.7.000989.

[168] Monica Morales-Masis et al. “Low-Temperature High-Mobility Amorphous IZO for Silicon Heterojunction Solar Cells”. In: *IEEE Journal of Photovoltaics* 5.5 (2015), pp. 1340–1347. ISSN: 21563381. DOI: 10.1109/JPHOTOV.2015.2450993.

[169] S. L. Ren et al. “Ellipsometric determination of the optical constants of C 60 (Buckminsterfullerene) films”. In: *Applied Physics Letters* 59.21 (1991), pp. 2678–2680. ISSN: 00036951. DOI: 10.1063/1.105907.

[170] Jérémie Werner et al. “Complex Refractive Indices of Cesium-Formamidinium-Based Mixed-Halide Perovskites with Optical Band Gaps from 1.5 to 1.8 eV”. In: *ACS Energy Letters* 3.3 (2018), pp. 742–747. ISSN: 23808195. DOI: 10.1021/acsenergylett.8b00089.

[171] D. Alonso-Álvarez et al. “Thermal emissivity of silicon heterojunction solar cells”. In: *Solar Energy Materials and Solar Cells* 201.May (2019), p. 110051. ISSN: 09270248. DOI: 10.1016/j.solmat.2019.110051.

[172] Kevin M. McPeak et al. “Plasmonic films can easily be better: Rules and recipes”. In: *ACS Photonics* 2.3 (2015), pp. 326–333. ISSN: 23304022. DOI: 10.1021/ph5004237. arXiv: 1603.02132.

[173] Mark W. Knight et al. “Aluminum for plasmonics”. In: *ACS Nano* 8.1 (2014), pp. 834–840. ISSN: 19360851. DOI: 10.1021/nn405495q.

[174] Celine Pahud et al. “Plasmonic silicon solar cells: impact of material quality and geometry”. In: *Optics Express* 21.S5 (2013), A786. ISSN: 1094-4087. DOI: 10.1364/OE.21.00A786.

[175] P. B. Johnson and R. W. Christy. “Optical constants of the noble metals”. In: *Physical Review B* 6.12 (1972), pp. 4370–4379. ISSN: 01631829. DOI: 10.1103/PhysRevB.6.4370. arXiv: arXiv:1011.1669v3.

[176] William R. Erwin et al. “Light trapping in mesoporous solar cells with plasmonic nanostructures”. In: *Energy Environ. Sci.* 9.5 (2016), pp. 1577–1601. ISSN: 1754-5692. DOI: 10.1039/C5EE03847B.

[177] Olivia Nicoletti et al. “Three-dimensional imaging of localized surface plasmon resonances of metal nanoparticles”. In: *Nature* 502.7469 (2013), pp. 80–84. ISSN: 00280836. DOI: 10.1038/nature12469.

[178] Paul R. West et al. “Searching for better plasmonic materials”. In: *Laser and Photonics Reviews* 4.6 (2010), pp. 795–808. ISSN: 18638880. DOI: 10.1002/lpor.200900055. arXiv: 0911.2737.

[179] Edward D. Palik. *Handbook of Optical Constants of Solids*. Academic Press, 1985.

[180] H.-J. Hagemann, W. Gudat, and C. Kunz. “Optical constants from the far infrared to the x-ray region: Mg, Al, Cu, Ag, Au, Bi, C, and Al_2O_3”. In: *Journal of the Optical Society of America* 65.6 (1975), p. 742. ISSN: 0030-3941. DOI: 10.1364/JOSA.65.000742.

[181] D. W. Lynch, C. G. Olson, and J. H. Weaver. “Optical properties of Ti, Zr, and Hf from 0.15 to 30 eV”. In: *Physical Review B* 11.10 (May 1975), pp. 3617–3624. ISSN: 0556-2805. DOI: 10.1103/PhysRevB.11.3617.

[182] Robert L. Olmon et al. “Optical dielectric function of gold”. In: *Physical Review B - Condensed Matter and Materials Physics* 86.23 (2012), pp. 1–9. ISSN: 10980121. DOI: 10.1103/PhysRevB.86.235147. arXiv: 0801.4433.

[183] Aleksandar D. Rakić et al. “Optical properties of metallic films for vertical-cavity optoelectronic devices”. In: *Applied Optics* 37.22 (1998), p. 5271. ISSN: 0003-6935. DOI: 10.1364/AO.37.005271.

[184] Wolfgang S.M. Werner, Kathrin Glantschnig, and Claudia Ambrosch-Draxl. “Optical constants and inelastic electron-scattering data for 17 elemental metals”. In: *Journal of Physical and Chemical Reference Data* 38.4 (2009), pp. 1013–1092. ISSN: 00472689. DOI: 10.1063/1.3243762.

[185] Tobias A. F. Konig et al. “Electrically tunable plasmonic behavior of nanocube-polymer nanomaterials induced by a redox-active electrochromic polymer”. In: *ACS Nano* 8.6 (2014), pp. 6182–6192. ISSN: 1936086X. DOI: 10.1021/nn501601e.

[186] J.W. Matthews and A.E. Blakeslee. “Defects in epitaxial multilayers: I. Misfit dislocations”. In: *Journal of Crystal Growth* 27 (Dec. 1974), pp. 118–125. ISSN: 00220248. DOI: 10.1016/S0022-0248(74)80055-2.

[187] R. People and J. C. Bean. “Calculation of critical layer thickness versus lattice mismatch for Ge x Si 1− x /Si strained-layer heterostructures”. In: *Applied Physics Letters* 47.3 (Aug. 1985), pp. 322–324. ISSN: 0003-6951. DOI: 10.1063/1.96206.

[188] Wei Wang et al. “Critical thickness for strain relaxation of Ge 1− x Sn x (x 0.17) grown by molecular beam epitaxy on Ge(001)”. In: *Applied Physics Letters* 106.23 (June 2015), p. 232106. ISSN: 0003-6951. DOI: 10.1063/1.4922529.

[189] Yichun Yin et al. “Temperature dependence of the fundamental direct transitions of bulk Ge and two Ge/SiGe multiple-quantum-well structures”. In: *Physical Review B* 52.12 (Sept. 1995), pp. 8951–8958. ISSN: 01631829. DOI: 10.1103/PhysRevB.52.8951.

[190] Werner Klingenstein and Heinz Schweizer. “Direct gap recombination in germanium at high excitation level and low temperature”. In: *Solid State Electronics* 21.11-12 (1978), pp. 1371–1374. ISSN: 00381101. DOI: 10.1016/0038-1101(78)90210-1.

[191] H.M. van Driel et al. “Photoluminescence spectra of germanium at high excitation intensities”. In: *Solid State Communications* 20.9 (Dec. 1976), pp. 837–840. ISSN: 00381098. DOI: 10.1016/0038-1098(76)91286-2.

[192] T. Schmidt, K. Lischka, and W. Zulehner. “Excitation-power dependence of the near-band-edge photoluminescence of semiconductors”. In: *Physical Review B* 45.16 (1992), pp. 8989–8994. ISSN: 01631829. DOI: 10.1103/PhysRevB.45.8989.

[193] J. Weber and M. I. Alonso. “Near-band-gap photoluminescence of Si-Ge alloys”. In: *Physical Review B* 40.8 (Sept. 1989), pp. 5683–5693. ISSN: 0163-1829. DOI: 10.1103/PhysRevB.40.5683.

[194] Y.P. Varshni. “Temperature dependence of the energy gap in semiconductors”. In: *Physica* 34.1 (1967), pp. 149–154. ISSN: 00318914. DOI: 10.1016/0031-8914(67)90062-6. arXiv: arXiv:1011.1669v3.

[195] Radek; Roucka et al. “3J solar cells comprising a lattice matched epitaxial SiGeSn subcell”. In: *2016 IEEE 43rd Photovoltaic Specialists Conference (PVSC)*. IEEE, June 2016, pp. 2362–2365. ISBN: 978-1-5090-2724-8. DOI: 10.1109/PVSC.2016.7750062.

[196] Martin A. Green et al. “Solar cell efficiency tables (version 26)”. In: *Progress in Photovoltaics: Research and Applications* 13.5 (Aug. 2005), pp. 387–392. ISSN: 1062-7995. DOI: 10.1002/pip.651.

[197] Pierre Marie Coulon et al. "Displacement Talbot lithography for nano-engineering of III-nitride materials". In: *Microsystems and Nanoengineering* 5.1 (2019). ISSN: 20557434. DOI: 10.1038/s41378-019-0101-2.

[198] Harun H. Solak, Christian Dais, and Francis Clube. "Displacement Talbot lithography: a new method for high-resolution patterning of large areas". In: *Optics Express* 19.11 (2011), p. 10686. DOI: 10.1364/oe.19.010686.

[199] Eduardo Camarillo Abad, Hannah J. Joyce, and Louise C. Hirst. "Light management in ultra-thin solar cells: a guided optimisation approach". In: *Optics Express* 28.26 (Dec. 2020), p. 39093. ISSN: 1094-4087. DOI: 10.1364/OE.408664.

[200] Pierre Chausse et al. ""Double" displacement Talbot lithography: fast, wafer-scale, direct-writing of complex periodic nanopatterns". In: *Optics Express* 27.22 (Oct. 2019), p. 32037. ISSN: 1094-4087. DOI: 10.1364/oe.27.032037.

[201] C. J. Fu and Z. M. Zhang. "Nanoscale radiation heat transfer for silicon at different doping levels". In: *International Journal of Heat and Mass Transfer* 49.9-10 (2006), pp. 1703–1718. ISSN: 00179310. DOI: 10.1016/j.ijheatmasstransfer.2005.09.037.

[202] Honghua U. Yang et al. "Optical dielectric function of silver". In: *Physical Review B* 91.23 (June 2015), p. 235137. ISSN: 1098-0121. DOI: 10.1103/PhysRevB.91.235137.

[203] Martin A. Green et al. "40% efficient sunlight to electricity conversion". In: *Progress in Photovoltaics: Research and Applications* 23.6 (June 2015), pp. 685–691. ISSN: 10627995. DOI: 10.1002/pip.2612.

[204] Yajie Jiang et al. "Design of an intermediate Bragg reflector within triple-junction solar cells for spectrum splitting applications". In: *Solar Energy Materials and Solar Cells* 193 (May 2019), pp. 259–269. ISSN: 0927-0248. DOI: 10.1016/J.SOLMAT.2019.01.011.

[205] Alexander Slade and Vahan Garboushian. "27.6 % Efficient Silicon Concentrator Solar Cells for Mass Production". In: *Technical Digest, 15th International Photovoltaic Science and Engineering Conference, Beijing* July (2015).

[206] E. Ochoa-Martínez et al. "Refractive indexes and extinction coefficients of n- and p-type doped GaInP, AlInP and AlGaInP for multijunction solar cells". In: *Solar Energy Materials and Solar Cells* 174.April 2017 (2018), pp. 388–396. ISSN: 09270248. DOI: 10.1016/j.solmat.2017.09.028.

[207] Wangqing Yuan and D. C. Hall. "Variable-angle spectroscopic ellipsometry of InAlP native oxide dielectric layers for GaAs metal-oxide-semiconductor field effect transistor applications". In: *Journal of Applied Physics* 113.10 (2013). ISSN: 00218979. DOI: 10.1063/1.4794817.

[208] Huade Yao, Paul G. Snyder, and John A. Woollam. "Temperature dependence of optical properties of GaAs". In: *Journal of Applied Physics* 70.6 (Sept. 1991), pp. 3261–3267. ISSN: 0021-8979. DOI: 10.1063/1.349285.

[209] Phoebe Pearce et al. "Design of photonic light-trapping structures for ultra-thin solar cells". In: *Physics, Simulation, and Photonic Engineering of Photovoltaic Devices IX*. Ed. by Alexandre Freundlich, Masakazu Sugiyama, and Stéphane Collin. March. SPIE, Mar. 2020, p. 28. ISBN: 9781510633131. DOI: 10.1117/12.2550136.

Appendices

Appendix A

Proof of Adachi dielectric function representation

To prove:

$$\lim_{\nu \to 0} \epsilon_1(\omega + i\nu) = \epsilon_1(\omega) + i\epsilon_2(\omega) \tag{A.1}$$

Relevant identities are the first Kramers-Kronig relation (eq. A.2), the functional representation of the Dirac delta function as the limit of a Poisson kernel (eq. A.3) and an identity relating to the composition of the delta function with a general function $g(x)$ (A.4):

$$\epsilon_1(\omega) = 1 + \frac{2}{\pi} \int_0^\infty \frac{\omega' \epsilon_2(\omega')}{(\omega')^2 - \omega^2} d\omega' \tag{A.2}$$

$$\delta(x) = \lim_{\gamma \to 0} \Big(\frac{1}{\pi} \frac{\gamma}{\gamma^2 + x^2} \Big) \tag{A.3}$$

$$\delta(g(x)) = \sum_i \frac{\delta(x - x_i)}{|g'(x_i)|} \tag{A.4}$$

where in the final equation x_i are the roots of $g(x) = 0$ and $g'(x)$ is the first derivative of $g(x)$.

Eq. A.4 can be used with the specific function $g(x) = x^2 - a^2$ to give:

$$\delta(x^2 - \alpha^2) = \frac{1}{2|\alpha|} (\delta(x + \alpha) + \delta(x - \alpha)) \tag{A.5}$$

Starting from the LHS of eq. A.1, and plugging the argument $\omega + i\nu$ into the Kramers-Kronig relation (eq. A.2):

$$\begin{aligned} \epsilon_1(\omega + i\nu) &= 1 + \frac{2}{\pi} \int_0^\infty \frac{\omega' \epsilon_2(\omega')}{(\omega')^2 - (\omega + i\nu)^2} d\omega' \\ &= 1 + \frac{2}{\pi} \int_0^\infty \frac{\omega' \epsilon_2(\omega')}{(\omega')^2 - \omega^2 - 2i\omega\nu + \nu^2} d\omega' \\ &= 1 + \frac{2}{\pi} \int_0^\infty \frac{\omega' \epsilon_2(\omega') [(\omega')^2 - \omega^2 + \nu^2 + 2i\omega\nu]}{[(\omega')^2 - \omega^2 + \nu^2]^2 + 4\omega^2\nu^2} d\omega' \end{aligned} \tag{A.6}$$

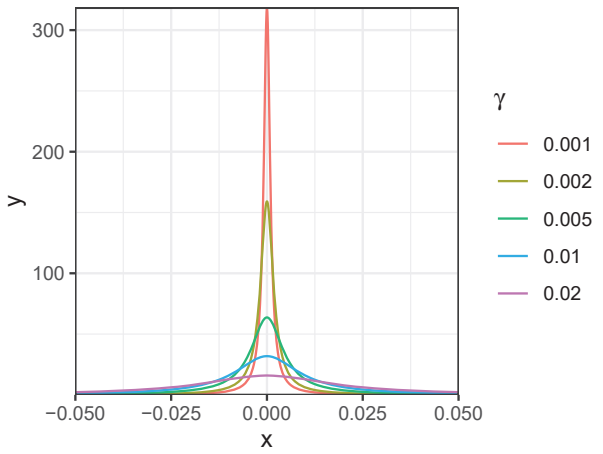


Figure A.1: The function $y = \frac{\gamma}{x^2+\gamma^2}$ evaluated at different values of γ.

In the third step, the denominator has been realized, so now the real and imaginary parts can be separated easily:

$$\begin{aligned}\mathrm{Re}\{\epsilon_1(\omega+i\nu)\} &= 1+\frac{2}{\pi}\int_0^\infty \frac{\omega'\epsilon_2(\omega')[(\omega')^2-\omega^2+\nu^2]}{[(\omega')^2-\omega^2+\nu^2]^2+4\omega^2\nu^2}d\omega' \\ \mathrm{Im}\{\epsilon_1(\omega+i\nu)\} &= \frac{2}{\pi}\int_0^\infty \frac{2\omega\nu\omega'\epsilon_2(\omega')}{[(\omega')^2-\omega^2+\nu^2]^2+4\omega^2\nu^2}d\omega'\end{aligned} \tag{A.7}$$

Now taking the limit $\nu \to 0$ in the real part:

$$\begin{aligned}\lim_{\nu\to 0}\mathrm{Re}\{\epsilon_1(\omega+i\nu)\} &= 1+\frac{2}{\pi}\lim_{\nu\to 0}\int_0^\infty \frac{\omega'\epsilon_2(\omega')[(\omega')^2-\omega^2+\nu^2]}{[(\omega')^2-\omega^2+\nu^2]^2+4\omega^2\nu^2}d\omega' \\ &= 1+\frac{2}{\pi}\int_0^\infty \frac{\omega'\epsilon_2(\omega')[(\omega')^2-\omega^2]}{[(\omega')^2-\omega^2]^2}d\omega' \\ &= 1+\frac{2}{\pi}\int_0^\infty \frac{\omega'\epsilon_2(\omega')}{(\omega')^2-\omega^2}d\omega' \\ &= \epsilon_1(\omega)\end{aligned} \tag{A.8}$$

With the last line following from eq. A.2. The real part of the LHS of eq. A.1 is equal to $\epsilon_1(\omega)$, as required. Now, considering the imaginary part we make the substitutions $\gamma = 2\omega\nu$ and $x = (\omega')^2 - \omega^2 + \nu^2$. It follows that as $\nu \to 0$, $\gamma \to 0$ also. We can rewrite A.7, and take the relevant limit, as:

$$\lim_{\nu\to 0}\mathrm{Im}\{\epsilon_1(\omega+i\nu)\} = 2\frac{1}{\pi}\int_0^\infty \lim_{\gamma\to 0}\frac{\gamma\omega'\epsilon_2(\omega)}{x^2+\gamma^2}d\omega' \tag{A.9}$$

Comparing this to eq. A.3, we can pick out the definition of the delta function and write:

$$\lim_{\nu\to 0}\mathrm{Im}\{\epsilon_1(\omega+i\nu)\} = 2\int_0^\infty \epsilon_2\omega'\delta(x)d\omega' = 2\int_0^\infty \epsilon_2\omega'\delta((\omega')^2-\omega^2)d\omega'$$

Then using the identity eq. A.5:

$$\begin{aligned}\lim_{\nu\to 0}\mathrm{Im}\{\epsilon_1(\omega+i\nu)\} &= \int_0^\infty \frac{2}{2|\omega|}\epsilon_2(\omega')\omega'[\delta(\omega'+\omega)+\delta(\omega'-\omega)]d\omega' \\ &= \frac{1}{|\omega|}\omega\epsilon_2(\omega) \\ &= \epsilon_2(\omega)\end{aligned} \tag{A.10}$$

Where in the second line, we have used the sampling property of the delta function, taking into account the fact that the integral covers the range 0 to ∞ to determine that only the second delta function contributes. Since ω is then positive, $|\omega| = \omega$.

We have thus proved that $\lim_{\nu\to 0}\epsilon_1(\omega+i\nu) = \epsilon_1(\omega) + i\epsilon_2(\omega)$. ν can be interpreted as a damping parameter: as $\nu \to 0$ (so $\gamma \to 0$) in A.9, the $\frac{\gamma}{x^2+\gamma^2}$ term becomes a delta function, picking out ϵ_2 at $\omega' = \omega$ exactly. As ν increases, the distribution becomes less narrow, and no longer picks out just $\omega' = \omega$ so the values of ϵ_2 get 'smeared out' (see Fig. A.1). Similarly, looking at A.8, increasing ν means the denominator does not equal zero for any values of ω/ω', reducing peak height and similarly smearing out ϵ_1.

Appendix B

Wavevectors and power flow in absorbing media

For a general plane wave (assuming without loss of generality that we are in the $x-z$ plane, where the incidence medium lies at $z=0$):

$$\vec{k_f} = \frac{2\pi(n+i\kappa)}{\lambda}(\sin\tilde{\theta}, 0, \cos\tilde{\theta}) \tag{B.1}$$

If $k=0$ (non-absorbing medium), this is fine. But if we have $k \neq 0$, strange things happen. Specifically, $\tilde{n}\sin\tilde{\theta}$ may not be a real number, which implies that there is dissipation of power in the direction parallel to the incident medium, i.e. not an infinite plane wave. So $\tilde{n}\sin\tilde{\theta}$ has to be real, and if $\tilde{n}$ is complex, this means $\sin\tilde{\theta}$ is complex, and thus $\tilde{\theta}$ is complex. This is equivalent to saying Snell's law ($\tilde{n}_0\sin\theta_0 = \tilde{n}_1\sin\theta_1$) holds even for interfaces between absorbing media.

Let's say we know the angle α from which *power*, i.e. the real part of the Poynting vector, is incident. Can we relate this to a complex angle $\tilde{\theta}$ for the wavevector k_f? The time-averaged Poynting vector $\langle\vec{S}\rangle$ can be related to the electric and magnetic fields through[1]:

$$\begin{aligned}
&\vec{k_f} = \tfrac{2\pi\tilde{n}}{\lambda}(\sin\tilde{\theta}, 0, \cos\tilde{\theta}) \\
&\vec{E_f} = (0, E_f, 0) \\
&\vec{H_f} \propto \vec{k_f} \times \vec{E_f} \\
&\vec{H_f} \propto (-\cos\tilde{\theta}, 0, \sin\tilde{\theta}) \\
&\langle\vec{S}\rangle = \mathrm{Re}\{\vec{E_f} \times \vec{H_f^*}\} \\
&\langle\vec{S}\rangle \propto \mathrm{Re}\{(\tilde{n}\sin\tilde{\theta})^*, 0, (\tilde{n}\cos\tilde{\theta})^*\} = \mathrm{Re}\{\tilde{n}\sin\tilde{\theta}, 0, \tilde{n}\cos\tilde{\theta}\}
\end{aligned} \tag{B.2}$$

Since we are asserting that for the wave to be a plane wave, $\tilde{n}\sin\tilde{\theta}$ is real, this reduces to:

$$\langle\vec{S}\rangle \propto (\tilde{n}\sin\tilde{\theta}, 0, \mathrm{Re}\{\tilde{n}\cos\tilde{\theta}\}) \tag{B.3}$$

Where we have used notation as used by Byrnes [91] and the standard expression for real power from the Poynting vector. The last step in (B.2) uses the fact that the real part of a complex number is the same

[1] The following is for *s*-polarization, but as it turns out, things work out the same for *p*-polarization (the fact that $\mathrm{Re}\{\vec{E_f} \times \vec{H_f^*}\} = \mathrm{Re}\{\vec{E_f^*} \times \vec{H_f}\}$ for the Poynting vector is useful in that case so the maths is the same).

as the real part of its complex conjugate. So say that we know *power*, or rather, want to assert that power is incident from an angle α, this angle is given by:

$$\tan\alpha = \frac{\tilde{n}\sin\tilde{\theta}}{\mathrm{Re}\{\tilde{n}\cos\tilde{\theta}\}} \tag{B.4}$$

Taking the real part of $\tilde{n}\sin\tilde{\theta}$ is not shown explicitly since, as discussed above, it must be real. Some notation:

$$\begin{aligned} k_x &= \tilde{n}\sin\tilde{\theta} \\ k_{z,r} &= \mathrm{Re}\{\tilde{n}\cos\tilde{\theta}\} \\ k_{z,i} &= \mathrm{Im}\{\tilde{n}\cos\tilde{\theta}\} \end{aligned} \tag{B.5}$$

Where the k notation represents that these quantities are proportional to the vector entries of the wavevector, and the last two lines are the real and imaginary parts of k_z. That means that:

$$\tan\alpha = \frac{k_x}{k_{z,r}} \tag{B.6}$$

Clearly, for the *complex* angle $\tilde{\theta}$ of the wavevector, we have (referring back to (B.2)):

$$\tan\tilde{\theta} = \frac{\tilde{n}\sin\tilde{\theta}}{\tilde{n}\cos\tilde{\theta}} = \frac{k_x}{k_z} = \frac{k_x}{k_{z,r} + ik_{z,i}} \tag{B.7}$$

Some identities we can use: since $\sin^2\theta + \cos^2\theta = 1$ (even for complex angles!), $k_x^2 + (k_{z,r} + ik_{z,i})^2 = \tilde{n}^2 = (n + i\kappa)^2$. Separating out real and imaginary parts gives us two equations:

$$\begin{aligned} k_x^2 + k_{z,r}^2 - k_{z,i}^2 &= n^2 - \kappa^2 \\ k_{z,r}k_{z,i} &= n\kappa \end{aligned} \tag{B.8}$$

So if we know α and want to find θ, we should express $\tan\theta$ in terms of things we know (n, κ and α). I actually solved for $k_{z,r}$, since it is easy to then get $k_{z,i}$ and k_x through the identities above.

Squaring (B.6) and plugging the first identity from (B.8) in to get rid of k_x^2:

$$\tan^2\alpha = \frac{k_x^2}{k_{z,r}^2} = \frac{n^2 - \kappa^2 - k_{z,r}^2 + k_{z,i}^2}{k_{z,r}^2} \tag{B.9}$$

Then getting rid of $k_{z,i}^2$ by substituting the second identity from (B.8):

$$\tan^2\alpha = \frac{n^2 - \kappa^2 - k_{z,r}^2 + \frac{n^2\kappa^2}{k_{z,r}^2}}{k_{z,r}^2} \tag{B.10}$$

Now by multiplying both sides by $k_{z,r}^4$ we get:

$$\tan^2\alpha k_{z,r}^4 + (\kappa^2 - n^2)k_{z,r}^2 - n^2\kappa^2 = 0 \tag{B.11}$$

This is a quadratic equation for $x = k_{z,r}^2$. As it turns out, we have to take the positive root for the solution to be real. The answer is:

$$k_{z,r} = \cos\alpha\sqrt{\frac{1}{2}(n^2 - \kappa^2) + \frac{1}{2}\sqrt{((\kappa^2 - n^2)^2 + 4n^2\kappa^2\sec^2\alpha}} \tag{B.12}$$

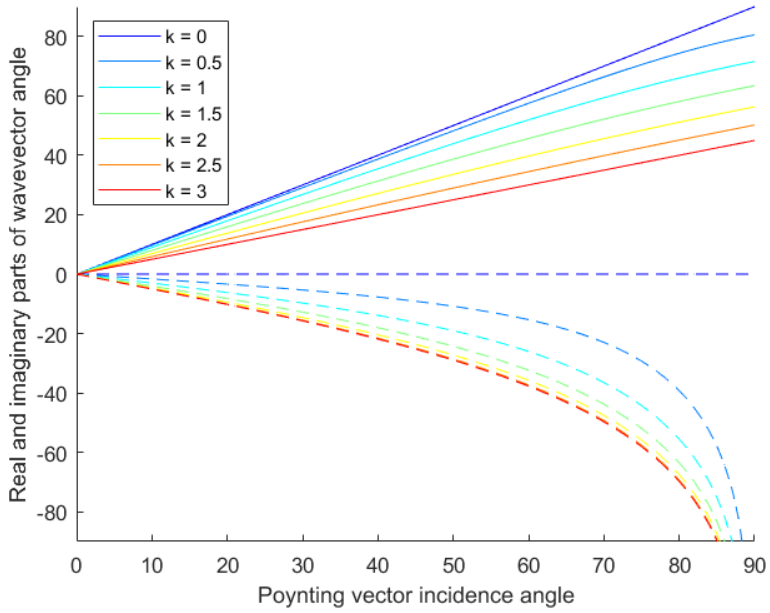


Figure B.1: Variation of the real (solid lines) and imaginary (dashed lines) part of the complex wavevector angle $\tilde{\theta}$ where the Poynting vector is travelling at a certain incidence angle in a medium with refractive index $\tilde{n} = 3 + i\kappa$ with varying κ.

This can of course be used to find a direct expression for $\tilde{\theta}$, but if you have numerical inputs for n, κ and α, the quantities $k_{z,r}$ and thus $k_{z,i}$, k_x and $\tilde{\theta}$ are all easy to calculate. Note that if $\kappa = 0$, this expression reduces to:

$$k_{z,r} = n \cos \alpha \tag{B.13}$$

as expected.

If you know complex $\tilde{\theta}$ but want to calculate α, that is much more straightforward, as you can simply use (B.6) directly. The reason we want to use α in an angular matrix formalism is that we want to know about how incident power is distributed and absorbed throughout the cell, and we are binning in terms of the angular directions in which power travels. In many cases (i.e. media which are not strongly absorbing) these are equivalent to the wavevector directions, but in strongly absorbing media (e.g. metals, direct semiconductors or highly doped layers) this assumption may not be valid. Fig. B.1 shows the difference between α and the real and imaginary parts of $\tilde{\theta}$ for increasing values of κ. Fig. B.2 shows how R and T vary with increasing κ of the transmission interface, showing that for highly absorbing media assuming the lossless case will give completely incorrect results. Fig. B.3 shows a situation in which total internal reflection (TIR) occurs for a non-absorbing medium, and how R is affected by increasing absorption in the transmission medium.

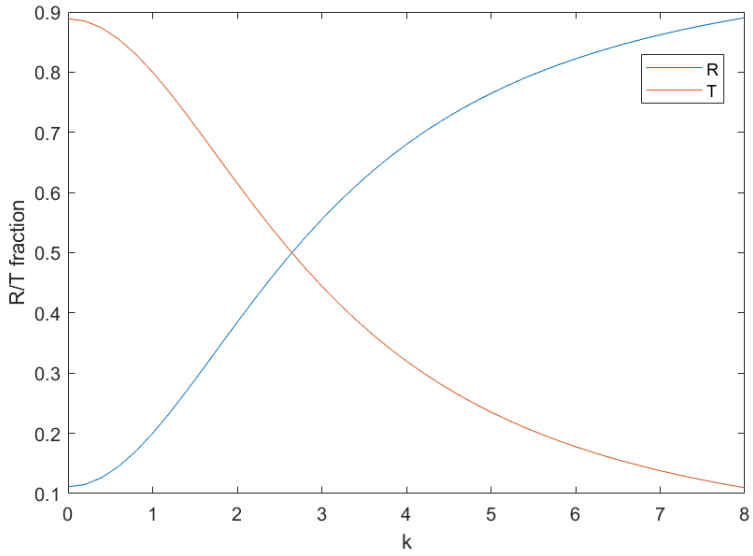


Figure B.2: R and T for unpolarized (average of s and p-polarization) light incident from air ($n = 1$) on a medium with n (real part of the refractive index) $= 2$ and varying κ.

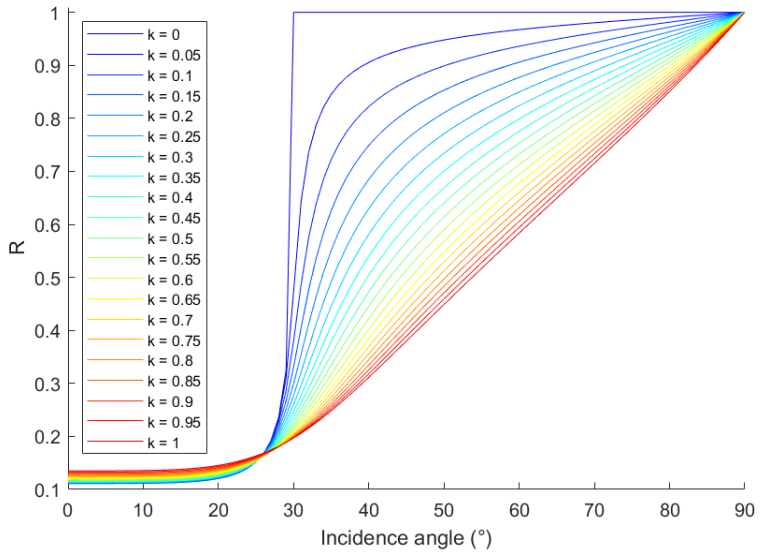


Figure B.3: R for light incident from a medium with $n = 4$ on a medium with $n = 2$ and varying imaginary part of the refractive index κ, at incidence angles θ between 0 and 90 degrees.

Appendix C

Solcore code listings

Code Listing C.1: Defining structures for use with the RCWA solver S^4.

```
from solcore import si , material
from solcore.structure import Layer
Air = material('Air')(T=298)
TiO2 = material('TiO2', sopra=True)(T=298)
# Define four geometry types , as a list of dictionaries: circles , rectangles , a general polygon
# (in this case, a triangle) and ellipses. All the shapes are made of TiO2.
geometry_circles = [{'type': 'circle', 'mat': TiO2 , 'center': (100, 100), 'radius': 50}]
geometry_rectangles = [{'type': 'rectangle', 'mat': TiO2 , 'center':    (200, 200) , 'angle': 30,
     'halfwidths': (50, 75)}]
# rotation angle is in degrees
geometry_polygons = [{'type': 'polygon', 'mat': TiO2 , 'center': (200, 200) , 'angle': 0, '
    vertices': ((-100, -100), (100, -100), (0, 100))}]
# vertices must be defined counter-clockwise around the center (origin) for the unrotated polygon
geometry_ellipses = [{'type': 'ellipse', 'mat': TiO2 , 'center': (200, 200) , 'angle': 0, '
    halfwidths': (50, 75)}]
# Define a layer of air with TiO2 nanopillars 50nm high.
cylinder_layer = Layer(width=si('50nm'), material=Air, geometry=geometry_circles)
```

Code Listing C.2: Adding custom materials to Solcore's database.

```
from solcore import material
from solcore import si
from solcore.material_system import create_new_material
import matplotlib.pyplot as plt
import numpy as np

"""
When adding custom materials - or getting the refractive index database - the
information will be stored in the Solcore's users folder. These can be setup by setting
the SOLCORE_USER_DATA environmental variable to your prefered location or, by default,
it will be in your home directory, in a directory called .solcore.

Need to have n and k data, and a parameter file in the correct format -
see examples of parameter files in e.g. material_data/Adachi/binaries.txt
create a new material, silicon-germanium-tin, from input files. Here,
the parameters in SiGeSn_params.txt have been copied directly from Ge.
"""

create_new_material('SiGeSn', 'data/SiGeSn_n.txt', 'data/SiGeSn_k.txt', 'data/SiGeSn_params.txt')

# can now create an instance of it like any Solcore material
SiGeSn = material('SiGeSn')()

wl = si(np.arange(300, 1700, 5), 'nm')
plt.figure(figsize=(4.5, 3.5))
plt.plot(wl*1e9, SiGeSn.n(wl), label='n')
plt.plot(wl*1e9, SiGeSn.k(wl), label=r'$\kappa$')

plt.xlabel('Wavelength (nm)')
plt.ylabel('Refractive index')
plt.legend()
plt.show()
```

Code Listing C.3: Using the refractiveindex.info database to define materials in Solcore.

```
from solcore.absorption_calculator.nk_db import download_db, search_db
from solcore import material
from solcore import si
import numpy as np
import matplotlib.pyplot as plt

"""
Using the refractiveindex.info database for optical constants for silver.
"""

download_db()
# Can search the database to select an appropriate entry. Search by element/chemical formula.
# In this case, look for silver.

search_db('Ag', exact = True)
# This prints out, line by line, matching entries. This shows us entries with "pageid"s 0 to 14
    correspond to silver.

# Let's compare the optical behaviour of some of those sources:
# pageid = 0, Johnson
# pageid = 2, McPeak
# pageid = 8, Hagemann
# pageid = 12, Rakic (BB)

Ag_Joh = material(name = '0', nk_db=True)()
Ag_McP = material(name = '2', nk_db=True)()
Ag_Hag = material(name = '8', nk_db=True)()
Ag_Rak = material(name = '12', nk_db=True)()

Ag_Sol = material(name = 'Ag')() # Solcore built-in (from SOPRA)

wl = si(np.arange(100, 900, 5), 'nm')

plt.figure(figsize=(9, 3.5))
plt.subplot(121)
plt.plot(wl*1e9, Ag_Joh.n(wl), label='Johnson')
plt.plot(wl*1e9, Ag_McP.n(wl), label='McPeak')
plt.plot(wl*1e9, Ag_Hag.n(wl), label='Hagemann')
plt.plot(wl*1e9, Ag_Rak.n(wl), label='Rakic')
plt.plot(wl*1e9, Ag_Sol.n(wl), label='SOPRA')
plt.xlabel('Wavelength (nm)')
plt.ylabel('n')
plt.legend()

plt.subplot(122)
plt.plot(wl*1e9, Ag_Joh.k(wl))
plt.plot(wl*1e9, Ag_McP.k(wl))
plt.plot(wl*1e9, Ag_Hag.k(wl))
plt.plot(wl*1e9, Ag_Rak.k(wl))
plt.plot(wl*1e9, Ag_Sol.k(wl))
plt.xlabel('Wavelength (nm)')
plt.ylabel(r'$\kappa$')
plt.show()
```

Appendix D

Convergence of ray-tracing calculations

Broadly speaking, increasing the number of rays used in the Monte Carlo ray-tracing algorithm will lead to more accurate results and longer computation times; however, there are multiple ways in which the number of rays can be increased. In order to accurately capture the behaviour of the surface, it is necessary to scan across an entire unit cell. For instance, if the number of rays is set at 2500 per wavelength, it is possible to trace 2500 rays incident on exactly the same point on the surface's unit cell, or 25 points on the surface 100 times, or 2500 points once. In addition, the scanned points can be chosen to cover the surface in a systematic way (e.g. by generating a grid of n_x points in the x-direction and n_y points in the y-direction and scanning the same number of points ($(n_x \times n_y)$ until the total number of rays is reached) or by generating a random position for each ray.

Fig. D.1 shows how the number of surface points and total rays traced affects the absorption calculated, using a regular grid to generate the (x, y) position at which the incident ray will strike the unit cell. The structure used is 200 µm of Si with regular inverted pyramids with size 5 µm on the front surface and a planar rear surface. The absorption in the Si was calculated at 300-1200 nm at 20 nm intervals. The RMS difference, summed over all wavelengths, in Fig. D.1a is calculated with respect to the result with 50000 rays and 50 x/y points ($50^2 = 2500$ surface points), the largest number of rays and surface points. The fraction of light absorbed in the Si, weighted by the absorption coefficient α at that wavelength, is shown in Fig. D.1b. This weighting is used since as the Si becomes more transparent, more rays will have multiple interactions with the interfaces, meaning any systematic deviation in the calculated result should increase, thus weighting these points more heavily will emphasize systematic differences. The RMS difference is sensitive to both systematic deviations between different calculations, and fluctuations between adjacent wavelengths points due to the stochastic nature of the simulation, while the weighted absorption should be less sensitive to the stochastic fluctuations. It is clear from both figures that calculations with a relatively small number of surface points deviate strongly in both metrics, while increasing the number of surface points leads to convergence. Increasing the number of rays decreases the RMS difference, though the additional benefit after 20,000 rays or so is quite minimal. Increasing the number of rays has a much smaller effect on the weighted absorption, indicating that, as expected, the overall trend is correct even for a smaller number of rays but increasing the number of rays decreases the size of random fluctuations due to the stochastic nature of the calculations. Both metrics indicate that in general, increasing the number of surface points is a much more efficient way of obtaining accurate result than only increasing the number of rays.

Fig. D.2 shows the full absorption results for several combinations of the number of rays and surface

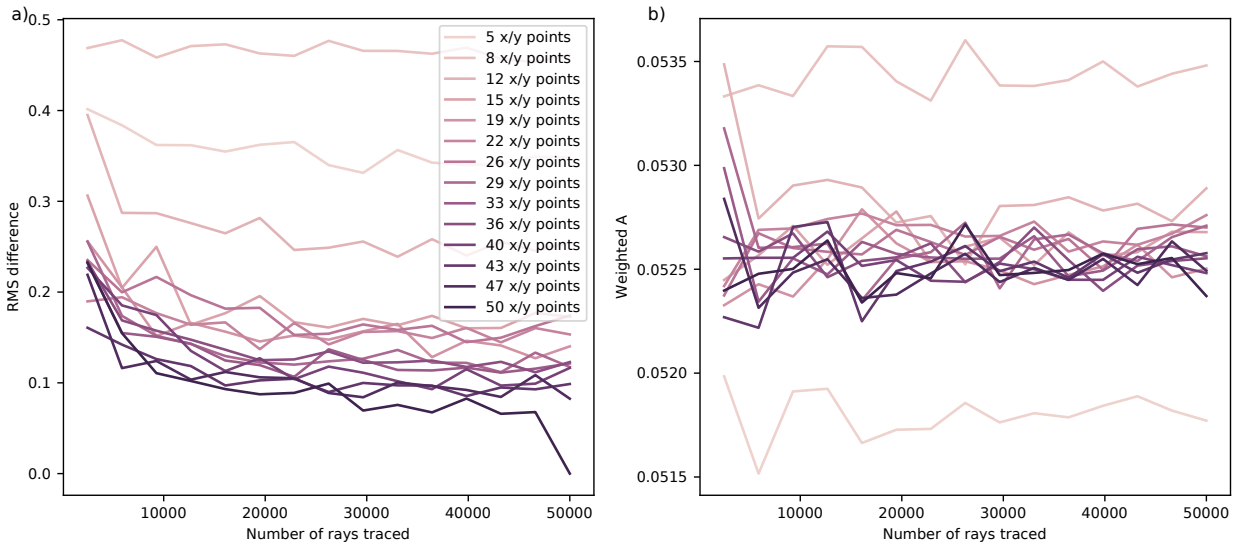


Figure D.1: a) Summary of the RMS difference in the calculated absorption, summed over wavelength values shown in Fig. D.2, for different numbers of surface points and total number of rays traced. The reference values (RMS error = 0) were taken from the simulation with the maximum number of rays and surface points (50,000 rays and 50 x and y surface points, 2500 surface points total). b) The fraction of light absorbed in the Si, weighted by the absorption coefficient of Si, depending on the number of rays and surface points traced.

points. The result with a single x/y point (not shown in Fig. D.1 due to its large offset making it difficult to see the rest of the results) is extremely far off, predicting a much higher A; this is expected, since the single ray strikes in the centre of the unit cell, at the apex of pyramid, meaning the ray will generally be reflected many times within this pyramid and have a very well-randomized (Lambertian-like) path inside the cell compared to a ray striking the pyramid closer to its base. The other results show convergence appears to happen quickly, and the number of surface points (different line colors) is more important for convergence than the number of rays (different line types).

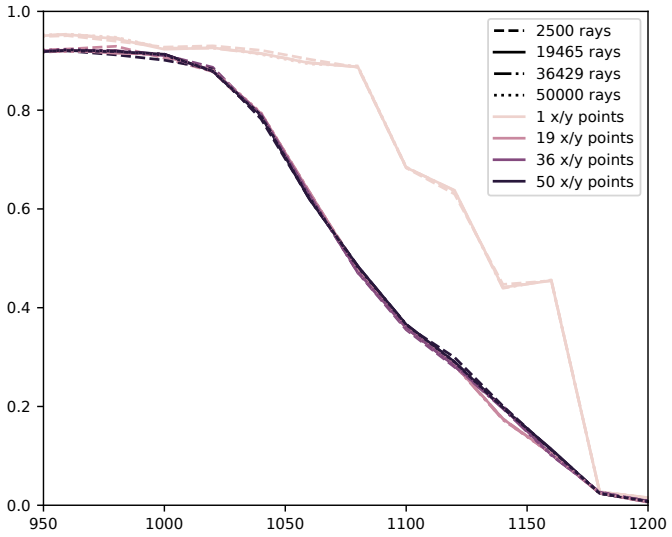


Figure D.2: Absorption vs. wavelength for a 200 µm Si wafer with inverted, regular pyramids on the front surface and a planar rear surface using different numbers of rays and x and y scanning the surface (e.g. for 36 x/y points a total of $36^2 = 1296$ surface points were scanned.

Appendix E

Ellipsometry of ultra-thin cell structures

When dealing with a multi-layer structure such as the thin-film GaAs epitaxial structures shown in Fig. 6.1, it is difficult to fit the layer thicknesses based on a single SE measurement of the full stack due to the number of parameters involved, and due to the fact that SE is a very surface-sensitive measurement. In the case of the structure as-grown, the top layer is 300 nm of GaAs which will serve as the n-type contact, and will be etched away over the majority of the cell area; thus, an ellipsometry measurement of the stack will be strongly influenced by a layer which does not affect the optical design. In order to obtain accurate layer thicknesses, selective chemical etches were used to remove one epitaxial layer at a time. Six samples were made this way in total, each exposing a different top layer (this was done by Larkin Sayre at the University of Cambridge).

All six samples were used for SE measurements over a wavelength range of 250 to 1000 nm at incidence angles of 65°, 70°, 75°. To fit the layer thicknesses, a multi-layer model as described in Section 3.2.2 was first fit to Sample 1 (the sample with all epitaxial layers except the InAlP etch stop removed, see Table E.1). Then, using this as a starting point and allowing all layer thicknesses to vary, the data for Sample 2 was fitted with an appropriate multi-layer model, adding in the GaAs layer. This was repeated for the other samples, adding one layer at a time and only fitting the optical constants of the top layer for each measurement. Starting values for the layer thicknesses were set at the nominal values supplied by IQE plc. For each sample, it was assumed a surface oxide was present, which was fit to have a thickness of 0.5-2 nm in each case. The ellipsometry data and multi-layer model fit to Sample 5 are shown in Fig. E.1.

Special attention was given to the effects of sub-bandgap absorption due to free carriers in the highly

Table E.1: Structure of the six epitaxial samples with different layers removed through chemical etching, and the layer thicknesses fitted to these structures, starting from the thinnest structure on the left. The optical constants fitted to each material are shown in Fig. 6.3.

Sample 1		Sample 2		Sample 3		Sample 4		Sample 5		Sample 6	
Structure:	**Fitted:**	**Structure:**	**Fitted:**	**Structure:**	**Fitted:**	**Structure:**	**Fitted:**	**Structure:**	**Fitted:**	**Structure:**	**Fitted:**
										GaAs ox.	2.528
								InAlP ox.	1.990	GaAs	318.3
						GaAs ox.	1.307	InAlP	16.51	InAlP	18.00
				InGaP ox. [2]	0.5780	GaAs	86.41	GaAs	87.05	GaAs	86.70
		GaAs ox.	1.479	$In_{0.49}GaP$	19.59	$In_{0.49}GaP$	19.42	$In_{0.49}GaP$	18.97	$In_{0.49}GaP$	18.97
InAlP ox. [1]	1.994	GaAs	25.11	GaAs	24.93	GaAs	24.88	GaAs	25.07	GaAs	25.07
$In_{0.47}AlP$	144.2	$In_{0.47}AlP$	147.4	$In_{0.47}AlP$	148.7	$In_{0.47}AlP$	148.8	$In_{0.47}AlP$	148.7	$In_{0.47}AlP$	148.7
GaAs	Semi-infinite	GaAs	Semi-infinite	GaAs	Semi-infinite	GaAs	Semi-infinite	GaAs	Semi-infinite	GaAs	Semi-infinite

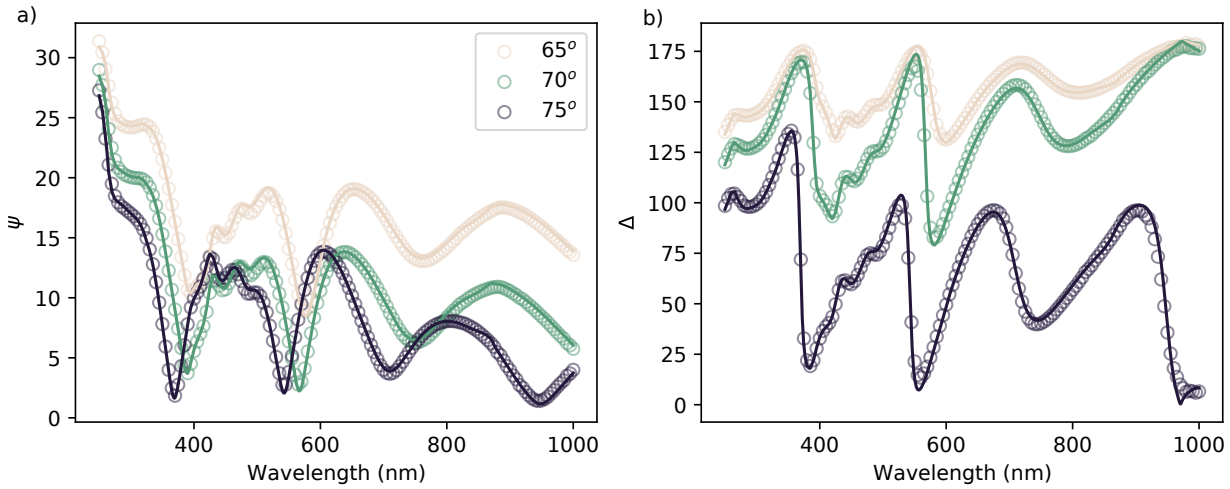


Figure E.1: Spectroscopic ellipsometry data (open circles) and multi-layer model fit (lines) at three different incidence angles for Sample 5 as listed in Table E.1.

doped layers. Layers made of the same material with the same targeted composition may have different optical constants due to differing doping levels, as was shown for $Ga_{0.51}In_{0.49}P$ and $Al_{0.53}In_{0.47}P$ in [206]; increasing doping levels (both n and p-type) make the absorption edge around the E_0 transition (the bandgap for these III-V alloys) less sharp. To take into account this possible variation in optical constants, a Herzinger-Johs parametric oscillator (Psemi) model as discussed in Section 3.2.2 was used to describe the dielectric functions of GaAs, $Ga_{0.51}In_{0.49}P$ and $Al_{0.53}In_{0.47}P$. The Psemi model is a type of parametric, Kramers-Kronig consistent model for the real and imaginary parts of the dielectric function. Due to the flexible peak shape of the Psemi model, it is possible to include effects such as bandgap narrowing and changes in the absorption edge due to doping. The starting point for the InAlP and GaInP layers was the Psemi model parameters given in [207], while for GaAs a Psemi model was constructed to match literature data from [208] closely. The dielectric function was thus allowed to vary for each layer, with differently-doped layers of the same material composition treated separately, but it was found that the optical constants obtained in this way were very close to the literature values

Appendix F

Critical point fitting

F.1 Details of photoreflectance equation

The full derivation of low-field modulation spectroscopy as a third-derivative technique is given in Aspnes (1973) [138]. The key result is:

$$\frac{\Delta R}{R} = \mathrm{Re}\left\{ \left[C_\mathrm{s} C_\mathrm{ex} C_\mathrm{in} e^i e^j \Delta\varepsilon^{ij} \right] \right\} \tag{F.1}$$

$$\begin{aligned} C_\mathrm{s} &= 2n_\mathrm{a} / \left[n \left(\varepsilon - \varepsilon_a \right) \right] \\ C_\mathrm{ex} &= \left[1 - g(\varepsilon - 1) \right]^2, \quad g \leqslant 0 \\ C_\mathrm{in} &= -2\mathrm{i}k \int_{-\infty}^{0} \mathrm{d}z' \mathrm{e}^{-2\mathrm{i}kz'} \left[E\left(z'\right) / E(0) \right]^2 \end{aligned} \tag{F.2}$$

C_s and C_{ex} depend on the refractive index of the substrate, which is energy-dependent; this is generally neglected when fitting photoreflectance or related data, since the change in the refractive index of the substrates is generally small over the energy ranges of interest. For instance, between 0.9 and 1.1 eV (the approximate energy range over which the critical point for the E_0 transition of SiGeSn is fitted), the refractive index of Ge varies between 4.25 and 4.34, while the refractive index of GaAs varies between 3.4 and 3.45. C_{in} appears to be energy-dependent (dispersive) due to the factor of the wavevector k, but examining the integral (which depends on the electric field distribution, which is generally unknown) indicates that this will produce a factor of k^{-1}, thus making this term overall not dispersive. The factors e^i and e^j describe the polarization of the incident probe light and are also not dispersive.

Parameter	Description
e_i, e_j	Cartesian components of the unit polarization vector $\hat{e}$
$\Delta\varepsilon^{ij}$	Change in the dielectric function (second-rank tensor)
n_a	Complex refractive index of ambient material (= 1, Air in this case)
n	Unperturbed complex refractive index
ε_a	Dielectric function of ambient material = n_a^2 (= 1, Air in this case)
ε	Unperturbed dielectric function = n^2
g	Strength parameter for the electron-hole Coulomb interaction (assumed constant)
k	Wavenumber in the substrate = $n\omega/c$
$E(0), E(z)$	Electric field strength at the surface and a depth z

F.2 Photoreflectance model fitting details

Table F.1: All parameters used in fitting the photoreflectance data to a model incorporating both the critical point feature and the effects of thin-film interference in the SiGeSn layer. The ticks in the final two columns indicate whether the parameter affects the fit of the interference fringes, the critical point feature, or both.

Parameter	Description	Interference fringes	CP PR signal
E_0	E_0 CP ($\Gamma \to \Gamma$) centre energy	✓	✓
Δ_0	Split-off hole energy	✓	✓
A_0	Strength of the E_0 transition	✓	
Γ_{0/Δ_0}	Broadening of the E_0 transition	✓	✓
γ	Exponent for envelope	✓	
A_n	Strength of n modulation	✓	
$A_{CP,0}$	Strength of E_0 CP signal		✓
Φ_{0/Δ_0}	Phase of E_0 and $E_0 + \Delta_0$ CP signal		✓
A_{CP,Δ_0}	Strength of $E_0 + \Delta_0$ CP signal		✓
E_{ex}	E_0 exciton binding energy transition energy		✓
A_{ex}	Strength of the exciton PR signal		✓
Γ_{ex}	Broadening of the exciton PR signal		✓
Φ_{ex}	Phase of the exciton PR signal		✓
d_{SiGeSn}	Thickness of the SiGeSn layer	✓	
d_{GaAs}	Thickness of the GaAs layer (Set B only)	✓	
Φ_{PR}	Overall phase of the PR measurement	✓	✓
C	Constant offset of measurement	✓	✓

The real and imaginary parts of the dielectric constant, and thus the refractive index n, are calculated according to: [134]

$$\begin{aligned}
&\varepsilon = AE_0^{-1.5}\left\{f(\chi_0) + \tfrac{1}{2}\left(\tfrac{E_0}{E_0+\Delta_0}\right)^{1.5} f(\chi_{\mathrm{so}})\right\}\\
&f(\chi_0) = \chi_0^{-2}\left[2 - (1+\chi_0)^{0.5} - (1-\chi_0)^{0.5}\right]\\
&f(\chi_{\mathrm{so}}) = \chi_{\mathrm{so}}^{-2}\left[2 - (1+\chi_{\mathrm{so}})^{0.5} - (1-\chi_{\mathrm{so}})^{0.5}\right]\\
&\chi_0 = \tfrac{\hbar\omega + i\Gamma_{0/\Delta_0}}{E_0}\\
&\chi_{\mathrm{so}} = \tfrac{\hbar\omega + i\Gamma_{0/\Delta_0}}{E_0+\Delta_0}\\
&n = \mathrm{Re}\{\sqrt{\varepsilon}\}
\end{aligned} \tag{F.3}$$

The change in the refractive index of SiGeSn due to modulation by the pump beam is given by (using the n from eq. F.3):

$$\begin{aligned}
&\delta_n = A_n e^{\gamma E}\left(n^2 - 1\right)\\
&\tilde{n} = n + \delta n
\end{aligned} \tag{F.4}$$

This modulated refractive index is fed into the TMM model of the layer stack to calculate R'; R is similarly calculated with the unmodulated refractive index n, so that the change in reflectivity $\Delta R = R' - R$ due to interference can be calculated. The interference signal IS is given by $(R' - R)/R$.

The critical point feature in the photoreflectance data is fitted using:

$$CP = \mathrm{Re}\left[\frac{A_{CP,0}e^{i\Phi_0}}{(E - E_0 + i\Gamma_{0/\Delta_0})^{5/2}} + \frac{A_{ex}e^{i\Phi_{ex}}}{(E - E_{ex} + i\Gamma_{ex})^{2}} + \frac{A_{CP,\Delta_0}e^{i\Phi_{\Delta_0}}}{(E - (E_0+\Delta_0) + i\Gamma_{\Delta_0})^{5/2}}\right] \tag{F.5}$$

Finally, the overall modeled value for the PR signal is the sum of the contributions, plus a constant offset. In addition, a phase factor is fitted (this is due to the phase chosen for the lock-in amplifier during

the measurement):

$$\frac{\Delta R}{R} = \mathrm{Re}\{(CP + IS + C)e^{i\Phi_{PR}}\} \tag{F.6}$$

The symbols used for each parameter, and their physical meaning, are given in Table F.1. The fitting parameters obtained for each sample are given in Table F.3.

F.3 Second-derivative critical point fits

The figures in this section show the critical point fits to the second derivative of the dielectric function (multiplied by E^2) of the SiGeSn samples, obtained through fits to SE data. Table F.2 lists all the fitting parameters obtained. In each case, the phase of the fit was kept constant between samples, since during the fitting of the dielectric function to the SE data only the broadening, peak strength and centre energy were allowed to vary. The phase is kept fixed at the value which was found to give the best fit overall.

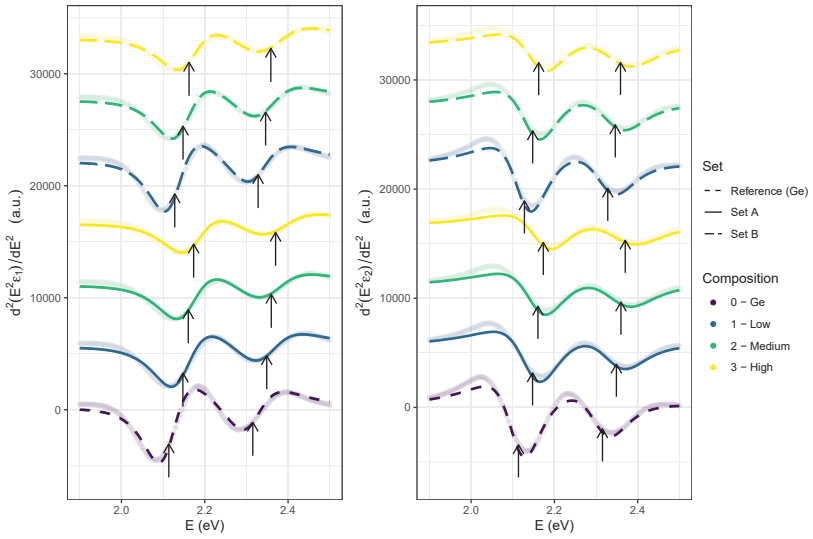


Figure F.1: Fits (lines) to the E_1 and $E_1 + \Delta_1$ critical point for Ge and Set A and Set B SiGeSn samples. The arrows indicate the critical point centre energies fitted.

Fig. F.1 shows the differentiated data and fits to the E_1 and $E_1 + \Delta_1$ critical points. The phase was kept fixed at 0.93 radians. Fig. F.2 shows the differentiated data and fits to the feature around 3 eV, assumed to be a combination of one or more of the E_0', $E_0' + \Delta_0'$ and $E_0' + \Delta_0' + \Delta_0$ transitions; it is fitted as a single critical point with phase 1.18 radians, although there appears to be a secondary weak feature around 3.5 eV. Fig. F.3 shows the differentiated data and fits to the E_2 critical point, with the phase fixed at 2.22 radians.

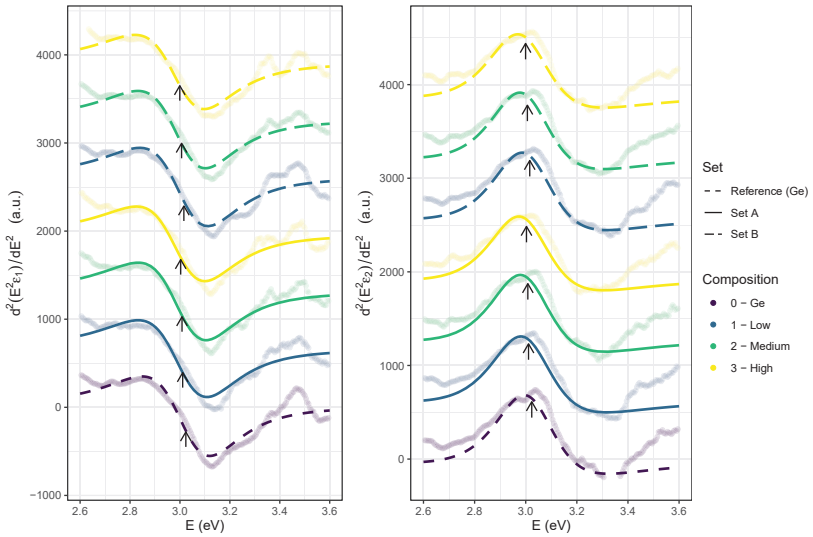


Figure F.2: Fits (lines) to the E_0' critical point for Ge and Set A and Set B SiGeSn samples. The arrows indicate the critical point centre energies fitted.

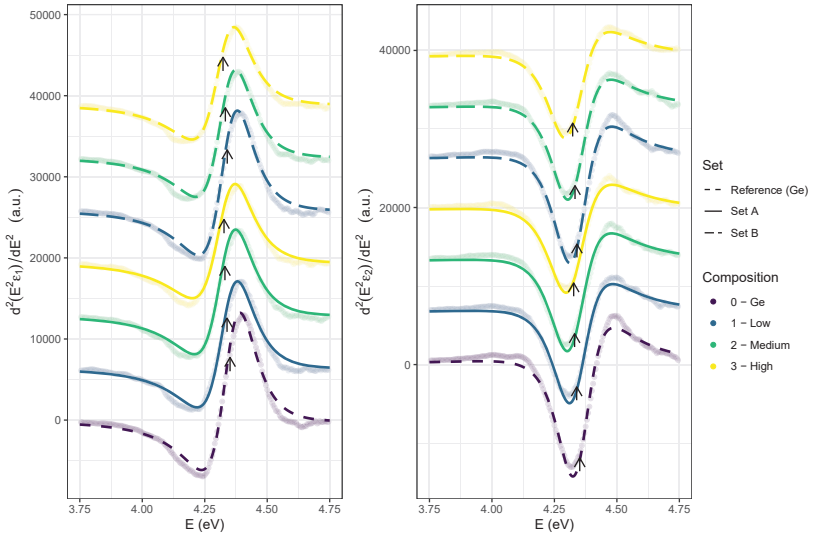


Figure F.3: Fits (lines) to the E_2 critical point for Ge and Set A and Set B SiGeSn samples. The arrows indicate the critical point centre energies fitted.

Table F.2: Parameters fitted to second derivative of the real and imaginary parts of the dielectric function of Ge and SiGeSn samples. The dielectric function was obtained through fits to ellipsometry data. The phase for each critical point was kept fixed across samples and is listed in the table headings for each transition. A is dimensionless, while E_{centre} and Γ have units of eV.

Sample	$\mathbf{E_0}$ ($\Phi = -\pi/2$ rad)			$\mathbf{E_1}$ ($\Phi = 0.93$ rad)			$\mathbf{E_1 + \Delta_1}$ ($\Phi = 0.93$ rad)			$\mathbf{E_0'}$ ($\Phi = -1.18$ rad)			$\mathbf{E_2}$ ($\Phi = 2.22$ rad)		
	A	E_{centre}	Γ	A	E_{centre}	Γ	A	E_{centre}	Γ	A	E_{centre}	Γ	A	E_{centre}	Γ
Ge	0.615	0.799	3.822E-02	31.3	2.11	7.58E-02	22.6	2.32	8.62E-02	36.9	3.024	0.229	239	4.351	0.125
A1	0.722	0.934	5.261E-02	30.8	2.15	8.87E-02	23.2	2.35	1.02E-01	36.8	3.011	0.233	212	4.339	0.132
A2	0.967	0.975	4.050E-02	26.8	2.16	9.12E-02	26.3	2.36	1.15E-01	36.3	3.008	0.230	219	4.331	0.135
A3	0.481	1.023	2.921E-02	23.0	2.17	9.27E-02	28.5	2.37	1.28E-01	35.4	3.003	0.232	217	4.327	0.140
B1	0.685	0.849	4.514E-02	29.1	2.13	7.69E-02	23.6	2.33	9.13E-02	36.9	3.016	0.231	228	4.340	0.127
B2	0.742	0.906	3.986E-02	26.6	2.15	8.45E-02	25.1	2.35	1.03E-01	35.7	3.007	0.229	212	4.332	0.131
B3	0.676	0.977	6.077E-02	23.9	2.16	9.04E-02	27.6	2.36	1.18E-01	36.1	2.999	0.235	205	4.323	0.137

Table F.3: Full results of fits to the photoreflectance data using the combined thin-film interference and critical point model. The meaning of the parameters is given in Table F.1. The fit is run 10 times for each sample; the values given are the mean result across the 10 fitting runs, with the standard deviation given in brackets.

Sample	$\mathbf{A_0}$	$\mathbf{E_0}$ (eV)	$\mathbf{\Gamma_0}$ (eV)	$\mathbf{\Delta_0}$ (eV)	$\mathbf{A_{CP,0}}$ $\times 10^8$	$\mathbf{\Phi_{0/\Delta_0}}$ (rad)	$\mathbf{A_{CP,\Delta_0}}$ $\times 10^9$	$\mathbf{A_{ex}}$ $\times 10^8$	$\mathbf{E_{ex}}$ (meV)	$\mathbf{\Phi_{ex}}$ (rad)	$\mathbf{d_{SiGeSn}}$ (nm)	$\mathbf{d_{GaAs}}$ (nm)	γ (eV^{-1})	$\mathbf{A_n}$ $\times 10^6$	$\mathbf{\Phi_{PR}}$ (rad)
A1	3.1 (0.4)	0.94 (0.007)	0.065 (0.003)	0.284 (0.01)	2.0 (0.5)	-1.6 (0.3)	14.5 (4.0)	8.6 (0.8)	5 (2)	0.4 (0.3)	1811 (41)	n/a	1.2 (0.2)	0.08 (0.01)	-1.3 (1.2)
A2	3.7 (0.3)	1.001 (0.024)	0.142 (0.004)	0.273 (0.02)	9.1 (0.6)	-1.2 (0.5)	25.5 (14.0)	3.9 (1.0)	6 (2)	1.2 (0.7)	1746 (6)	n/a	1.8 (0.1)	0.09 (0.01)	-0.1 (0.2)
A3	3.9 (0.0)	1.014 (0.002)	0.112 (0.006)	0.294 (0.01)	1.1 (0.2)	-1.9 (0.3)	19.8 (5.0)	9.3 (0.5)	6 (2)	-2.3 (0.1)	1828 (2)	n/a	1.6 (0.1)	0.09 (0.01)	-0.1 (0.2)
B1 - thin	1.9 (0.5)	0.866 (0.007)	0.037 (0.002)	0.291 (0.01)	1.5 (0.4)	1.1 (1.5)	3.4 (2.0)	3.9 (1.6)	6 (3)	-0.6 (2.0)	332 (11)	503 (16)	0.5 (0.4)	2.18 (1.08)	-0.3 (1.5)
B1 - thick	3.1 (0.4)	0.866 (0.003)	0.037 (0.002)	0.29 (0.01)	1.3 (0.3)	-2.5 (0.2)	1.8 (2.0)	4.3 (1.0)	5 (1)	-0.4 (0.2)	2073 (16)	504 (4)	0.4 (0.3)	1.48 (0.48)	2.3 (0.1)
B2 - thin	2.9 (0.4)	0.911 (0.003)	0.027 (0.001)	0.301 (0.01)	2.0 (0.2)	-0.8 (0.3)	4.4 (2.0)	7.9 (1.4)	6 (2)	1.7 (0.4)	362 (8)	502 (15)	0.4 (0.3)	2.28 (1.31)	-0.4 (1.3)
B2 - thick	3.1 (0.4)	0.907 (0.015)	0.036 (0.002)	0.292 (0.01)	1.4 (0.1)	-0.3 (1.5)	4.1 (2.0)	4.6 (1.8)	7 (2)	-0.1 (1.8)	2017 (39)	506 (8)	0.7 (0.4)	4.43 (1.85)	1.5 (0.2)
B3 - thin	2.6 (0.6)	0.953 (0.012)	0.039 (0.001)	0.292 (0.01)	1.4 (0.4)	-1.4 (0.6)	7.0 (1.0)	3.3 (1.4)	7 (2)	-0.0 (0.5)	353 (7)	515 (9)	0.4 (0.3)	2.45 (1.04)	0.2 (1.4)
B3 - thick	3.6 (0.3)	0.949 (0.008)	0.035 (0.003)	0.295 (0.01)	1.3 (0.3)	1.9 (0.6)	3.2 (2.0)	4.6 (2.0)	6 (2)	-1.6 (1.7)	2036 (49)	497 (11)	0.8 (0.5)	3.67 (2.22)	1.5 (0.2)

Appendix G

SiGeSn photoluminescence & structural measurements

This appendix shows XRD and optical microscopy scans for the Set A SiGeSn samples in more detail (G.1), in addition to further room-temperature (G.2) and temperature-dependent (G.3) PL data. The final section shows the Python code for using Solcore to optimize a four-junction device structure containing a SiGeSn sub-cell (G.4).

G.1 Structural measurements

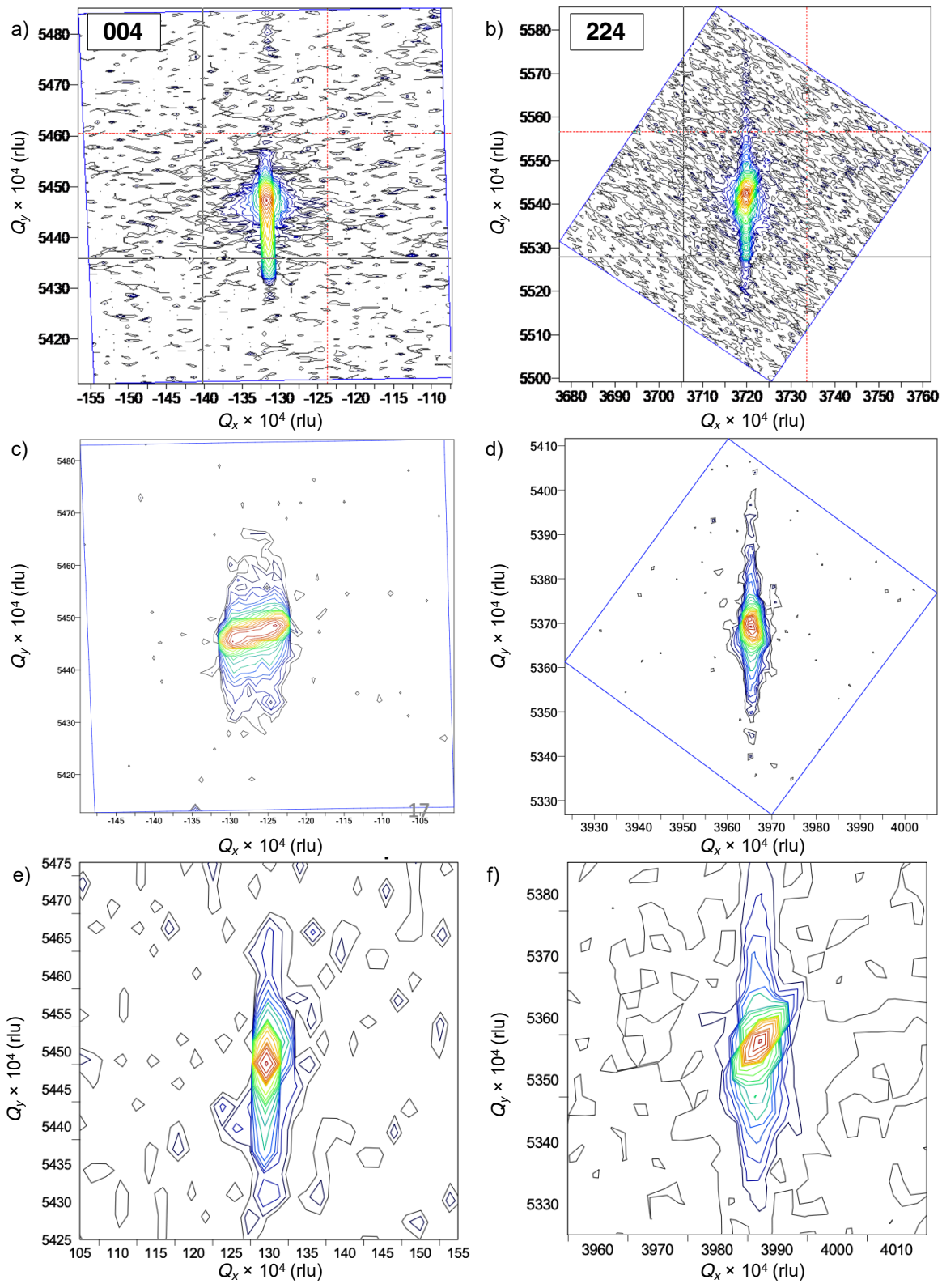


Figure G.1: XRD reciprocal space maps (RSM) for Set A SiGeSn samples around the (004) (left-hand column) and (224) (right-hand column) reciprocal space directions in terms of the reciprocal lattice coordinates Q_x and Q_y in reciprocal lattice units (rlu). a-b) RSMs for sample A1, c-d) RSMs for sample A2, e-f) RSMs for sample A3.

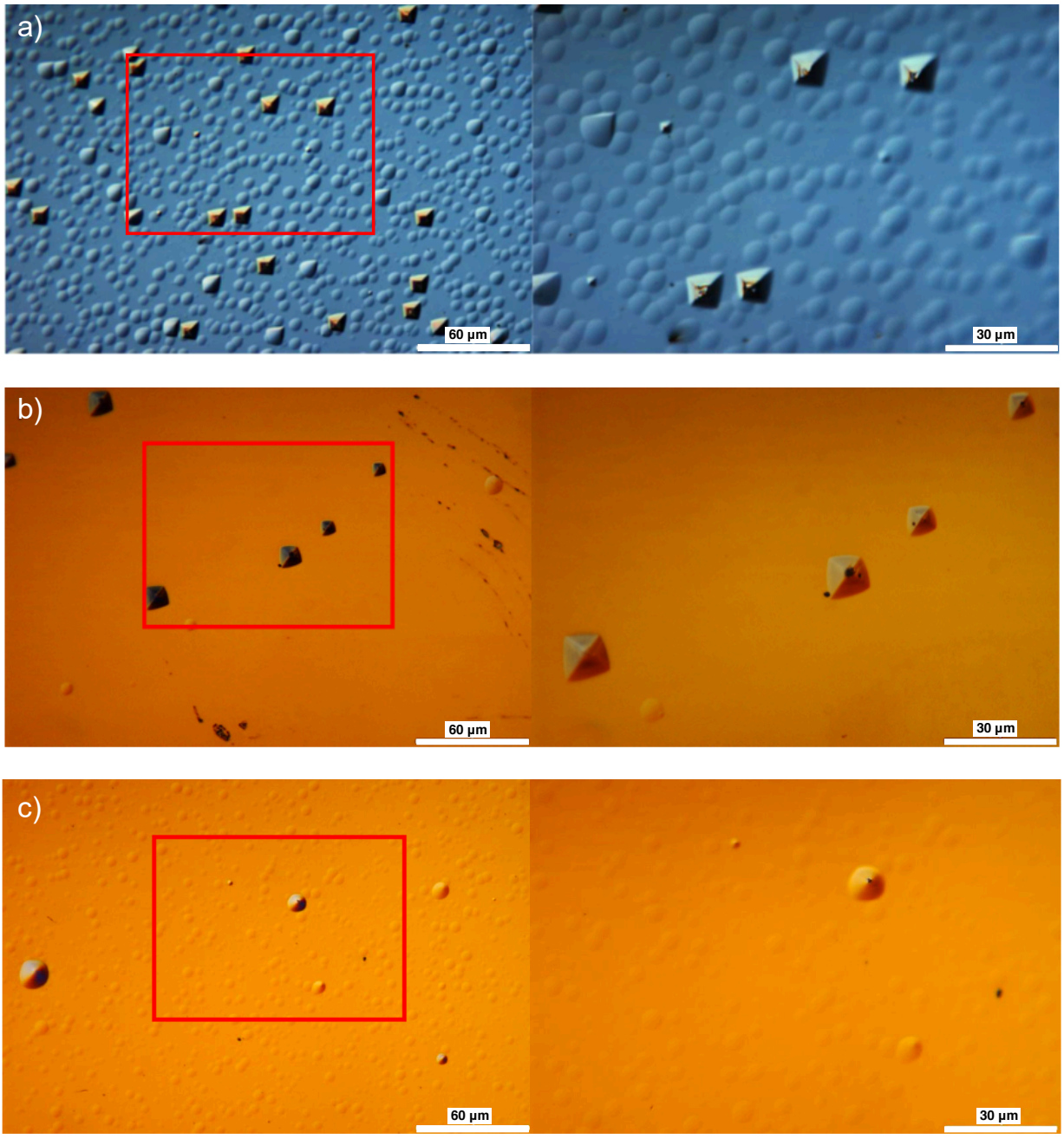


Figure G.2: Optical microscopy using a polarizer and Nomarski prism at 50× (left-hand images) and 100× (right-hand images) for the Set A SiGeSn samples. a) sample A1, b) sample A2 and c) sample A3.

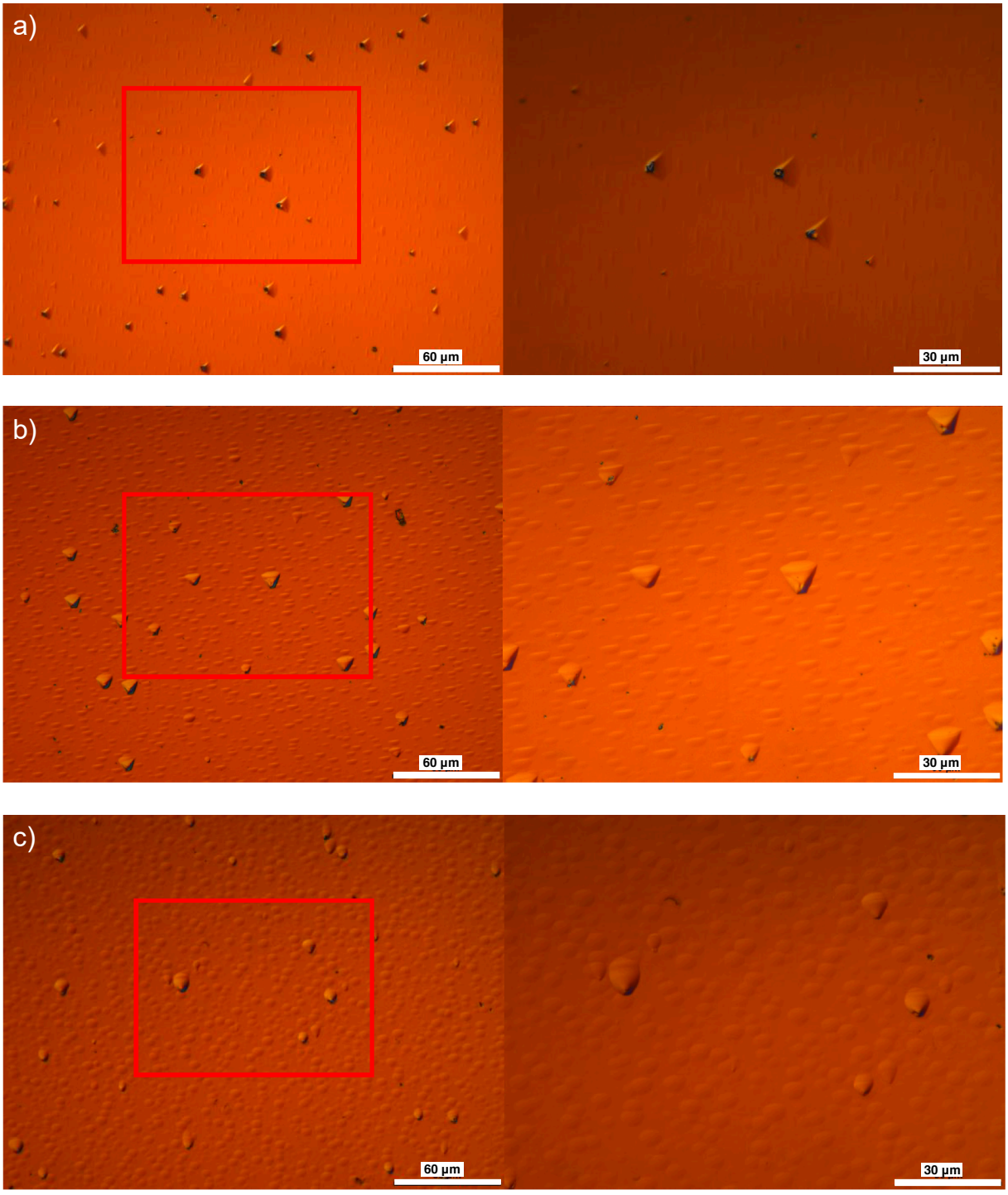


Figure G.3: Optical microscopy using a polarizer and Nomarski prism at 50× (left-hand images) and 100× (right-hand images) for the Set B SiGeSn samples. a) sample B1, b) sample B2 and c) sample B3.

G.2 Room-temperature photoluminescence of SiGeSn

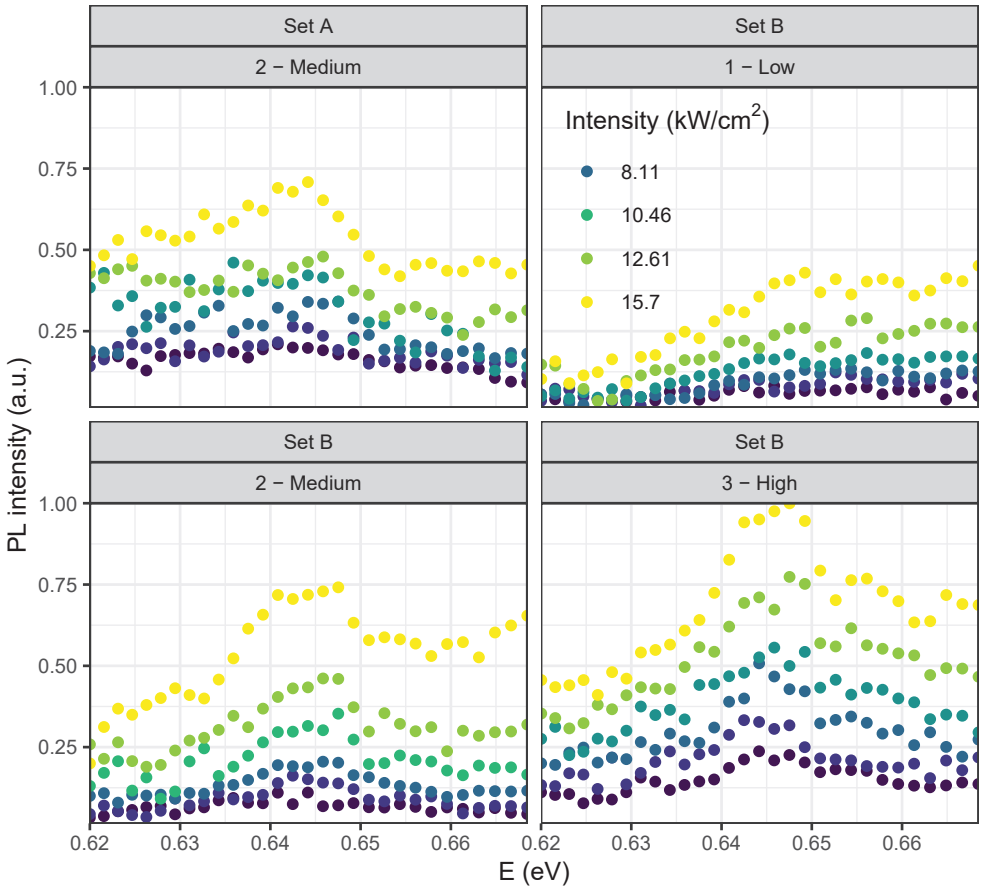


Figure G.4: Low-energy power-dependent PL at room temperature of the four SiGeSn samples with weaker PL intensities.

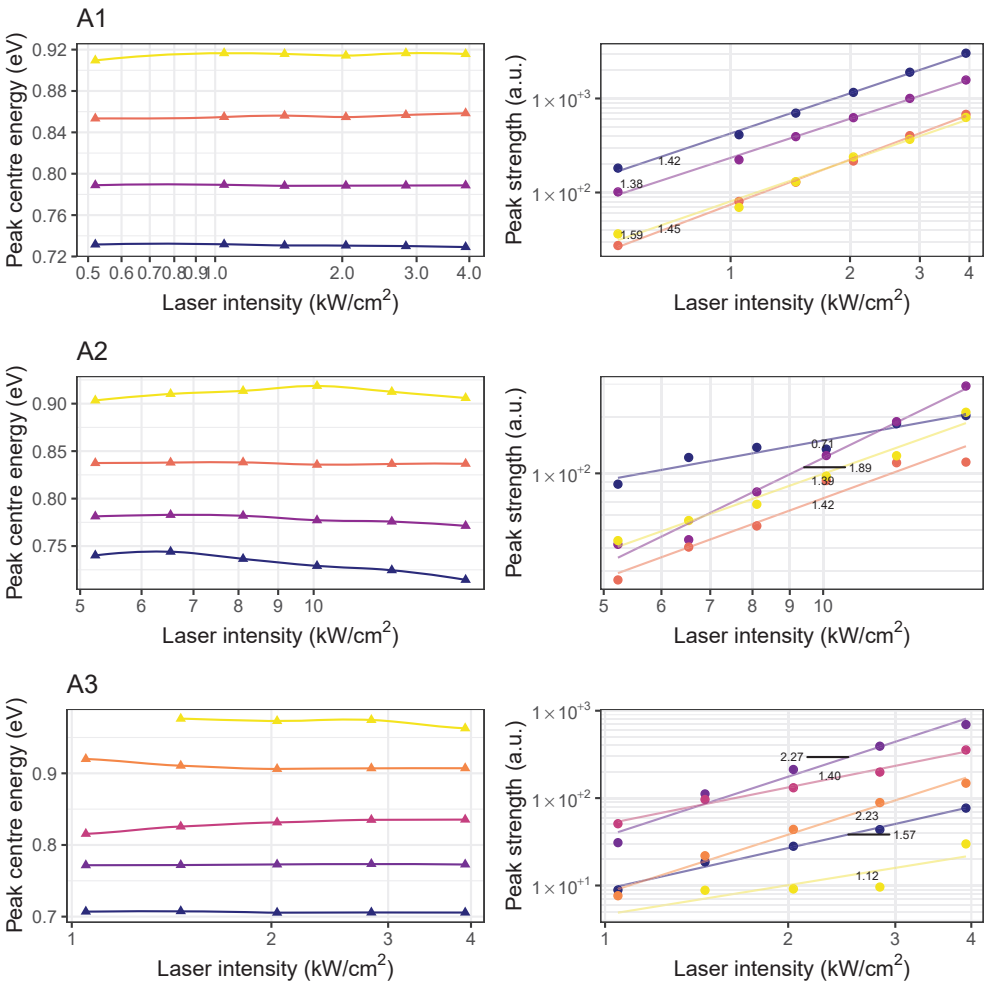


Figure G.5: Dependence of fitted peak centre energy (left) and peak strength (right) on incident laser intensity for the four (A1 and A2) or five (A3) individual peaks fitted to Set A SiGeSn photoluminescence data. The numbers in the right-hand plots indicate the power law exponent of the peak strength (area).

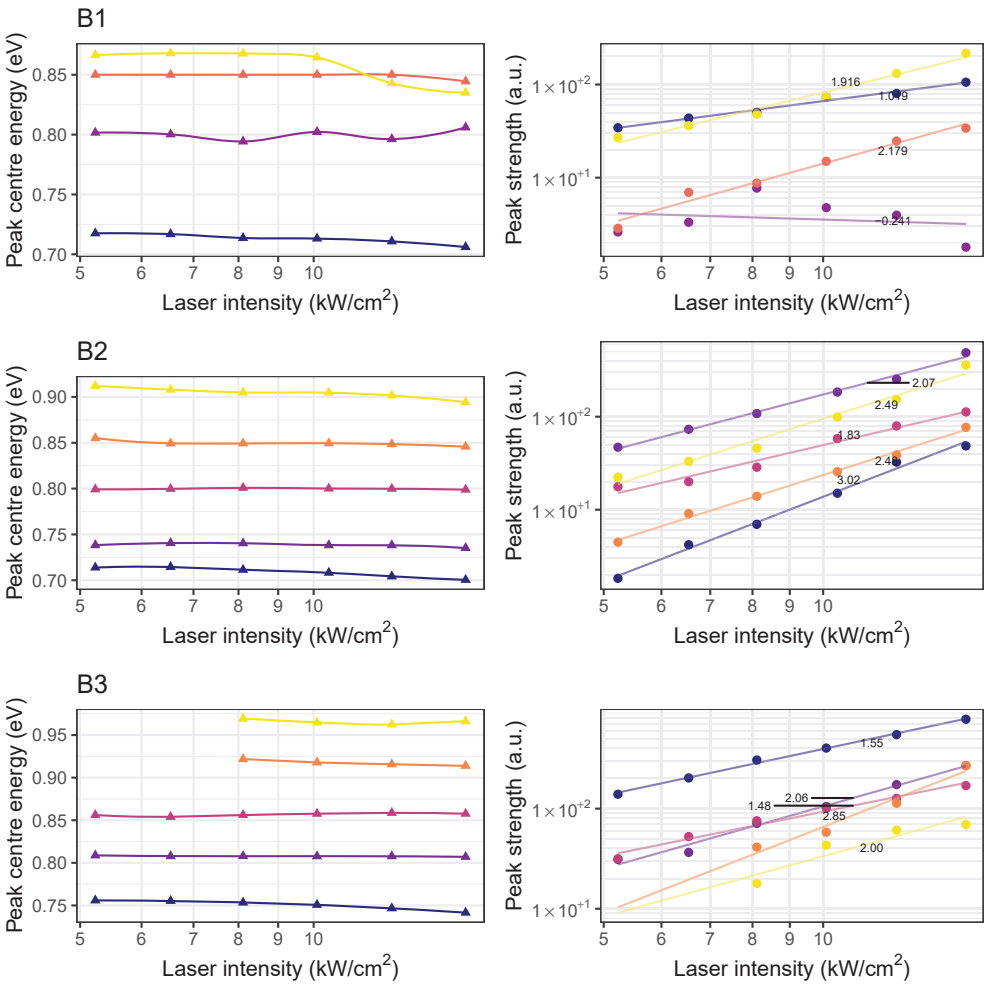


Figure G.6: Dependence of fitted peak centre energy (left) and peak strength (right) on incident laser intensity for the four (B1) or five (B2 and B3) individual peaks fitted to Set B SiGeSn photoluminescence data. The numbers in the right-hand plots indicate the power law exponent of the peak strength (area).

G.3 Temperature-dependent PL

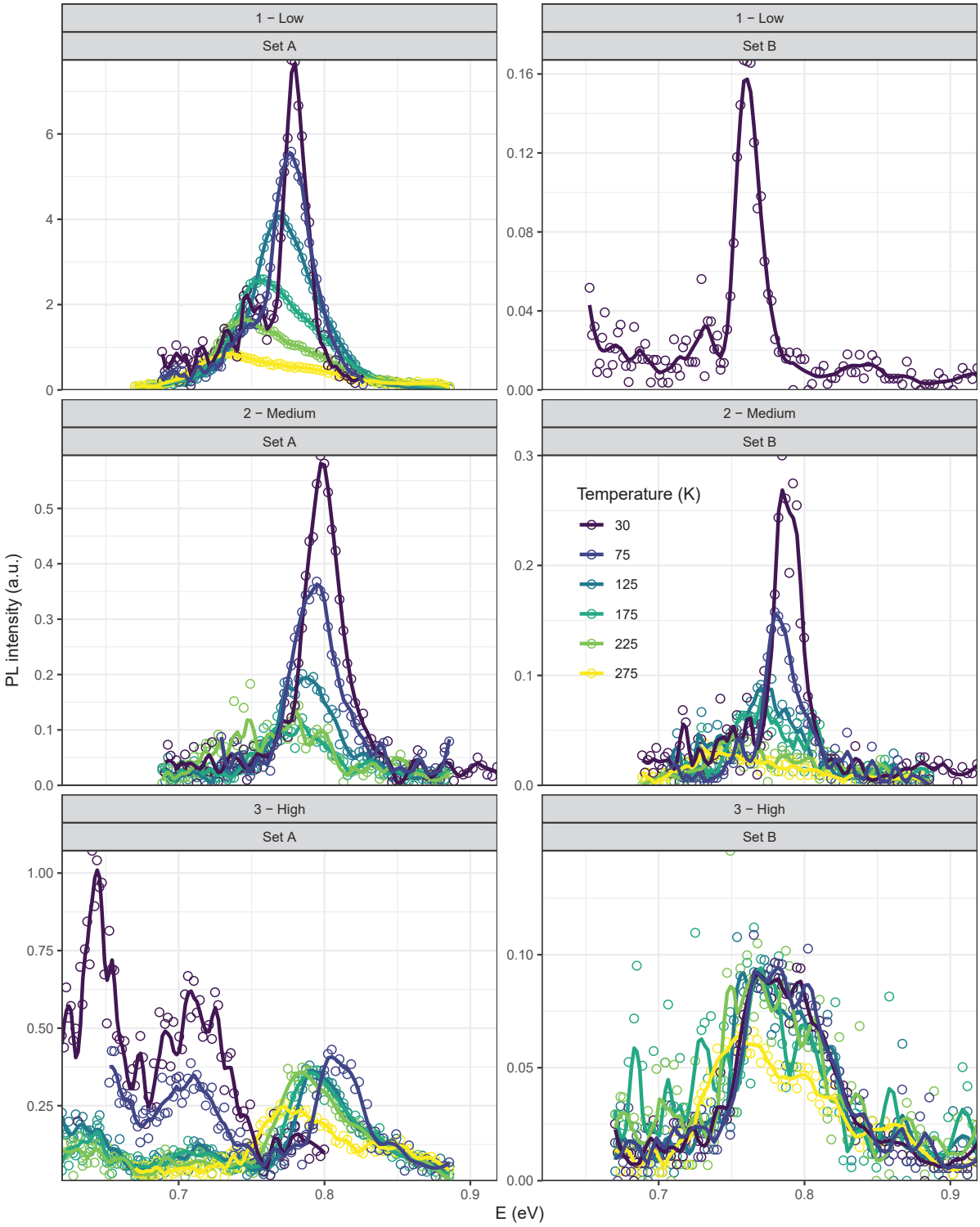


Figure G.7: Temperature-dependent PL of SiGeSn, showing the raw data (open circles) and smoothed lines. Measurements were made starting at 30K with increasing temperatures. Data at some temperatures is missing where no data could be obtained for that sample.

G.4 Multi-junction device simulation

The code below is an example of a differential evolution optimization of a solar cell structure in Solcore, demonstrating both a purely optical simulation and a device simulation. The parameters for SiGeSn are given explicitly based on available data (bandgap, optical constants, diffusion length [37]) or otherwise assumed to be the same as Ge.

```
import numpy as np

from solcore import material, si
from solcore.optics.tmm import OptiStack, calculate_rat
from solcore.optimization import PDE
from solcore.light_source import LightSource

from solcore.solar_cell import SolarCell
from solcore.structure import Junction, Layer
from solcore.solar_cell_solver import solar_cell_solver
from solcore.constants import q, kb
from solcore.material_system import create_new_material

import seaborn as sns
import matplotlib.pyplot as plt

class calc_min_Jsc():

    def __init__(self):
        # initialize an instance of the class; set some information which will be used in each iteration of the
            calculation:
        # materials, wavelengths, the light source
        T = 298
        wl = np.arange(290, 1900, 2.5)

        # materials
        SiGeSn = material('SiGeSn')(T=T)

        GaAs = material('GaAs')(T=T)
        InGaP = material('GaInP')(In=0.5, T=T)
        Ge = material('Ge')(T=T)

        self.wl = wl
        self.SiGeSn = [self.wl, SiGeSn.n(self.wl*1e-9), SiGeSn.k(self.wl*1e-9)]
        self.Ge = [self.wl, Ge.n(self.wl*1e-9), Ge.k(self.wl*1e-9)]
        self.InGaP = [self.wl, InGaP.n(self.wl*1e-9), InGaP.k(self.wl*1e-9)]
        self.GaAs = [self.wl, GaAs.n(self.wl*1e-9), GaAs.k(self.wl*1e-9)]
        self.MgF2 = [self.wl, material('MgF2')().n(self.wl*1e-9), material('MgF2')().k(self.wl*1e-9)]
        self.Ta2O5 = [self.wl, material('410',
                                        nk_db=True)().n(self.wl*1e-9), material('410',
                                                                                nk_db=True)().k(self.wl*1e-9)]

        # assuming an AM1.5G spectrum
        self.spectr = LightSource(source_type='standard', version='AM1.5g', x=self.wl,
                                  output_units='photon_flux_per_nm', concentration=1).spectrum(self.wl)[1]

    def calculate(self, x):

        # x[0] = MgF2 thickness (anti-reflection coating)
        # x[1] = Ta2O5 thickness (anti-reflection coating)
        # x[2]  = InGaP (top junction) thickness
        # x[3] = GaAs (second junction) thickness
        # x[4] = SiGeSn (third junction) thickness
        # keep the thickness of the bottom cell constant; from an optical point of view, this should be
            infinitely thick
        Ag = material('Ag_Jiang')()
```

```
        SC = [[x[0]] + self.MgF2, [x[1]] + self.Ta2O5, [x[2]] + self.InGaP, [x[3]] + self.GaAs, [x[4]] + self.
            SiGeSn, [300e3]+self.Ge]

        # create the OptiStack
        full_stack = OptiStack(SC, no_back_reflection=False, substrate=Ag)

        # calculate reflection, transmission, and absorption in each layer. We are specifying that the last
            layer,
        # a very thick Ge substrate, should be treated incoherently, otherwise we would see very narrow,
            unphysical oscillations
        # in the R/A/T spectra.
        RAT = calculate_rat(full_stack, self.wl, no_back_reflection=False, coherent=False,
                            coherency_list=['c', 'c', 'c', 'c', 'c', 'i'])

        # extract absorption per layer
        A_InGaP = RAT['A_per_layer'][3]
        A_GaAs = RAT['A_per_layer'][4]
        A_SiGeSn = RAT['A_per_layer'][5]
        A_Ge = RAT['A_per_layer'][6]

        ## calculate photo-generated currents using the AM1.5 G spectrum for each layer
        Jsc_InGaP = 0.1 * q * np.trapz(A_InGaP* self.spectr, self.wl)
        Jsc_GaAs = 0.1 * q * np.trapz(A_GaAs * self.spectr, self.wl)
        Jsc_SiGeSn = 0.1 * q * np.trapz(A_SiGeSn* self.spectr, self.wl)
        Jsc_Ge = 0.1 * q* np.trapz(A_Ge * self.spectr, self.wl)

        return [[Jsc_InGaP, Jsc_GaAs, Jsc_SiGeSn, Jsc_Ge], RAT]

    def evaluate(self, x):

        results = self.calculate(x)
        # find the limiting current by checking which junction has the lowest current. Then take the negative
            since
        # we need to minimize (not maximize)
        limiting_Jsc = -min(results[0])

        return limiting_Jsc

    def plot(self, x):

        results = self.calculate(x)
        RAT = results[1]
        A_InGaP = RAT['A_per_layer'][3]
        A_GaAs = RAT['A_per_layer'][4]
        A_SiGeSn = RAT['A_per_layer'][5]
        A_Ge = RAT['A_per_layer'][6]

        plt.figure()
        plt.plot(self.wl, A_InGaP, label='InGaP')
        plt.plot(self.wl, A_GaAs, label='A_GaAs')
        plt.plot(self.wl, A_SiGeSn, label='SiGeSn')
        plt.plot(self.wl, A_Ge, label = 'Ge')
        plt.plot(self.wl, RAT['T'], label='T')
        plt.plot(self.wl, RAT['R'], label='R')
        plt.text(500, 0.6, np.round(results[0][0], 1))
        plt.text(740, 0.6, np.round(results[0][1], 1))
        plt.text(1000, 0.6, np.round(results[0][2], 1))
        plt.text(1450, 0.6, np.round(results[0][3], 1))
        plt.legend()
        plt.xlabel('Wavelength (nm)')
        plt.ylabel('R/A/T')
        plt.show()

class calc_min_Jsc_DA():
```

```
def __init__(self, ARC_thickness):
    self.ARC = ARC_thickness

def make_cell(self, x):

    #x[0]: total InGaP thickness
    #x[1]: total InGaAs thickness
    #x[2]: total SiGeSn thickness
    #x[3]: total Ge thickness

    #x[4]: InGaP emitter thickness
    #x[5]: InGaAs emitter thickness
    #x[6]: SiGeSn emitter thickness
    #x[7]: Ge emitter thickness
    e_charge = si('1eV')
    # materials
    SiGeSn = material('SiGeSn') # based on sample A3
    GaAs = material('GaAs')
    InGaP = material('GaInP')
    Ge = material('Ge')
    MgF2 = material('MgF2')()
    Ta2O5 = material('410', nk_db=True)()
    AlInP = material("AlInP")
    Ag = material('Ag_Jiang')()

    window_material = AlInP(Al=0.52)

    GaInP_mobility_h = 0.03
    GaInP_lifetime_h = 1e-8
    GaInP_D_h = GaInP_mobility_h * kb * 300 / e_charge
    GaInP_L_h = np.sqrt(GaInP_D_h * GaInP_lifetime_h)
    GaInP_mobility_e = 0.015
    GaInP_lifetime_e = 1e-8
    GaInP_D_e = GaInP_mobility_e * kb * 300 / e_charge
    GaInP_L_e = np.sqrt(GaInP_D_e * GaInP_lifetime_e)

    top_cell_n_material = InGaP(In=0.5, Nd=si("2e18cm-3"), hole_diffusion_length=GaInP_L_h,
                                relative_permittivity=11.75, hole_mobility=GaInP_mobility_h)
    top_cell_p_material = InGaP(In=0.5, Na=si("2e17cm-3"), electron_diffusion_length=GaInP_L_e,
                                relative_permittivity=11.75, electron_mobility=GaInP_mobility_e)

    # MID CELL  - GaAs
    GaAs_mobility_h = 0.85
    GaAs_lifetime_h = 1e-8
    GaAs_D_h = GaAs_mobility_h * kb * 300 / e_charge
    GaAs_L_h = np.sqrt(GaAs_D_h * GaAs_lifetime_h)
    GaAs_mobility_e = 0.08
    GaAs_lifetime_e = 1e-8
    GaAs_D_e = GaAs_mobility_e * kb * 300 / e_charge
    GaAs_L_e = np.sqrt(GaAs_D_e * GaAs_lifetime_e)

    mid_cell_n_material = GaAs(Nd=si("1e18cm-3"), hole_diffusion_length=GaAs_L_h,
                               relative_permittivity=13.1, hole_mobility=GaAs_mobility_h)
    mid_cell_p_material = GaAs(Na=si("1e17cm-3"), electron_diffusion_length=GaAs_L_e,
                               relative_permittivity=13.1, electron_mobility=GaAs_mobility_e)

    SiGeSn.band_gap = si('0.745eV') # from PL measurement
    SiGeSn_L_h = si('0.35um')
    SiGeSn_L_e = si('5um') # from Roucka et al. device data fitting
    SiGeSn_lifetime_e = 1e-6
    SiGeSn_lifetime_h = 1e-6
    SiGeSn_mobility_h = SiGeSn_L_h ** 2 * e_charge / (SiGeSn_lifetime_h * kb * 300)
    SiGeSn_mobility_e = SiGeSn_L_e ** 2 * e_charge / (SiGeSn_lifetime_e * kb * 300)

    pen_cell_n_material = SiGeSn(Nd=si("1e18cm-3"), hole_diffusion_length=SiGeSn_L_h,
```

```
                                relative_permittivity=16, hole_mobility=SiGeSn_mobility_h)
    pen_cell_p_material = SiGeSn(Na=si("1e17cm-3"), electron_diffusion_length=SiGeSn_L_e,
                                relative_permittivity=16, electron_mobility=SiGeSn_mobility_e)

    Ge_lifetime_h = 1e-6
    Ge_L_h = si('500nm')
    Ge_mobility_h = Ge_L_h ** 2 * e_charge / (Ge_lifetime_h * kb * 300)
    Ge_mobility_e = 0.18
    Ge_lifetime_e = 1e-6
    Ge_D_e = Ge_mobility_e * kb * 300 / e_charge
    Ge_L_e = np.sqrt(Ge_D_e * Ge_lifetime_e)

    bot_cell_n_material = Ge(Nd=si("2e18cm-3"), hole_diffusion_length=Ge_L_h,
                             relative_permittivity=16, hole_mobility=Ge_mobility_h)
    bot_cell_p_material = Ge(Na=si("1e17cm-3"), electron_diffusion_length=Ge_L_e,
                             relative_permittivity=16, electron_mobility=Ge_mobility_e)


    # And, finally, we put everything together, adding also the surface recombination velocities. We also
        add some shading
    # due to the metallisation of the cell = 8%, and indicate it has an area of 0.7x0.7 mm2 (converted to
        m2)
    solar_cell = SolarCell([
        Layer(si(self.ARC[0], 'nm'), material=MgF2), Layer(si(self.ARC[1], 'nm'), material=Ta2O5),
        Junction([Layer(si(25, 'nm'), material=window_material, role='window'),
                  Layer(si(x[4], 'nm'), material=top_cell_n_material, role='emitter'),
                  Layer(si(x[0]-x[4], 'nm'), material=top_cell_p_material, role='base'),
                  ], sn=1, sp=1, kind='DA'),
        Junction([Layer(si(x[5], 'nm'), material=mid_cell_n_material, role='emitter'),
                  Layer(si(x[1]-x[5], 'nm'), material=mid_cell_p_material, role='base'),
                  ], sn=1, sp=1, kind='DA'),
        Junction([Layer(si(x[6], 'nm'), material=pen_cell_n_material, role='emitter'),
                  Layer(si(x[2]-x[6], 'nm'), material=pen_cell_p_material, role='base'),
                  ], sn=1, sp=1, kind='DA'),
        Junction([Layer(si(x[7], 'nm'), material=bot_cell_n_material, role='emitter'),
                  Layer(si(x[3]-x[7], 'nm'), material=bot_cell_p_material, role='base'),
                  ], sn=1, sp=1, kind='DA'),
    ], shading=0.0, substrate=Ag)

    return solar_cell

def calculate(self, x, eqe=False, conc=1):
    light_source = LightSource(source_type='standard', version='AM1.5g', concentration=conc)
    wl = np.arange(280, 1900, 2.5) * 1e-9
    solar_cell = self.make_cell(x)

    position = [1e-9] * 10 + [1e-8]
    V = np.linspace(0, 3.5, 300)
    solar_cell_solver(solar_cell, 'iv',
                      user_options={'voltages': V, 'light_iv': True, 'wavelength': wl, 'mpp': True,
                                    'light_source': light_source, 'pol': 's',
                                    'optics_method': 'TMM', 'BL_correction': True, 'position': position})
    if eqe:
        solar_cell_solver(solar_cell, 'qe', user_options={'wavelength': wl})

    return solar_cell, wl, V

def evaluate(self, x):

    SC = self.calculate(x)[0]
    efficiency = SC.iv["Eta"]

    return -efficiency # yabox DE implementation is a minimization algorithm

def plot(self, x, conc=1):
```

```
        cols = sns.color_palette("hls", 6)
        SC, wl, V = self.calculate(x, eqe=True, conc=conc)
        efficiency = SC.iv["Eta"]
        pmax = SC.iv["Pmpp"]
        ff = SC.iv["FF"]
        voc = SC.iv["Voc"]
        isc = SC.iv["Isc"]

        plt.figure()
        plt.plot(V, SC.iv['IV'][1] / 10, 'k', linewidth=3, label='Total')
        plt.plot(V, -SC[2].iv(V) / 10, label='GaInP', color=cols[0])
        plt.plot(V, -SC[3].iv(V) / 10, label='GaAs', color=cols[1])
        plt.plot(V, -SC[4].iv(V) / 10, label='SiGeSn (A3)', color=cols[2])
        plt.plot(V, -SC[5].iv(V) / 10, label='Ge', color=cols[3])
        plt.text(1.6, 8, '$\eta = $' + str(round(efficiency * 100, 1)) + '%')
        plt.text(1.6, 7,'P$_{max}$ = '+str(round(pmax,1))+' W/m$^2$')
        plt.text(1.6, 6, 'FF = ' + str(round(ff * 100, 1)) + '%')
        plt.text(1.6, 5,'V$_{oc}$ = '+str(round(voc,2))+' V')
        plt.text(1.6, 4, 'J$_{sc}$ = '+str(round(0.1*isc,1))+' mA/cm$^2$')

        plt.legend(loc='upper right')
        plt.ylim(0, 17)
        plt.xlim(0, 3.5)
        plt.ylabel('Current (mA/cm$^2$)')
        plt.text(-(3.5)*0.1, 14, 'b)')
        plt.xlabel('Voltage (V)')
        plt.show()

        plt.figure()
        plt.plot(wl * 1e9, SC.absorbed * 100, 'k--', label='Absorption')
        plt.plot(wl * 1e9, SC[2].eqe(wl) * 100, label='InGaP', color=cols[0])
        plt.plot(wl * 1e9, SC[3].eqe(wl) * 100, label='InGaAs', color=cols[1])
        plt.plot(wl * 1e9, SC[4].eqe(wl) * 100, label='SiGeSn (A3)', color=cols[2])
        plt.plot(wl * 1e9, SC[5].eqe(wl) * 100, label='Ge', color=cols[3])
        plt.legend(loc='upper right')
        plt.xlim(280, 1850)
        plt.ylim(0, 100)
        plt.ylabel('EQE (%)')
        plt.xlabel('Wavelength (nm)')
        plt.text(280-(1850-280)*0.12, 100, 'a)')
        plt.show()

        return SC, wl

if __name__ == "__main__":
    # number of iterations for Differential Evolution optimization of the optical stack
    maxiters=100

    # make an instance of the class the DE algorithm is going to use, as defined above
    DE_class = calc_min_Jsc()
    PDE_obj = PDE(DE_class.evaluate, bounds=[[10,150], [10,105], [200, 1000], [500, 10000], [500, 10000]],
        maxiters=maxiters)

    # to run the DE, use the .solve() function of the PDE object class
    res = PDE_obj.solve(show_progress=True)
    # best population:
    best_pop = res[0]
    DE_class.plot(best_pop)

    ## Now that the layer thicknesses have been optimized from an optical point of view, we want to design the
        device (or
    # at least a simplified version, by calculating a more realistic EQE. Obviously additional parameters like
        the doping of the
    # layers could be varied too.
    # x[0]: total InGaP thickness
```

```
# x[1]: total InGaAs thickness
# x[2]: total SiGeSn thickness
# x[3]: total Ge thickness

# x[4]: InGaP n thickness
# x[5]: InGaAs n thickness
# x[6]: SiGeSn n thickness
# x[7]: Ge n thickness
# generate upper and lower bounds: total layer thickness between 75% and 125% of values fitted in TMM
    calculation. Ge
# starting value is 200 um
starting_params = np.append(best_pop[2:], [200000])

lower = 0.75*starting_params
upper = 1.25*starting_params

# upper and lower bounds for the n-type (highly doped) layers
lower_ntype = [40, 40, 40, 40]
upper_ntype = [200, 300, 300, 500]
all_lower = np.append(lower, lower_ntype)
all_upper = np.append(upper, upper_ntype)
# full list of bounds
all_bounds = np.stack((all_lower, all_upper)).T

# DE calculation for the electrical simulation
maxiters_DA = 5
# keep the ARC thicknesses fixed at the values obtained in the optical simulation
DE_class_DA = calc_min_Jsc_DA(best_pop[0:2])
# default population size = 5*number of params
PDE_obj_DA = PDE(DE_class_DA.evaluate, bounds=all_bounds, maxiters=maxiters_DA)
# solve, i.e. minimize the problem
res_DA = PDE_obj_DA.solve(show_progress=True)
best_pop_DA = res_DA[0]
# plot the result at these best parameters
solar_cell=DE_class_DA.plot(best_pop_DA)
```

Appendix H

Copyright permissions

Fig. 4.4 is from ref. [128], which is published Open Access under the terms of the Creative Commons Attribution 4.0 International License, allowing reproduction with attribution. Fig. 4.19 contains figures from [86], which is also Open Access.

Content from refs. [117, 204, 171], all published in Solar Energy Materials and Solar Cells, is contained in Chapters 4 and 6. As a (co-)author, the right to reproduce text and figures from these publications here is retained: "Please note that, as the author of this Elsevier article, you retain the right to include it in a thesis or dissertation, provided it is not published commercially. Permission is not required, but please ensure that you reference the journal as the original source."

Chapter 6.1 contains content from [209], published as SPIE conference proceedings: "For articles published under SPIE copyright, authors, or their employers in the case of works made for hire, retain the following rights: [...] The right to prepare derivative publications based on the Paper, including books or book chapters, journal papers, and magazine articles, provided that publication of a derivative work occurs subsequent to the official date of publication by SPIE. Thus, authors may reproduce their original figures and text in new publications."

For the remaining figures from other publications, licenses for reproduction are included on the subsequent pages.

JOHN WILEY AND SONS LICENSE TERMS AND CONDITIONS

Aug 13, 2020

This Agreement between Imperial College London -- Phoebe Pearce ("You") and John Wiley and Sons ("John Wiley and Sons") consists of your license details and the terms and conditions provided by John Wiley and Sons and Copyright Clearance Center.

License Number	4877130107183
License date	Jul 27, 2020
Licensed Content Publisher	John Wiley and Sons
Licensed Content Publication	PROGRESS IN PHOTOVOLTAICS: RESEARCH AND APPLICATIONS
Licensed Content Title	Fundamental losses in solar cells
Licensed Content Author	Nicholas J. Ekins-Daukes, Louise C. Hirst
Licensed Content Date	Aug 26, 2010
Licensed Content Volume	19
Licensed Content Issue	3
Licensed Content Pages	8
Type of Use	Dissertation/Thesis
Requestor type	University/Academic
Format	Print and electronic
Portion	Figure/table
Number of figures/tables	1
Will you be translating?	No
Title	Novel materials and device architectures forhigh-efficiency photovoltaic devices
Institution name	Imperial College London
Expected presentation date	Aug 2020
Portions	Fig. 6
Requestor Location	Imperial College London Department of Physics Imperial College London London, SW7 2AZ United Kingdom Attn: Imperial College London
Publisher Tax ID	EU826007151
Total	**0.00 GBP**
Terms and Conditions	

TERMS AND CONDITIONS

This copyrighted material is owned by or exclusively licensed to John Wiley & Sons, Inc. or one of its group companies (each a"Wiley Company") or handled on behalf of a society with which a Wiley Company has exclusive publishing rights in relation to a particular work (collectively "WILEY"). By clicking "accept" in connection with completing this licensing transaction, you agree that the following terms and conditions apply to this transaction (along with the billing and payment terms and conditions established by the Copyright Clearance Center Inc., ("CCC's Billing and Payment terms and conditions"), at the time that you opened your RightsLink account (these are available at any time at http://myaccount.copyright.com).

Terms and Conditions

- The materials you have requested permission to reproduce or reuse (the "Wiley Materials") are protected by copyright.
- You are hereby granted a personal, non-exclusive, non-sub licensable (on a stand-alone basis), non-transferable, worldwide, limited license to reproduce the Wiley Materials for the purpose specified in the licensing process. This license, **and any CONTENT (PDF or image file) purchased as part of your order,** is for a one-time use only and limited to any

SPRINGER NATURE LICENSE TERMS AND CONDITIONS

Aug 13, 2020

This Agreement between Imperial College London -- Phoebe Pearce ("You") and Springer Nature ("Springer Nature") consists of your license details and the terms and conditions provided by Springer Nature and Copyright Clearance Center.

License Number	4877130637054
License date	Jul 27, 2020
Licensed Content Publisher	Springer Nature
Licensed Content Publication	Springer eBook
Licensed Content Title	Optical Properties I
Licensed Content Author	Peter Y. Yu, Manuel Cardona
Licensed Content Date	Jan 1, 2010
Type of Use	Thesis/Dissertation
Requestor type	academic/university or research institute
Format	print and electronic
Portion	figures/tables/illustrations
Number of figures/tables/illustrations	3
Will you be translating?	no
Circulation/distribution	1 - 29
Author of this Springer Nature content	no
Title	Novel materials and device architectures forhigh-efficiency photovoltaic devices
Institution name	Imperial College London
Expected presentation date	Aug 2020
Portions	FIg. 6.9, Fig. 6.16, Fig. 6.50
Requestor Location	Imperial College London Department of Physics Imperial College London London, SW7 2AZ United Kingdom Attn: Imperial College London
Total	**0.00 USD**
Terms and Conditions	

Springer Nature Customer Service Centre GmbH
Terms and Conditions

This agreement sets out the terms and conditions of the licence (the **Licence**) between you and **Springer Nature Customer Service Centre GmbH** (the **Licensor**). By clicking 'accept' and completing the transaction for the material (**Licensed Material**), you also confirm your acceptance of these terms and conditions.

1. Grant of License

1. 1. The Licensor grants you a personal, non-exclusive, non-transferable, world-wide licence to reproduce the Licensed Material for the purpose specified in your order only. Licences are granted for the specific use requested in the order and for no other use, subject to the conditions below.

1. 2. The Licensor warrants that it has, to the best of its knowledge, the rights to license reuse of the Licensed Material. However, you should ensure that the material you are requesting is original to the Licensor and does not carry the

AIP PUBLISHING LICENSE TERMS AND CONDITIONS

Aug 13, 2020

This Agreement between Imperial College London -- Phoebe Pearce ("You") and AIP Publishing ("AIP Publishing") consists of your license details and the terms and conditions provided by AIP Publishing and Copyright Clearance Center.

License Number	4887230465594
License date	Aug 13, 2020
Licensed Content Publisher	AIP Publishing
Licensed Content Publication	Journal of Applied Physics
Licensed Content Title	Optical dispersion relations for Si and Ge
Licensed Content Author	Sadao Adachi
Licensed Content Date	Oct 1, 1989
Licensed Content Volume	66
Licensed Content Issue	7
Type of Use	Thesis/Dissertation
Requestor type	Student
Format	Print and electronic
Portion	Figure/Table
Number of figures/tables	1
Title	Novel materials and device architectures forhigh-efficiency photovoltaic devices
Institution name	Imperial College London
Expected presentation date	Aug 2020
Portions	Fig. 6
Requestor Location	Imperial College London Department of Physics Imperial College London London, SW7 2AZ United Kingdom Attn: Imperial College London
Total	**0.00 GBP**
Terms and Conditions	

AIP Publishing -- Terms and Conditions: Permissions Uses

AIP Publishing hereby grants to you the non-exclusive right and license to use and/or distribute the Material according to the use specified in your order, on a one-time basis, for the specified term, with a maximum distribution equal to the number that you have ordered. Any links or other content accompanying the Material are not the subject of this license.

1. You agree to include the following copyright and permission notice with the reproduction of the Material:"Reprinted from [FULL CITATION], with the permission of AIP Publishing." For an article, the credit line and permission notice must be printed on the first page of the article or book chapter. For photographs, covers, or tables, the notice may appear with the Material, in a footnote, or in the reference list.
2. If you have licensed reuse of a figure, photograph, cover, or table, it is your responsibility to ensure that the material is original to AIP Publishing and does not contain the copyright of another entity, and that the copyright notice of the figure, photograph, cover, or table does not indicate that it was reprinted by AIP Publishing, with permission, from another source. Under no circumstances does AIP Publishing purport or intend to grant permission to reuse material to which it does not hold appropriate rights.
   You may not alter or modify the Material in any manner. You may translate the Material into another language only if you have licensed translation rights. You may not use the Material for promotional purposes.

Copyright Clearance Center Marketplace™

Springer - License Terms and Conditions

This is a License Agreement between Phoebe Pearce ("You") and Springer ("Publisher") provided by Copyright Clearance Center ("CCC"). The license consists of your order details, the terms and conditions provided by Springer, and the CCC terms and conditions.

All payments must be made in full to CCC.

Order Date	01-Aug-2020	**Type of Use**	Republish in a thesis/dissertation
Order license ID	1052553-1		
ISBN-13	9783540428763	**Publisher**	Springer
		Portion	Chart/graph/table/figure

LICENSED CONTENT

Publication Title	Semiconductors. Subvolume A1, Group IV elements, IV-IV and III-V compounds	**Country**	Germany
		Rightsholder	Springer
		Publication Type	Book
Author/Editor	Rössler, Ulrich, Adachi, Sadao		
Language	English		

REQUEST DETAILS

Portion Type	Chart/graph/table/figure	**Distribution**	U.K. and Commonwealth (excluding Canada)
Number of charts / graphs / tables / figures requested	3	**Translation**	Original language of publication
Format (select all that apply)	Print, Electronic	**Copies for the disabled?**	No
		Minor editing privileges?	Yes
Who will republish the content?	Academic institution	**Incidental promotional use?**	No
Duration of Use	Current edition and up to 5 years	**Currency**	GBP
Lifetime Unit Quantity	Up to 499		
Rights Requested	Main product		

NEW WORK DETAILS

Title	Novel materials and device architectures forhigh-efficiency photovoltaic devices	**Institution name**	Imperial College London
		Expected presentation date	2020-09-01
Instructor name	n/a		

ADDITIONAL DETAILS

Order reference number	N/A	**The requesting person / organization to appear on the license**	Phoebe Pearce

REUSE CONTENT DETAILS

AIP PUBLISHING LICENSE TERMS AND CONDITIONS

Aug 13, 2020

This Agreement between Imperial College London -- Phoebe Pearce ("You") and AIP Publishing ("AIP Publishing") consists of your license details and the terms and conditions provided by AIP Publishing and Copyright Clearance Center.

License Number	4877121478755
License date	Jul 27, 2020
Licensed Content Publisher	AIP Publishing
Licensed Content Publication	Journal of Applied Physics
Licensed Content Title	The direct and indirect bandgaps of unstrained SixGe1−x−ySny and their photonic device applications
Licensed Content Author	P. Moontragoon, R. A. Soref, Z. Ikonic
Licensed Content Date	Oct 1, 2012
Licensed Content Volume	112
Licensed Content Issue	7
Type of Use	Thesis/Dissertation
Requestor type	Student
Format	Print and electronic
Portion	Figure/Table
Number of figures/tables	1
Title	Novel materials and device architectures forhigh-efficiency photovoltaic devices
Institution name	Imperial College London
Expected presentation date	Aug 2020
Portions	Fig. 2
Requestor Location	Imperial College London Department of Physics Imperial College London London, SW7 2AZ United Kingdom Attn: Imperial College London
Total	**0.00 GBP**
Terms and Conditions	

AIP Publishing -- Terms and Conditions: Permissions Uses

AIP Publishing hereby grants to you the non-exclusive right and license to use and/or distribute the Material according to the use specified in your order, on a one-time basis, for the specified term, with a maximum distribution equal to the number that you have ordered. Any links or other content accompanying the Material are not the subject of this license.

1. You agree to include the following copyright and permission notice with the reproduction of the Material:"Reprinted from [FULL CITATION], with the permission of AIP Publishing." For an article, the credit line and permission notice must be printed on the first page of the article or book chapter. For photographs, covers, or tables, the notice may appear with the Material, in a footnote, or in the reference list.
2. If you have licensed reuse of a figure, photograph, cover, or table, it is your responsibility to ensure that the material is original to AIP Publishing and does not contain the copyright of another entity, and that the copyright notice of the figure, photograph, cover, or table does not indicate that it was reprinted by AIP Publishing, with permission, from another source. Under no circumstances does AIP Publishing purport or intend to grant permission to reuse material to which it does not hold appropriate rights.
   You may not alter or modify the Material in any manner. You may translate the Material into another language only if you have licensed translation rights. You may not use the Material for promotional purposes.

ELSEVIER LICENSE TERMS AND CONDITIONS

Aug 13, 2020

This Agreement between Imperial College London -- Phoebe Pearce ("You") and Elsevier ("Elsevier") consists of your license details and the terms and conditions provided by Elsevier and Copyright Clearance Center.

License Number	4877131389449
License date	Jul 27, 2020
Licensed Content Publisher	Elsevier
Licensed Content Publication	Solar Energy Materials and Solar Cells
Licensed Content Title	Mid-infrared emissivity of crystalline silicon solar cells
Licensed Content Author	A. Riverola,A. Mellor,D. Alonso Alvarez,L. Ferre Llin,I. Guarracino,C.N. Markides,D.J. Paul,D. Chemisana,N. Ekins-Daukes
Licensed Content Date	Jan 1, 2018
Licensed Content Volume	174
Licensed Content Issue	n/a
Licensed Content Pages	9
Start Page	607
End Page	615
Type of Use	reuse in a thesis/dissertation
Portion	figures/tables/illustrations
Number of figures/tables/illustrations	1
Format	both print and electronic
Are you the author of this Elsevier article?	No
Will you be translating?	No
Title	Novel materials and device architectures forhigh-efficiency photovoltaic devices
Institution name	Imperial College London
Expected presentation date	Aug 2020
Portions	Fig. A1
Requestor Location	Imperial College London Department of Physics Imperial College London London, SW7 2AZ United Kingdom Attn: Imperial College London
Publisher Tax ID	GB 494 6272 12
Total	**0.00 USD**
Terms and Conditions	

INTRODUCTION

1. The publisher for this copyrighted material is Elsevier. By clicking "accept" in connection with completing this licensing transaction, you agree that the following terms and conditions apply to this transaction (along with the Billing and Payment terms and conditions established by Copyright Clearance Center, Inc. ("CCC"), at the time that you opened your Rightslink account and that are available at any time at http://myaccount.copyright.com).

GENERAL TERMS

2. Elsevier hereby grants you permission to reproduce the aforementioned material subject to the terms and conditions indicated.
3. Acknowledgement: If any part of the material to be used (for example, figures) has appeared in our publication with credit or acknowledgement to another source, permission must also be sought from that source. If such permission is not obtained then

Print

SPRINGER NATURE LICENSE TERMS AND CONDITIONS

Jan 15, 2021

This Agreement between Imperial College London -- Phoebe Pearce ("You") and Springer Nature ("Springer Nature") consists of your license details and the terms and conditions provided by Springer Nature and Copyright Clearance Center.

License Number	4990220170483
License date	Jan 15, 2021
Licensed Content Publisher	Springer Nature
Licensed Content Publication	Nature Energy
Licensed Content Title	A 19.9%-efficient ultrathin solar cell based on a 205-nm-thick GaAs absorber and a silver nanostructured back mirror
Licensed Content Author	Hung-Ling Chen et al
Licensed Content Date	Aug 5, 2019
Type of Use	Thesis/Dissertation
Requestor type	academic/university or research institute
Format	print and electronic
Portion	figures/tables/illustrations
Number of figures/tables/illustrations	1
High-res required	no
Will you be translating?	no